Unmixing of Phosphorus-bearing Melts on Earth and Mars

Dissertation

zur Erlangung des mathematisch-naturwissenschaftlichen Doktorgrades

"Doctor rerum naturalium"

der Georg-August-Universität Göttingen

im Promotionsprogramm Geowissenschaften / Geographie

der Georg-August University School of Science (GAUSS)

vorgelegt von

Tamara Miranda Busche

(geborene Jakobczyk)

aus Danzig, Polen

Göttingen, 2019

Betreuungsausschuss:

Prof. Dr. Sharon L. Webb
Abteilung experimentelle und angewandte Mineralogie
Geowissenschaftliches Zentrum der Georg-August-Universität Göttingen

Dr. Burkhard C. Schmidt
Abteilung experimentelle und angewandte Mineralogie
Geowissenschaftliches Zentrum der Georg-August-Universität Göttingen

Mitglieder der Prüfungskommission:

Referent 1
Prof. Dr. Sharon L. Webb
Abteilung experimentelle und angewandte Mineralogie
Geowissenschaftliches Zentrum der Georg-August-Universität Göttingen

Referent 2
Prof. Dr. Gerhard Wörner
Abteilung Geochemie
Geowissenschaftliches Zentrum der Georg-August-Universität Göttingen

Referent 3
Dr. Kirsten S. Techmer
Abteilung experimentelle und angewandte Mineralogie
Geowissenschaftliches Zentrum der Georg-August-Universität Göttingen

Weitere Mitglieder der Prüfungskommission:

Prof. Dr. Harald Behrens
Institut für Mineralogie
Leibniz Universität Hannover

Dr. Burkhard C. Schmidt
Abteilung experimentelle und angewandte Mineralogie
Geowissenschaftliches Zentrum der Georg-August-Universität Göttingen

Dr. Sara Fanara
Abteilung experimentelle und angewandte Mineralogie
Geowissenschaftliches Zentrum der Georg-August-Universität Göttingen

Tag der mündlichen Prüfung:

26.03.2019

Abstract

The aim of this study lies in the investigation on unmixing in aluminosilicate melts. Therefore, six glasses of peralkaline and peraluminous compositions were synthesized in the system CaO-Al_2O_3-SiO_2, Na_2O-Al_2O_3-SiO_2 and Na_2O-CaO-Al_2O_3-SiO_2. Additionally, a melt of Champagne composition was synthesized. Champagne is part of the Wishstone class rocks found on Gusev Crater on Mars and chemically resembles a basaltic melt with the exception that it exhibits naturally high P_2O_5 concentrations up to 10 wt% (Usui et al. 2008).

Afterwards, concentrations of up to 8 mol% P_2O_5 were added to the melts. Furthermore, up to 8 mol% B_2O_3, 6 mol% F^- and 6 mol% H_2O were added to selected melts. The synthesis of the water-free samples was performed in a 1 atm furnace whereas the synthesis of the water-bearing melts was conducted in an internally heated pressure vessel (IHPV).

Samples were analyzed with respect to the rheology and structure of the melts. The viscosity of the melts was measured by use of the micropenetration technique in the range of $10^{8.5}$ Pa s to $10^{13.5}$ Pa s. The heat capacity of the melts was determined using Differential Scanning Calorimetry (DSC). The structure of the glasses was analyzed using Raman Spectroscopy as well as Scanning Electron Microscopy (SEM). Additionally, an Fe^{2+}/Fe_{tot} determination was performed on the iron-bearing samples of Champagne composition by use of the micro-colorimetric determination of ferrous iron as described by Schuessler et al. (2008). This method was first introduced by Wilson (1960).

The addition of P_2O_5 to the melt shows a different effect on peralkaline than on peraluminous melts. In peralkaline melts the addition of P_2O_5 results in an increase in viscosity caused by a higher polymerisation of the melt network. The increase in viscosity occurs up to a maximum viscosity, further increasing P_2O_5 concentration in the melt after the viscosity maximum results in a decreasing viscosity and, hence, a depolymerisation of the melt. The effect of P_2O_5 on viscosity is strongest in melts containing both Na and Ca whereas the lowest effect on viscosity is observed in only Ca-bearing melts. In peraluminous melts the addition of P_2O_5 results in a decreasing viscosity and, thus, decreasing polymerisation of the melt. A similar trend was described by Toplis and Dingwell (1996a).

In iron-bearing melts the addition of P_2O_5 to the melts causes an increase in Fe^{2+}/Fe_{tot} ratio, which poses a contradiction to viscosity data. This implies that the effect of iron speciation on structure is less pronounced than the effect of P_2O_5.

The addition of B_2O_3 to the melt results in a decreasing viscosity. In case of peraluminous melts viscosity decreases linearly. In peralkaline melts viscosity decreases only slightly at

low B_2O_3 concentrations whereas the decrease of viscosity becomes stronger at higher B_2O_3 concentrations. The incorporation of fluorine into the melt structure also results in a decreasing viscosity of the melt. The addition of fluorine to P_2O_5-bearing melts from Champagne series as well as the addition of water to all investigated melts results in crystallization of apatite.

Unmixing of melts was mainly observed in peralkaline melts with high P_2O_5 concentrations that contain Fe and Ca as well as Na and Ca. Melts from the system CaO-Al_2O_3-SiO_2 begin unmixing upon tempering of the samples. The unmixed phases consist of spheres of both melts. In iron-free melts the average size of the spheres ranges from approximately 200 – 500 nm. However, the spheres can reach a size up to 100 µm as observed in Champagne melt with the highest P_2O_5 concentration. Chemical analysis of both melt phases indicate that the original homogeneous melts separates into a Si-Al as well as a Ca-(Fe)-P-rich melt. Furthermore, it is observed that divalent cations are preferably enriched in the Ca-(Fe)-P-rich melt.

Calculation of viscosity as well as heat capacities with models (Stebbins et al. 1984; Richet and Bottinga 1985; Richet 1987; Giordano et al. 2008b) demonstrates the strong effect of P_2O_5, B_2O_3 and F^- on melt structure since the calculated values differ from the measured values. Therefore, these elements should be included into future models.

Zusammenfassung

Das Ziel dieser Studie ist es den Einfluss von P_2O_5 auf die Entmischung in aluminosilikatischen Schmelzen zu untersuchen. Zu diesem Zweck wurden sechs Gläser von peralkaliner und peraluminöser Zusammensetzung aus dem CaO-Al_2O_3-SiO_2, Na_2O-Al_2O_3-SiO_2 und Na_2O-CaO-Al_2O_3-SiO_2 System synthetisiert. Zusätzlich wurde die Champagne Zusammensetzung hergestellt. Dabei handelt es sich um eine Gesteinsklasse aus der Whishstone class Zusammensetzung, die im Gusev Krater auf dem Mars zu finden ist. Champagne ähnelt von der chemischen Zusammensetzung her einem Basalt, mit der Ausnahme, dass es natürlich hohe P_2O_5 Gehalte bis zu 10 wt% aufweist (Usui et al. 2008).

Bis zu 8 mol% P_2O_5 wurden zu den Schmelzen hinzugefügt. Darüber hinaus wurden zu ausgewählten Schmelzen zusätzlich bis zu 8 mol% B_2O_3, 6 mol% F^- sowie 6 mol% H_2O hinzugegeben. Die Synthese der wasserfreien Proben erfolgte in einem 1 atm Ofen, wohingegen die Synthesen der wasserhaltigen Gläser in einer intern beheizten Gasdruckanlage (IHPV) durchgeführt wurden.

Die Schmelzen wurden anschließend eingehend auf ihre Rheologie und Struktur untersucht. Die Viskositäten der Schmelzen wurden mittels der Mikropenetrationsmethode im Bereich von $10^{8.5}$ Pa s bis $10^{13.5}$ Pa s gemessen. Die Wärmekapazität der Schmelzen wurde mittels dynamischer Differenz Kalorimetrie (DSC) bestimmt. Die Struktur der Gläser wurde mittels Raman Spektroskopie sowie Rasterelektronenmikroskopie (REM) aufgelöst. In den eisenhaltigen Gläsern der Champagne Serie wurde zusätzlich auch das Fe^{2+}/Fe_{tot} Verhältnis nasschemisch nach der Methode von Wilson (1960) bestimmt, die in Schuessler et al. (2008) beschrieben ist.

Die Zugabe von P_2O_5 zeigt einen unterschiedlichen Einfluss auf peralkaline und peraluminöse Schmelzen. In peralkalinen Schmelzen führt die Zugabe von P_2O_5 zu einer Erhöhung der Viskosität, die im Zusammenhang mit einer höheren Polymerisierung der Schmelze steht. Die Zunahme der Viskosität erfolgt bis zu einem Viskositätsmaximum, danach führt die weitere Zugabe von P_2O_5 zu einer Abnahme der Viskosität und somit zu einer Depolymerisierung der Schmelze. Dieser Effekt ist am stärksten zu beobachten in Schmelzen, die sowohl Na als auch Ca enthalten. Der geringste Einfluss von P_2O_5 auf die Viskosität wird in nur Ca-haltigen Schmelzen beobachtet. In peraluminösen Schmelzen führt die Zugabe von P_2O_5 zu einer Abnahme der Viskosität und somit einer Depolymerisierung der Schmelze. Ein ähnlicher Trend wurde von Toplis and Dingwell (1996a) beobachtet.

In eisenhaltigen Gläsern bewirk die Zugabe von P_2O_5 eine Erhöhung des Fe^{2+}/Fe_{tot}-Verhältnisses, was im Widerspruch zu den Viskositätsdaten steht. Das zeigt, dass der Einfluss der Eisenspezifikation auf die Struktur geringer ist, als der Einfluss von P_2O_5.

Die Zugabe von B_2O_3 führt zu einer Abnahme der Viskosität. Im Fall von peraluminösen Schmelzen nimmt die Viskosität linear ab, wohingegen in peralkalinen Schmelzen zunächst nur eine leichte Abnahme und bei höheren B_2O_3 Konzentrationen eine stärkere Abnahme der Viskosität verzeichnet wird. Der Einbau von Fluor in die Schmelzstruktur resultiert ebenfalls in einer Abnahme der Viskosität. Die Zugabe von Fluor zu P_2O_5-haltigen Schmelzen der Champagne Zusammensetzung sowie die Zugabe von H_2O zu allen untersuchten Schmelzen hat eine Kristallisation von Apatit zur Folge.

Die Entmischung von Schmelzen wurde hauptsächlich in peralkalinen Schmelzen mit hohen P_2O_5 Konzentrationen beobachtet, die Fe und Ca sowie Na und Ca enthalten. Schmelzen aus dem CaO-Al_2O_3-SiO_2 System beginnen beim Tempern zu entmischen. Die entmischten Phasen sind als Sphären zu erkennen. In den eisenfreien Schmelzen liegt die durchschnittliche Größe der Sphären bei ca. 200 – 500 nm. Bei der P_2O_5-reichsten Schmelze der Champagne Zusammensetzung erreichen die Sphären eine Größe bis ca. 100 µm. Messungen der chemischen Zusammensetzung beider Phasen ergeben, dass sich aus der ursprünglichen, homogenen Schmelze eine Ca-(Fe)-P reiche Schmelze entmischt und eine Si-Al-reiche Matrixschmelze zurückbleibt. Darüber hinaus ist zu erkennen, dass zweiwertige Kationen ebenso bevorzugt in der Ca-(Fe)-P reichen Schmelze angereichert werden.

Die Modellierung der Viskositäten sowie der Wärmekapazitäten nach gängigen Modellen (Stebbins et al. 1984; Richet and Bottinga 1985; Richet 1987; Giordano et al. 2008b) zeigt, dass P_2O_5, B_2O_3 und F^- die Schmelzstrukur stark beeinflussen. Daher sollten diese Oxide bei der Entwicklung von neuen Modellen berücksichtigt werden.

Preface

The idea for this study was proposed by Prof. Dr. Sharon Webb in form of a DFG proposal. This study focusses mainly on the effect of P_2O_5 on unmixing of aluminosilicate melts. Furthermore, the effect B_2O_3, F^- and H_2O on unmixing was investigated.

Liquid immiscibility in melts is of high interest in geological and technical processes. For instance, unmixing of melts is a dominant feature in ternary sodium borosilicate melts which encompass the chemical compositions of many commercial glasses (Haller et al. 1970).

Furthermore, liquid immiscibility is one of the possible mechanisms by which magmas may produce a variety of different rock types (Cassidy and Segnit 1955). Liquid immiscibility in natural rocks was first recognized by Roedder and Weiblen (1971a) for lunar rocks. Since then, liquid immiscibility between felsic Si-dominated and Fe-rich mafic silicate liquids was documented in many geological formations such as layered intrusions (Fischer et al. 2016; Holness et al. 2011; Jakobsen et al. 2011) and mid-ocean ridge magma chambers (Dixon and Rutherford 1979). It is also important in the understanding of the formation of ore deposits depending on the partitioning of the elements. Lester et al. (2013) found, that P, S, F and Cl preferentially partition into the Fe-rich immiscible liquid.

However, there is little data on the sole effect of P_2O_5 on unmixing in Fe-bearing and no data on the effect of P_2O_5 on unmixing of Fe-free melts. In this study we focus on the effect of the sole elements on unmixing to gain better understanding of the more complex geological processes in future.

This study is divided into four chapters. The 3rd chapter of this study focusses on the effect of only P_2O_5 or B_2O_3 on unmixing of peralkaline and peraluminous Fe-free melts. The 4th chapter describes the effect of P_2O_5 on unmixing of Champagne melt from Gusev Crater on Mars, which resembles a basaltic composition with naturally high P_2O_5 concentrations up to 10 wt% (Usui et al. 2008). Chapter 5 investigates the combined effect of P_2O_5, B_2O_3, F^- and H_2O on unmixing. In the last chapter we demonstrate the effect of tempering on unmixing of melts.

Danksagung

Ein besonderer Dank gilt Frau Prof. Dr. Sharon Webb und Dr. Burkhard Schmidt für die Bereitstellung des Themas der Doktorarbeit sowie die sehr gute Betreuung während ihrer Durchführung und ihr stets offenes Ohr für Fragen und Diskussionen.

Ich danke ebenso meiner Freundin und Kollegin Wiebke Pischel, die mir jederzeit bei praktischen und theoretischen Fragen mit hilfreichen Diskussionen zur Seite stand. Ich möchte mich ebenso bei meinen Freunden und Arbeitskollegen für die nette Arbeitsatmosphäre sowie Unterstützung bei den Versuchen und technischen Fragen bedanken. Besonders danke ich hierbei Dr. Sara Fanara, Bettina Schlieper-Ludewig, Marina Horstmann, Petra Wolfrath, Alexander Masurowski, Max Schanofski, Christin Kleest, Caren Sundermeyer und Jan Tomasek.

Darüber hinaus möchte ich mich ganz herzlich bei Frau Dr. Techmer für die Betreuung am REM, bei Herrn Dr. Andreas Kronz für seine Unterstützung an der Mikrosonde sowie Lucia Pappalardo vom INGV in Neapel für die Durchführung der röntgentomographischen Messungen bedanken.

Ich möchte mich ebenso bei Sören Henning für das Korrekturlesen meiner Arbeit und seine hilfreichen Anmerkungen zu meiner Doktorarbeit bedanken.

Der größte Dank gilt meiner Familie und vor allem meinem Ehemann Christopher Busche für die Ermutigung und Unterstützung während meiner Doktorarbeit.

Content

1 Introduction

1.1 Structure of Silicate Glasses

Glasses are widespread materials in our everyday environment, whereby there is a difference between natural and synthetic glasses. Natural glasses such as obsidian are formed through the rapid cooling of a lava. Early in human history, obsidian was used to produce weapons and knifes due to its sharp edges (Shelby 2005).

Nowadays, there is a wide range of applications for technical glasses and their purpose strives far from the original purpose of drinking and window glasses. For example, borosilicate glasses are highly valuable due to their high chemical resistance. Furthermore, optical glass fibres revolutionized our telecommunication by presenting a method of quick and flawless data transmit all over the world (Shelby 2005).

Glasses are formed by the rapid cooling of a melt and characterized by two main properties. First, glasses are amorphous solids which exhibit only a short-range order. Second, and even more important is the fact that glasses exhibit a time-dependent glass transformation behaviour which occurs over the glass transition temperature range (Shelby 2005; Stebbins 2016).

When speaking of glasses most people think of silicate glasses. However, there is also a number of organic glasses and recently, metallic glasses become more popular (Shelby 2005). The structure of silicate glasses is described in Fig. 1. The structure of glasses is mainly built by network formers such as e.g. Si^{4+}, Al^{3+} and Fe^{3+} which occupy tetrahedral positions and connect to other tetrahedra via oxygen bonds. These oxygen bonds are bridging oxygens (BO) since they connect the tetrahedra and thus increase the polymerisation of the melt structure. Trivalent cations result in a negative charge of the tetrahedra which are compensated by mono- or divalent cations such as e.g. Na^{+} and Ca^{2+}. These are called charge balancing cations (Shelby 2005; Stebbins 2016).

However, mono- and divalent cations which are not needed for charge compensation bond to oxygens from tetrahedra and produce non-bridging oxygen bonds (NBO). The formation of NBO's decreases the polymerisation of the melt and these cations are called network modifying cations (Stebbins 2016).

Phosphorus occurs in natural melts in low concentrations of approximately 2 – 3 wt% (Kushiro 1975; Mysen et al. 1981a). Higher phosphorus concentrations are found in pegmatites (Thomas and Webster 2000; London 2008). The highest P_2O_5 concentrations of ~10 wt% were reported in Champagne rocks from Gusev Crater on Mars (Usui et al. 2008). Furthermore, phosphorus is of high interest in the development of biomedical

glasses which may serve as a replacement for human bones (Hill and Brauer 2011) as well as tissue engineering (Ahmed et al. 2004).

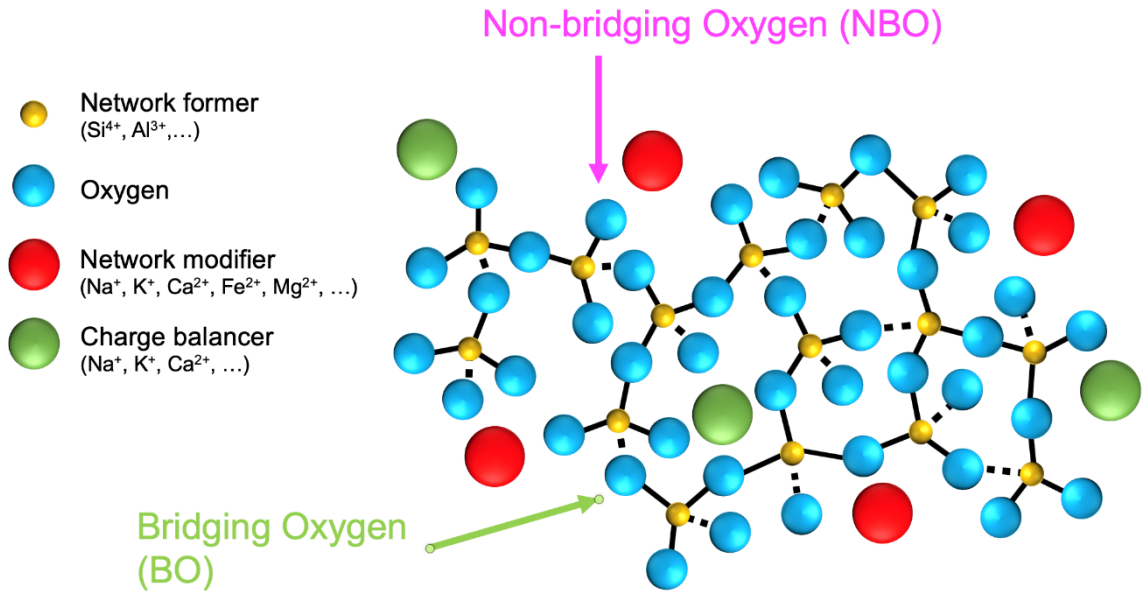

***Fig. 1**: The structure of aluminosilicate melts modified after Stebbins (2016).*

P_2O_5 was found to enter the melt structure as tetrahedrally coordinated PO_4^{3-} with three single and one double bond to the oxygen atoms (e.g Mysen et al. 1981a). Previous studies on structure of P_2O_5-bearing glasses and melts demonstrate the complex incorporation mechanism of P_2O_5 into the melt structure (e.g. Mysen 1998b). The incorporation mechanism of P_2O_5 is dependent on the peralkalinity of the melt. For instance, Toplis and Schaller (1998) have shown that in peralkaline melts, PO_4^{3-} behaves as a network former and bonds to cations in network modifying positions such as Na^+ and Ca^{2+} which results in a polymerisation of the melt structure due to the formation of more bridging oxygen bonds.

In peraluminous melts, however, PO_4^{3-} complexes remove Al^{3+} from tetrahedral positions, resulting the formation of structural units similar to $AlPO_4$ as found in berlinite (Mysen 1998b) and in the freeing of cations in previously charge balancing roles which now act as network modifier and depolymerise the melt structure. Weather the PO_4^{3-} structural units remain in the silicate melt network or form a separate melt phase remains a matter for discussion.

1.2 Immiscibility in Silicate Melts

The most prominent example for liquid immiscibility is demonstrated by the mixing of water and oil. When mixed, these two liquids do not result in one homogeneous liquid but rather

in the formation of oil droplets which are embedded in a continuous matrix of the water phase. With time, the two liquid phases will separate completely whereby the liquid with lower density will be floating on top of the liquid with higher density (Shelby 2005).

Liquid-liquid immiscibility is a common process in liquid systems and also melts and is reported for several systems such as, for example, ternary sodium borosilicate systems which are of importance as commercial glasses (Haller et al. 1970; Shelby 2005). Furthermore, liquid immiscibility was also reported for several natural systems and is a possible differentiation mechanism in diverse magmas (Lester et al. 2013).

Liquid immiscibility in natural samples was first recognized in lunar rocks (Roedder and Weiblen 1971a) and is currently a matter for debate for the formation of large layered intrusions such as the Bushveld complex (Fischer et al. 2016), Sept-Iles layered intrusion (Jakobsen et al. 2005, 2011; Holness et al. 2011) as well as the formation of large iron oxide-apatite deposits (Hou et al. 2018). Furthermore, it was also documented in mid-ocean ridge magma chambers (Dixon and Rutherford 1979).

The formation of phase separation is described by the free energy of mixing (ΔG_m) which is described by following equation (e.g. Shelby 2005; Ryerson and Hess 1978):

$$\Delta G_m = \Delta H_m - T\Delta S_m \qquad (Eq.\,I)$$

Whereby ΔH_m represents the enthalpy of mixing, ΔS_m is the entropy of mixing and T is the temperature.

If the mixing of two components results in a lower free energy of the system, the melt will remain homogeneous. However, if the free energy of the system is increased by mixing, the melts or liquid will separate into two liquids (Shelby 2005).

The common mechanisms for liquid separation have been described by several authors (e.g. De Wys. E. C. 1960; Shelby 2005; Wheaton and Clare 2007) and are summarized in Fig. 2 for a simple binary system consisting of oxide X and Y. Liquid immiscibility occurs in two mechanisms, which are described as the nucleation and growth process and spinodal decomposition (Shelby 2005; Wheaton and Clare 2007). The nucleation and growth process is characterised by the formation of small droplets of phase B which are embedded in a continuous matrix of phase A. The nucleation occurs spontaneously and the formed melt droplets show a poor connectivity. As the concentration of phase B increases, the system moves to the spinodal decomposition region. This process begins as small chemical fluctuations which, if given time, grow into two continuous interpenetrating phases. At further

increasing concentration of oxide Y the system returns to the nucleation and growth process whereby small spheres of phase A are embedded in a continuous matrix of phase B (Wheaton and Clare 2007).

Previous studies have shown that P_2O_5 bonds to Al^{3+} as well as cations in network modifying positions resulting in the formation of phosphate complexes (e.g. Toplis and Schaller 1998; Mysen 1998b; Gan and Hess 1992b). Gan and Hess (1992b) argued that these complexes reside outside the aluminosilicate melt structure but found no direct evidence for this hypothesis. In this study we focus on the effect of P_2O_5 on unmixing of melts and provide evidence for the theory provided by Gan and Hess (1992b).

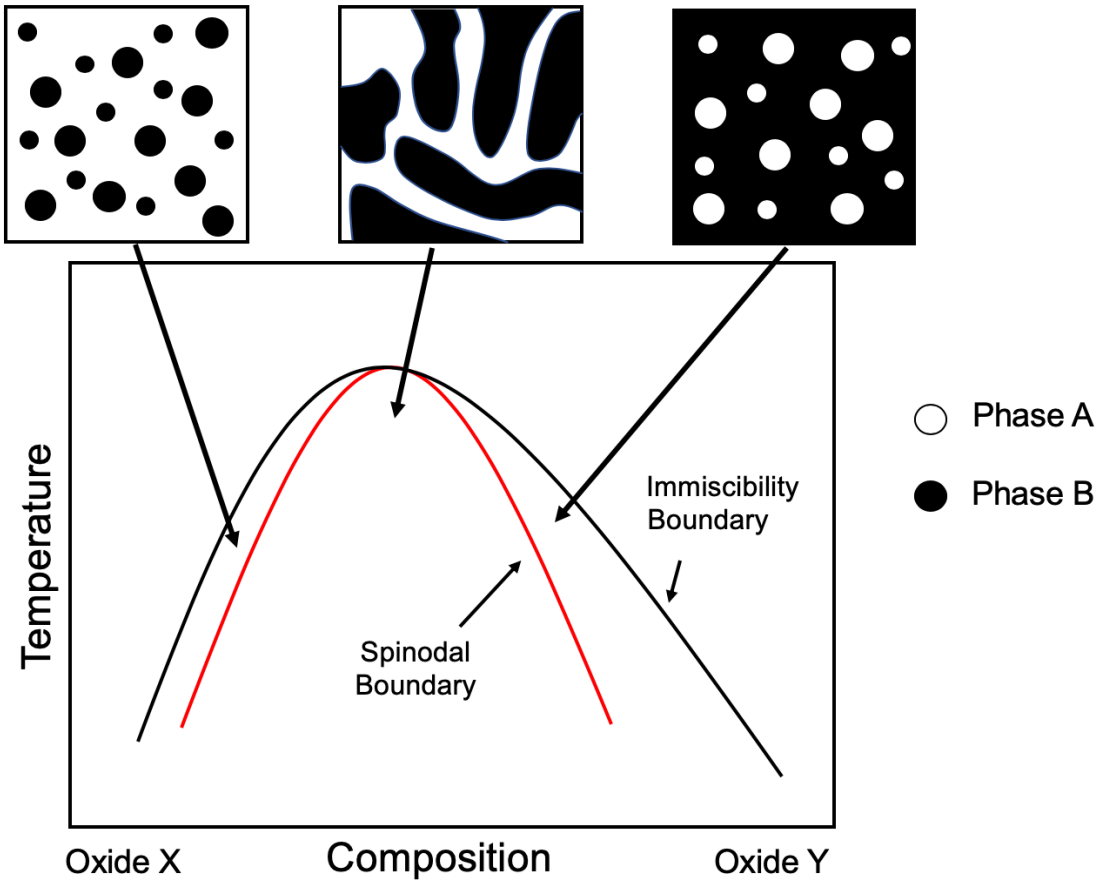

***Fig. 2**: Schematic immiscibility diagram for a binary composition consisting of two oxides X and Y modified after Wheaton and Clare (2007).*

2 Experimental Methods

2.1 Electron Microprobe Analysis (EMPA)

The chemical composition of the samples was determined by measurements on a JEOL JXA 8900 microprobe which is equipped with a wavelength as well as an energy dispersive system. For this study the wavelength dispersive spectrometers were used for quantitative element analysis.

For these measurements, samples were fixed in epoxy and polished up to a grain size of 1 µm diameter. In case of B_2O_3-bearing samples the polishing refinement was increased to 0.5 µm. Afterwards, samples were dried in a vacuum cabinet dryer at 343 K and afterwards coated with carbon.

Measurements of the chemical compositions were performed by analysing 10 points on one sample in order to confirm homogeneity of the samples. Furthermore, element mappings were obtained for chosen samples. Samples were measured with an accelerating voltage of 15 kV and a beam current of 15 nA as well as a spot size of 30 µm. In case of B_2O_3-bearing samples the accelerating voltage was reduced to 10 kV.

2.2 Micro-colorimetric Determination of Ferrous Iron

The Fe^{2+}/Fe_{tot} ratios were acquired using the method after Wilson (1960) which is described in Schuessler et al. (2008). The powdered samples were decomposed in hydrofluoric acid in the presence of ammonium vanadate for 24 h, where the following reversible reaction takes place:

$$Fe^{2+} + V^{5+} \underset{pH \sim 5}{\Longleftrightarrow} Fe^{3+} + V^{4+} \qquad Eq.(II)$$

Under strongly acidic conditions the reaction shifts to the right side, resulting in the oxidation of Fe^{2+} released from the samples. After complete decomposition saturated boric acid was added in order to neutralize the HF. Ammonium acetate was added as a buffer to raise the pH of the solution to pH = 5, at which the Fe^{2+} is regenerated by the oxidation of V^{4+}. A 2:2'bipyridil was added which forms a red coloured complex with the dissolved Fe^{2+}.

In order to measure the total iron, ~5 mg of hydroxylamine hydrochloride were added to reduce all present Fe^{3+} to Fe^{2+}.

The oxidized and reduced samples were measured with an AvaSpec-UV/VIS/NIR – dual channel broad band spectrometer. The peak intensities of the absorption at 523 cm^{-1} correspond to Fe^{2+}. The Fe^{2+}/Fe_{tot} ratios were thus obtained directly from the absorption spectra with the following equation:

$$\frac{Fe^{2+}}{Fe_{tot}} = \frac{A_{523}\ oxidized\ samples}{A_{523}\ reduced\ samples} \qquad Eq.(III)$$

For the calculation of Fe^{2+} concentration a calibration was done by measuring 8 Fe^{2+} solutions of known Fe^{2+} concentration. Measured Fe^{2+}/Fe_{tot} concentrations were checked by measuring standards of known Fe^{2+}/Fe_{tot} ratios to ensure the accurateness of the measurements. Fe^{2+} concentration was calculated utilizing following equation:

$$Fe^{2+}[wt\%] = \frac{\frac{(A_{523})}{\varepsilon_{523} * l} * V_{dil}}{m_{sample} * 10} \qquad Eq.(IV)$$

Where A_{523} is the baseline-corrected absorbance of the sample, ε is the extinction coefficient in ml μg^{-1} cm^{-1}, V_{dil} is the volume of the flask in ml, l is the length of the cuvette (1 cm) an m is the sample weight in mg.

The error is given by following equation:

$$\pm Fe^{2+}[wt\%] = Fe^{2+}[wt\%] * \sqrt{\left(\frac{\Delta A_{523}}{A_{523}}\right)^2 + \left(\frac{\Delta \varepsilon_{523}}{\varepsilon_{523}}\right)^2 + \left(\frac{\Delta m_{sample}}{m_{sample}}\right)^2 + \left(\frac{\Delta V_{dil}}{AV_{dil}}\right)^2} \qquad Eq.(V)$$

Where ΔA_{523}, $\Delta\varepsilon$, Δm_{sample} and ΔV_{dil} are the errors of the absorption (0.004 abs units), the extinction coefficient (uncertainty of the slope), the sample weight (0.01 mg) and volume of the volumetric flask (0.1 mL), respectively.

2.3 Micropenetration Viscometry

The viscosity η of a melt is defined as the ratio between stress (σ) and strain rate (ε) as described by the following equation (Webb and Dingwell 1995):

$$\eta = \frac{\sigma}{\varepsilon} \qquad (Eq.VI)$$

Therefore, the viscosity is determined by the mechanism by which silicate melts flow, whereby the most common mechanism is the exchange of Si-O bonds (Webb et al. 2007).

High viscosities in the Range of $10^{8.5}$ Pa s to $10^{13.5}$ Pa s of the melts were measured using the micropenetration technique on a Netzsch TMA 402 dilatometer, based on the method described by Pocklington (1940). The method is based on the penetration of a sphere of a known diameter into a polished glass cylinder by applying force at a fixed temperature and over time. Fig. 3 shows the setting inside the sample holder prepared for viscosity measurements.

***Fig. 3**: Sample holder as used for viscosity determination by using the micropenetration technique.*

The samples were heated with 10 K min^{-1} up to 20 K below the desired temperature, the last 20 K were heated with a rate of 3 K min^{-1}. This is necessary in order to allow thermal relaxation of the glasses. Viscosities were obtained by forcing a single sphere of a known diameter of approximately 2000 µm into the melt. Therefore, we applied force in the range of 0.1 N to 150 N, depending on the temperature.

The temperature was measured with an S-type thermocouple with an accuracy of ± 0.5 K. The thermocouple was calibrated to the melting temperatures of Bi (271.4°C), Zn (419.6°C), Al (660.3°C), NaCl (801°C) and Ag (961.8°C). The accuracy of the viscosity determination was determined from measurements of the viscosity of the DGG-1 standard glass. An error of ± 0.08 $\log_{10}$ Pa s is given for each viscosity determination.

The viscosities were calculated using the following equation after Pocklington (1940):

$$\eta = \frac{0.1875\ F\ t}{\sqrt{r}\sqrt{l^3}} \qquad Eq.(VII)$$

Where η is the viscosity in Pa s, F the applied force in kg m s^{-2}, t the time in s, r the diameter of the penetrating sphere in m and l the indent distance in m.

2.4 Differential Scanning Calorimetry (DSC)

Measurements of the heat capacities of the samples were performed on a Netzsch DSC 404C differential scanning calorimeter in Ar atmosphere. The samples were polished and placed in Pt crucibles and heated and cooled with 20 K min^{-1} up to the temperature of the relaxed melt (viscosity ~ 10^9 Pa s). The heat capacities of the samples were measured against the heat capacity of an empty crucible. Fig. 4 shows the sample holder as used for the measurements. The calorimeter was calibrated by measuring the heat capacity of a single crystal of Al_2O_3 and the heat capacity data of Robie et al. (1978b) .

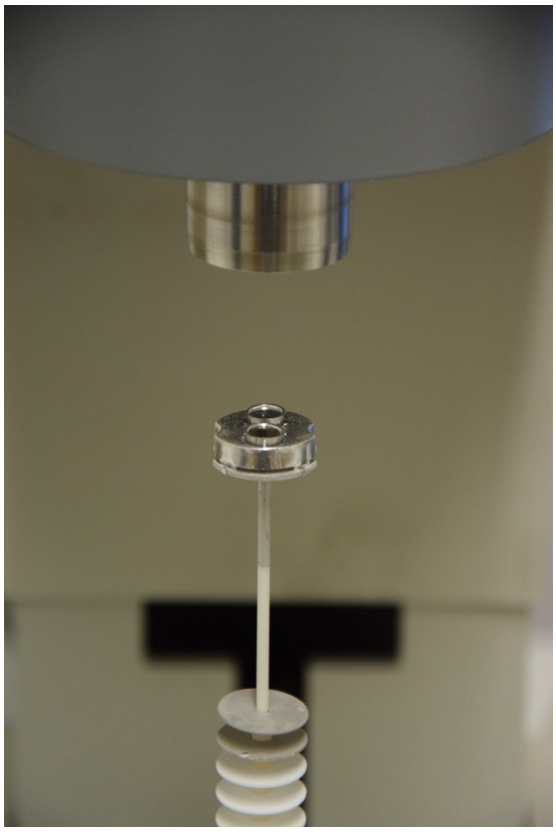

***Fig. 4**: Sample holder as used for heat capacity measurements.*

Samples were measured at least two times and calibration was repeated after 10 - 15 measurements, leaving an error of the heat capacity data of < 1%.

Heat capacity data describes the thermal history of a melt. In particular, the magnitude of the heat capacity C_p as well as the configurational entropy S_{conf} of the melt is of high importance in the modelling of thermodynamic behaviour during the cooling of a magma chamber as well as crystallisation and eruption processes (Webb 2008). The fictive temperature T_f' describes the structure of the frozen glass (Webb 1997).

In order to calculate the heat capacity of the glass (C_{pg}), the heat capacity of the liquid (C_{pl}), the configurational heat capacity (C_p^{conf}), the fictive temperature (T_f') as well as S_{conf} data was fitted using the equation after Maier and Kelley (1932):

$$C_p = \ a + bT - cT^{-2} \qquad Eq.(VIII)$$

Where *T* is the temperature in K and *a*, *b* and *c* are fit parameters of the Maier-Kelley equation. The Maier-Kelley fit was applied to the onset of the glass transition range.

2.5 Raman Spectroscopy

The structure of the melts was investigated by measuring unpolarised Raman spectra of the glasses in the range 250 cm^{-1} - 2000 cm^{-1} on a Horiba Jobin Yvon LabRam HR800UV spectrometer (Fig. 5) which is equipped with an Olympus BX41 optical microscope. This method is based on the Raman effect. The Raman effect is described as the inelastic scattering of light which is caused by molecules (Long 1977).

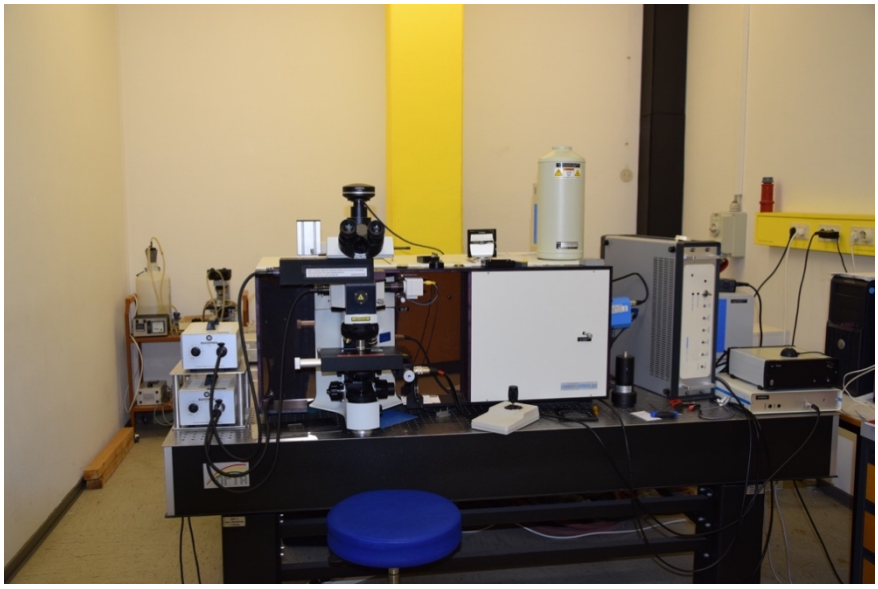

***Fig. 5**: Picture of the Raman spectrometer JOBIN YVON LabRam HR800UV.*

Sample excitation was achieved by using a 488 nm diode laser operating at 50 mW. Measurements were performed at a 100x magnification whereby the confocal hole was set to 100 µm. A grating of 600 grooves mm^{-1} was applied. The acquisition time was set to 60 s by a repetition of two. All spectra are baseline-corrected as well as temperature- and frequency-corrected after Long (1977).

The artificial high intensity at low frequency is corrected using the correction factor R(ν) which is described as follows (Di Muro et al. 2009):

$$R(\nu) = \frac{\nu_0^3 * \left[1 - \exp\left(\frac{-hc\,\nu_i}{kT}\right)\right] * \nu_i}{(\nu_0 - \nu_i)^4} \qquad Eq.(IX)$$

Where ν_0 is the frequency of laser excitation in cm^{-1}, ν_i the frequency of the Raman shift in cm^{-1}, *h* the Planck constant, *k* the Boltzmann constant, *c* the velocity of light in cm s^{-1} and *T* is the temperature in K.

2.6 Scanning Electron Microscopy (SEM)

Backscattered and secondary electron images of the samples were taken on a FEI Quanta 200 FEG scanning electron microscope, which is equipped with an EDAX EDX detector. Samples were coated with carbon before measurements. The accelerating voltage was set between 15 and 25 kV by a probe current of 15 nA.

EDX measurements of the samples were acquired by collecting count rates over a time span of approximately 60 live seconds (actual time of measurement subtracted by the dead time of the detector). Furthermore, for selected samples element mappings were obtained by EDX measurements over 7h.

2.7 IHPV Experiments

Since pressure is needed in order to incorporate water into the structure of melts, the synthesis of those melts was performed in an Internally Heated Pressure Vessel (IHPV) (see Fig. 6). An amount of approximately 100 mg of glass powder was weighted into $Au^{75}Pd^{25}$ capsules. Amounts of 3 and 6 mol% of liquid water were added to all samples before closing the capsules by using a PUK welding device from Lambert GmbH. The closed capsules were heated to 383 K for approximately 24 h in order to perform a leak test.

***Fig. 6**: Internally Heated Pressure Vessel (IHPV).*

The synthesis of the water-bearing samples was performed at 1533 K for a duration of 24 h and at 2 kbar pressure, whereby Ar was used a pressure medium. The temperature in the IHPV is controlled by 3 thermocouples. The capsules were placed in Pt crucibles and hung on a Pt wire. The IHPV is equipped with a rapid quench device, which reaches quench rates of 150 K min^{-1} by melting the Pt wire with a current pulse and thus enables an isobaric cooling process.

3 The effect of P_2O_5 and B_2O_3 on structure and rheology of silicate melts

3.1 Abstract

In this study we investigate the effect of P_2O_5 and B_2O_5 on the structure and unmixing of aluminosilicate melts. Therefore, six glasses of peraluminous and peralkaline composition were synthesized in the CaO-Al_2O_3-SiO_2, Na_2O-Al_2O_3-SiO_2 and Na_2O-CaO-Al_2O_3-SiO_2 system at 1 atm in air. Afterwards, the melts were doped with P_2O_5 and B_2O_3 concentrations up to 8 mol%. The rheology of the melts was investigated using micropenetration viscometry and Differential Scanning Calorimetry (DSC). The structure of the melts was analysed by Scanning Electron Microscopy (SEM) as well as Raman spectroscopy. P_2O_5 shows a different effect on viscosity of peralkaline and peraluminous melts. In peraluminous melts the addition of P_2O_5 results in a decrease of viscosity and thus a depolymerisation of the melt, whereas in peralkaline melts viscosity increases up to a maximum and then decreases with further increasing P_2O_5 concentration, indicating a stronger polymerisation of the melt at low P_2O_5 concentrations followed by a depolymerisation of the melt structure at higher P_2O_5 concentrations. The addition of B_2O_3 to the melt results in a decrease of viscosity and thus in a depolymerisation of the melt structure. In peraluminous melts a constant decrease in viscosity is observed whereas in peralkaline melts viscosity decreases only slightly at low B_2O_3 concentrations. At higher B_2O_3 concentrations the viscosity decreases more strongly. P_2O_5 enters the melts structure as PO_4^{3-} species which is visible in form of a peak at ~950 cm^{-1}. Unmixing occurs in P_2O_5-bearing melts from peralkaline NCAS13 series whereby the melt presumably separates into a Si- and a P-rich melt. Unmixing is evident in form of a second glass transition peak in heat capacity data. Furthermore, the unmixed melt phases are recognized as small light-grey spheres (~200 nm) in a continuous, dark-grey matrix by SEM technique. No unmixing is observed for peraluminous P_2O_5-bearing as well as all B_2O_3-bearing melts.

3.2 Introduction

P_2O_5 is generally present in low concentrations in natural silicate melts (Mysen et al. 1981a; Mysen 1998b). Despite its low abundance of < 2 - 3 wt% P_2O_5 is known to have a strong effect on the structure of melts (Kushiro 1975; Mysen et al. 1981a; Mysen 1998b). In some cases, rock compositions with higher P_2O_5 concentrations of up to 10 wt% have been found on Earth in pegmatites and on Mars (London 1987; Usui et al. 2008). P_2O_5 also plays an important role in applied sciences, for instance in biomedical glasses (Hill and Brauer 2011). The structural role of P_2O_5 in silicate melts has been previously investigated and found to be strongly dependent on the alkali/Al ratio of the melts (Ryerson and Hess 1980; Mysen et al. 1981a; Gan and Hess 1992b; Toplis and Dingwell 1996a; Toplis and Reynard 2000;).

B_2O_3 is strongly enriched (> 3 wt%) in pegmatites as evident from crystallized intrusions (London 1987). Furthermore, Dingwell et al. (1992) demonstrated the viscosity decreasing effect of low concentrations of up to 10 wt% B_2O_3 on haplogranitic melts. In addition, B_2O_3 is of great importance in technical glasses and as such there are many studies investigating the structural role of B_2O_3 in silicate melts (Konijnendijk 1975; Meera and Ramakrishna 1993; Lenoir et al. 2008; Koroleva et al. 2011; Cochain et al. 2013).

Immiscibility of natural magmas can occur due to the structural rearrangement upon the cooling of a melt (Thompson et al. 2007). It was first recognized in lunar rocks (Roedder and Weiblen 1971a) and remains a matter of discussion until now. Liquid immiscibility on Earth has also been reported as a mechanism for large apatite layered intrusions (Jakobsen et al. 2005, 2011; Holness et al. 2011; Fischer et al. 2016; Hou et al. 2018). Due to the fact that P_2O_5 is an incompatible element, its enrichment in late stage magmas may result in liquid immiscibility (Dixon and Rutherford 1979).

Several studies discuss the expanding of the immiscibility gap between felsic and mafic melts with increasing P_2O_5 concentrations (e.g. Ryerson and Hess 1980; Mysen et al. 1981a). The effect of P_2O_5 on immiscibility and rare-earth element partitioning in silicate melts has also been known to show a significant role in pegmatites (Thomas and Webster 2000; London 2009). High B_2O_3 concentrations in melts have also been found to result in liquid immiscibility of the melts (Haller et al. 1970; Tomozawa et al. 1992).

However, only few studies directly investigate the effect of P_2O_5 on unmixing. In this study we prepared six different simple melt compositions with constant Si, Al, Na and Ca contents in order to investigate solely the effect of P_2O_5 on unmixing.

Three of those melts are peralkaline and three melts are peraluminous to cover all the known incorporation mechanisms of P_2O_5. In addition, two of those samples were chosen to investigate the effect of B_2O_3 on liquid immiscibility in the melts.

The exact compositions of the melts were measured with electron microprobe analysis. The structure and physical properties of the melts was characterized by using micropenetration viscometry, differential scanning calorimetry (DSC), Raman spectroscopy as well as scanning electron microscopy (SEM).

3.3 Starting Material

In order to gain better understanding of the effect of P_2O_5 and B_2O_3 on unmixing, simple Na_2O-Al_2O_3-SiO_2 (NAS), CaO-Al_2O_3-SiO_2 (CAS) and Na_2O-CaO-Al_2O_3-SiO_2 (NCAS) with the same SiO_2, Al_2O_3 and alkali content were chosen as peralkaline and peraluminous melts. Glasses were synthesized from oxide and carbonate compounds which were previously dried at 383 K (Al_2O_3, $CaCO_3$ and Na_2CO_3) and 1273 K (SiO_2). After mixing, the powders were decarbonatized at 1273 K for a duration of 12 h. Afterwards, glasses were melted at least two times and crushed in order to improve homogeneity at temperatures between 1773 and 1873 K in a $MoSi_2$ furnace at 1 atm and afterwards quenched in water.

Subsequently, amounts of 2, 4, 6 and 8 mol% of P_2O_5 and B_2O_3 were added in form of $(NH_4)_2HPO_4$ and H_3BO_3 to the melts and synthesized again at 1773 and 1873 K for 3 – 6 h for the phosphorus-bearing glasses and at 1773 K for 3 – 4 h for the boron-bearing glasses. All glasses were investigated by optical microscopy and some with X-Ray diffraction and were found to be free of bubbles and crystals.

The exact compositions of the P_2O_5-bearing glasses were measured with a JEOL JXA 8900RL electron microprobe with a beam diameter of 30 µm and an accelerating voltage of 15 kV and are shown in Table 1 and Table 2. The microprobe was calibrated by using Wollastonite (Si), Anorthite (Ca, Al), Albite (Na) and Apatite (P) as standards.

Samples containing B_2O_3 were measured with a beam diameter of 30 µm and an accelerating voltage of 10 kV. Danburite was used as a standard for boron. Boron is very difficult to measure with an electron microprobe and it has to be noted that while measuring B_2O_3 all samples contained a small amount of B_2O_3 (<0.4 wt%), even the B_2O_3-free samples. Therefore, it has to be noted that the measured B_2O_3 concentrations are slightly higher than the actual concentrations in the glasses, but since the error is constant it does not change the observed trends in this study.

***Table 1**: Glass composition in wt% as measured by electron microprobe analysis*

[wt%]	SiO_2	2σ	Al_2O_3	2σ	Na_2O	2σ	CaO	2σ	P_2O_5	2σ	B_2O_3	2σ	total
CAS19	60.26	0.17	21.02	0.10	-	-	17.17	0.10	-	-	-	-	98.45
CAS19-P2	57.57	0.16	19.69	0.09	-	-	16.64	0.10	3.82	0.09	-	-	97.73
CAS19-P4	54.91	0.16	18.77	0.09	-	-	15.87	0.10	7.36	0.12	-	-	96.91
CAS19-P6	52.40	0.16	17.81	0.09	-	-	15.13	0.10	10.79	0.14	-	-	96.13
CAS19-P8	51.01	0.15	17.37	0.09	-	-	14.40	0.10	15.74	0.17	-	-	98.52
CAS14	58.96	0.17	26.59	0.11	-	-	12.83	0.09	-	-	-	-	98.38
CAS14-P2	56.71	0.17	26.20	0.11	-	-	11.98	0.09	3.93	0.10	-	-	98.81
CAS14-P4	54.26	0.16	25.25	0.11	-	-	11.57	0.09	7.82	0.14	-	-	98.91
CAS14-P6	52.44	0.16	24.06	0.11	-	-	11.10	0.08	11.34	0.17	-	-	98.94
CAS14-P8	50.53	0.16	23.14	0.10	-	-	10.73	0.08	14.67	0.19	-	-	99.07
NAS19	59.77	0.17	21.76	0.10	18.11	0.13	-	-	-		-	-	99.64
NAS19-P2	58.24	0.17	21.23	0.10	17.16	0.13	-	-	2.94	0.08	-	-	99.57
NAS19-P4	56.24	0.16	20.29	0.10	14.56	0.12	-	-	7.75	0.12	-	-	98.84
NAS19-P6	53.43	0.16	18.70	0.10	15.82	0.12	-	-	11.17	0.16	-	-	99.11
NAS19-P8	51.22	0.16	18.88	0.10	14.01	0.11	-	-	13.53	0.23	-	-	97.63
NAS14	58.24	0.17	28.16	0.12	13.27	0.11	-	-	-	-	-	-	99.67
NAS14-P2	56.45	0.17	26.14	0.11	12.93	0.11	-	-	3.84	0.10	-	-	99.35
NAS14-P4	54.42	0.17	25.27	0.11	12.29	0.11	-	-	7.17	0.13	-	-	99.15
NAS14-P6	52.83	0.17	24.47	0.11	11.36	0.10	-	-	10.29	0.15	-	-	98.94
NAS14-P8	51.56	0.16	23.78	0.11	10.86	0.10	-	-	12.90	0.18	-	-	99.10

***Table 1**: continued*

[wt%]	SiO_2	2σ	Al_2O_3	2σ	Na_2O	2σ	CaO	2σ	P_2O_5	2σ	B_2O_3	2σ	total
NCAS13	59.68	0.17	20.58	0.10	12.94	0.11	5.73	0.06	-	-	-	-	98.94
NCAS13-P2	57.93	0.17	20.34	0.10	11.64	0.11	5.57	0.06	3.76	0.08	-	-	99.23
NCAS13-P4	55.44	0.16	19.81	0.10	11.17	0.10	5.33	0.06	7.52	0.12	-	-	99.27
NCAS13-P6	53.08	0.16	19.10	0.09	10.59	0.10	5.09	0.06	11.15	0.14	-	-	99.00
NCAS13-P8	51.36	0.15	18.36	0.09	9.76	0.10	4.96	0.06	14.43	0.16	-	-	98.86
NCAS13-B2	60.62	0.14	20.70	0.08	12.11	0.08	5.77	0.07	-	-	1.39	0.09	100.58
NCAS13-B4	60.16	0.16	20.63	0.09	11.67	0.08	5.75	0.07	-	-	2.03	0.10	100.24
NCAS13-B6	59.27	0.11	20.27	0.06	11.24	0.06	5.85	0.05	-	-	3.38	0.08	100.02
NCAS13-B8	58.96	0.16	20.07	0.09	11.38	0.08	5.50	0.07	-	-	3.91	0.12	99.81
NCAS10	56.76	0.16	26.84	0.11	9.65	0.10	4.31	0.05	-	-	-	-	97.56
NCAS10-P2	56.41	0.17	26.10	0.11	8.81	0.09	4.16	0.05	3.93	0.10	-	-	99.41
NCAS10-P4	54.13	0.16	25.02	0.11	8.45	0.09	3.94	0.05	7.61	0.14	-	-	99.15
NCAS10-P6	53.32	0.16	24.62	0.10	7.76	0.12	3.68	0.05	9.93	0.16	-	-	99.31
NCAS10-P8	49.69	0.16	23.19	0.10	7.26	0.08	3.83	0.05	14.85	0.19	-	-	98.81
NCAS10-B2	58.54	0.16	27.32	0.10	9.06	0.07	4.24	0.06	-	-	1.42	0.10	100.57
NCAS10-B4	57.56	0.16	26.73	0.10	9.05	0.07	4.22	0.06	-	-	2.57	0.10	100.13
NCAS10-B6	57.02	0.15	26.51	0.10	8.82	0.07	4.23	0.06	-	-	3.55	0.12	100.12
NCAS10-B8	56.39	0.09	26.15	0.06	8.61	0.04	4.17	0.04	-	-	4.53	0.08	99.84

Results are mean values of 10 single point measurements

***Table 2**: Glass composition in mol% as measured by electron microprobe analysis*

[mol%]	SiO_2	2σ	Al_2O_3	2σ	Na_2O	2σ	CaO	2σ	P_2O_5	2σ	B_2O_3	2σ	ɣ	NBO/T	g.atom
CAS19	66.18	0.19	13.61	0.09	-	-	20.21	0.13	-	-	-	-	0.60	0.14	3.07
CAS19-P2	64.96	0.10	13.10	0.04	-	-	20.12	0.10	1.83	0.04	-	-	0.61	0.15	3.13
CAS19-P4	63.78	0.11	12.85	0.06	-	-	19.75	0.13	3.62	0.03	-	-	0.61	0.15	3.20
CAS19-P6	62.62	0.15	12.54	0.08	-	-	19.38	0.10	5.46	0.05	-	-	0.61	0.16	3.28
CAS19-P8	61.21	0.21	12.28	0.08	-	-	18.51	0.14	8.00	0.12	-	-	0.60	0.15	3.38
CAS14	66.71	0.27	17.73	0.17	-	-	15.56	0.13	-	-	-	-	0.47	-0.04	3.20
CAS14-P2	65.33	0.11	17.78	0.07	-	-	14.79	0.08	1.91	0.06	-	-	0.45	-0.06	3.28
CAS14-P4	63.83	0.12	17.51	0.05	-	-	14.59	0.11	3.90	0.05	-	-	0.45	-0.06	3.35
CAS14-P6	62.84	0.13	16.99	0.08	-	-	14.25	0.12	5.75	0.09	-	-	0.46	-0.06	3.42
CAS14-P8	61.63	0.13	16.63	0.07	-	-	14.02	0.13	7.58	0.05	-	-	0.46	-0.06	3.49
NAS19	66.31	0.16	14.22	0.06	19.47	0.16	-	-	-	-	-	-	0.58	0.11	3.28
NAS19-P2	65.71	0.40	14.12	0.11	18.77	0.26	-	-	1.41	0.22	-	-	0.57	0.10	3.34
NAS19-P4	65.71	0.72	13.97	0.11	16.49	0.33	-	-	3.83	0.35	-	-	0.54	0.05	3.43
NAS19-P6	63.14	0.27	13.02	0.03	18.12	0.19	-	-	5.59	0.12	-	-	0.58	0.11	3.48
NAS19-P8	62.73	0.83	13.62	0.16	16.63	0.37	-	-	7.01	0.54	-	-	0.55	0.07	3.55
NAS14	66.41	0.11	18.92	0.06	14.67	0.10	-	-	-	-	-	-	0.44	-0.08	3.38
NAS14-P2	65.55	0.10	17.89	0.08	14.56	0.13	-	-	1.89	0.06	-	-	0.45	-0.07	3.43
NAS14-P4	64.46	0.26	17.66	0.13	14.13	0.12	-	-	3.64	0.15	-	-	0.44	-0.07	3.50
NAS14-P6	63.87	0.33	17.43	0.16	13.32	0.08	-	-	5.27	0.21	-	-	0.43	-0.08	3.56
NAS14-P8	63.15	0.31	17.16	0.33	12.90	0.10	-	-	6.69	0.12	-	-	0.43	-0.09	3.61

***Table 2**: continued*

[mol%]	SiO_2	2σ	Al_2O_3	2σ	Na_2O	2σ	CaO	2σ	P_2O_5	2σ	B_2O_3	2σ	γ	NBO/T	g.atom
NCAS13	65.95	0.09	13.40	0.07	13.86	0.08	6.78	0.06	-	-	-	-	0.61	0.16	3.20
NCAS13-P2	65.27	0.11	13.50	0.05	12.71	0.09	6.72	0.12	1.79	0.05	-	-	0.59	0.13	3.27
NCAS13-P4	63.85	0.15	13.44	0.06	12.47	0.11	6.58	0.15	3.66	0.04	-	-	0.59	0.12	3.35
NCAS13-P6	62.61	0.13	13.28	0.09	12.11	0.11	6.43	0.06	5.57	0.06	-	-	0.58	0.12	3.42
NCAS13-P8	61.83	0.09	13.03	0.06	11.39	0.10	6.40	0.08	7.36	0.08	-	-	0.58	0.11	3.49
NCAS13-B2	65.95	0.23	13.27	0.06	12.77	0.14	6.72	0.11	-	-	1.30	0.11	-	-	3.22
NCAS13-B4	65.72	0.17	13.28	0.09	12.36	0.07	6.73	0.04	-	-	1.92	0.16	-	-	3.24
NCAS13-B6	64.92	0.13	13.08	0.07	11.94	0.12	6.87	0.08	-	-	3.20	0.11	-	-	3.26
NCAS13-B8	64.74	0.36	12.98	0.11	12.11	0.10	6.47	0.16	-	-	3.70	0.25	-	-	3.27
NCAS10	65.59	0.11	18.27	0.06	10.80	0.11	5.34	0.08	-	-	-	-	0.47	-0.04	3.31
NCAS10-P2	65.25	0.09	17.79	0.08	9.88	0.07	5.15	0.05	1.92	0.04	-	-	0.46	-0.05	3.38
NCAS10-P4	64.05	0.10	17.44	0.07	9.70	0.13	5.00	0.07	3.81	0.05	-	-	0.46	-0.06	3.45
NCAS10-P6	63.86	0.27	17.37	0.03	9.01	0.19	4.72	0.02	5.03	0.12	-	-	0.44	-0.07	3.50
NCAS10-P8	61.51	0.15	16.91	0.05	8.71	0.09	5.08	0.05	7.78	0.13	-	-	0.45	-0.07	3.60
NCAS10-B2	65.64	0.13	18.05	0.08	9.85	0.09	5.10	0.10	-	-	1.37	0.14	-	-	3.338
NCAS10-B4	64.80	0.13	17.74	0.08	9.88	0.09	5.09	0.10	-	-	2.49	0.14	-	-	3.354
NCAS10-B6	64.22	0.10	17.59	0.05	9.63	0.09	5.11	0.05	-	-	3.45	0.07	-	-	3.370
NCAS10-B8	63.70	0.25	17.41	0.09	9.43	0.13	5.04	0.04	-	-	4.42	0.19	-	-	3.386

γ = (Na_2O + CaO) / (Na_2O + CaO + Al_2O_3) from mole fractions (e.g. Toplis et al. 1997a; Webb et al. 2007; Baasner et al. 2013b)

NBO/T: non-bridging oxygens per tetrahedral unit as an indicator for the degree of melt polymerization

g.atoms: $g.atom = \sum_i x_i * a$ whereby *x* is the mole fraction of oxide and *a* is the number of atoms in oxide (Sehlke and Whittington 2016)

3.4 Results

3.4.1 Effect of P_2O_5 and B_2O_3 on the Viscosity

The micropenetration viscometry technique was used to determine viscosities in the range of $10^{8.5}$ – $10^{13.5}$ Pa s. The measured viscosities of all melts are illustrated in Fig. 7. The single measurements are summarized Table 3 and Table 4 and were fitted using an Arrhenian equation of the type:

$$\log_{10}\eta = \log A + \frac{10000\ B}{T} \qquad Eq.(X)$$

A and B represent fit parameters which are listed in Table 5.

It can be observed that for all peralkaline melt compositions viscosity increases with the addition of P_2O_5 to the melt up to a maximum viscosity and then decreases with further addition of P_2O_5 after the maximum. The addition of P_2O_5 to peraluminous melts, however, results in a steady decrease of viscosity.

For CAS19 series viscosity increases by approximately 0.7 log units up to a P_2O_5 concentration of 3.62 mol% P_2O_5. With further addition of P_2O_5 to the melt viscosity decreases by also approximately 0.7 log units and is similar to the viscosity of the P_2O_5-free starting melt composition. For sample CAS19-P8 containing 8 mol% P_2O_5 there are only 3 measured viscosities. It was only possible to measure the high viscosities (~$10^{11.5}$ – $10^{12.5}$ Pa s) for this melt composition due to macroscopic changes in the sample occurring during viscosity measurements. For measurements at higher temperatures the viscosity of the sample increased by several log units and the colour of the sample changed from crystal clear to a still clear glass with a slightly blueish hue. The measured viscosities before the macroscopic changes in the melt refer to the quenched melt and are shown in Fig. 7. Further investigations on sample CAS19-P8 have been conducted and are described in Chapter 6.

The addition of P_2O_5 to the peralkaline NAS19 melt leads to an increase of viscosity by approximately 1.7 log units up to a P_2O_5 concentration of 3.83 mol% while further addition of P_2O_5 after the maximum viscosity was reached results in a decrease of viscosity by approximately 1.6 log units. The addition of P_2O_5 to the peralkaline NCAS13 melts results in the strongest increase in viscosity by ~4 log units up to a P_2O_5 concentration of 3.66 mol%. Further addition of P_2O_5 after the maximum yields in a decrease of viscosity by ~1.8 log units.

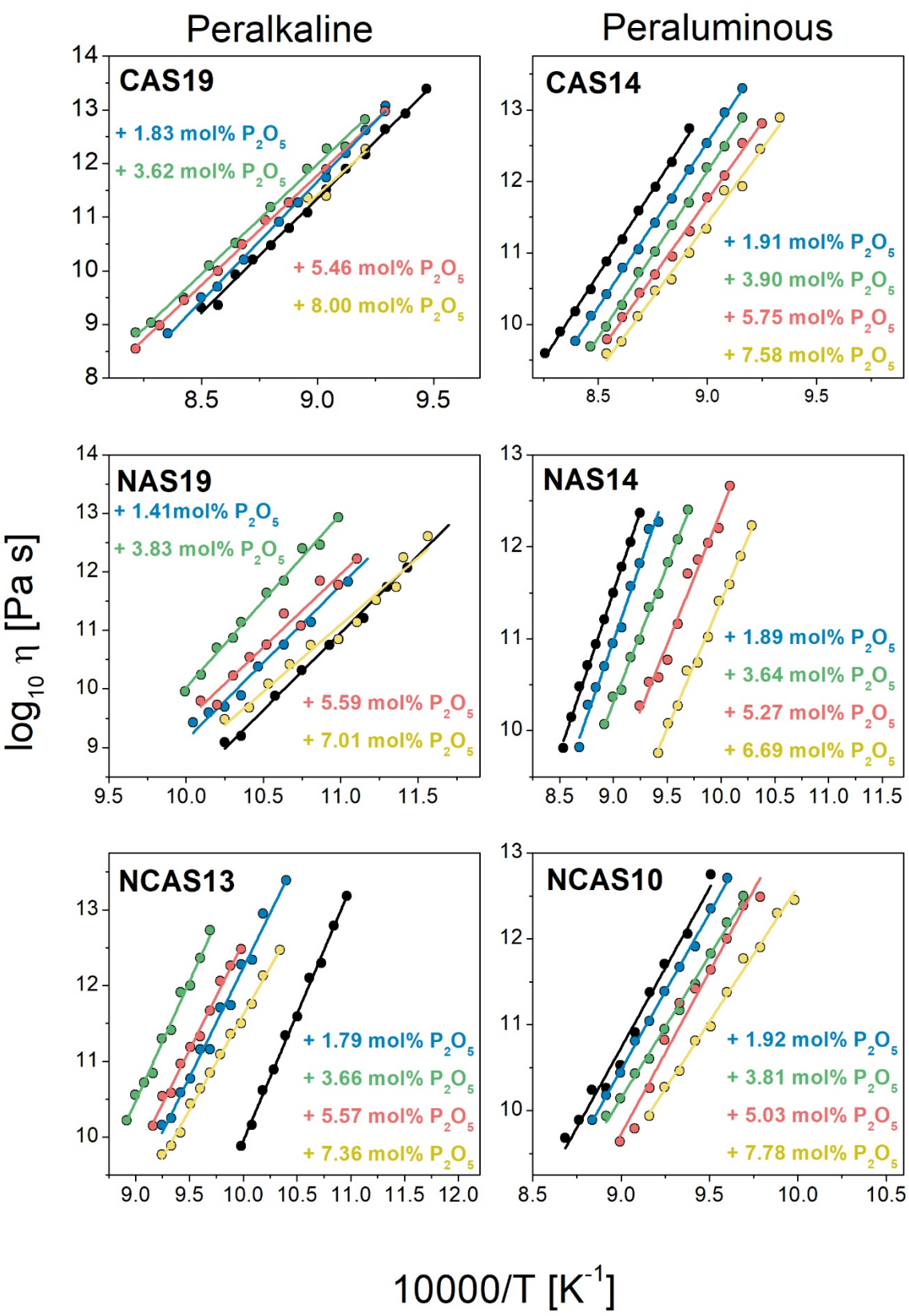

***Fig. 7**: Viscosities of all P_2O_5-bearing peralkaline and peraluminous melts measured by micropenetration technique. Black symbols and lines represent the P_2O_5-free starting composition. Error bars are smaller than symbols.*

In peraluminous melts the addition of P_2O_5 results in constant decrease in viscosity. For CAS14 melt the addition of up to 7.58 mol% P_2O_5 results in a decrease of viscosity by ~1.6 log units, whereas for NAS14 melt viscosity decreases by approximately 2.9 log units at a P_2O_5 concentration of 6.69 mol%. The addition up to 7.78 mol% P_2O_5 to the peraluminous NCAS10 melts leads to a decrease of viscosity by ~1.8 log units.

For better comparison $\Delta\log_{10}\eta$ was calculated for all P_2O_5 bearing melts and is illustrated in Fig. 8. $\Delta\log_{10}\eta$ represents the difference in viscosity calculated for the temperature at which the viscosity of the P_2O_5-free melt equals 10^{12} Pa s.

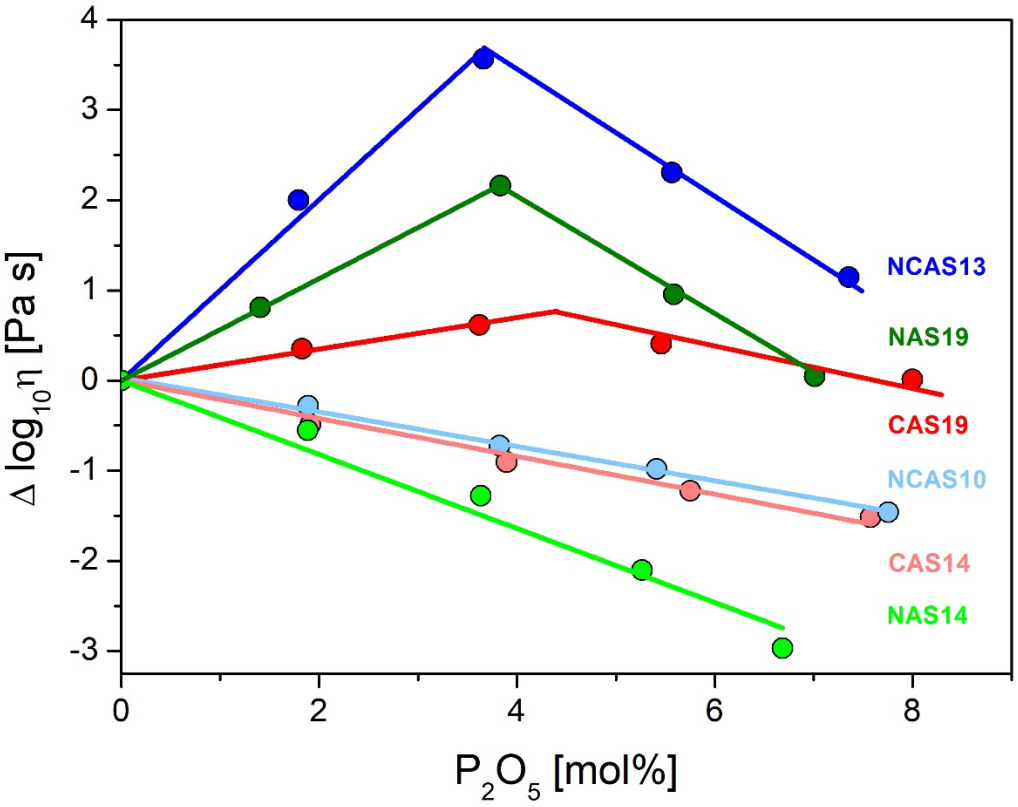

***Fig. 8**: The difference in viscosity as a function of P_2O_5-concentration calculated for the temperature at which the viscosity of the P_2O_5-free starting composition equals 10^{12} Pa s. Error bars are smaller than symbols.*

The increase and the decrease in viscosity caused by the addition of P_2O_5 to the melts both follow a linear trend. The viscosity maximum of the peralkaline melts can be found around a P_2O_5 concentration of ~4 mol% for all peralkaline compositions. The increase of viscosity in the Na-bearing NAS19 melt is stronger than in the Ca-bearing CAS19 melt. The strongest effect of P_2O_5 on melt viscosity is observed for NCAS13 melts containing both Ca and Na.

The addition of P_2O_5 to the Na-bearing, peraluminous NAS14 melt results in the strongest decrease in viscosity. The viscosity decreasing effect of P_2O_5 on the Ca-bearing CAS14 melt is similar to that of Ca-Na-bearing NCAS10 melt.

***Table 3**: Viscosity of peralkaline P_2O_5-bearing melts measured by micropenetration technique*

T	η	T	η	T	η	T	η	T	η
K	log_{10} Pa s	K	log_{10} Pa s	K	log_{10} Pa s	K	log_{10} Pa s	K	log_{10} Pa s
CAS19		**CAS19-P2**		**CAS19-P4**		**CAS19-P6**		**CAS19-P8**	
1056.1	13.39	1076.2	13.07	1086.3	12.82	1076.2	12.97	1106.4	11.40
1066.1	12.93	1086.2	12.62	1096.4	12.31	1106.4	11.89	1116.4	11.36
1076.2	12.64	1096.3	12.19	1106.3	12.28	1126.5	11.27	1086.2	12.27
1086.2	12.17	1106.4	11.74	1116.6	11.90	1139.5	10.94		
1096.3	11.90	1121.4	11.27	1136.6	11.19	1152.7	10.49		
1106.5	11.51	1131.9	10.91	1156.7	10.52	1166.8	10.00		
1116.5	11.09	1137.3	10.52	1171.9	10.10	1187.0	9.45		
1126.5	10.79	1151.6	10.21	1187.1	9.49	1202.0	8.98		
1136.5	10.47	1167.0	9.70	1207.2	9.03	1217.3	8.55		
1146.6	10.21	1176.8	9.50	1217.3	8.85				
1156.7	9.93	1197.0	8.83						
1166.7	9.36								
1176.8	9.32								
NAS19		**NAS19-P2**		**NAS19-P4**		**NAS19-P6**		**NAS19-P8**	
854.8	12.93	895.0	12.44	910.4	12.93	900.3	12.22	864.8	12.61
874.9	12.07	905.1	11.83	920.4	12.46	910.4	11.78	876.9	12.25
885.0	11.74	925.2	11.14	930.2	12.40	920.4	11.85	880.3	11.74
897.0	11.21	940.4	10.76	940.4	11.85	930.8	11.08	890.5	11.52
910.2	10.85	955.4	10.38	950.4	11.64	940.5	11.29	900.4	11.14
915.1	10.75	965.5	9.89	965.5	11.14	950.5	10.76	910.4	10.85
930.5	10.32	975.6	9.70	970.4	10.87	960.5	10.54	925.4	10.75
945.5	9.88	985.6	9.60	980.7	10.70	970.5	10.23	937.3	10.42
965.6	9.20	995.6	9.43	990.4	10.24	980.4	9.73	949.4	10.09
975.5	9.09			1000.8	9.96	990.6	9.80	960.7	9.68
								975.6	9.48
NCAS13		**NCAS13-P2**		**NCAS13-P4**		**NCAS13-P6**		**NCAS13-P8**	
912.2	13.18	961.4	13.39	1031.8	12.73	1001.9	12.48	967.0	12.47
922.2	12.79	982.0	12.95	1041.7	12.36	1011.8	12.26	982.0	12.13
932.2	12.30	991.4	12.34	1051.7	12.00	1021.8	12.06	991.9	11.76
942.1	12.10	1001.9	12.28	1061.6	11.91	1031.8	11.67	1001.9	11.50
952.1	11.59	1011.4	11.74	1071.6	11.41	1041.8	11.33	1011.9	11.36
962.2	11.34	1021.9	11.71	1081.6	11.30	1051.7	11.19	1021.9	11.09
972.3	10.89	1031.8	11.16	1091.7	10.84	1061.6	10.97	1031.7	10.85
982.2	10.62	1041.7	11.16	1101.5	10.72	1071.6	10.58	1041.7	10.64
992.0	10.16	1051.7	10.77	1111.5	10.56	1081.6	10.54	1051.8	10.44
1001.9	9.88	1061.6	10.59	1121.6	10.22	1091.5	10.15	1061.7	10.06
		1071.6	10.25					1071.6	9.89

***Table 4**: Viscosity of peraluminous P_2O_5-bearing melts measured by micropenetration technique*

T	η	T	η	T	η	T	η	T	η
K	$\log_{10}$ Pa s	K	$\log_{10}$ Pa s	K	$\log_{10}$ Pa s	K	$\log_{10}$ Pa s	K	$\log_{10}$ Pa s
CAS14		**CAS14-P2**		**CAS14-P4**		**CAS14-P6**		**CAS14-P8**	
1121.4	12.74	1091.5	13.30	1091.5	12.89	1081.5	12.81	1071.6	12.89
1131.4	12.27	1101.5	12.96	1101.5	12.49	1091.5	12.53	1081.9	12.45
1141.3	11.92	1111.4	12.53	1111.4	12.19	1101.5	12.08	1091.5	11.93
1151.3	11.59	1121.4	12.16	1121.6	11.70	1111.4	11.77	1101.6	11.87
1161.3	11.19	1131.4	11.76	1131.4	11.39	1121.4	11.30	1111.8	11.34
1171.2	10.88	1141.3	11.42	1141.3	11.02	1131.5	10.95	1121.4	11.00
1181.2	10.49	1151.3	11.05	1151.4	10.73	1141.6	10.70	1131.8	10.63
1191.1	10.18	1161.2	10.79	1161.6	10.27	1151.4	10.44	1141.5	10.47
1201.1	9.90	1171.3	10.42	1171.4	9.97	1161.3	10.10	1151.8	10.11
1211.2	9.60	1181.2	10.12	1181.3	9.69	1171.2	9.79	1161.7	9.76
		1191.1	9.77					1171.3	9.59
NAS14		**NAS14-P2**		**NAS14-P4**		**NAS14-P6**		**NAS14-P8**	
1081.6	12.37	1061.7	12.27	1031.7	12.40	991.9	12.66	972.2	12.23
1091.5	12.05	1071.7	12.19	1041.7	12.08	1002.1	12.20	982.1	11.90
1101.6	11.78	1081.7	11.82	1051.7	11.83	1012.0	12.04	992.0	11.59
1111.4	11.50	1091.5	11.57	1061.7	11.49	1022.1	11.86	1001.9	11.41
1121.5	11.21	1101.9	11.12	1071.8	11.34	1031.8	11.71	1012.1	11.02
1131.5	10.94	1111.6	10.95	1081.8	10.99	1041.9	11.16	1021.9	10.74
1141.5	10.71	1121.4	10.70	1091.7	10.80	1052.0	10.77	1033.0	10.65
1151.3	10.48	1131.6	10.47	1101.6	10.44	1061.7	10.58	1041.8	10.27
1161.4	10.15	1141.5	10.28	1111.6	10.37	1071.8	10.53	1051.9	10.08
1171.4	9.81	1151.5	9.82	1121.5	10.07	1081.7	10.27	1061.9	9.76
NCAS10		**NCAS10-P2**		**NCAS10-P4**		**NCAS10-P6**		**NCAS10-P8**	
1051.7	12.75	1041.7	12.71	1031.7	12.50	1021.8	12.49	1001.9	12.45
1066.6	12.06	1051.7	12.35	1041.7	12.19	1031.7	12.39	1011.9	12.30
1081.5	11.71	1061.7	11.91	1051.7	11.83	1041.8	12.00	1021.8	11.90
1091.5	11.38	1071.7	11.67	1061.7	11.47	1051.8	11.64	1031.9	11.77
1101.5	10.91	1081.7	11.39	1071.6	11.17	1061.7	11.42	1041.9	11.38
1111.5	10.53	1091.6	11.04	1081.7	10.95	1071.7	11.25	1051.8	10.98
1121.6	10.26	1101.5	10.81	1091.6	10.60	1081.6	10.82	1061.7	10.81
1131.9	10.24	1111.5	10.44	1101.5	10.43	1091.6	10.26	1071.8	10.46
1141.4	9.89	1121.6	10.18	1111.5	10.14	1101.8	9.79	1081.6	10.27
1151.5	9.68	1131.4	9.89	1121.5	9.94	1111.9	9.64	1091.7	9.94

***Table 5**: Arrhenian Fit parameter of the viscosities of P_2O_5-bearing melts*

Sample	A	ΔA	B	ΔB	E	T_g^{12}	ΔT_g^{12}	m
	$\log_{10}$ Pa s	$\log_{10}$ Pa s	$\log_{10}$ Pa s 10^4 K	$\log_{10}$ Pa s 10^4 K	kJ mol^{-1}	K	K	
CAS19	-26.93	0.64	4.25	0.07	813.8	1091.7	0.2	39
CAS19-P2	-28.49	0.61	4.46	0.07	854.0	1101.5	0.2	40
CAS19-P4	-24.88	0.84	4.10	0.10	785.1	1111.7	0.3	37
CAS19-P6	-25.00	0.36	4.09	0.04	783.2	1105.4	0.1	37
CAS19-P8	-23.57	10.30	3.89	1.14	744.9	1093.6	3.8	36
CAS14	-29.47	0.53	4.73	0.06	905.7	1140.6	0.2	41
CAS14-P2	-28.91	0.37	4.61	0.04	882.7	1126.9	0.1	41
CAS14-P4	-29.66	0.52	4.64	0.06	888.5	1113.8	0.2	42
CAS14-P6	-27.04	0.81	4.31	0.09	825.3	1104.0	0.3	39
CAS14-P8	-25.92	1.03	4.15	0.12	794.7	1094.4	0.4	38
NAS19	-18.02	0.67	2.63	0.06	503.6	876.1	0.4	30
NAS19-P2	-17.24	1.38	2.64	0.13	505.5	902.9	0.8	29
NAS19-P4	-19.60	0.83	2.96	0.08	566.8	936.7	0.4	32
NAS19-P6	-15.57	1.86	2.50	0.18	478.7	906.8	1.1	28
NAS19-P8	-14.69	1.27	2.35	0.12	450.0	880.5	0.8	27
NAS14	-19.98	0.51	3.50	0.06	670.2	1094.4	0.2	32
NAS14-P2	-19.07	1.07	3.34	0.12	639.6	1075.0	0.5	31
NAS14-P4	-16.49	0.67	2.98	0.07	570.6	1046.0	0.3	28
NAS14-P6	-16.57	1.51	2.90	0.16	555.3	1015.1	0.8	29
NAS14-P8	-16.22	0.73	2.76	0.07	528.5	978.0	0.4	28
NCAS13	-23.59	0.67	3.35	0.06	641.5	941.3	0.3	36
NCAS13-P2	-16.66	1.04	2.89	0.11	553.4	1008.4	0.5	29
NCAS13-P4	-17.99	1.09	3.16	0.12	605.1	1053.7	0.5	30
NCAS13-P6	-15.83	0.89	2.84	0.09	543.8	1020.5	0.4	28
NCAS13-P8	-13.49	0.47	2.51	0.05	480.6	984.7	0.3	25
NCAS10	-22.69	1.45	3.71	0.16	710.4	1069.5	0.6	35
NCAS10-P2	-22.33	0.53	3.65	0.06	698.9	1063.2	0.2	34
NCAS10-P4	-19.79	0.71	3.33	0.08	637.6	1047.5	0.3	32
NCAS10-P6	-24.39	1.94	3.79	0.21	725.7	1041.5	0.7	36
NCAS10-P8	-18.79	0.87	3.14	0.09	601.3	1019.8	0.4	31

E: activation energy for viscous flow

T_g^{12}: temperature at which viscosity equals 10^{12} Pa s

m: fragility of the melt

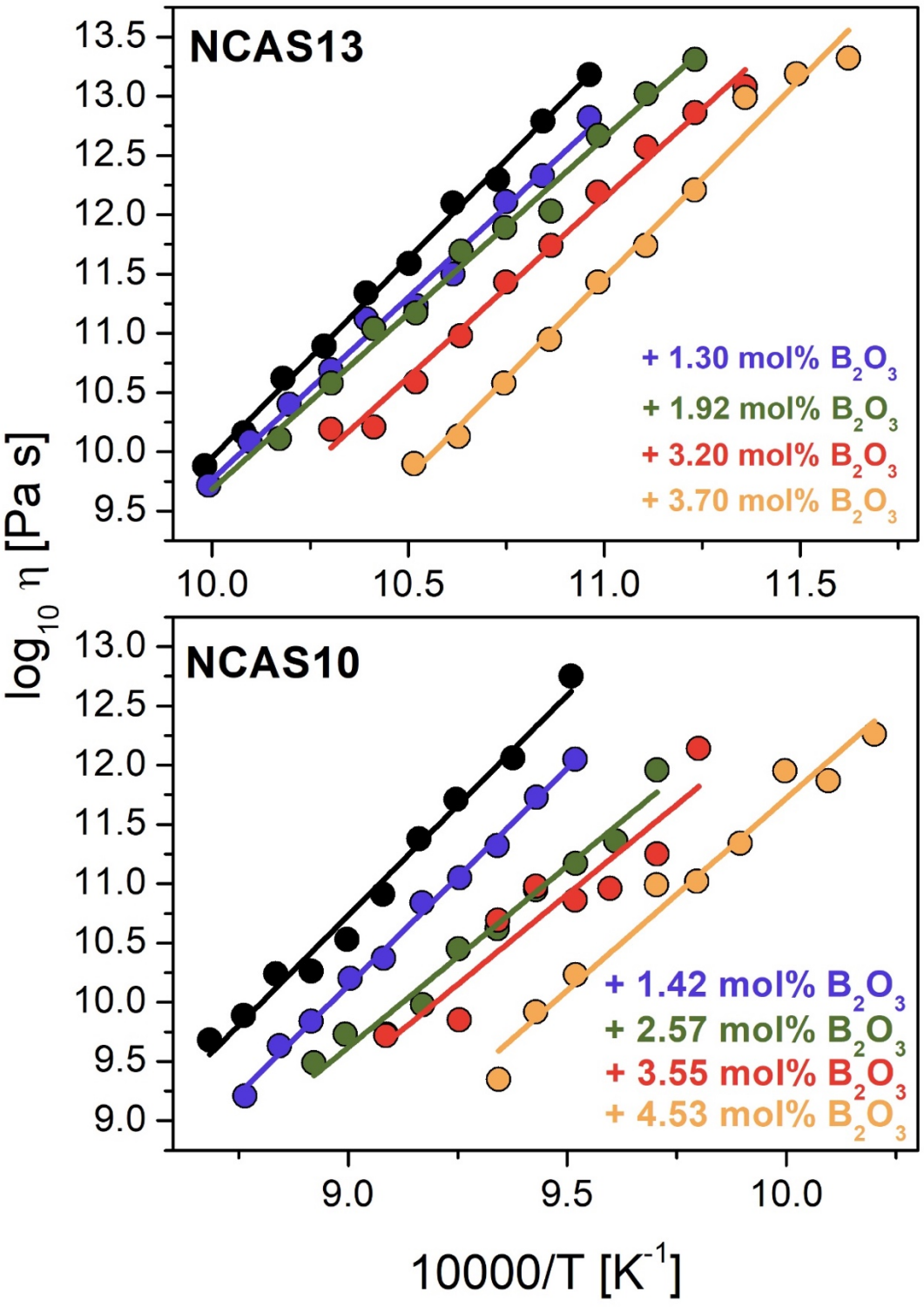

***Fig. 9**: Viscosity data for peralkaline NCAS13 and peraluminous NCAS10 melts with different B_2O_3 concentrations. Black symbols and lines represent the B_2O_3-free starting composition. Error bars are smaller than symbols.*

The viscosities of the boron-bearing melts of the peralkaline NCAS13 and the peraluminous NCAS10 series are illustrated in Fig. 9. The viscosity data is summarized in Table 6 and the parameters of the Arrhenian fits for the melts are given in Table 7. In both cases the addition of B_2O_3 to the melt results in a decrease of viscosity. The addition of up to 4.53 mol% B_2O_3 to the peraluminous NCAS10 melt decreases viscosity constantly by approximately 2.4 log units. The addition of B_2O_3 to NCAS13 melt at first leads to a slight decrease of viscosity by ~0.9 log units up to a B_2O_3 concentration of 3.2 mol%. Further addition of B_2O_3 to the melts results in a stronger decrease of viscosity.

***Table 6**: Viscosities of B_2O_3-bearing melts measured by micropenetration technique*

T	η	T	η	T	η	T	η
K	$\log_{10}$ Pa s	K	$\log_{10}$ Pa s	K	$\log_{10}$ Pa s	K	$\log_{10}$ Pa s
NCAS13-B2		**NCAS13-B4**		**NCAS13-B6**		**NCAS13-B8**	
912.2	12.82	890.3	13.31	880.3	13.08	860.4	13.32
922.2	12.33	900.3	13.02	890.3	12.86	870.3	13.19
930.4	12.11	910.3	12.67	900.3	12.57	880.3	12.99
942.1	11.50	920.4	12.03	910.4	12.19	890.4	12.21
950.5	11.23	930.5	11.89	920.4	11.74	900.4	11.74
962.1	11.12	940.4	11.69	930.4	11.43	910.4	11.43
970.6	10.69	950.6	11.17	940.4	10.98	920.8	10.95
980.7	10.40	960.4	11.04	950.6	10.59	930.7	10.58
990.5	10.09	970.5	10.58	960.4	10.21	940.9	10.13
1000.8	9.72	983.2	10.11	970.6	10.19	951.1	9.90
NCAS10-B2		**NCAS10-B4**		**NCAS10-B6**		**NCAS10-B8**	
1050.6	12.05	1030.5	11.96	1020.4	12.14	980.4	12.26
1060.5	11.73	1040.5	11.36	1030.4	11.25	990.6	11.87
1070.7	11.32	1050.5	11.17	1041.9	10.96	1000.4	11.95
1080.6	11.05	1060.7	10.95	1050.6	10.86	1010.6	11.34
1090.6	10.84	1070.6	10.62	1060.7	10.98	1020.9	11.02
1101.2	10.37	1081.0	10.45	1070.6	10.69	1030.6	10.99
1110.6	10.20	1090.6	9.98	1080.7	9.85	1040.4	11.07
1121.6	9.84	1100.5	9.73	1100.6	9.72	1050.5	10.23
1130.8	9.63	1112.0	9.73			1060.7	9.92
1141.0	9.21	1120.9	9.49			1070.3	9.35

***Table 7**: Arrhenian Fit parameter for the viscosities of B_2O_3-bearing melts*

Sample	A	Δ A	B	Δ B	E	T_g^{12}	Δ T_g^{12}	m
	$\log_{10}$ Pa s	$\log_{10}$ Pa s	$\log_{10}$ Pa s 10^4 K	$\log_{10}$ Pa s 10^4 K	kJ mol^{-1}	K	K	
NCAS13-B2	-20.98	1.05	3.07	0.10	588.71	932.2	0.5	33
NCAS13-B4	-19.95	1.13	2.96	0.11	567.43	927.5	0.5	32
NCAS13-B6	-21.04	1.17	3.02	0.11	577.45	912.9	0.6	33
NCAS13-B8	-25.51	1.50	3.36	0.14	643.59	896.0	0.6	38
NCAS10-B2	-22.80	0.69	3.66	0.08	700.74	1051.7	0.3	35
NCAS10-B4	-17.87	1.54	3.05	0.16	584.94	1022.6	0.7	30
NCAS10-B6	-17.89	4.37	3.03	0.46	580.51	1014.2	2.1	30
NCAS10-B8	-20.73	2.03	3.24	0.21	621.33	991.5	0.9	33

E: activation energy for viscous flow

T_g^{12}: temperature at which viscosity equals 10^{12} Pa s

m: fragility of the melt

3.4.2 Effect of P_2O_5 and B_2O_3 on the Heat Capacity

Fig. 10 shows the heat capacities of the peralkaline CAS19, NAS19 and NCAS13 melts. For all peralkaline melts the addition of P_2O_5 results in an increase of the T_g peak up to a maximum temperature. Further addition of P_2O_5 to the melt shifts the T_g peak back to lower temperatures. For CAS19 melt T_g increases by 13 K up to a P_2O_5 concentration of 3.62 mol% and then decreases by 46 K with further addition of P_2O_5.

The addition of phosphorus to the NAS19 melt shows stronger shifts in T_g peaks. The T_g peak shifts from 923 K to 982 K with the addition of up to 3.83 mol% P_2O_5. Further increase of P_2O_5 concentration in the melt shifts the T_g peak slightly to 972 K for a P_2O_5 content of 7.01 mol%.

The strongest effect of P_2O_5 on the T_g peak is observed for NCAS13 melt. It shows the strongest shift of the T_g peak from 995 K to 1100 K with the addition of 3.66 mol% P_2O_5. Further addition of P_2O_5 shifts the peak to 1055 K for a P_2O_5 content of 7.36 mol%. Moreover, there is a second T_g peak present in the melt containing 3.66 mol% (NCAS13-P4) at ~815 K. In case of NCAS13-P6 melt containing 5.57 mol% P_2O_5 two more T_g peaks can be found around ~805 K and 1140 K, indicating the presence of more than one melt phase.

For all peralkaline melts it can be observed that the T_g peak broadens at higher P_2O_5 concentrations.

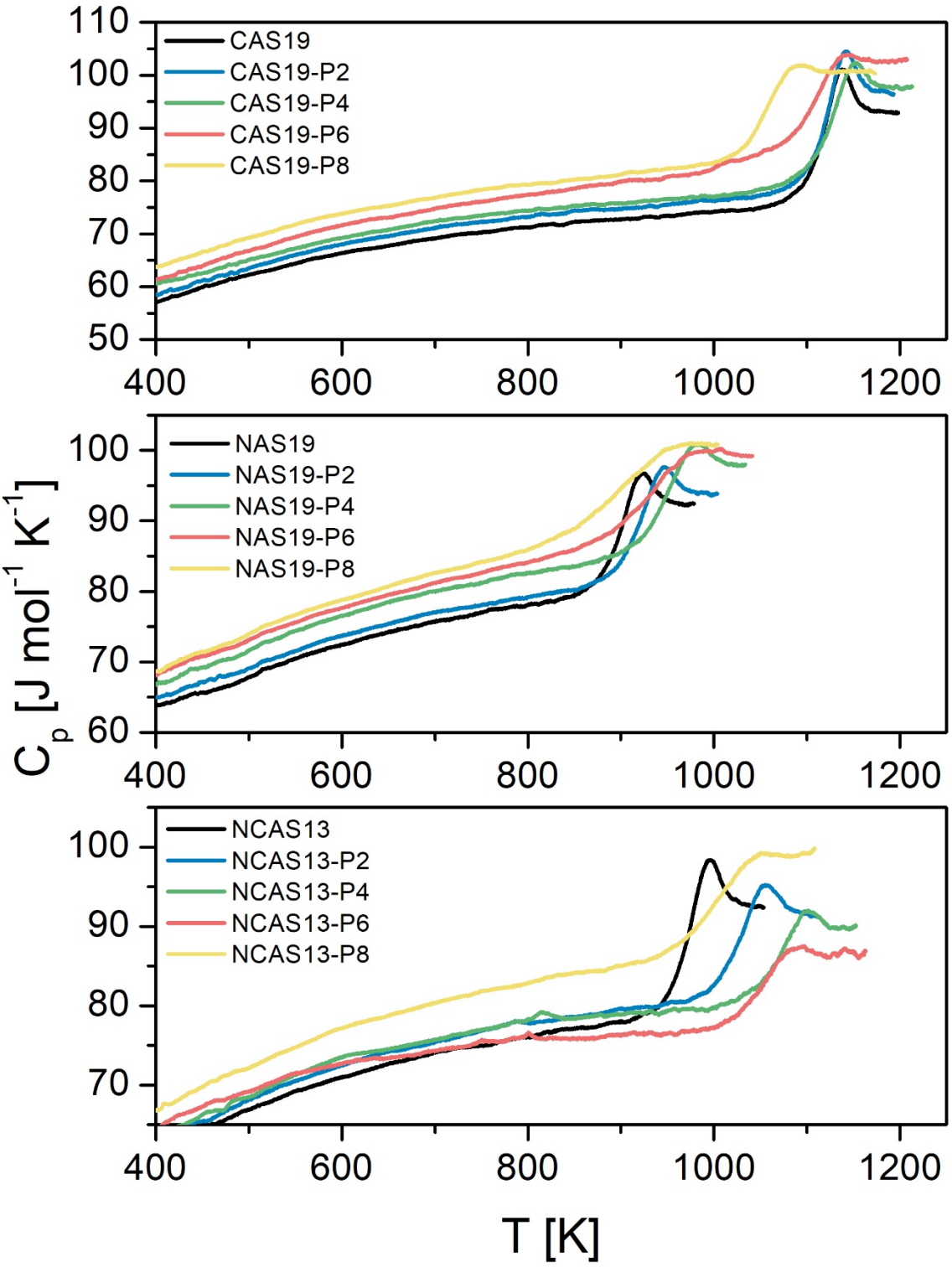

***Fig. 10**: Molar heat capacities of the peralkaline P_2O_5-bearing melts.*

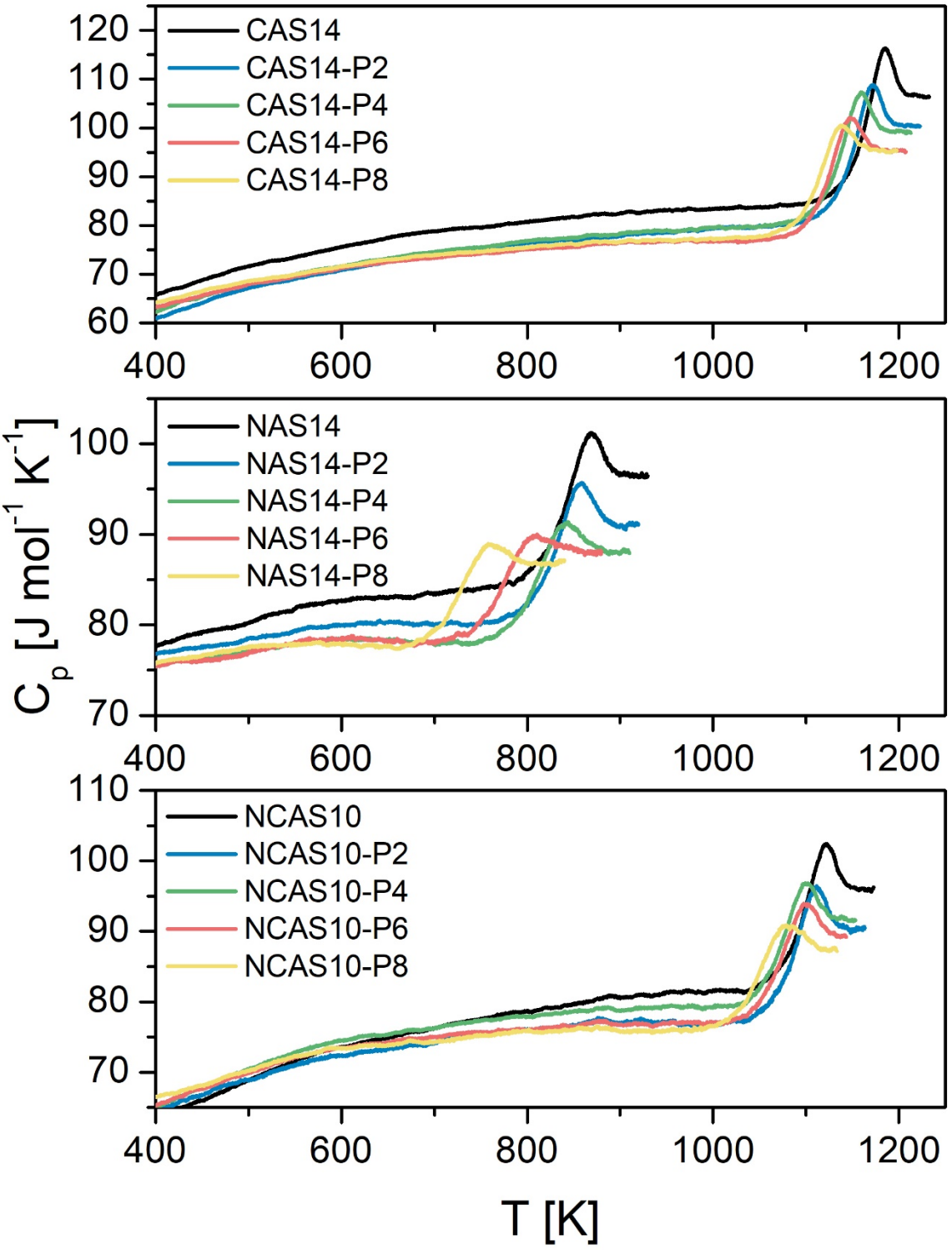

***Fig. 11**: Molar heat capacities of the peraluminous P_2O_5-bearing melts.*

The heat capacities for the peraluminous CAS14, NAS14 and NCAS10 melts are depicted in Fig. 11. For all compositions, the T_g peak shifts to lower temperatures with increasing P_2O_5 concentration, indicating a depolymerisation of the melt. The effect of P_2O_5 in CAS19 and NCAS10 melts is similarly strong and the T_g peak shifts by approximately 40 K to 50 K. In case of CAS14 melt, the T_g peak shifts from 1185 K to 1138 K with the addition of up to 7.58 mol% P_2O_5 and in case of sample NCAS10 from 1120 K to 1080 K with the addition of up to 7.78 mol% P_2O_5. The strongest effect is observed for sample NAS14. With the addition of up to 6.69 mol% P_2O_5 the T_g peak shifts by 110 K from 870 K to 760 K.

The fictive temperature T_f' was calculated by the method described by Moynihan et al. (1976). S_{conf}, B_e and C_p^{conf} are calculated from the heat capacity curves by applying the Adam-Gibbs theory of viscosity (Adam and Gibbs 1965; Webb 2008) using the following equation:

$$log_{10}\eta(T) = A_e + \frac{B_e}{\ln 10 * [S_{conf}(T_g) + \int_{T_g}^{T} \frac{C_p^{conf}}{T} dT] * T} \qquad Eq.(XI)$$

Where A_e and B_e are constants, T is the temperature in K, η is the viscosity and C_p^{conf} is the configurational heat capacity. The configurational heat capacity is calculated from the difference between the heat capacity of the liquid (C_{pl}) and the heat capacity of the glass (C_{pg}) as summarized in the following equation:

$$C_p^{conf} = C_{pl} - C_{pg} \qquad Eq.(XII)$$

C_{pg} and C_{pl} are calculated directly from heat capacity measurements by use of the Maier-Kelley equation (*Eq. IV*) (Maier and Kelley 1932).

The calculated entropies and configurational heat capacities of all phosphorus-bearing glasses are summarized in Table 9. The parameters of the Maier-Kelley fit are presented in Table 8.

S_{conf} as a function of P_2O_5 concentration is illustrated in Fig. 12 for the peralkaline as well as the peraluminous melts. S_{conf} is a measure for the disorder in melts. For the peralkaline melt compositions CAS19, NAS19 and NCAS13 S_{conf} does not change significantly within the error range. In case of the NACS13 melt, S_{conf} was calculated solely for the P_2O_5-free melt as well as NCAS13-P2 melt. Due to the presence of more than one T_g peak, it was not possible to calculate C_{pg}, C_{pl}, T_f', S_{conf} and B_e for the melts with higher P_2O_5 concentrations.

***Table 8**: Maier-Kelley fit parameter of P_2O_5-bearing melts*

	a	Δ a	b	Δ b	c	Δ c
sample	J g^{-1} K^{-1}	J g^{-1} K^{-1}	10^{-4} J g^{-1} K^{-2}	10^{-4} J g^{-1} K^{-2}	10^{4} J g^{-1} K	10^{4} J g^{-1} K
CAS19	1.013	0.001	1.644	0.011	-3.265	0.014
CAS19-P2	1.006	0.002	1.820	0.018	-3.232	0.019
CAS19-P4	0.995	0.002	1.811	0.018	-2.848	0.021
CAS19-P6	0.949	0.001	2.651	0.014	-2.741	0.015
CAS19-P8	0.990	0.001	2.135	0.013	-2.902	0.014
CAS14	1.064	0.001	1.071	0.010	-3.514	0.013
CAS14-P2	1.046	0.001	1.446	0.008	-3.505	0.010
CAS14-P4	1.037	0.001	1.297	0.007	-3.242	0.009
CAS14-P6	1.038	0.001	0.675	0.009	-3.035	0.012
CAS14-P8	1.010	0.001	0.776	0.009	-2.723	0.011
NAS19	0.910	0.003	3.707	0.034	-1.648	0.029
NAS19-P2	0.951	0.002	3.165	0.025	-1.978	0.023
NAS19-P4	0.981	0.002	3.136	0.024	-2.342	0.023
NAS19-P6	0.922	0.001	3.733	0.013	-1.745	0.011
NAS19-P8	0.892	0.002	4.144	0.021	1.652	0.016
NAS14	1.116	0.001	1.550	0.015	-3.784	0.018
NAS14-P2	1.164	0.001	0.389	0.014	-3.963	0.017
NAS14-P4	1.148	0.002	0.029	0.016	-3.730	0.019
NAS14-P6	1.086	0.002	0.448	0.015	-3.114	0.018
NAS14-P8	1.103	0.002	0.070	0.17	-3.123	0.018
NCAS13	1.002	0.002	2.459	0.018	-2.571	0.018
NCAS13-P2	1.030	0.002	2.134	0.019	-2.892	0.021
NCAS13-P4	1.103	0.002	1.023	0.022	-3.591	0.025
NCAS13-P6	1.111	0.001	0.194	0.013	-3.189	0.014
NCAS13-P8	1.004	0.001	2.480	0.014	-2.786	0.014
NCAS10	1.101	0.001	1.456	0.013	-3.724	0.016
NCAS10-P2	1.199	0.001	0.557	0.015	-3.134	0.016
NCAS10-P4	1.142	0.001	0.222	0.010	-3.797	0.012
NCAS10-P6	1.115	0.001	-0.111	0.010	-3.386	0.012
NCAS10-P8	1.089	0.001	-0.233	0.013	-2.977	0.015

***Table 9**: Adam-Gibbs fit parameter of P_2O_5-bearing melts*

sample	A_e	B_e	ΔB_e	S_{conf}	ΔS_{conf}	C_{pg}	C_{pl}	C_p^{conf}	ΔC_p^{conf}	T_f'
		kJ mol^{-1}	kJ mol^{-1}	J mol^{-1} K^{-1}	J mol^{-1} K^{-1}	J mol^{-1} K^{-1}	J mol^{-1} K^{-1}	J mol^{-1} K^{-1}	J mol^{-1} K^{-1}	K
CAS19	-4.55	464.55	13.76	11.22	0.34	76.67	92.91	16.24	2.15	1094.9
CAS19-P2	-4.55	446.56	7.23	10.65	0.18	79.51	96.74	17.23	2.05	1100.4
CAS19-P4	-4.55	519.41	25.15	12.28	0.62	80.49	97.40	16.91	1.97	1108.7
CAS19-P6	-4.55	501.83	16.43	11.93	0.41	85.59	102.16	16.57	1.97	1092.0
CAS19-P8	-4.55	526.86	273.16	12.66	6.66	85.95	100.86	14.92	1.79	1052.4
CAS14	-4.55	542.16	7.73	12.49	0.18	78.25	96.98	18.73	2.13	1144.7
CAS14-P2	-4.55	495.86	7.11	11.58	0.17	82.07	99.86	17.78	2.12	1129.9
CAS14-P4	-4.55	456.89	11.49	10.77	0.28	81.80	99.28	17.48	1.98	1118.7
CAS14-P6	-4.55	474.01	14.96	11.28	0.37	78.36	94.74	16.38	1.83	1105.9
CAS14-P8	-4.55	496.57	21.33	11.92	0.53	78.41	95.11	16.70	1.72	1100.7
NAS19	-4.55	339.99	13.41	10.17	0.42	83.01	92.31	9.30	2.19	883.1
NAS19-P2	-4.55	372.26	36.96	10.82	1.12	84.38	93.83	9.45	2.16	905.9
NAS19-P4	-4.55	363.44	25.77	10.32	0.74	88.81	98.53	9.71	2.13	936.9
NAS19-P6	-4.55	365.97	3.50	10.52	0.11	90.78	98.52	7.74	2.06	921.0
NAS19-P8	-4.55	372.18	7.91	11.05	0.24	92.68	100.58	7.90	1.97	898.9
NAS14	-4.55	394.99	15.79	9.47	0.39	86.72	96.28	9.56	2.21	1091.2
NAS14-P2	-4.55	389.54	30.14	9.51	0.76	81.80	90.81	9.01	2.03	1077.7
NAS14-P4	-4.55	471.45	25.25	11.84	0.65	79.14	88.32	9.19	1.89	1067.4
NAS14-P6	-4.55	326.12	41.16	8.45	1.09	81.22	87.69	6.47	1.84	1030.7
NAS14-P8	-4.55	387.59	24.41	10.38	0.67	78.76	86.78	8.02	1.72	987.4
NCAS13	-4.55	333.98	13.82	9.31	0.39	81.45	92.62	11.17	2.12	950.2
NCAS13-P2	-4.55	408.96	34.13	10.66	0.90	83.30	91.36	8.06	2.06	1007.7
NCAS13-P4	-4.55	385.73	30.21	9.60	0.77	81.74	89.98	8.24	1.87	1060.0
NCAS13-P6	-4.55	453.69	36.09	11.67	0.95	77.89	86.31	8.42	1.71	1041.6
NCAS13-P8	-4.55	596.14	32.39	15.88	0.89	89.40	98.70	9.30	1.84	999.7
NCAS10	-4.55	364.58	4.76	9.09	0.13	83.98	96.17	12.19	2.10	1078.0
NCAS10-P2	-4.55	357.71	3.44	8.78	0.09	78.76	90.51	11.75	1.98	1072.0
NCAS10-P4	-4.55	438.59	4.44	10.97	0.12	80.36	91.64	11.28	1.87	1056.2
NCAS10-P6	-4.55	389.93	3.32	9.77	0.09	77.18	88.61	11.43	1.78	1053.7
NCAS10-P8	-4.55	430.51	5.89	11.03	0.16	76.44	87.46	11.02	1.62	1032.2

Error of the fictive Temperature T_f' is 3 K

Error of C_{pg} and C_{pl} is < 1%

In peraluminous melts two different trends for S_{conf} are observed. For the Ca-bearing CAS14 melt S_{conf} decreases with the addition of P_2O_5 from 12.49 to 10.77 J mol^{-1} K^{-1} and increases with further addition of P_2O_5 to 11.92 J mol^{-1} K^{-1}. The Na- as well as the Na-Ca-bearing NAS14 and NCAS10 melts show a contrary trend for S_{conf}.

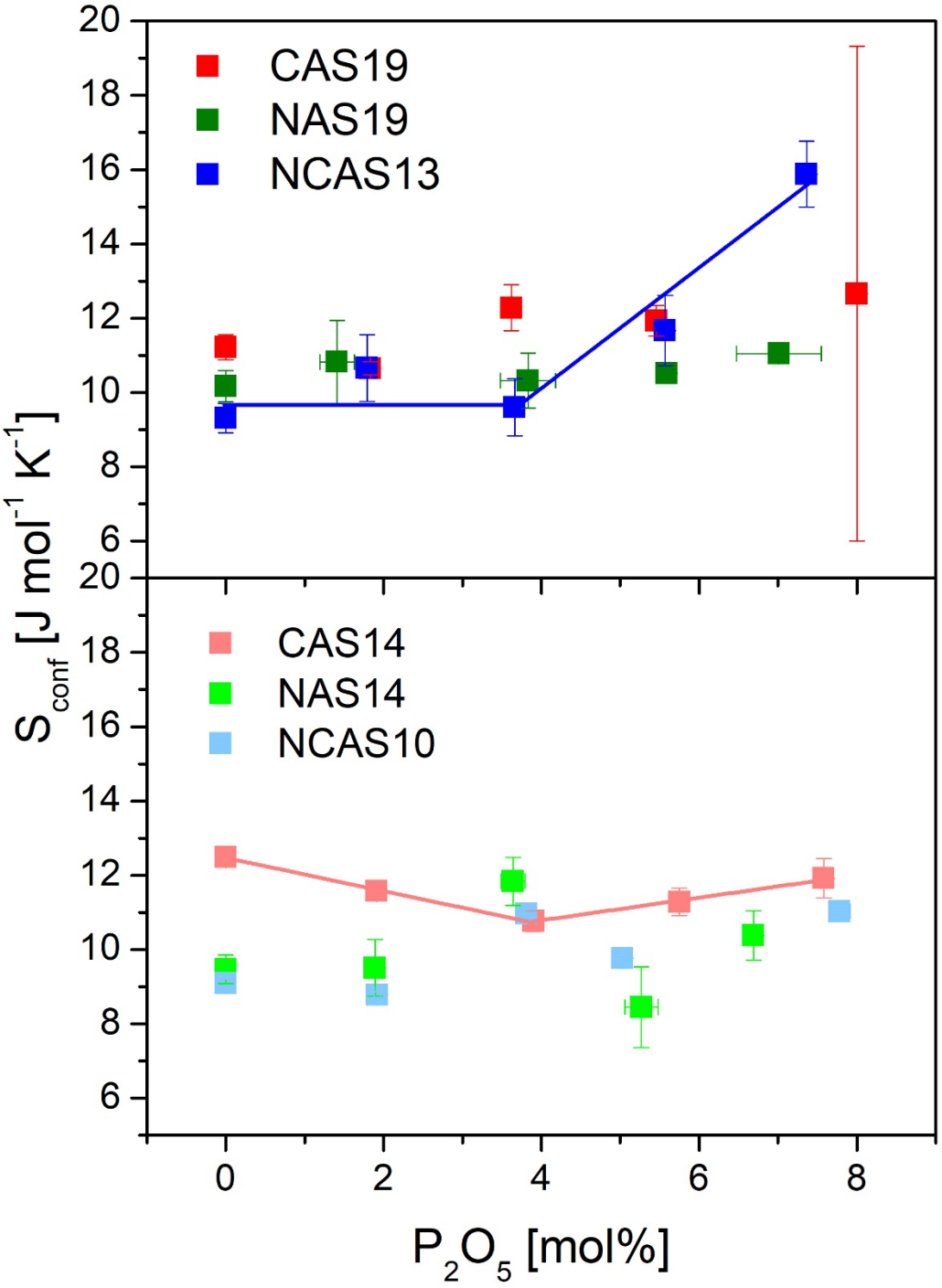

***Fig. 12**: S_{conf} as a function of P_2O_5 concentration for peralkaline as well as peraluminous P_2O_5-bearing melt compositions.*

The addition of low P_2O_5 concentrations (up to 2 mol%) to both melts lowers S_{conf} slightly by approximately 0.3 J mol^{-1} K^{-1}. Around 4 mol% of P_2O_5 in the melt a maximum in S_{conf} is reached for both melts. Between a P_2O_5 concentration of 4 mol% to 6 mol% S_{conf} decreases and increases again at higher P_2O_5 concentrations. Generally, the calcium-bearing CAS melts show the highest configurational entropies.

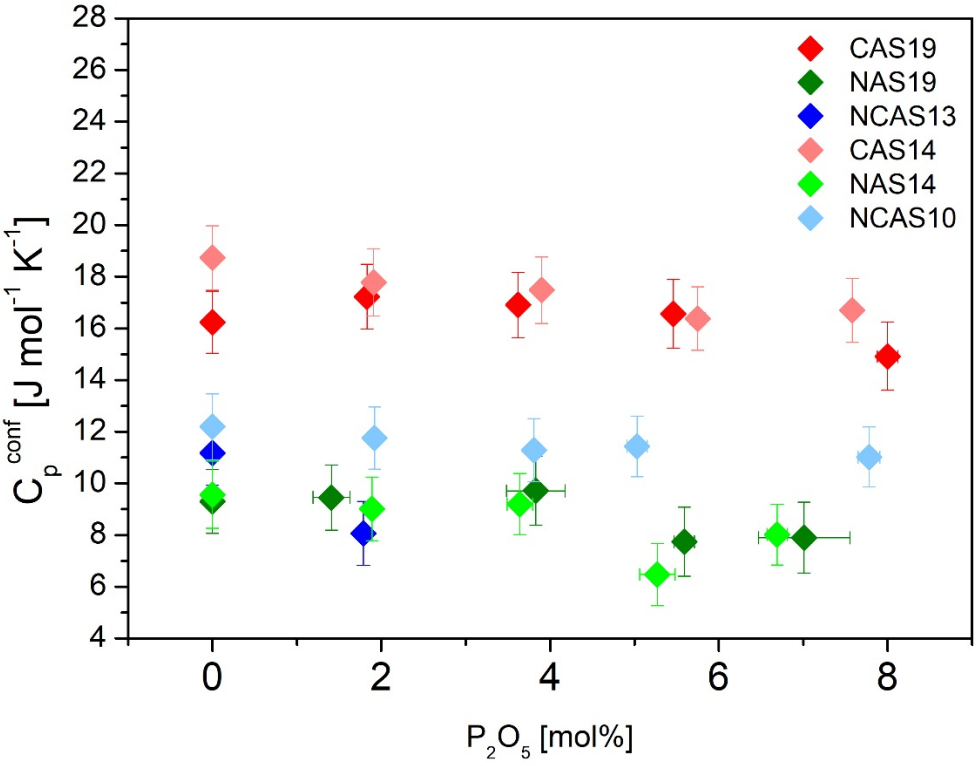

***Fig. 13**: C_p^{conf} as a function of P_2O_5 concentration for peralkaline as well as peraluminous melts.*

The configurational heat capacities for the phosphorus-bearing peralkaline and peraluminous melts are demonstrated in Fig. 13 as a function of P_2O_5 content. C_p^{conf} is defined as the energy that is required to move the structure from the glassy to liquid state (Richet et al. 1986). There is no significant change in C_p^{conf} within the error. Ca-bearing melts of CAS series exhibit the highest C_p^{conf} of 16 – 18 J mol^{-1} K^{-1}. Na-bearing NAS melts show the lowest configurational entropies of 7 – 9 J mol^{-1} K^{-1}. C_p^{conf} of the NCAS melts containing both Na and Ca lie in between by values of 11 – 13 J mol^{-1} K^{-1}.

Fig. 14 illustrates the fictive temperature T_f' as a function of P_2O_5 concentrations. The fictive temperatures follow a trend similar to that observed for the viscosities of the melts. For peralkaline melts such as CAS19 and NAS19 the fictive temperatures increase with the addition of P_2O_5 up to a maximum and decrease after the maximum at higher P_2O_5 concentrations in the melt.

For CAS19 T_f' increases from 1095 K to 1109 K around a maximum at a P_2O_5 concentration of ~4 mol% and decreases at higher P_2O_5 concentration up to 8 mol% to 1052 K. For NAS19 melt T_f' increases from 885 K to 940 K and decreases after the maximum around 4 mol% P_2O_5 to 900 K up to a P_2O_5 concentration of 7 mol%. In peraluminous melts T_f' decreases with higher P_2O_5 concentrations up to 8 mol% by ~50 K for CAS14 and NCAS10. The strongest decrease in T_f' by approximately 110 K is observed for NAS14 melt, which is consistent with viscosity data.

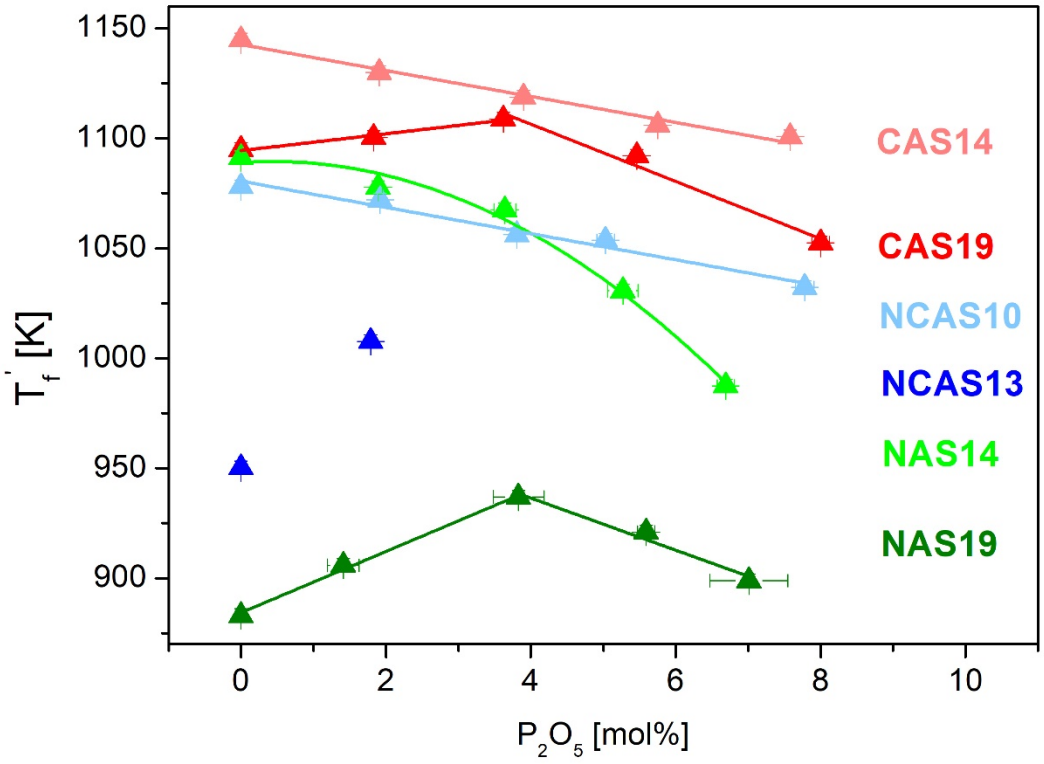

***Fig. 14**: Fictive temperatures (T_f') as a function of P_2O_5 concentration for peralkaline and peraluminous melt compositions.*

The B_e term for the peralkaline and peraluminous melts is shown in Fig. 15. B_e is higher for Ca-bearing CAS19 melts than for Na- as well as Na- and Ca- bearing NAS19 and NCAS13 melts. In peralkaline melts no trend for B_e can be observed within the error range. In peraluminous melts a decrease in B_e is observed followed by a slight increase between 5 mol% and 8 mol% P_2O_5 in the melt. However, both Na-bearing melts show a maximum B_e value near a P_2O_5 concentration of 4 mol% which does not follow the trend.

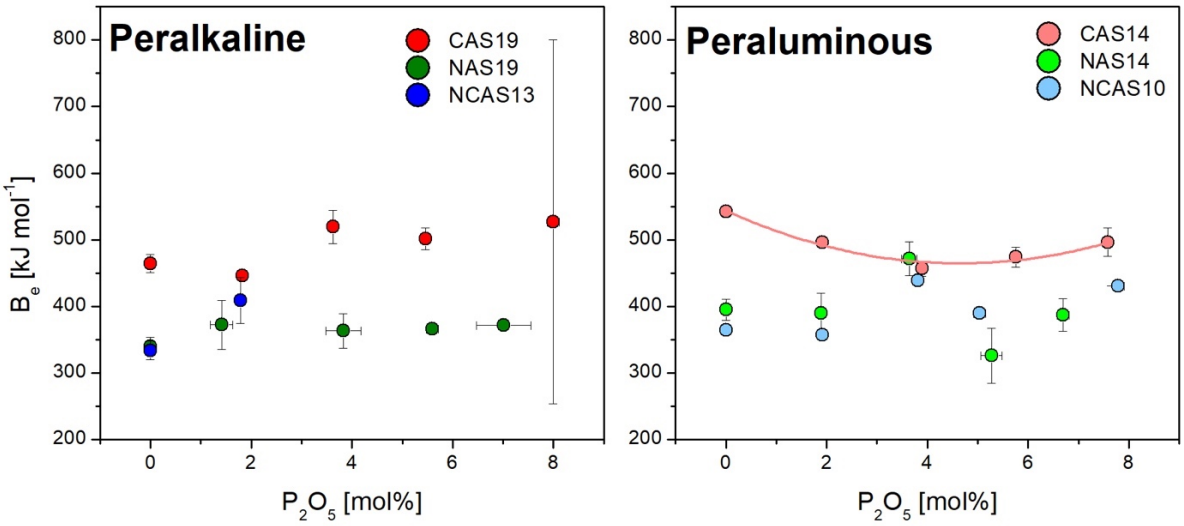

***Fig. 15**: Activation energy for viscous flow (B_e) as a function of P_2O_5 concentration for peralkaline as well as peraluminous melt compositions.*

The B_e/S_{conf} term is described in Fig. 16. For both the peralkaline and peraluminous melts B_e/S_{conf} follows the same trend as observed in viscosity data. In peralkaline melts, B_e/S_{conf} increases up to a P_2O_5 concentration around 4 mol% and decreases at higher P_2O_5 concentrations. The strongest effect of P_2O_5 on B_e/S_{conf} is observed for only Na-bearing NAS melts and lowest for only Ca-bearing CAS melts. The CAS melts exhibit the highest B_e/S_{conf} while the lowest B_e/S_{conf} are observed in NAS melts.

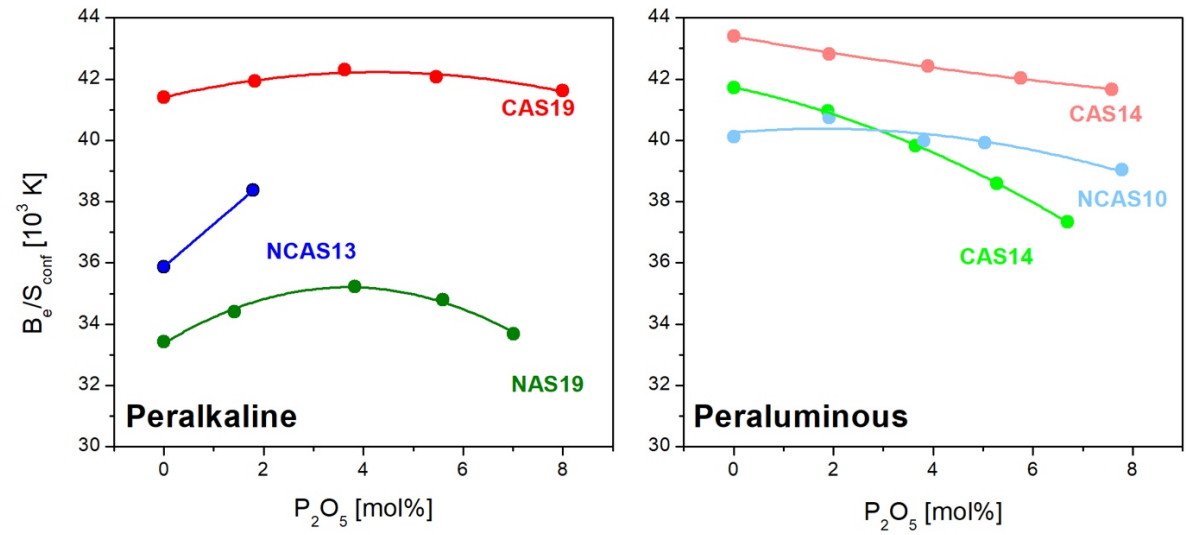

***Fig. 16**: B_e/S_{conf} as a function of P_2O_5 concentration for peralkaline as well as peraluminous melts.*

B_e and S_{conf} are strongly correlated in the Adam-Gibbs equation. A plot of the activation energy B_e against the configurational entropy S_{conf} is demonstrated in Fig. 17. For all investigated peralkaline as well as peraluminous melt compositions, a linear correlation is observed. The high error observed in CAS19 melt is a result of the Adam-Gibbs fit with only three measured viscosities.

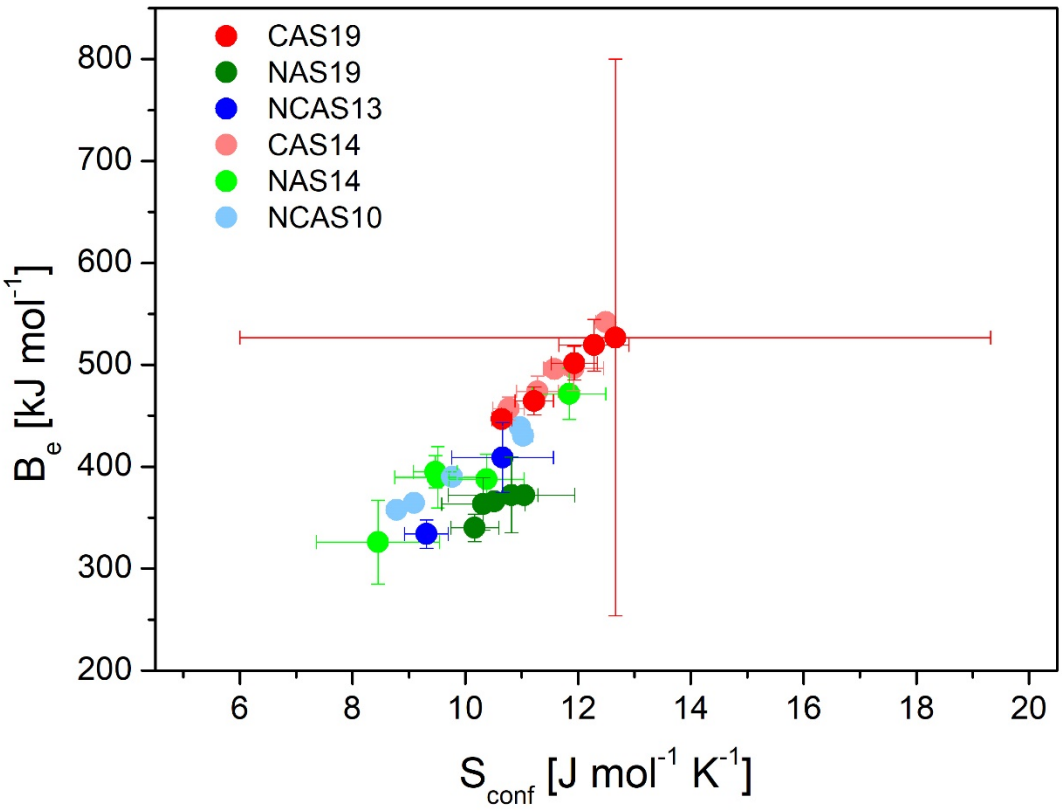

***Fig. 17**: B_e as a function of S_{conf} for peralkaline as well as peraluminous melts containing P_2O_5.*

The heat capacities of the boron-bearing samples of the peralkaline NCAS13 and peraluminous NCAS10 series are illustrated in Fig. 18. For both melts, the T_g peaks shifts to lower temperatures with increasing B_2O_3 concentration, indicating a depolymerisation of the melt. The glass transition in NCAS10 melt occurs at higher temperatures (1125 K) than for the NCAS13 melt (997 K). The effect of B_2O_3 on the glass transition is similar for both melts. The T_g peak in peralkaline NCAS13 melt shifts by 52 K to 945 K with the addition of 3.70 mol% P_2O_5 and by 43 K to 1068 K for the peraluminous NCAS10 melt.

Furthermore, it can be observed that in case of NCAS13 the heat capacities of the melts and glasses are lower by approximately 10 J mol^{-1} K^{-1} for B_2O_3 concentrations between 0 and 2 mol% than for the B_2O_3-free melt as well as melts with B_2O_3 concentrations > 2 mol%. The shift of the glass transition peak to lower temperatures is consistent with results obtained through viscosity measurements. The reason for the strong difference in C_{pg} and

C_{pl} is unclear but is probably linked to changes in incorporation mechanism of B_2O_3 into the melt structure. The B_2O_3-bearing melts were measured together by use of the same calibration whereas the B_2O_3-free base composition was measured beforehand. Therefore, the fact that samples NCAS13-B6 and NCAS13-B8 are close to the B_2O_3-free NCAS13 melt demonstrates the goodness of the calibration and thus excludes an error of the measurement.

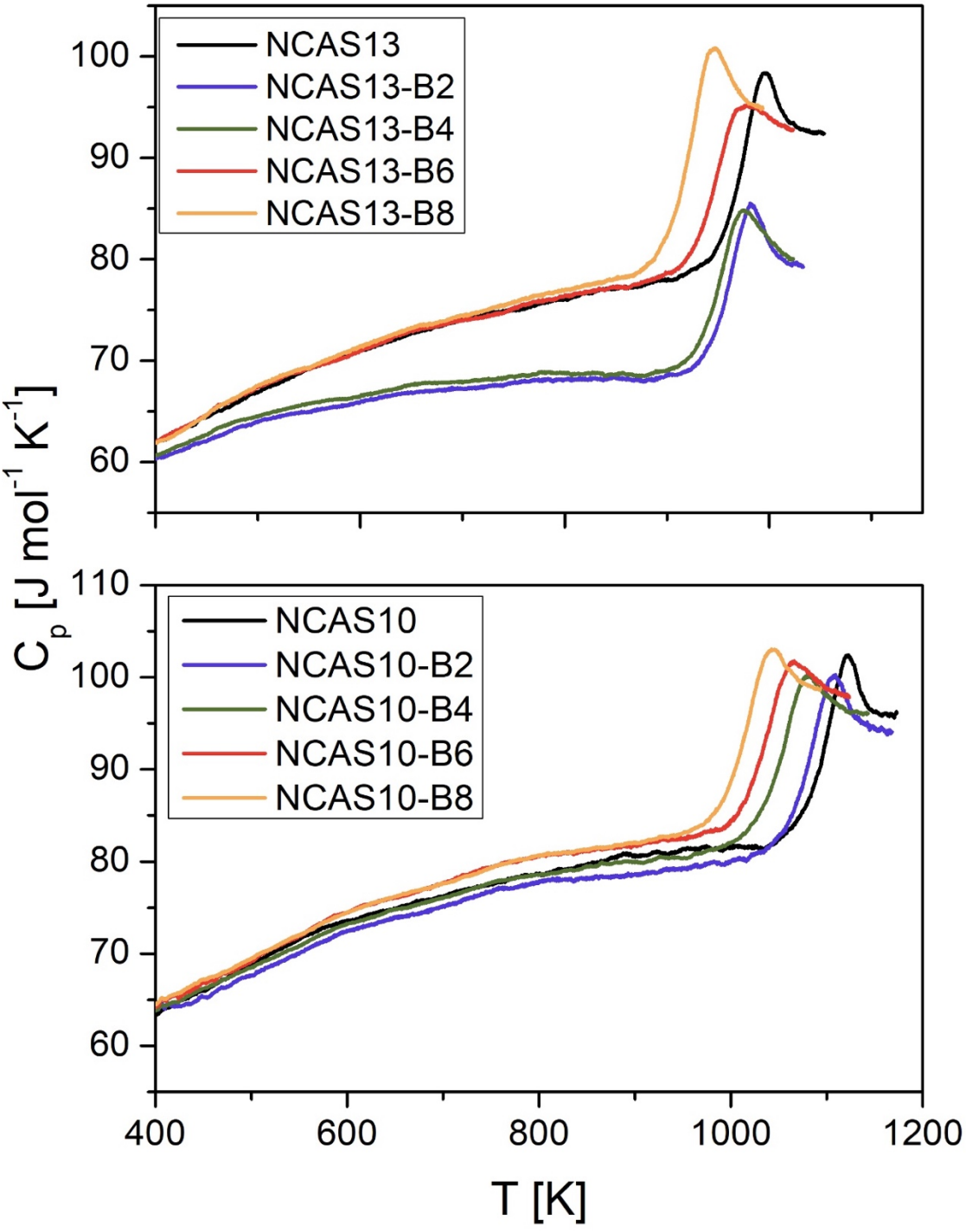

***Fig. 18**: Heat capacities of peralkaline NCAS13 and peraluminous NCAS10 B_2O_3-bearing melts.*

The fit parameters of the Maier-Kelley equation are presented in Table 10. S_{conf} and B_e are summarized in Table 11.

***Table 10**: Maier-Kelley fit parameter for B_2O_3-bearing melts*

sample	a	Δ a	b	Δ b	c	Δ c
	J g^{-1} K^{-1}	J g^{-1} K^{-1}	10^{-4} J g^{-1} K^{-2}	10^{-4} J g^{-1} K^{-2}	10^{4} J g^{-1} K	10^{4} J g^{-1} K
NCAS13-B2	1.08	0.00	-0.10	0.01	-2.65	0.01
NCAS13-B4	1.11	0.00	-0.29	0.01	-2.84	0.01
NCAS13-B6	1.01	0.00	2.38	0.01	-2.62	0.01
NCAS13-B8	0.98	0.00	2.80	0.02	-2.50	0.01
NCAS10-B2	1.06	0.00	1.62	0.02	-3.16	0.03
NCAS10-B4	1.05	0.00	1.94	0.02	-3.05	0.02
NCAS10-B6	1.06	0.00	2.14	0.02	-3.30	0.03
NCAS10-B8	1.03	0.00	2.48	0.02	-2.97	0.02

***Table 11**: Adam-Gibbs parameter for B_2O_3-bearing melts*

sample	A_e	B_e	Δ B_e	S_{conf}	Δ S_{conf}	C_{pg}	C_{pl}	C_p^{conf}	Δ C_p^{conf}	T_f'
		kJ mol^{-1}	kJ mol^{-1}	J mol^{-1} K^{-1}	J mol^{-1} K^{-1}	J mol^{-1} K^{-1}	J mol^{-1} K^{-1}	J mol^{-1} K^{-1}	J mol^{-1} K^{-1}	K
NCAS13-B2	-4.55	349.03	21.50	9.83	0.62	69.02	79.54	10.52	2.83	935.7
NCAS13-B4	-4.55	392.63	30.20	11.12	0.86	69.08	79.61	10.53	2.00	922.2
NCAS13-B6	-4.55	401.01	30.65	11.54	0.89	80.96	92.80	11.85	1.56	936.2
NCAS13-B8	-4.55	363.33	28.57	10.66	0.85	80.99	94.82	13.83	3.80	901.9
NCAS10-B2	-4.55	367.86	15.41	9.16	0.40	82.66	94.18	11.52	1.57	1057.2
NCAS10-B4	-4.55	512.57	56.10	13.12	1.51	83.99	96.18	12.19	1.69	1034.9
NCAS10-B6	-4.55	519.29	170.52	13.41	4.58	86.05	98.25	12.20	1.21	1022.2
NCAS10-B8	-4.55	475.63	99.41	12.57	2.72	86.75	98.95	12.20	2.77	999.2

Error of the fictive Temperature T_f' is 3 K

Error of C_{pg} and C_{pl} is < 1%

S_{conf} as a function of B_2O_3 content is shown in Fig. 19. The increase of B_2O_3 in the melt also increases the configurational entropy for both the peralkaline and peraluminous melt composition. S_{conf} reaches a maximum between 3 and 3.5 mol% of B_2O_3. At higher concentrations S_{conf} decreases in both melts. For NCAS13 melt S_{conf} increases from 9.31 J mol^{-1} K^{-1} up to 11.54 J mol^{-1} K^{-1} and decreases afterwards to 10.66 J mol^{-1} K^{-1} with further addition of B_2O_3. In case of NCAS10 melt S_{conf} increases from 9.09 J mol^{-1} K^{-1} to 13.42 J mol^{-1} K^{-1} and decreases after the maximum S_{conf} to 12.57 J mol^{-1} K^{-1} . However, the

variations in S_{conf} are probably lower or higher due to the high uncertainty. An exponential fit of the data might be more accurate but for the purpose of this study a linear trend is used. The configurational entropy is slightly higher for peraluminous NCAS10 than for the peralkaline NCAS13 melt.

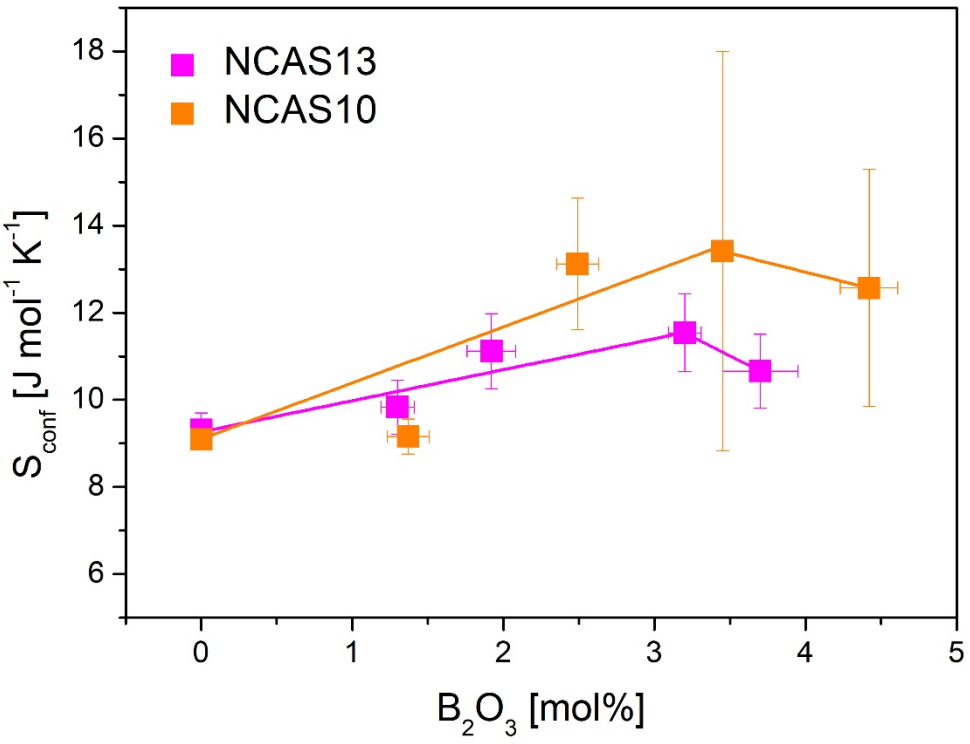

***Fig. 19**: Configurational entropy S_{conf} of peralkaline NCAS13 and peraluminous NCAS10 melt as a function of B_2O_3 concentration.*

The configurational heat capacity C_p^{conf} of the melt as a function of B_2O_3 content is illustrated in Fig. 20. C_p^{conf} is higher for the peraluminous NCAS10 melt than for the peralkaline NCAS13 melts. For these melt compositions, no significant change in C_p^{conf} is observed within the error range of the measurements.

The fictive temperature T_f' of the melt is demonstrated in Fig. 21 as a function of B_2O_3 concentration. T_f' is higher for the peraluminous NCAS10 melt than for the peralkaline NCAS13 melt. In both cases T_f' decreases with increasing B_2O_3 concentration in the melt. In case of NCAS10 T_f' decreases from 1078 K to 999 K whereas in NCAS13 melt T_f' decreases from 950 K to 902 K. However, there is a maximum in T_f' for the peralkaline NCAS melt around 3 mol% of B_2O_3.

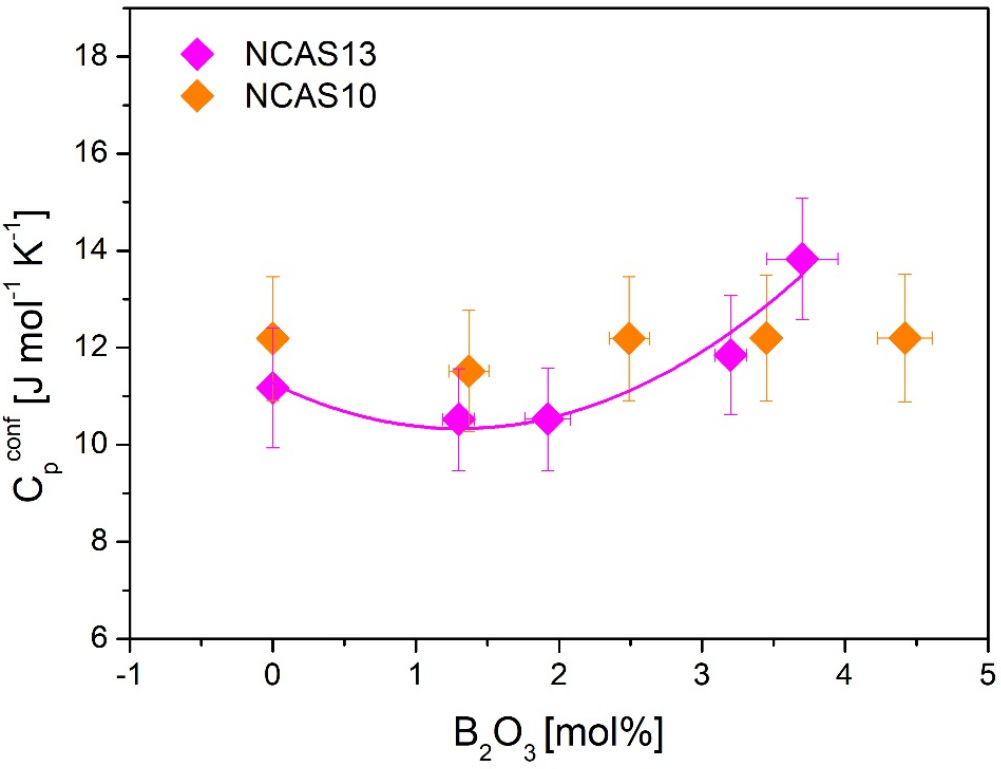

***Fig. 20**: Configurational heat capacity C_p^{conf} as a function of B_2O_3 concentration for peralkaline NCAS13 and peraluminous NCAS10 melt.*

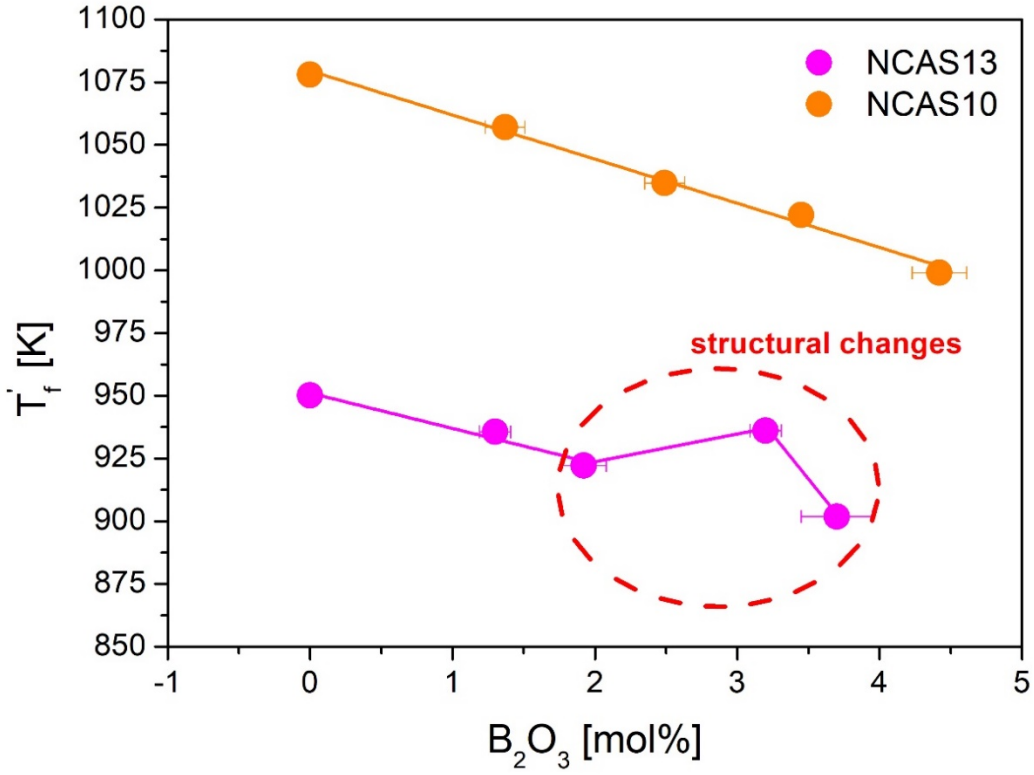

***Fig. 21**: Fictive temperatures T_f' as a function of B_2O_3 concentration for peralkaline NCAS13 and peraluminous NCAS10 melt.*

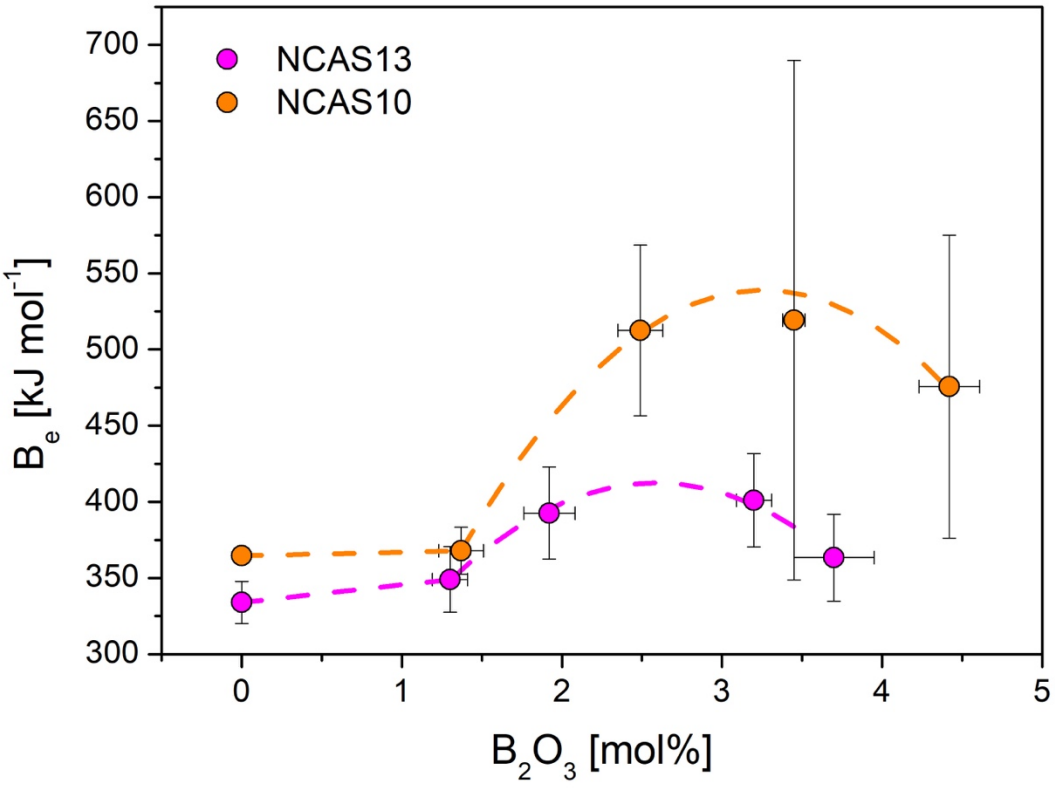

***Fig. 22**: Activation energy for viscous flow (B_e) as a function of B_2O_3 concentration of the peralkaline NCAS13 and peraluminous NCAS10 melt.*

B_e as a function of B_2O_3 content is illustrated in Fig. 22. For both the peralkaline and peraluminous melts the B_e value remains constant up to a B_2O_3 concentration of ~1.3 mol%. After that B_e increases in both melts up to a concentration of approximately 3.2 - 3.4 mol% and decreases with further addition of B_2O_3 to the melts. The B_e terms are higher for peralkaline than for peraluminous melts. The strongest increase and decrease in B_e is observed in the peralkaline melt.

Fig. 23 shows the B_e/S_{conf} for the B_2O_3-bearing melts. B_e/S_{conf} follows a similar trend as observed in viscosity data of the samples. In peraluminous melts B_e/S_{conf} decreases with increasing B_2O_3 concentration. In peralkaline melts, B_e/S_{conf} decreases at first slightly with the addition of B_2O_3 up to a concentration of 3.2 mol% and then decreases more strongly with further increasing B_2O_3 concentration in the melt. Generally, B_e/S_{conf} is higher and the decrease in B_e/S_{conf} stronger in peraluminous than in peralkaline melts.

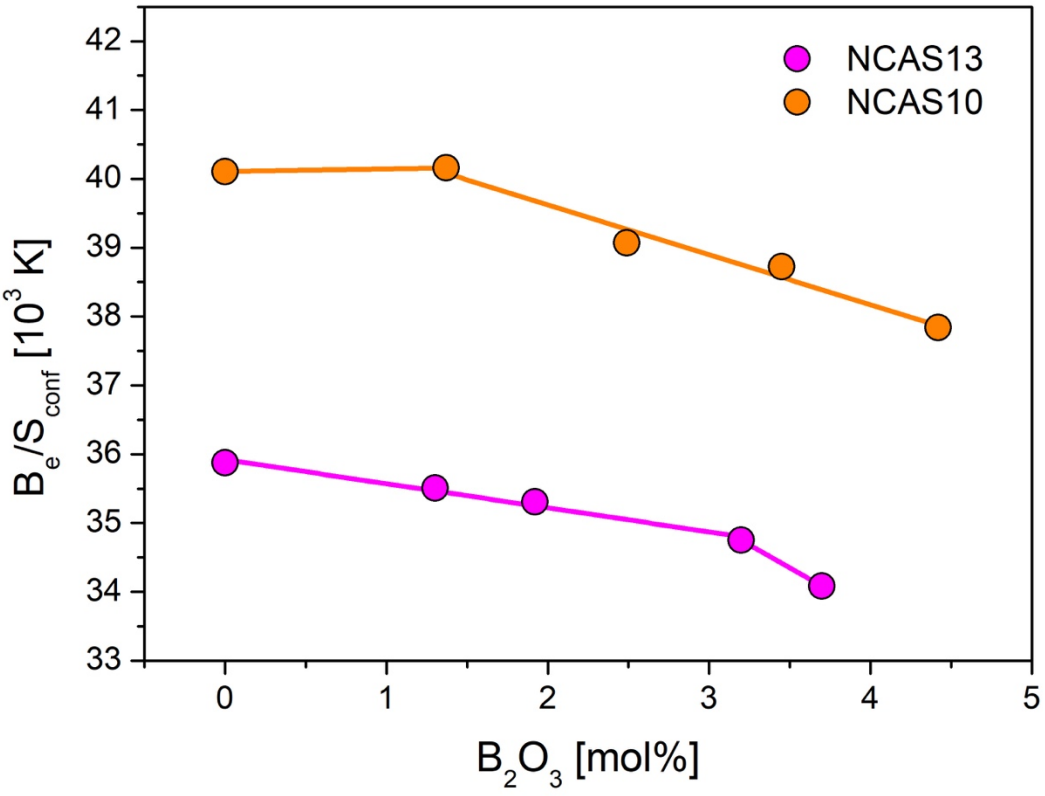

***Fig. 23**: B_e/S_{conf} as a function of B_2O_3 concentration for peralkaline NCAS13 and peraluminous NCAS10 melt.*

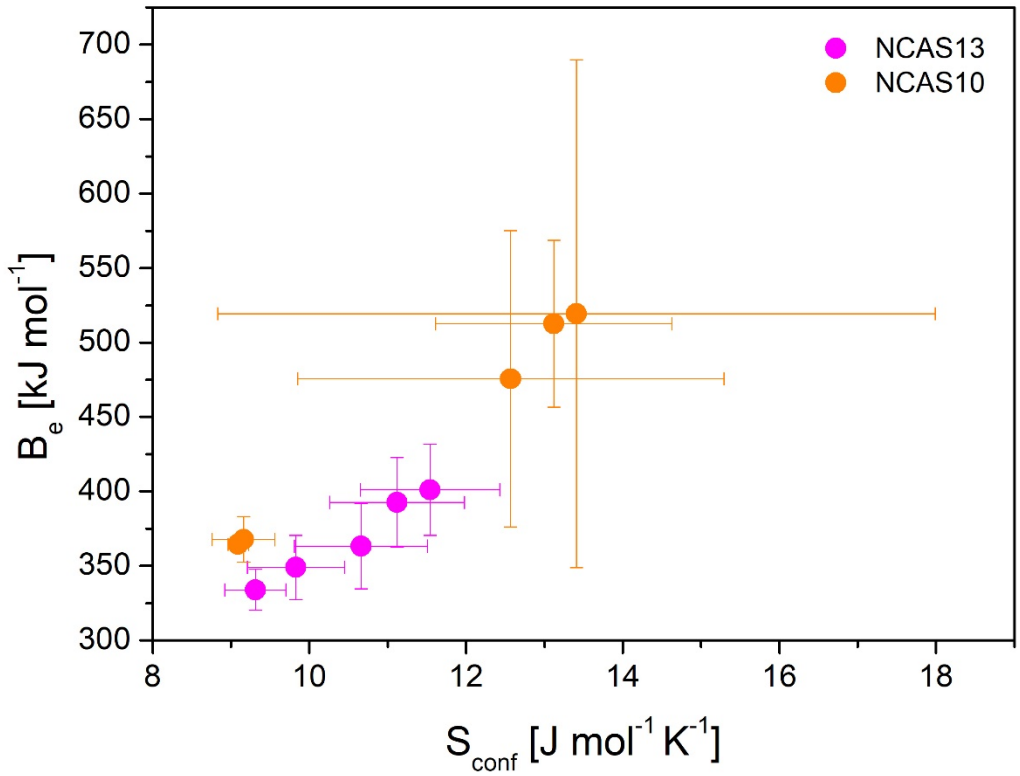

***Fig. 24**: B_e as a function of S_{conf} for B_2O_3-bearing peralkaline NCAS13 and peraluminous NCAS10 melt.*

B_e and S_{conf} are strongly correlated in the Adam-Gibbs equation. A plot of the activation energy B_e against the configurational entropy S_{conf} is demonstrated in Fig. 24. For the investigated peralkaline as well as the peraluminous melt composition, a linear correlation is observed.

3.4.3 Raman Spectroscopy

The Raman spectra of the P_2O_5-bearing peralkaline (CAS19, NAS19, NCAS13) and the peraluminous (CAS14, NAS14, NCAS10) melts are depicted in Fig. 25. The spectra are baseline- and Long-corrected (Long 1977; Di Muro et al. 2009) (see Eq. IX) and are normalized to the peak at 500 cm^{-1} for better comparison of the structural changes occurring due to the addition of P_2O_5 to the melt.

CAS19 shows two prominent peaks, one in the low frequency region at ~500 cm^{-1} with a prominent shoulder at ~590 cm^{-1} and one in the high frequency region at ~1030 cm^{-1}. With the addition of P_2O_5 to the melt the intensity of the high frequency band increases with respect to the low frequency band. Furthermore, a broadening of the high frequency band is observed. For P_2O_5 concentrations between 1.83 mol% and 6.48 mol% a small shoulder at ~950 cm^{-1} appears. Furthermore, a broad shoulder appears at ~1200 cm^{-1} for melts containing more than 3.62 mol% P_2O_5.

NAS19 also exhibits two prominent peaks, one in the low frequency region at ~500 cm^{-1} with a prominent shoulder at ~580 cm^{-1} and one in the high frequency region at ~1065 cm^{-1}. With increasing P_2O_5 concentration in the melt, the intensity of the high frequency region band increases with respect to the low frequency band. Furthermore, both bands broaden at higher P_2O_5 concentrations. For melt compositions containing P_2O_5, a small peak emerges from the high frequency region at ~980 cm^{-1}. This peak grows in intensity up to a P_2O_5 concentration of 3.83 mol% and loses intensity at higher P_2O_5 concentrations, developing into a small shoulder. Additionally, a second broad shoulder appears in the high frequency band at P_2O_5 concentrations > 3.83 mol%.

The strongest changes occur in the peralkaline NCAS13 melt. NCAS13 also shows the same vibrational band at ~500 cm^{-1} with a shoulder at ~580 cm^{-1} and a second band at ~1055 cm^{-1}. As in the other two peralkaline melts, an increase of the high frequency band with respect to the low frequency band is observed with increasing P_2O_5 concentration. The P_2O_5-bearing melts exhibit a sharp and narrow band of high intensity that emerges from the high frequency band at ~960 cm^{-1}. The intensity of this band increases up to a P_2O_5 concentration of 3.66 mol% and decreases with further addition of P_2O_5. For the highest

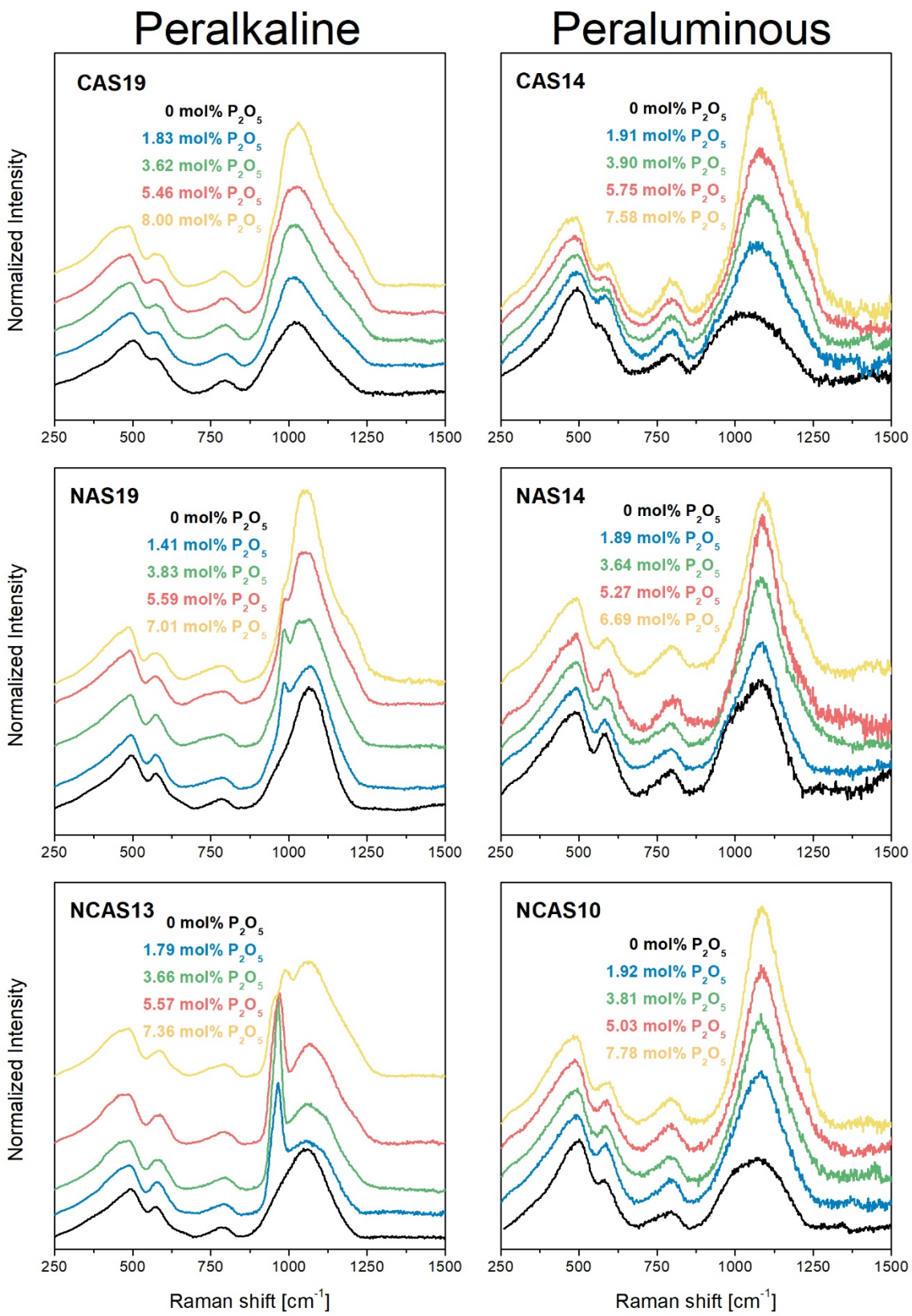

***Fig. 25**: Baseline and Long-corrected Raman spectra of peralkaline and peraluminous P_2O_5-bearing glasses. Spectra were normalized to the Intensity of the peak at ~500 cm^{-1}.*

P_2O_5 concentration of 7.26 mol%, this peak splits into a shoulder at ~950 cm^{-1} and a small peak at ~1000 cm^{-1}. Furthermore, a broadening of the high and low frequency band is observed with increasing P_2O_5 concentration.

In the peraluminous melts CAS14, NAS14 and NCAS10 there are also two prominent bands, one in the low frequency region at ~500 cm^{-1} with a shoulder around 580 cm^{-1} and one in the high frequency region. The position of the low frequency bands is the same in all three peraluminous compositions and no significant changes are observed in this region. The structural changes caused by the presence of P_2O_5 in the melt occur in the high frequency region.

With increasing P_2O_5 concentration in the melt, the intensity of the high frequency band increases with respect to the low frequency band. Furthermore, a sharpening and shift of the high frequency band to higher wavenumbers is observed. In case of CAS14 melt the high frequency band shifts from ~1030 cm^{-1} to ~1090 cm^{-1} with increasing P_2O_5 concentration. For the highest P_2O_5 concentration of 7.58 mol% a shoulder appears at ~1200 cm^{-1}.

In the only Na-bearing NAS14 melt, the high frequency band shifts from ~1060 cm^{-1} to 1090 cm^{-1} and in case of the Na- and Ca-bearing NCAS10 melt the high frequency band shifts from ~1050 cm^{-1} to ~1090 cm^{-1}. For both melts the same sharpening of the high frequency band as well as the appearance of a shoulder at ~1200 cm^{-1} is observed as for the only Ca-bearing CAS14 melt.

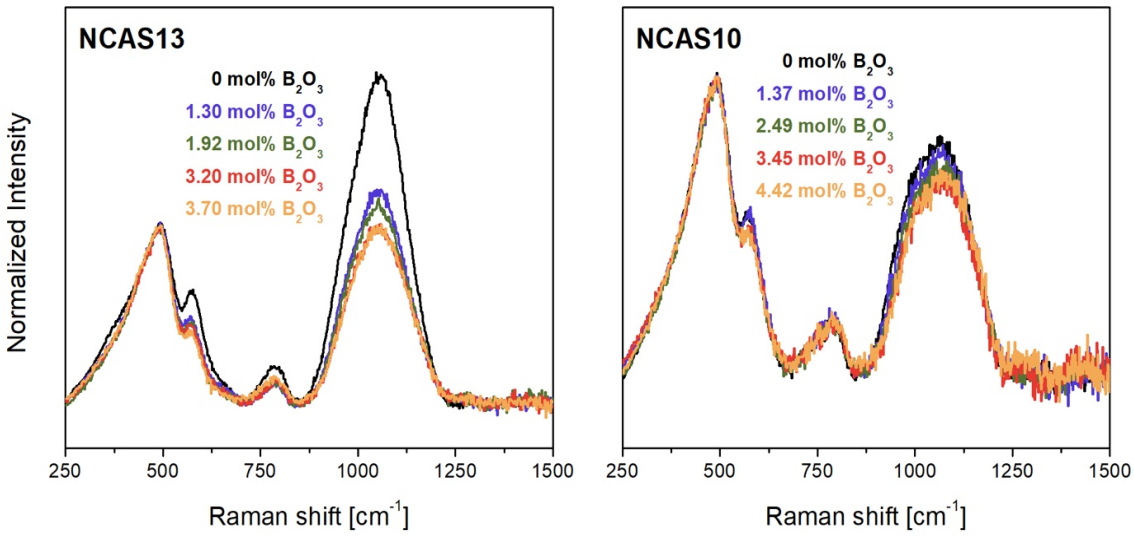

***Fig. 26**: Baseline- and Long-corrected Raman spectra of peralkaline NCAS13 and peraluminous NCAS10 glass containing B_2O_3. Spectra were normalized to the Intensity of the peak at ~500 cm^{-1}.*

The Raman spectra of the B_2O_3-bearing peralkaline NCAS13 and peraluminous NCAS10 melts are shown in Fig. 26. NCAS13 spectra consist of two prominent vibrational bands.

The first one is the low frequency band at ~500 cm^{-1} accompanied by a shoulder at ~580 cm^{-1} and the second one is found in the high frequency region at ~1050 cm^{-1}. With increasing B_2O_3 concentration in the melt the intensity of the high frequency band decreases with respect to the low frequency region. The highest changes in intensity are observed between the B_2O_3-free sample and the sample containing 1.30 mol% B_2O_3. With further increase of B_2O_3 solely a small decrease in intensity is found. Furthermore, a decrease in intensity of the shoulder at 580 cm^{-1} is found at higher B_2O_3 concentrations.

Sample NCAS10 also exhibits one prominent band in the low frequency region at ~500 cm^{-1} with a shoulder around 580 cm^{-1} and one in the high frequency region at ~1060 cm^{-1}. No structural changes are found in the low frequency region with increasing B_2O_3 concentration. In the high frequency region, a slight decrease of the intensity with respect to the low frequency region is observed.

3.4.4 SEM

In order to visualize the structural changes due to incorporation of P_2O_5 or B_2O_3 backscattered electron micrographs were taken of the samples. An electron micrograph of the P_2O_5- and B_2O_3-free sample NCAS13 is shown in Fig. 27 as an example of a homogeneous melt.

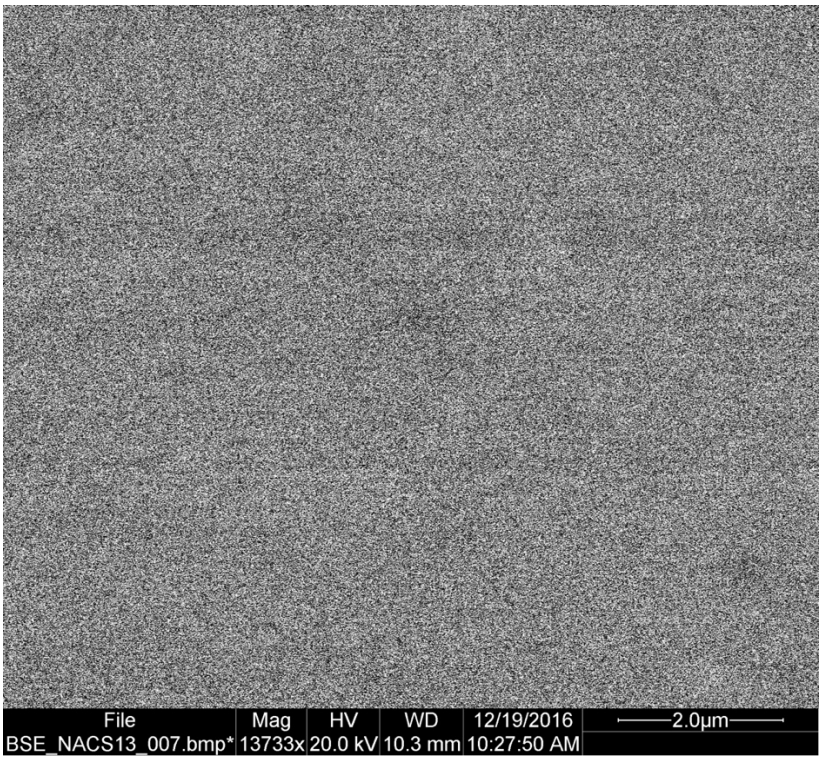

***Fig. 27**: BSE image of P_2O_5-free NCAS13 melt showing a homogeneous melt structure as observed in all unmixed melts.*

No visible structure is apparent for the P_2O_5- and B_2O_3-free melts. Also, samples of the peralkaline NAS19 and peraluminous CAS14, NAS14 and NCAS10 P_2O_5 as well as B_2O_3 series show no structural changes and, therefore, will not be further discussed. Their structure strongly resembles the structure of NCAS13 shown in Fig. 27.

Structural changes in the peralkaline Ca-bearing CAS19 melt occurred only for the sample containing 8 mol% P_2O_5 and with temperature and time and will therefore be further discussed in Chapter 6. Visible structural changes of the quenched melts occurred solely for the peralkaline NCAS13 series with addition of P_2O_5 to the melt.

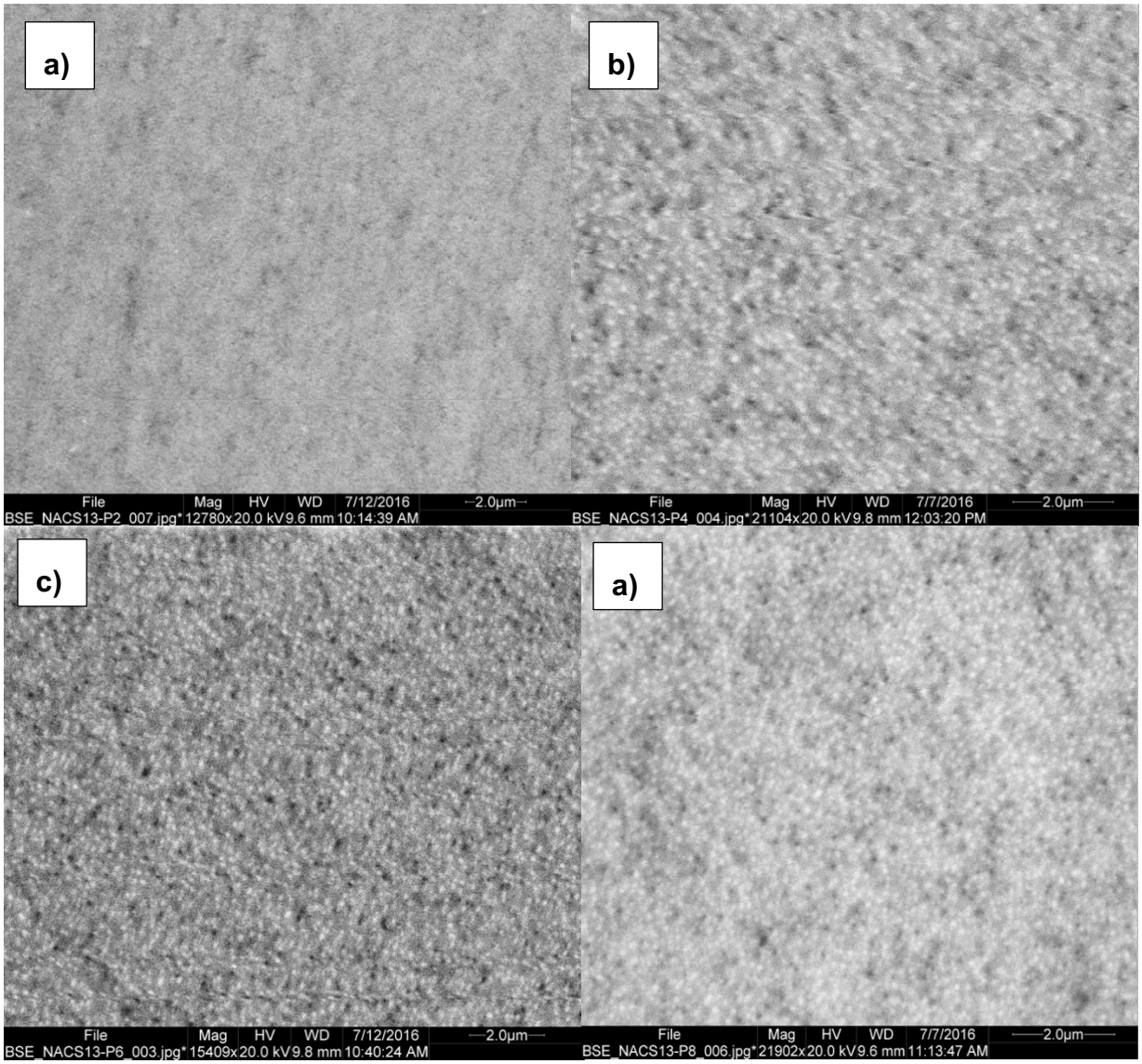

***Fig. 28**: Structure of peralkaline melts from NCAS13 series containing P_2O_5. a) NCAS13-P2, b) NCAS13-P4, c) NCAS13-P6 and d) NCAS13-P8.*

With the addition of 1.79 mol% of P_2O_5, no huge structural differences are visible, but the melt seems to rearrange itself (Fig. 28a). Though still homogeneous, small spots of lighter and darker colours seem to form. For all samples with higher P_2O_5 concentrations the melt separates into small spheres of light and dark colours, reflecting separated melt compositions (Fig. 28b-d). The spheres are in 100 – 300 nm range and can therefore not be measured with EDX. The spheres are approximately of the same size in all samples containing > 1.79 mol% P_2O_5, suggesting that no significant growth occurs simply due to the higher concentration of P_2O_5.

3.5 Discussion

3.5.1 The Effect of P_2O_5 on the Structure

Measurements show that P_2O_5 has a strong influence on the viscosity of the melts. The effect is different for peralkaline melts than for peraluminous melts (see Fig. 8). In peralkaline melts the viscosity of the melts increases with increasing P_2O_5 concentration up to a maximum and decreases with further addition of P_2O_5 to the melt. The increase in viscosity indicates a higher polymerisation of the melts. The polymerising effect of P_2O_5 on peralkaline melts is stronger for Na-bearing aluminosilicate melts than for Ca-bearing aluminosilicate melts. The strongest increase in viscosity, however, is observed for melts containing both Na and Ca.

The decrease in viscosity after the maximum indicates a depolymerisation of the melts at higher P_2O_5 concentrations. The strongest decreasing effect is observed for only Na-bearing aluminosilicate melts. A similar effect of P_2O_5 on melt viscosity for Na-bearing aluminosilicate melts was observed by Toplis and Dingwell (1996a), who performed viscosity measurements at low viscosities in the range 1 -$10^{3.5}$ Pa s for peralkaline and peraluminous Na_2O-Al_2O_3-SiO_2 melts with varying SiO_2 content.

Peralkaline melts contain more metal cations than necessary to charge balance negatively charged tetrahedra caused by the incorporation of Al^{3+} (Toplis and Dingwell 1996a). Those excess metal cations act as network modifiers. P_2O_5 enters the melt network in form of PO_4^{3-} tetrahedra which bond to those network modifiers. This results in the formation of metal phosphates as described by the following solution mechanism (Toplis and Dingwell 1996a):

$$2\ \text{Si-O-M} + \text{P-O-P} \rightarrow 2\ \text{P-O-M} + \text{Si-O-Si} \qquad (\textit{Eq. XIII})$$

whereby M represents a metal cation. The resulting formation of Si-O-Si bonds increases the NBO/T of the melts, resulting in a polymerisation of the melt. At the viscosity maximum observed for the present melts, the amount of network modifying metal cations is completely balanced by PO_4^{3-} units (Toplis and Dingwell 1996a).

After the viscosity maximum there are no more network modifying metal cations present in the melt. For instance, Gan and Hess (1992b) and Toplis and Dingwell (1996a) suggested that in this case PO_4^{3-} removes Al^{3+} from tetrahedral positions to form structural units similar to $AlPO_4$ structures in berlinite or simply acts as a charge balancer for Al tetrahedra. The removal of Al^{3+} from tetrahedral positions would result in the freeing of former charge balancing metal cations which then act as network modifiers and decrease the NBO/T of the melt, explaining the observed decrease in viscosity after the maximum.

In peraluminous melts no excess metal cations are present and the addition of P_2O_5 to the melt results in a steady decrease in viscosity due to apparently PO_4^{3-} removing Al^{3+} from tetrahedral positions. The removal of Na^+ has a stronger effect on melt polymerisation than the removal of divalent Ca^{2+}.

In addition, heat capacity measurements have shown that with increasing P_2O_5 concentration in the peralkaline melts, the glass transition peak shifts to higher temperatures up to a maximum temperature and then shifts back to lower temperatures with further increasing P_2O_5 concentration, indicating a stronger polymerisation of the melt and then a depolymerisation after the maximum in viscosity is reached. In peraluminous melts a steady shift to lower temperatures is observed with increasing P_2O_5 concentration. The effect of P_2O_5 is stronger for Na-bearing melts than for Ca-bearing melts. These observations are in agreement with results from viscosity measurements.

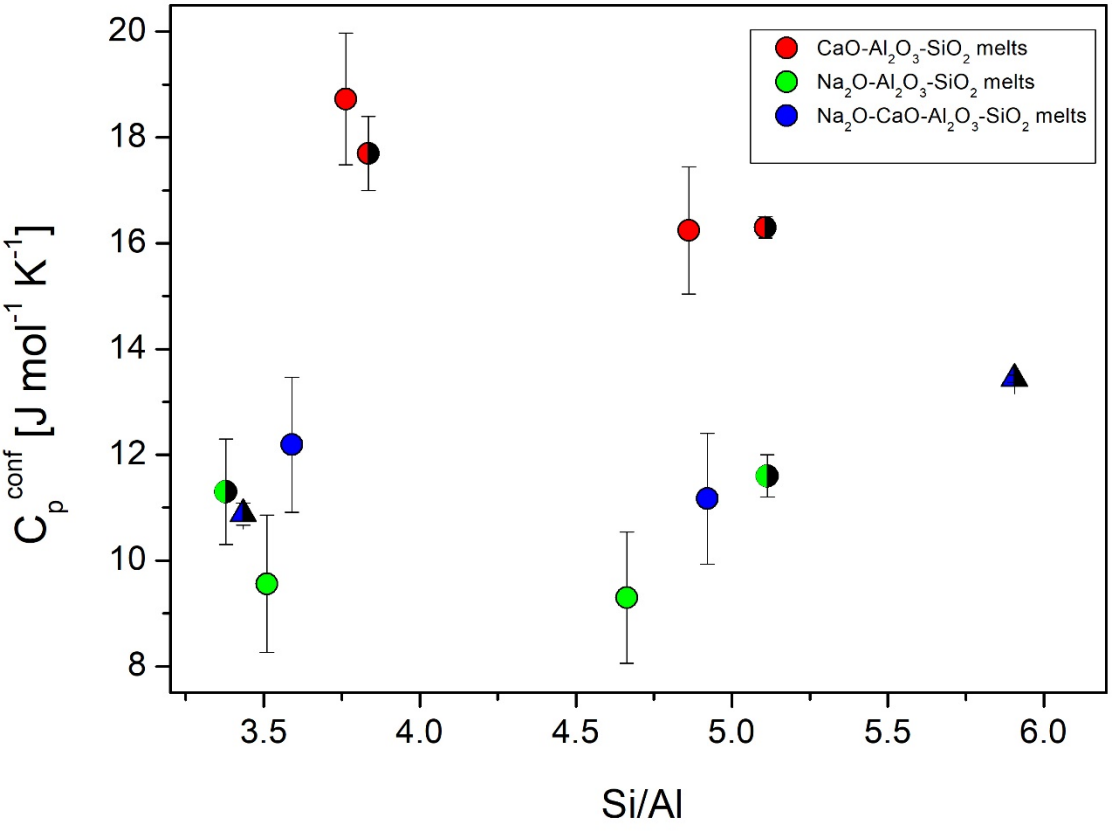

***Fig. 29**: C_p^{conf} as a function of Si/Al for P_2O_5- and B_2O_3-free melts of peralkaline and peraluminous composition together with melts of similar chemical compositions of Baasner et al. (2013a) (half-filled circles) and Webb (2008) (triangles). C_p^{conf} of this study are depicted by full symbols.*

A comparison of the heat capacities of the P_2O_5 free melts to melts with similar chemical composition is illustrated in Fig. 29 as a function of Si/Al ratio of the melts. The Na_2O-Al_2O_3-SiO_2 melts were compared to N3, N10, C10 and C27 melts of Webb (2008) as well as NACS and ANCS melts of Baasner et al. (2013a). It is shown that the measured C_p^{conf} are in good agreement with the previously published data. There is no heat capacity data for highly P_2O_5-rich melts with similar chemical composition.

3.5.2 The Effect of B_2O_3 on the Viscosity of Melts

B_2O_3 was observed to decrease the viscosity of the peralkaline as well as the peraluminous melts. While the decrease in viscosity for the peraluminous melt composition follows a linear trend, the viscosity decreasing effect of B_2O_3 in peralkaline melts is more complex. The viscosity decreases at the beginning slightly up to a B_2O_3 concentration of approximately 3.2 mol% and decreases more strongly with further addition of B_2O_3.

Fig. 30 illustrates the difference in viscosity $\Delta \log_{10} \eta$ of the B_2O_3-bearing melts in comparison to the P_2O_5-bearing melts of the same melt composition as a function of B_2O_3 or P_2O_5 content.

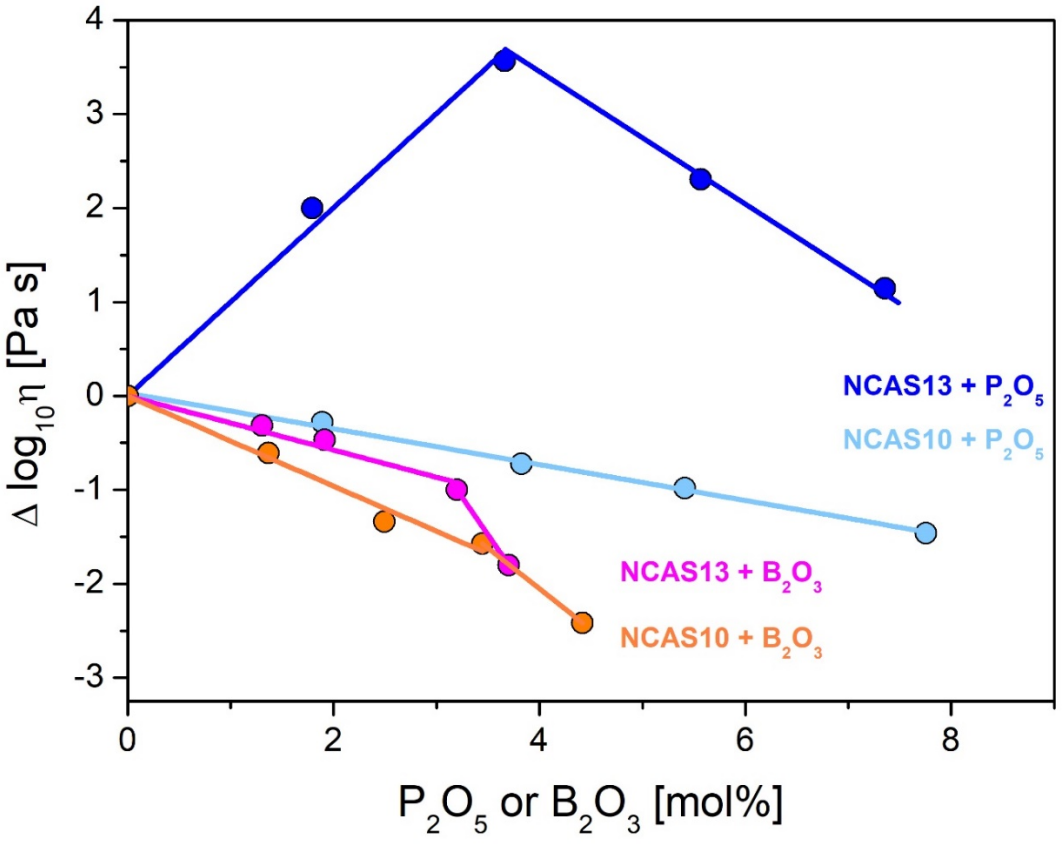

***Fig. 30**: Comparison of the difference in viscosities for P_2O_5- and B_2O_3-bearing melts. Viscosities were calculated at the temperature at which the viscosity of the P_2O_5- or B_2O_3-free melt equals 10^{12} Pa s.*

While the addition of P_2O_5 to the peralkaline NCAS13 melt results in an increase in viscosity up to a maximum and a decrease of viscosity with further addition of P_2O_5, it is interesting to see that the stronger decrease of viscosity in the B_2O_3-bearing melt occurs at approximately the same concentration of B_2O_3 as in the P_2O_5-bearing melt, indicating a direct connection to the excess metal cations in network modifying positions.

Many authors have discussed the structural role of boron in silicate melts. At ambient pressure boron is known to exist mainly in two coordination states, that are the trigonal threefold coordinated BO_3^0 and the tetrahedral fourfold coordinated BO_4^- (e.g. Konijnendijk 1975; Manara et al. 2009). The BO_3/BO_4^- ratio of the melt varies and is strongly dependant on the network modifying cations present in the melt (Wu and Stebbins 2009; Möncke et al. 2015). In the presence of network modifying cations, trigonal BO_3 is converted to tetrahedral BO_4^- up to a maximum network modifying cation concentration around 30 mol%, depending on the melt composition (Konijnendijk 1975).

Since in peralkaline melts network modifying cations are present, BO_4^- is likely to occur dominantly in the tetrahedral form. Tetrahedral BO_4^- behaves as a network former and should result in an increase of viscosity with increasing B_2O_3 concentration. Such a behaviour was also reported in previous studies (Konijnendijk 1975; Koroleva et al. 2011; Ha and Garofalini 2017). However, the results of this study show the exact opposite.

BO_3 acts as a network modifier and decreases viscosity. In peralkaline melts less excess metal cations are present than needed to charge balance negative charges caused by Al^{3+} in tetrahedral positions. Therefore, we suggest that B_2O_3 prefers the BO_3 state, resulting in the observed decrease in viscosity.

However, both BO_3 and BO_4^- are always present in the melt whereby the BO_3/BO_4^- ratio is dependent on the concentration of network modifying metal cations. Therefore, we suggest that in peralkaline melts, also a small amount of BO_3 is present. This leads to two competing mechanism of B_2O_3 incorporation in the melt.

Firstly, part of BO_3 is converted to BO_4^- due to the presence of excess network modifying metal cations Na^+ and Ca^{2+}. BO_4^- is a network former which results in a polymerisation of the melt network resulting in an increase of viscosity. Second, at the same time the remaining BO_3 act as network modifier and decrease the polymerisation of the melt. As a result of both mechanisms we observe a slight decrease in viscosity up to the point where all excess Na^+ and Ca^{2+} are used for charge compensation of AlO_4^- and BO_4^- tetrahedra, implying that the viscosity decreasing effect of BO_3 is stronger than the viscosity increasing effect of BO_4^-. Also, it is possible that though acting as a network former BO_4^- reduces the life time of a Si-O bond. At higher B_2O_3 concentrations only the viscosity decreasing effect

of BO_3 remains without the competing BO_4^- incorporation mechanism, resulting in a stronger decrease of viscosity.

From heat capacity measurements it was observed that in peralkaline melts there is a strong increase in C_{pg} and C_{pl} at the same B_2O_3 concentration as the stronger decrease in viscosity data is observed. We suggest that this increase in heat capacity is related to the changing incorporation mechanism of B_2O_3. Furthermore, there is a notable increase in T_f' where the incorporation mechanism changes. The shift of the T_g peak to lower temperatures implies a depolymerisation of the melt and is consistent with viscosity data.

Previous studies on B_2O_3-bearing melts have investigated the effect of high B_2O_3 concentrations (Konijnendijk 1975; Meera and Ramakrishna 1993; Manara et al. 2009; Cochain et al. 2013). This study demonstrates that the effect of B_2O_3 on melt structure is different at low B_2O_3 concentrations in peralkaline melts. A similar viscosity decreasing effect of B_2O_3 on the melt structure was observed for B_2O_3 concentration of 4.35 wt% and 8.92 wt% in haplogranite HPG8 by Dingwell et al. (1992).

3.5.3 Band Assignment in P_2O_5-bearing Glasses

Mysen (1992), Toplis et al. (1994b) as well as many other authors proposed that P_2O_5 enters the melt structure as PO_4^{3-} species. This is confirmed in this study by the appearance of the PO_4^{3-} band around 950 cm^{-1} – 980 cm^{-1}, which is visible in form of a small shoulder for peralkaline CAS melt and a prominent peak emerging from the high frequency peak in Na-bearing NAS and NCAS melts.

The high frequency peak consists of several overlapping peaks of Si-O stretching vibrations, which are mainly silicon Q^1-species at 900 cm^{-1}, Q^2 at ~970 cm^{-1} and Q^3 at ~1090 - 1100 cm^{-1} (Mysen 1992; Gan and Hess 1992a). In the low frequency range Q^4 species is found around 500 cm^{-1} (Mysen 1998a) together with various overlapping bending and stretching vibrations which are related to the more polymerised structural units such as e.g. different Si-O-Si bending modes at ~600 cm^{-1} (Mysen 1998b) and oxygen rocking motions at approximately 480 – 540 cm^{-1} (Mysen 1992). The slight shoulder around 1200 cm^{-1} which appears in the spectra of the melts with high P_2O_5 contents results from stretching vibrations of structural units similar to $AlPO_4$ structural units in berlinite (Gan and Hess 1992a; Mysen 1998a).

Based on the assumption that PO_4^{3-} tetrahedra bond to the excess Na and Ca in the melt (Mysen et al. 1981a ; Gan and Hess 1992b; Gwinn and Hess 1993; Toplis and Dingwell 1996a; Mysen 1998a) it is observed that the formation of Na_3PO_4 structural units shows a stronger effect on the intensity of the PO_4^{3-} band than the formation of $Ca_3(PO_4)_2$ units.

However, the strongest influence on the intensity on the PO_4^{3-} band is observed in melts containing both Na and Ca. The intensity of this peak increases up to the P_2O_5 concentration at which viscosity reaches its maximum and decreases at higher P_2O_5 concentration, implying that that the formation of phosphate species is dominant while there are still metal cations present in network modifying positions.

After the viscosity maximum it was proposed that PO_4^{3-} removes Al^{3+} from tetrahedral positions to form structural units resembling $AlPO_4$ structures in berlinite (Toplis and Dingwell 1996a; Mysen 1996, 1998b), which is also observed in this study by the appearance of the shoulder at ~1200 cm^{-1}. However, Mysen (1998b) also mentioned the formation of pyrophosphate P_2O_7 as a possible structural unit in P_2O_5-bearing melts. P_2O_7 shows a band around 1000 cm^{-1}. The formation of these structural units after the viscosity maximum is reached together with the formation of $AlPO_4$ units explains the decreasing intensity of the PO_4^{3-} band as well as the increase in the high frequency band compared to the band in the low frequency region. Additionally, the intensity of the high frequency band is also increased due to the formation of more silicon Q^3 species as the polymerisation of the melt increases.

In peraluminous melts, no prominent vibrational band around 950 cm^{-1} indicating the presence of PO_4^{3-} is observed. The strong sharpening of the high frequency band and the shift to higher wavenumbers indicates the presence of $AlPO_4$ structural units around 1200 cm^{-1} as well as probably some pyrophosphate P_2O_7 at ~1000 cm^{-1}.

3.5.4 Band Assignment B_2O_3 Melts

Two main vibrational regions are present in the B_2O_3-bearing Raman spectra of the peralkaline and peraluminous NCAS13 and NCAS10 melts, the low frequency region at 250 cm^{-1} – 500 cm^{-1} and the high frequency region at ~900 cm^{-1} to 1200 cm^{-1}.

The band in the high frequency region consists of several overlapping peaks of Si-O stretching vibrations which are generated through silicon Q^1-species at 900 cm^{-1}, Q^2 at ~970 cm^{-1} and Q^3 at ~1090 - 1100 cm^{-1} (Mysen 1992; Gan and Hess 1992a; Koroleva et al. 2011). Q^4 species is found around 500 cm^{-1} in the low frequency region (Mysen 1998a) together with various overlapping bending and stretching vibrations which are related to the more polymerised structural units such as e.g. different Si-O-Si bending modes at ~600 cm^{-1} (Mysen 1998b) and oxygen rocking motions at approximately 480 – 540 cm^{-1} (Mysen 1992).

The decrease in intensity in the high frequency region is caused by the depolymerisation of the melt with increasing B_2O_3 concentration due to the formation of probably more silicon Q^1 and Q^2 species. The decrease in intensity is less pronounced in peraluminous melts.

In previous studies of boron in silicate melts it was found that B_2O_3 enters the melt network as BO_3 or BO_4^- (Cochain et al. 2013). The vibrations of BO_3 rings are found at 610 cm^{-1} – 670 cm^{-1} and at ~1400 cm^{-1} for BO_3 with one NBO (Meera and Ramakrishna 1993; Koroleva et al. 2011; Cochain et al. 2013).

Vibrations of the BO_4^- groups are found at ~770 cm^{-1} – 800 cm^{-1} (Meera and Ramakrishna 1993; Koroleva et al. 2011). However, no significant changes in these vibrational regions are observed in the measured Raman spectra of both the peralkaline and peraluminous melts used in this study. Only the effect of B_2O_3 on the formation of more NBO's compared to the B_2O_3 melt can be observed. Previous studies of the structure of B_2O_3-bearing melts were conducted for melts containing much higher B_2O_3 concentrations than used in this study. Therefore, we assume that the intensities of the BO_3 and BO_4^- groups are too small and overlain by other vibrational bands from the silicate melt network.

3.5.5 Effect of P_2O_5 and B_2O_3 on Unmixing

A summary showing which melts unmix with the addition of P_2O_5 or B_2O_3 is given in Table 12. In only P_2O_5-bearing melts unmixing was observed solely in the peralkaline NCAS13 melt. While it is evident from structural changes during measurements that the peralkaline CAS19-P8 melt also shows an affinity to unmix, the quenched melts are unmixed and therefore no matter of further discussion in this chapter. The effect of tempering on CAS19 series is described in Chapter 6.

Samples from NCAS13 series show a second glass transition peak at lower temperatures for the melts containing 3.66 mol% and 5.57 mol% P_2O_5 indicating the presence of two separate melts. NCAS13-P8 shows only one glass transition peak. However, since melt separation is clearly evident in BSE images, we suggest that the heat capacity data of this melt should also include a second glass transition peak. This sample showed crystallisation during the first heat capacity measurement, which was visible from a prominent exothermal peak in the heat capacity data. The crystal content was less than 1 Vol% and does not affect the original melt composition significantly. However, it is possible that crystallisation increased the original heat capacity, overlapping the second T_g peak.

No unmixing was observed for the peraluminous P_2O_5-bearing melts as well as no B_2O_3-bearing melts with the used methods.

***Table 12**: Overview over unmixing as observed in the P_2O_5- and B_2O_3-bearing samples*

P_2O_5-bearing melts			**B_2O_3-bearing melts**		
sample	unmixing observed with DSC	unmixing observed with SEM	sample	unmixing observed with DSC	unmixing observed with SEM
CAS19	-	-	NCAS13-B2	-	-
CAS19-P2	-	-	NCAS13-B4	-	-
CAS19-P4	-	-	NCAS13-B6	-	-
CAS19-P6	-	-	NCAS13-B8	-	-
CAS19-P8	-	(x)	NCAS10-B2	-	-
CAS14	-	-	NCAS10-B4	-	-
CAS4-P2	-	-	NCAS10-B6	-	-
CAS14-P4	-	-	NCAS10-B8	-	-
CAS14-P6	-	-			
CAS14-P8	-	-			
NAS19	-	-			
NAS19-P2	-	-			
NAS19-P4	-	-			
NAS19-P6	-	-			
NAS19-P8	-	-			
NAS14	-	-			
NAS14-P2	-	-			
NAS14-P4	-	-			
NAS14-P6	-	-			
NAS14-P8	-	-			
NCAS13	-	-			
NCAS13-P2	-	-			
NCAS13-P4	x	x			
NCAS13-P6	x	x			
NCAS13-P8	-	x			
NCAS10	-	-			
NCAS10-P2	-	-			
NCAS10-P4	-	-			
NCAS10-P6	-	-			
NCAS10-P8	-	-			

Many authors have reported that P_2O_5 forms PO_4^{3-} structural units with excess metal cations in peralkaline melts and Al^{3+} in peraluminous melts (Mysen et al. 1981a; Gwinn and Hess 1993; Toplis and Dingwell 1996a). Boron has also been known to result in melt separation at high B_2O_3 concentrations (Konijnendijk 1975; Shelby 2005). These assumptions are in agreement with results of this study. However, whether these PO_4^{3-} units are directly linked

to the SiO_4 or AlO_4^- tetrahedra or reside outside the melt network still remains a matter for discussion. Gan and Hess (1992b) have suggested that these structural units reside outside the melt network but found no proof.

In this study we show that melt separation does in fact occur at high P_2O_5 concentrations in peralkaline Na- and Ca- bearing melts. Furthermore, we demonstrate that SEM and DSC are good methods to investigate the unmixing of melts. If unmixing occurs, it is observed with both methods. However, crystallisation affects heat capacity data and therefore it may not show unmixing as seen with sample NCAS13-P8.

Though the unmixed melt spheres are too small to be measured for their composition with the used methods, we suggest that the melt separates into a silica- and a phosphorus-rich melt.

Based on the assumptions made in previous as well as this study concerning the incorporation mechanism of P_2O_5 in silicate melts, we suggest that PO_4^{3-} forms the separate melt phase with the excess metal cations, whereby we believe that the formation of a Ca-P-rich silicate melt is more likely than a Na-P-rich melt, due to the fact that structural changes during measurements occurred for sample CAS19-P8. The slight structural changes occurring in sample NCAS13-P2 are interpreted as the beginning of unmixing in this melt composition.

However, Na also indirectly seems to play an important role for the unmixing of melts. Even though no unmixing was observed for solely Na-bearing melts, it is present in both Na- and Ca- bearing melts more so than in only Ca-bearing melts. Therefore, we suggest that though Na is not likely to become enriched in the P-rich melt at the investigated compositional range, it still enhances the separation of Ca from the silica-rich melt.

3.5.6 Comparison with Models

The measured viscosities of the melts have been compared to the calculated viscosities after Giordano et al. (2008b) and are presented in Fig. 31 for the P_2O_5-bearing melts and in Fig. 32 for the B_2O_3-bearing melts. Generally, it is observed that the model works better for the peralkaline melt compositions. The P_2O_5-free compositions fit the modelled values quite well while the peraluminous P_2O_5-free melt compositions are all overestimated by the model by approximately 2 log units.

The Na_2O concentrations of the melts in this study are slightly outside the boundaries used for modelling by Giordano et al. (2008b), but this is probably not the only reason for the deviation from the model since the peralkaline melts work well with the model and the

peralkaline NAS19 melt also exhibit slightly higher Na_2O concentrations than used for the model. Therefore, it is probably the different incorporation mechanism of P_2O_5 in peraluminous melts that causes the difference.

The model does not work for P_2O_5-bearing melts, which is expected since P_2O_5 is not included in the calculation of the model. In peralkaline melts, the P_2O_5 concentration seems to play an important role. The deviation from the model becomes higher with higher P_2O_5 concentration. The strongest deviation from the calculated viscosities is observed for only Na-bearing NAS19 melts and the lowest deviation is observed for only Ca-bearing CAS19 melts.

In peralkaline P_2O_5-bearig melts, the P_2O_5 concentration does not play a significant role in the calculation of the viscosities. With increasing P_2O_5 concentration the calculated values do not differ more than 0.5 to 0.7 log units from the P_2O_5-free NAS19 and NCAS13 melts. No deviation from the P_2O_5-free melt is observed for CAS19 melts.

This comparison shows that the effect of the incorporation mechanism of P_2O_5 on the viscosity is significant in peralkaline melts and should thus be included in future viscosity models. Furthermore, γ, which is the peralkalinity of the melt, should also be included in future models.

B_2O_3 also shows a strong effect on melt viscosity. The model overestimates the viscosities, which is expected since the model does not include B_2O_3 in the viscosity calculations, but it was observed from viscosity measurements that B_2O_3 decreases melt viscosity. With increasing B_2O_3 concentration the deviation from the model becomes higher. Other than what has been observed from the effect of P_2O_5, the addition of B_2O_3 to the melts causes the same overestimation for peralkaline as well as peraluminous melts. This implies that not the peralkalinity but solely the B_2O_3 concentration affects the model and should therefore be included in future viscosity models.

The heat capacity of the glass was modelled using the model after Richet (1987) and the heat capacities of the liquid were modelled after Stebbins et al. (1984) as well as Richet and Bottinga (1985) for both the P_2O_5- and B_2O_3 bearing melts. Partial molar heat capacities for P_2O_5 after Robie et al. (1978a) could be included in the model for C_{pg}. The results of the C_{pg} and C_{pl} modelling for the P_2O_5-bearing melts are illustrated in Fig. 33.

The results show, that the model for C_{pg} works well for the peralkaline melts, if the partial molar heat capacity of P_2O_5 glass is included. In peraluminous melts the model for C_{pg} works solely for the P_2O_5-free melts. At higher P_2O_5 concentrations the model underestimates the measured C_{pg} values by up to 20 J mol^{-1} K^{-1}, suggesting that probably the peralkalinity of the melt should also be included in future models.

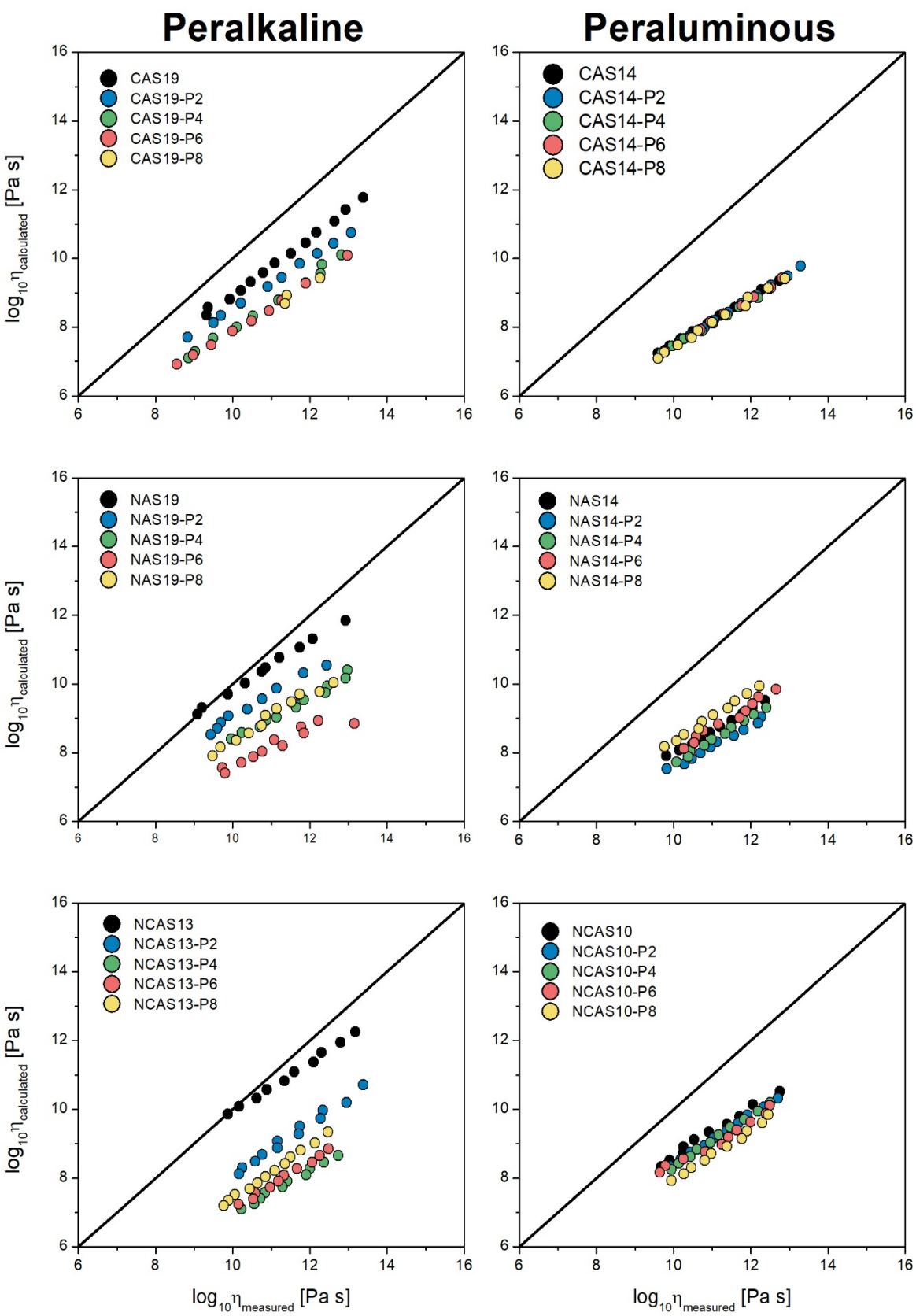

***Fig. 31**: Viscosities of P_2O_5-bearing peralkaline and peraluminous melts calculated after Giordano et al. (2008b).*

The liquid heat capacities C_{pl} show strong deviations from both models, which is probably caused by the fact that P_2O_5 is not included in the calculation of the modelled C_{pl}. Both models work quite well for the P_2O_5-free melt compositions and Na- as well as Na- and Ca-bearing melts from the peraluminous NAS14 and NCAS10 melts containing P_2O_5. Also, both models overestimate the C_{pl} values for the peralkaline compositions as well as the peraluminous only Ca-bearing CAS14 containing P_2O_5.

The results of the C_{pg} and C_{pl} modelling for the B_2O_3-bearing melts are shown in Fig. 34. All models differ from the measured values which is expected since all models do not include B_2O_3 in their calculation. For peralkaline NCAS13 series it is observed that all models for C_{pg} and C_{pl} either overestimate C_{pg} or C_{pl} at higher B_2O_3 concentrations or underestimate C_{pg} or C_{pl} at lower B_2O_3 concentrations by approximately 10 – 20 J mol^{-1} K^{-1} depending on the applied model. The reason here for lies within the results of the heat capacity measurements (see Fig. 18) where it is shown that there is a high increase in C_{pg} and C_{pl} at a B_2O_3 concentration > 1.92 mol%.

The C_{pg} as well as C_{pl} models work well for the B_2O_3-free melts and differ with increasing B_2O_3 concentration in the melt up to 10 J mol^{-1} K^{-1} for all models. This study shows that B_2O_3 affects C_{pg} and C_{pl} and should therefore be included in future models.

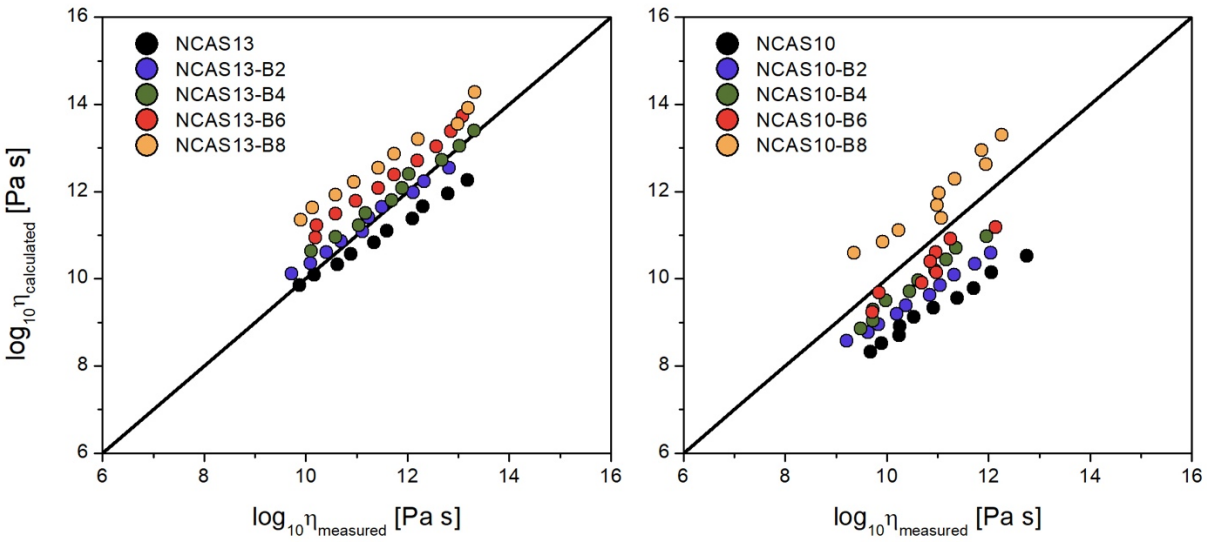

***Fig. 32**: Viscosities of B_2O_3-bearing peralkaline NCAS13 and peraluminous NCAS10 melt calculated after Giordano et al. (2008b).*

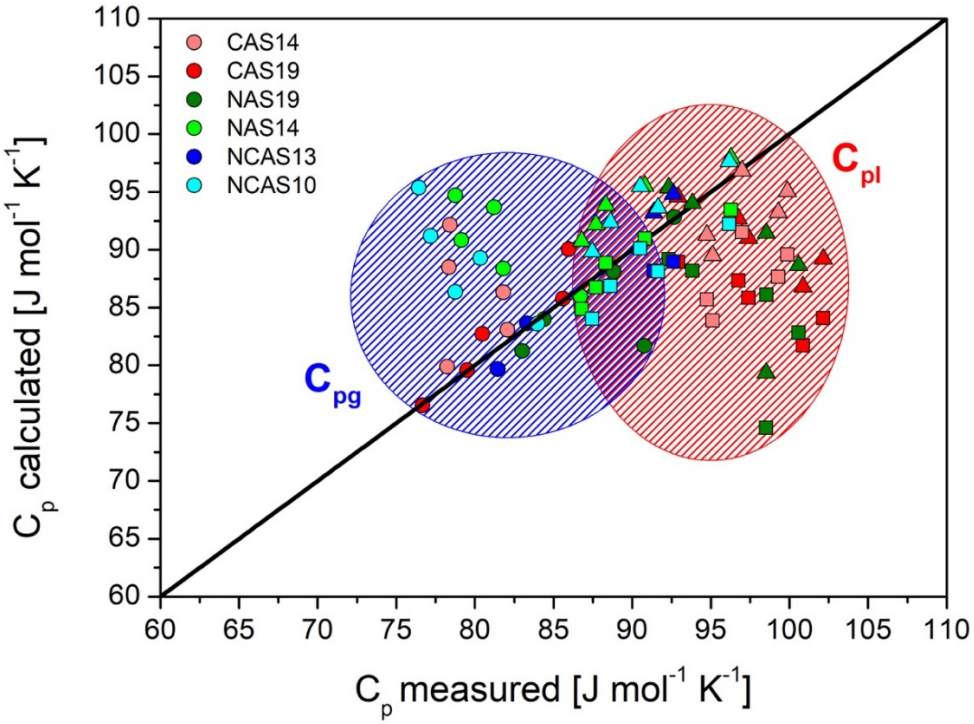

***Fig. 33**: C_{pg} calculated after Richet (1987) and C_{pl} calculated after Richet and Bottinga (1985) and Stebbins et al. (1984) for P_2O_5-bearing melts compared to measured values. Squares represent C_{pl} modelled after Richet and Bottinga (1985) and triangles represent C_{pl} modelled after Stebbins et al. (1984). Circles describe C_{pg} values. Blue area summarizes C_{pg} values whereas red area summarizes C_{pl} values.*

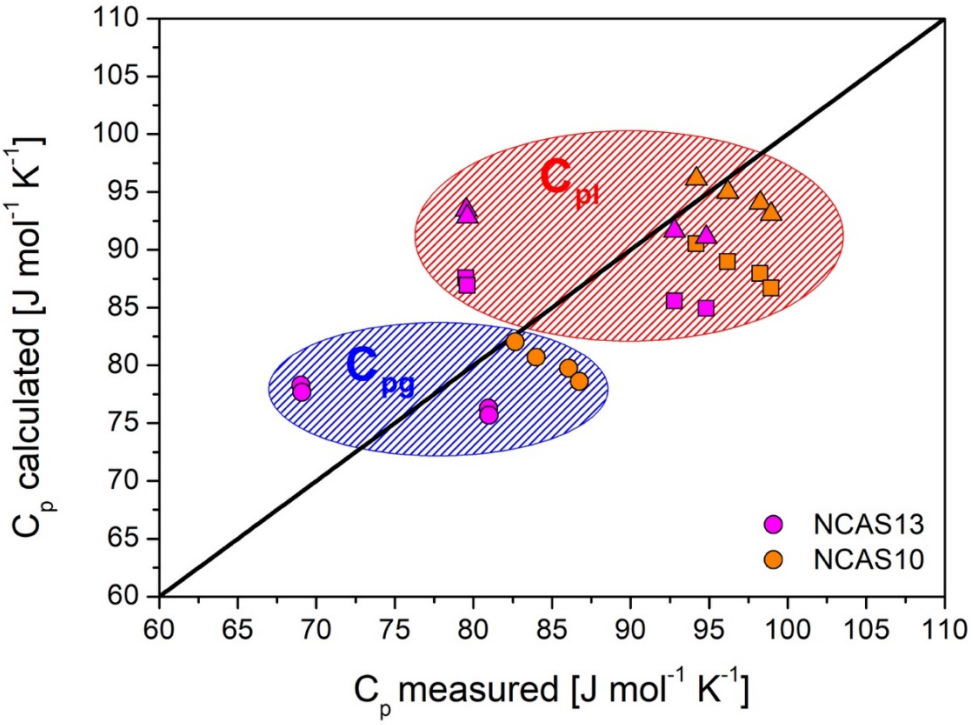

***Fig. 34**: C_{pg} calculated after Richet (1987) and C_{pl} calculated after Richet and Bottinga (1985) and Stebbins et al. (1984) for B_2O_3-bearing melts compared to measured values. Squares represent C_{pl} modelled after Richet and Bottinga (1985) and triangles represent C_{pl} modelled after Stebbins et al. (1984). Circles describe C_{pg} values. Blue area summarizes C_{pg} values whereas red area summarizes C_{pl} values.*

3.6 Conclusions

In this study we have shown that P_2O_5 as well as B_2O_3 have a strong effect on the structure and rheology of both the peralkaline and peraluminous melts. P_2O_5 enters the melts structure preferably as PO_4^{3-} species and can act as both a network former and a modifier. In peralkaline melts PO_4^{3-} acts as a network former by removing Na and Ca from network modifying positions by forming phosphate complexes and thus increases the polymerisation of the melt by increasing the NBO/T of the melt.

When all cations from former network modifying positions are used to compensate the charge of PO_4^{3-}, the incorporation mechanism of P_2O_5 in the melt changes and is similar to that observed in peraluminous melts, where no cations in network modifying positions are present.

In that case, P_2O_5 acts as a network modifier by taking Al^{3+} from tetrahedral positions or by charge balancing the Al^{3+} tetrahedra and thus releases Na and Ca from their charge balancing positions which then act as network modifiers and decrease the polymerisation of the melt by decreasing the NBO/T.

The effect of B_2O_3 on the melt structure is more complex. B_2O_3 can also act as a network former in form of BO_4^- and a network modifier in form of BO_3, whereby the BO_3/BO_4^- ratio is dependent on the concentration of network modifying cations. Cations in network modifying position such as Na and Ca in the peralkaline melt composition convert BO_3 triangles to BO_4^- tetrahedra, as described in previous studies.

Despite of the network forming role of BO_4^-, the viscosity of the melts decreases at first slightly up to the point where no more cations in network modifying roles are present and decreases more strongly with further addition of B_2O_3. This observation implies that in peralkaline melt compositions both BO_3 and BO_4^- are present and result in competing processes of melt polymerisation in case of BO_4^- and melt depolymerisation in case of BO_3 whereby the depolymerising effect of BO_3 outweighs the polymerising effect of BO_4^-. The steady decrease in viscosity in the peraluminous melt is caused by the presence of dominantly BO_3 triangles.

Unmixing was observed for the peralkaline NCAS13 melt composition containing both Na and Ca in network modifying roles, suggesting that the effect of P_2O_5 on unmixing is dependent on the network modifying cations present in the melt. The melt probably separates into a silica- and a phosphorus-rich melt, whereby the PO_4^{3-} tetrahedra that remove cations from network modifying positions form a separate melt that resides outside the silicate melt network.

It was insinuated that structural changes also occur at high P_2O_5 concentrations in only Ca-bearing peralkaline CAS19 melt after heat treatments, suggesting that also Ca has an effect on the unmixing of melts and probably also preferably enters the P-rich melt.

Despite no evidence in measurements for unmixed Na-P melts, unmixing was directly observed in melts containing both Ca and Na, suggesting that Na enhances the affinity of a Ca-P-rich melt to unmix. No unmixing caused by the presence of B_2O_3 was observed in this temperature and B_2O_3 concentration range.

4 Effect of P_2O_5 on structure, rheology, iron ratio and unmixing of Champagne glass from Gusev Crater, Mars

4.1 Abstract

This study focusses on the effect of P_2O_5 on unmixing of “Champagne” melt. “Champagne” is part of the Wishstone Class rocks found in Gusev Crater on Mars and exhibits naturally high P_2O_5 concentrations up to 10 wt%. A series of phosphorus-bearing glasses with concentrations up to 9.47 mol% P_2O_5 was synthesized to investigate the effect of phosphorus on the unmixing of basaltic melts and the Fe^{2+}/Fe_{tot} ratio. The glasses were synthesized in a 1 atm furnace in a temperature range between 1523 and 1573 K in air. The viscosity of the melts was determined in the range of $10^{8.5}$ to $10^{13.5}$ Pa s by using the micropenetration viscometry technique. The heat capacity of the samples was measured using Differential Scanning Calorimetry (DSC). The structure of the melts was investigated by Raman spectroscopy and electron microscopy. Furthermore, Fe speciation was investigated using a wet chemical technique for colorimetric determination of ferrous iron.

The addition of P_2O_5 to the melt causes strong structural changes and results in an increase in Fe^{2+}/Fe_{tot} as well as viscosity. Despite apparent depolymerization of the melt structure due to increasing the amount of network modifying iron, viscosity increases by approximately 4 log units with the addition of P_2O_5 up to a maximum around 6 mol% P_2O_5. With further increasing P_2O_5 concentration (> 6 mol% P_2O_5) in the melt the viscosity decreases. According to Raman spectra, phosphorus enters the melt network as orthophosphate (PO_4^{3-}) species, which is shown by intense Raman bands around 950 cm^{-1} as described in earlier studies. The melts with higher P_2O_5-concentration unmix into two separate melts, whereby the original homogeneous melt separates into a Si-Al- and a Ca-Fe-P-rich melt. Furthermore, there is evidence that other divalent metal cations also preferably enter the Ca-Fe-P-rich melt. Phase separation is observed by the appearance of a second transition peak in the heat capacity data as well as in backscattered electron micrographs where the second melt phase appears as spheres with an average diameter of 200 nm up to 100 µm for the melt containing 9.47 mol% P_2O_5. Our research shows that increasing phosphorus concentration in the melt enhances phase separation in natural basaltic melts.

4.2 Introduction

Champagne is part of the Wishstone class rocks found at Gusev Crater on Mars (Squyres et al. 2006). Chemical analysis of the rocks were conducted through Spirit Mars Rover which was equipped with an Alpha partical X-Ray spectrometer (Arvidson et al. 2006) and the data was presented by Gellert et al. (2006). Many authors discussed the classification of the rock and mineral compositions (e.g. McSween et al. 2006; Ruff et al. 2006; Squyres et al. 2006; McSween et al. 2008). Wishstone Class rocks were first found on the northwest flank of Husband Hill, are relatively unweathered and exhibit high P_2O_5 concentrations up to 5.2 wt% which strongly correlate with the calcium concentration (Squyres et al. 2006). Among Wishstone class Champage is the rock composition with highest measured P_2O_5 concentrations up to 10.2 wt% (Usui et al. 2008). The formation of these high P_2O_5 low SiO_2 rocks is uncertain. Usui et al. (2008) proposed an incorporation of merrilite crystals through explosive eruption as a reason for the high abundance of P_2O_5 in Wishstone Class rocks.

Champagne rocks resemble basalts and due to its naturally high P_2O_5 concentration, this rock composition was chosen for the study of the effect of phosphorus on melt structure and unmixing. For this study, the melts of the composition of Champagne composition after Usui et al. (2008) were synthesised. Different P_2O_5 concentrations up to 9.47 mol% were added to investigate the effect of P_2O_5 concentration on structure and rheology of the melts.

4.3 Starting Material

Glasses were synthesized by mixing oxide and carbonate compounds. Before melting, all powders were decarbonated at 1273 K for 12 h in a 1 atm Carbolite furnace. Afterwards, glasses were synthesized at 1523 K and quenched in water. The resulting glass was crushed and ground to a powder. Subsequently, 2, 4, 6, 8 and 10 mol% of P_2O_5 were added in the form of $(NH_4)_2HPO_4$ to the melts. Since samples CHAMP-P6, CHAMP-P8 and CHAMP-P10 were full of bubbles, the melting temperature of this samples was increased to 1573 K. All samples contain a small amount of crystals (<1 Vol%). The crystals are < 1 µm and therefore could not be analysed with the analytical techniques used in this study. However, since there are very few crystals present in the melt, they do not change the original melt composition significantly.

The exact chemical compositions were measured with a JEOL JXA 8900RL electron microprobe with a beam diameter of 30 µm and an accelerating voltage of 15 kV and are shown in Table 13. The microprobe was calibrated by using Wollastonite (Si), Anorthite (Ca, Al), Albite (Na), Apatite (P), Olivine (Mg) and Hematite (Fe) as standard minerals.

***Table 13**: Compositions of Champagne glasses as determined by electron microprobe analysis*

Sample	CHAMP	2σ	CHAMP-P2	2σ	CHAMP-P4	2σ	CHAMP-P6	2σ	CHAMP-P8	2σ	CHAMP-P10[a]	2σ
						composition in wt%						
SiO_2	43.51	0.15	41.75	0.14	40.11	0.14	39.11	0.14	36.86	0.13	37.10	0.12
Al_2O_3	15.52	0.09	14.70	0.09	14.03	0.08	13.82	0.08	13.16	0.08	13.34	0.07
Na_2O	5.83	0.08	5.60	0.08	5.34	0.08	5.03	0.08	4.54	0.07	3.94	0.05
CaO	15.68	0.10	14.86	0.10	14.10	0.10	13.20	0.09	12.93	0.09	11.88	0.10
MgO	3.04	0.05	2.89	0.04	2.78	0.04	2.62	0.04	2.57	0.04	2.34	0.03
FeO_{tot}	14.07	0.12	13.57	0.12	12.96	0.11	12.53	0.11	11.97	0.11	11.42	0.12
P_2O_5	-		3.98	0.12	7.86	0.17	10.90	0.20	15.24	0.24	18.41	0.19
total	**97.65**		**97.36**		**97.18**		**97.21**		**97.26**		**98.42**	
						composition in mol%						
SiO_2	47.60	0.14	46.85	0.18	46.11	0.14	45.87	0.22	44.33	0.23	45.06	1.64
Al_2O_3	10.00	0.04	9.72	0.06	9.51	0.07	9.55	0.08	9.32	0.04	9.55	0.21
Na_2O	6.18	0.12	6.09	0.09	5.95	0.08	5.71	0.03	5.29	0.08	4.63	1.19
CaO	18.38	0.09	17.87	0.13	17.37	0.06	16.58	0.18	16.66	0.12	15.46	0.69
MgO	4.96	0.08	4.83	0.06	4.77	0.06	4.58	0.12	4.61	0.12	4.23	0.24
FeO_{tot}	12.88	0.13	12.74	0.11	12.46	0.09	12.29	0.09	12.04	0.08	11.60	0.32
P_2O_5	-	-	1.89	0.07	3.83	0.12	5.41	0.12	7.76	0.17	9.47	0.51
γ[b]	0.81		0.81		0.81		0.80		0.81		0.79	
NBO/T[c]	0.27		0.14		0.02		0.09		0.13		0.15	
g.atom[d]	2.84		2.92		3.00		3.07		3.16		3.26	

[a] Matrix Composition

[b] γ = (Na_2O + CaO + MgO + FeO) / (Na_2O + CaO + MgO + FeO + Al_2O_3) from mole fractions (e.g. Toplis et al. 1997a; Webb et al. 2007; Baasner et al. 2013b). P_2O_5 was included as a network former as well as a network builder

[c] non-bridging oxygens per tetrahedral unit as an indicator for the degree of melt polymerization

[d] number of atoms in one mole of melt (Sehlke and Whittington 2016)

4.4 Results

4.4.1 The Effect of P_2O_5 on the Viscosity

The results of the micropenetration viscosity measurements are illustrated in Fig. 35. Data has been fitted using the Arrhenian equation of the type:

$$\log\eta = \log A + \frac{10000\ B}{T} \qquad Eq.(X)$$

Where *T* is the temperature in K and *A* and *B* are fit parameters listed in Table 15. With the addition of P_2O_5 to the melt, viscosity increases by approximately 4 log units up to a maximum viscosity around 5.41 mol% P_2O_5. Further addition of P_2O_5 results in a decrease of viscosity by approximately 2 log units for the sample with the highest P_2O_5 concentration. The effect of viscosity increase is much stronger than the effect of viscosity decrease after the maximum. The Arrhenian fits for CHAMP glasses with 7.76 and 9.47 mol% P_2O_5 intersect at viscosities of ~10^{13} Pa s.

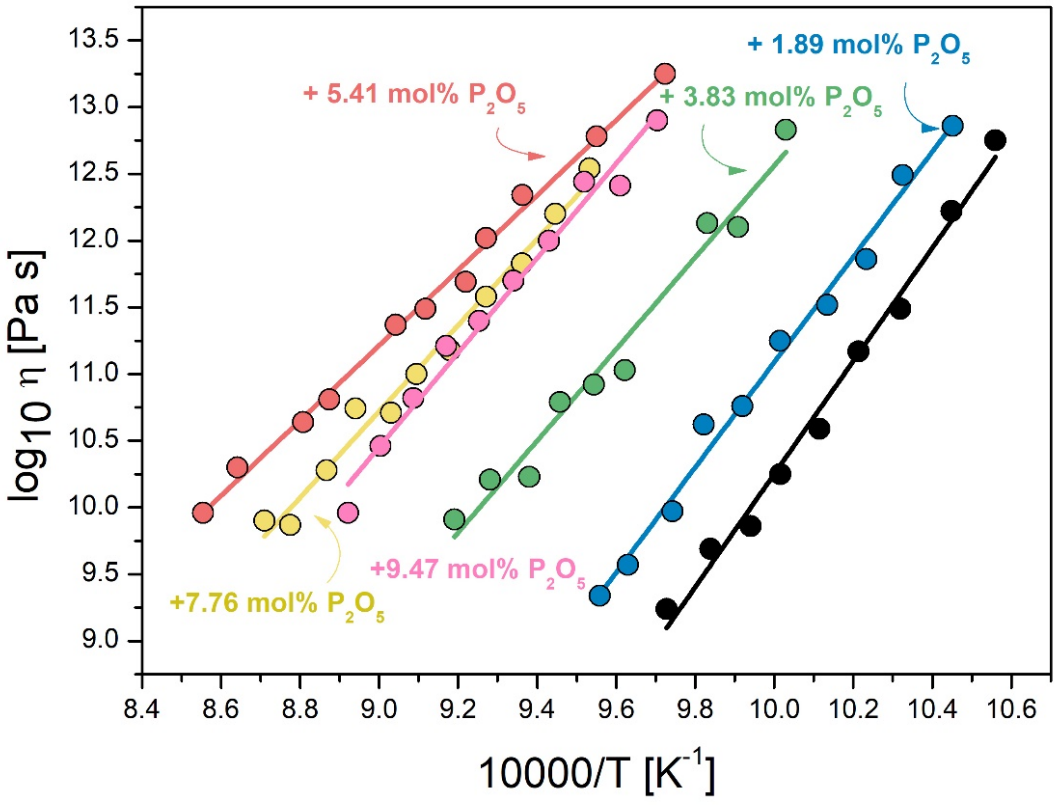

***Fig. 35**: Viscosity data for Champagne melts. Black line and symbols represent the phosphorus-free base composition.*

***Table 14**: Viscosity data as measured by micropenetration technique*

T K	η log_{10} Pa s	T K	η log_{10} Pa s	T K	η log_{10} Pa s
CHAMP		**CHAMP-P2**		**CHAMP-P4**	
915.3	13.89	956.7	12.86	997.1	12.83
947.0	12.75	968.5	12.49	1009.2	12.10
957.0	12.22	977.2	11.86	1017.3	12.13
969.1	11.49	986.7	11.52	1039.3	11.03
979.1	11.17	998.6	11.25	1047.8	10.92
988.7	10.59	1008.1	10.76	1057.3	10.79
998.5	10.25	1018.1	10.62	1066.1	10.23
1006.0	9.86	1026.4	9.97	1077.5	10.21
1016.4	9.69	1038.45	9.57	1088.0	9.91
1028.0	9.24	1046.2	9.34		
CHAMP-P6		**CHAMP-P8**		**CHAMP-P10**	
1028.4	13.25	1049.0	12.54	1030.5	12.90
1047.1	12.78	1058.7	12.20	1040.6	12.41
1068.0	12.34	1068.2	11.83	1050.5	12.44
1078.6	12.02	1078.6	11.58	1060.4	12.00
1084.7	11.69	1089.3	11.18	1070.7	11.70
1096.7	11.49	1099.5	11.00	1080.7	11.40
1105.8	11.37	1107.4	10.71	1090.6	11.21
1126.8	10.81	1118.5	10.74	1100.5	10.82
1135.3	10.64	1127.7	10.28	1110.6	10.46
1157.2	10.30	1139.5	9.87	1120.9	9.96
1168.9	9.96	1148.1	9.90		

***Table 15**: Arrhenian Fit parameters*

Sample	A	ΔA	B	ΔB	E	T_g^{12}	ΔT_g^{12}	m
	$\log_{10}$ Pa s	$\log_{10}$ Pa s	$\log_{10}$ Pa s 10^4 K	$\log_{10}$ Pa s 10^4 K	kJ mol^{-1}	K	K	
CHAMP	-32.09	1.63	4.23	0.16	810.7	960.4	0.6	44
CHAMP-P2	-28.31	1.39	3.94	0.14	754.4	977.4	0.5	40
CHAMP-P4	-21.82	2.04	3.44	0.21	658.4	1016.6	0.8	34
CHAMP-P6	-14.12	0.59	2.82	0.06	539.0	1077.7	0.3	26
CHAMP-P8	-18.36	1.20	3.23	0.13	618.7	1064.3	0.5	30
CHAMP-P10	-21.47	1.59	3.55	0.17	679.2	1059.7	0.6	33

E: activation energy for viscous flow

T_g^{12}: temperature at which the viscosity of the melt equals 10^{12} Pa s

m: fragility of the melt

4.4.2 Effect of P_2O_5 on Structure

Fig. 36 shows the Raman spectra of CHAMP glass series. The black line represents the P_2O_5-free melts. All spectra are baseline and temperature corrected by using *Eq. IX* (Long 1977; Di Muro et al. 2009). For better comparison of the relative peak intensities, all spectra have been normalized to the 555 cm^{-1} peak. Basically, there are two main, broad bands in the low and the high frequency area for all samples. The peak in the low frequency area appears at around 555 cm^{-1}, the peak in the high frequency region appears at ~950 cm^{-1}. With increasing amount of P_2O_5 the intensity of the peak at ~555 cm^{-1} increases with respect to the band at 950 cm^{-1}. Furthermore, more peaks in the low frequency range appear between 250 cm^{-1} and 500 cm^{-1}, resulting in a very broad band from 250 cm^{-1} to 600 cm^{-1}. For the sample CHAMP-P10, which contains 9.47 mol% P_2O_5 two peaks emerging from the low frequency peak range can be found at approximately 350 cm^{-1} and 450 cm^{-1}. The intensity of the high frequency peak at ~950 cm^{-1} decreases with respect to the 555 cm^{-1} band. Furthermore, the peak broadens and shifts to ~1030 cm^{-1}. For the samples with 3.83 mol% P_2O_5 and more a second, sharp peak emerges from the flat broad peak at ~1030 cm^{-1}.

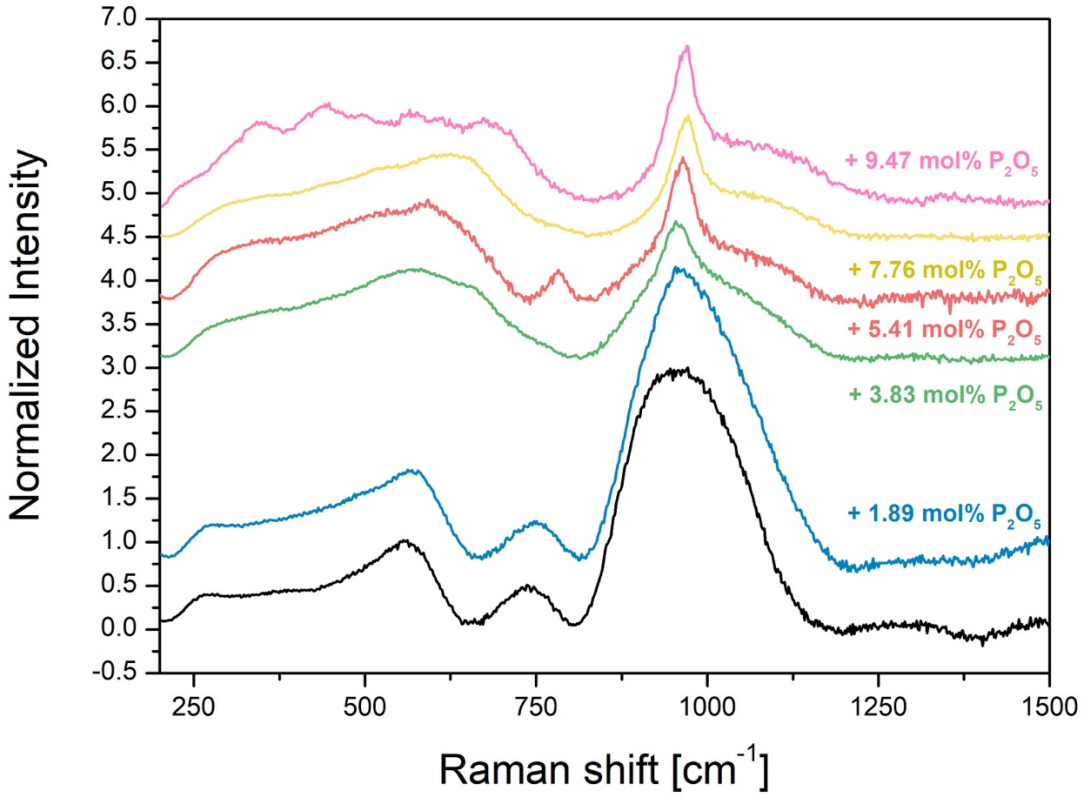

***Fig. 36**: Baseline- and Long-corrected Raman spectra for Champagne glass series. Spectra were normalized to 555 cm^{-1} peak. The black spectrum represents the phosphorus-free base composition.*

4.4.3 Colorimetric Determination of Ferrous Iron

The results from the colorimetric determination of Fe^{2+} are summarized in Table 16 and illustrated in Fig. 37. Red symbols represent the measured Fe^{2+}/Fe_{tot} ratios for CHAMP glass series quenched from 1523 K. The initial Fe^{2+}/Fe_{tot} ratio of the P_2O_5-free sample is 0.20. With the addition of P_2O_5 to the melt at the same temperature the Fe^{2+}/Fe_{tot} ratio increases up to 0.38 for the composition with highest P_2O_5 concentration. Additionally, samples CHAMP-P6 and CHAMP-P8 were also melted at 1573 K. It is shown, that at higher temperatures the Fe^{2+}/Fe_{tot} increases.

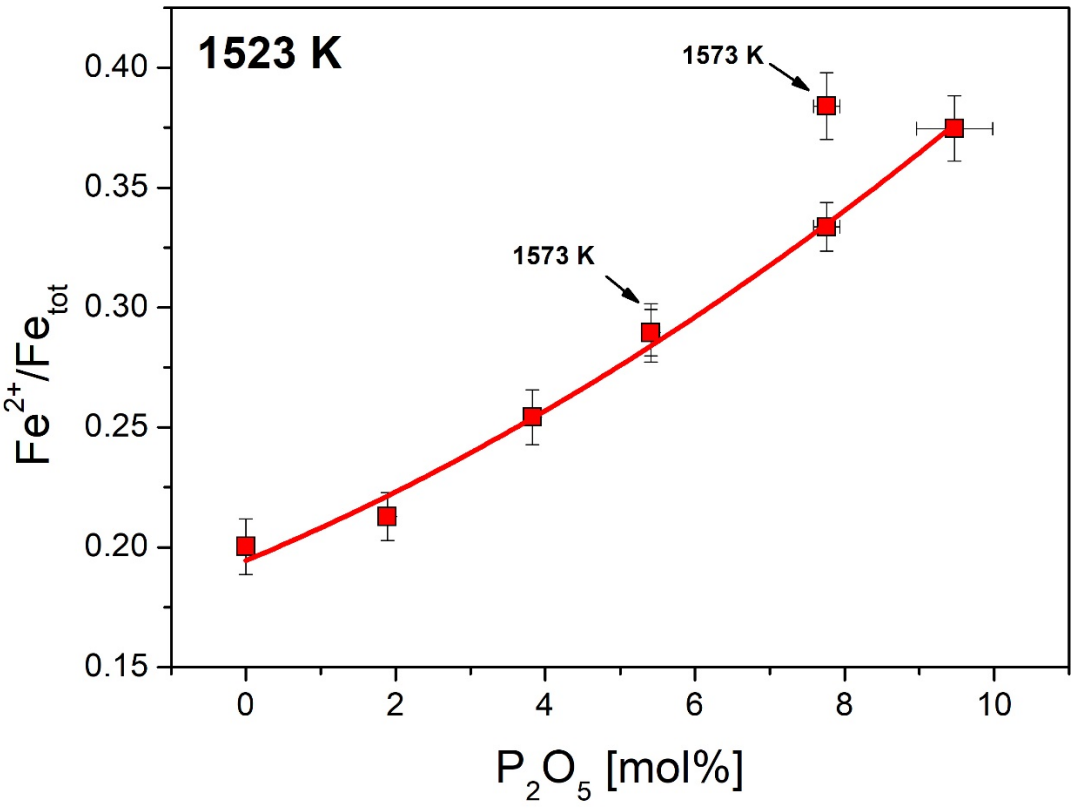

***Fig. 37**: Measured Fe^{2+}/Fe_{tot} ratios for different P_2O_5 concentrations for Champagne glass series melted at 1523 K and 1573 K.*

***Table 16**: Fe_{2+}/Fe_{tot} ratios measured by colorimetric determination of ferrous iron*

Sample	Fe^{2+}/Fe_{tot}	$\Delta Fe^{2+}/Fe_{tot}$	FeO*	ΔFeO	Fe_2O_2*	ΔFe_2O_3	FeO*	ΔFeO	Fe_2O_3*	ΔFe_2O_3
			mol%	mol%	mol%	mol%	wt%	wt%	wt%	wt%
CHAMP	0.20	0.01	2.58	0.08	5.15	0.15	2.82	0.08	12.51	0.31
CHAMP-P2	0.21	0.01	2.71	0.08	5.01	0.15	2.89	0.09	11.87	0.36
CHAMP-P4	0.25	0.01	3.14	0.10	4.65	0.14	3.29	0.10	10.74	0.32
CHAMP-P6	0.29	0.01	3.56	0.11	4.37	0.14	3.63	0.14	9.90	0.30
CHAMP-P8	0.33	0.01	4.62	0.14	3.71	0.11	4.60	0.14	8.20	0.30
CHAMP-P10	0.37	0.01	4.83	0.14	4.11	0.12	6.81	0.20	12.90	0.39

* calculations based on Fe^{2+}/Fe_{tot} ratios and FeO_{tot} content measured by EMPA (see Table 13)

4.4.4 Effect of P_2O_5 on Heat Capacity

The heat capacities for CHAMP series are shown in Fig. 38. Heat capacity data was fitted using the Maier-Kelley equation (Eq. IV). The fit parameters of the Maier-Kelley equation are summarized in Table 17. The T_g peak for the P_2O_5-free CHAMP glass appears at ~986 K. With increasing amount of P_2O_5 the T_g peak shifts to higher temperatures with a

maximum T_g for sample CHAMP-P8 at ~1200 K. Further addition of P_2O_5 to the melt results in a shift of T_g to ~1110 K. This observation is consistent with the results from viscosity measurements with the exception, that sample CHAMP-P8 marks the maximum instead of sample CHAMP-P6 as observed for the measured viscosities. The three samples with highest P_2O_5 concentration show two and, in case of sample CHAMP-P10, three glass transition peaks, indicating the presence of two or three unmixed melts and are not a result of crystallisation of the melt.

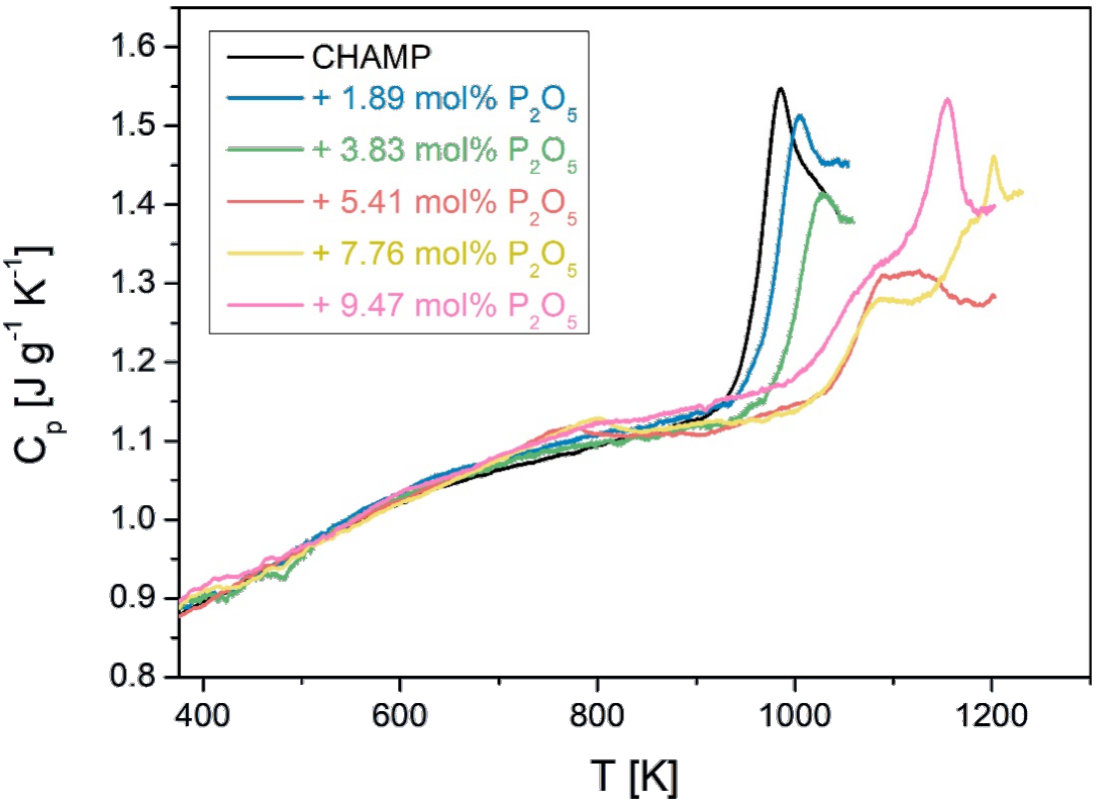

***Fig. 38**: Heat capacity data for P_2O_5-bearing Champagne melts.*

The calculated values for C_{pl}, C_{pg}, C_p^{conf}, T_f' and S^{conf} for samples with P_2O_5 contents up to 3.83 mol% of P_2O_5 are summarized in Table 18 and Table 19. There are no calculated values for samples CHAMP-P6, -P8 and –P10 due to the existence of more than one melt.

***Table 17**: Maier-Kelley-Fit parameter for P_2O_5-bearing Champagne melts*

	a	Δ a	b	Δ b	c	Δ c
sample	J g^{-1} K^{-1}	J g^{-1} K^{-1}	10^{-4} J g^{-1} K^{-2}	10^{-4} J g^{-1} K^{-2}	10^{4} J g^{-1} K	10^{4} J g^{-1} K
CHAMP	0.929	0.001	2.502	0.001	-2.197	0.015
CHAMP-P2	0.962	0.003	2.320	0.003	-2.574	0.029
CHAMP-P4	0.975	0.003	2.020	0.003	-2.679	0.037

***Table 18**: Heat capacities and fictive temperature of P_2O_5-bearing Champagne melts*

sample	C_{pg}	ΔC_{pg}	C_p liq	ΔC_{pl}	C_p^{conf}	ΔC_p^{conf}	T_f'
	J mol^{-1} K^{-1}	J mol^{-1} K^{-1}	J mol^{-1} K^{-1}	J mol^{-1} K^{-1}	J mol^{-1} K^{-1}	J mol^{-1} K^{-1}	K
CHAMP	74.46	0.89	91.79	1.09	17.33	1.41	948.2
CHAMP-P2	78.14	0.87	95.21	1.05	17.07	1.36	965.2
CHAMP-P4	77.88	0.83	92.66	0.98	14.77	1.28	994.2

Error of the fictive Temperature T_f' is 3 K

Error of C_{pg} and C_{pl} is < 1%

***Table 19**: Adam-Gibbs Parameter*

sample	A_e^*	B_e	ΔB_e	S_{conf}	ΔS_{conf}
		kJ mol^{-1}	kJ mol^{-1}	J mol^{-1} K^{-1}	J mol^{-1} K^{-1}
CHAMP	-4.55	336.23	14.68	9.18	0.42
CHAMP-P2	-4.55	405.29	25.85	10.89	0.72
CHAMP-P4	-4.55	504.26	55.24	13.02	1.47

* -4.55 set value

4.4.5 Effect of P_2O_5 on Phase Separation

Backscattered electron micrographs as well as EDX and EMPA mappings of CHAMP series were taken to demonstrate mass contrasts in glasses. Fig. 39 shows the homogeneous structure of the P_2O_5-free glass. BSE images for the P_2O_5 bearing melts are shown in Fig. 40. The P_2O_5-free melt as well as the melts containing up to 3.83 mol% P_2O_5 exhibit a homogeneous melt composition.

Further addition of P_2O_5 to the melt results in a visible separation of different melt phases. The structure of CHAMP-P6 containing 5.41 mol% P_2O_5 consist of tiny spheres of light- and dark-grey colours with an average diameter of approximately 100 – 200 nm. Further addition of P_2O_5 to the melt enhances unmixing and the spheres grow in size. Sample CHAMP-P8 containing 7.76 mol% P_2O_5 consist of white and dark-grey spheres, which are homogenously distributed throughout the sample and have an average diameter of approximately 300 nm.

The biggest structural changes can be seen in sample CHAMP-P10 containing the highest P_2O_5 concentration of 9.47 mol% P_2O_5. The melt structure is inhomogeneous and consist of two different melts, one being of a light-grey and the other of a dark-grey colour.

In contrast to the unmixed samples CHAMP-P6 and CHAMP-P8, the structure of CHAMP-P10 exhibits alongside perfect spheres also cloudy streaks which follow a random distribution. The size of the streaks varies between 50 µm and 300 µm whereas the diameter of the spheres ranges from approximately 2 µm to 20 µm. Both, the streaks and the bigger spheres have a light-grey colour and exhibit inclusions of the other dark-grey melt, but there are also perfect spheres of solely one melt composition present in the melt.

The matrix also consists of tiny spheres of both melt compositions with an average diameter of ~300 nm, similar to the structure of sample CHAMP-P8. Furthermore, bigger spheres are surrounded by a halo of only the dark-grey melt composition. In this area no spheres of the light-grey melt are present.

In case of sample CHAMP-P10 the spheres are big enough for point analysis and their composition was measures with EDX. In addition, EDX and EMPA mappings were performed on this sample. The results of the EDX measurements are summarized in Table 20.

It can be observed that the matrix composition (dark-grey) is significantly enriched in SiO_2 and Al_2O_3 with respect to the composition of the light grey spheres. The spheres, however, are strongly enriched in CaO, FeO and P_2O_5.

The mappings done by EMPA and EDX (Fig. 41) analysis demonstrate the distribution of Si, Al, Ca, P and Fe in the melts. The highest concentrations of Ca, P and Fe are found within the spheres. Complementary to that, Si and Al are enriched in the matrix as well as melt inclusions of the dark-grey melt within the light-grey spheres.

This distribution was already seen with SEM and measured with EDX analysis. In addition, there seems to be a gradient in Si concentration. The Si concentration is highest in regions, where no spheres of the Ca-Fe-P-rich melt are present.

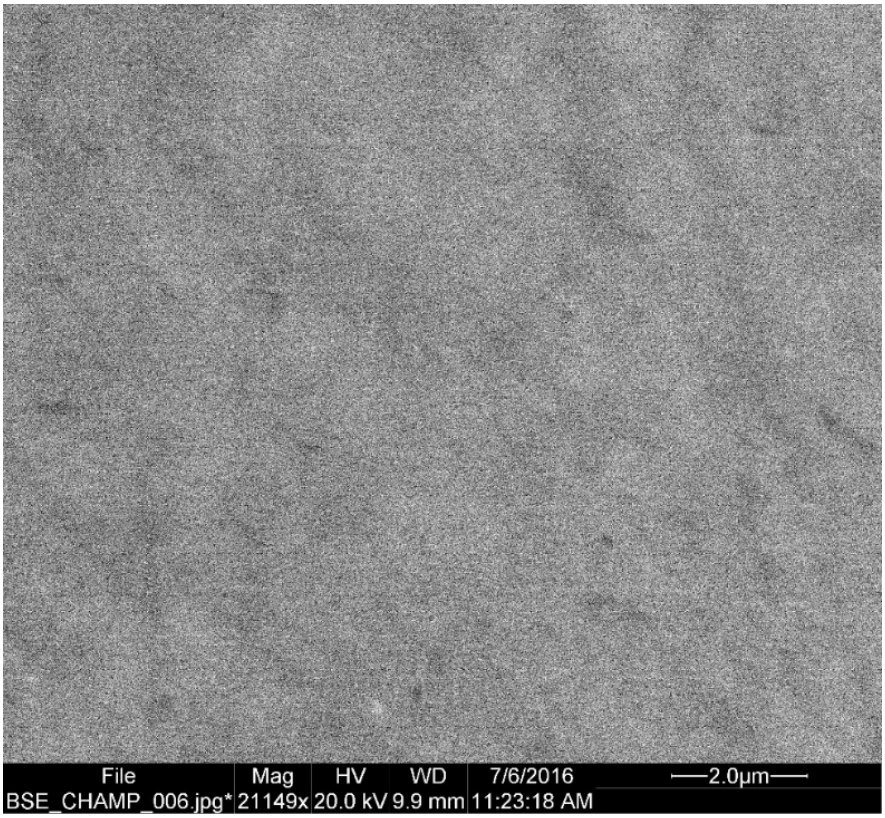

***Fig. 39**: Backscattered electron micrograph of the phosphorus-free, homogeneous Champagne base composition.*

***Table 20**: EDX results of sphere and matrix composition of sample CHAMP-P10*

	Matrix						Spheres					
Oxides	**At%**	**SD**	**wt%**	**SD**	**mol%**	**SD**	**At%**	**SD**	**wt%**	**SD**	**mol%**	**SD**
SiO_2	20.1	3.0	42.0	6.3	50.0	5.5	5.9	2.0	11.6	3.9	15.0	1.9
Al_2O_3	7.4	0.5	13.1	0.8	9.2	1.0	4.2	0.5	7.0	0.8	5.3	0.6
Na_2O	2.4	0.5	2.6	0.5	3.0	2.2	1.5	0.1	1.5	0.1	1.9	3.7
CaO	5.9	1.4	11.5	0.4	14.6	4.7	12.1	0.6	22.4	0.2	31.0	3.6
MgO	1.3	0.2	1.9	0.3	3.3	1.2	3.8	0.2	5.0	0.3	9.6	1.0
FeO_{total}	4.3	0.7	10.7	1.6	10.7	3.7	6.6	0.5	15.4	1.2	16.8	2.3
P_2O_5	7.4	1.8	18.3	4.4	9.2	3.9	15.9	0.8	37.2	1.8	20.3	3.2

Values are mean values of 3 – 6 single point measurements

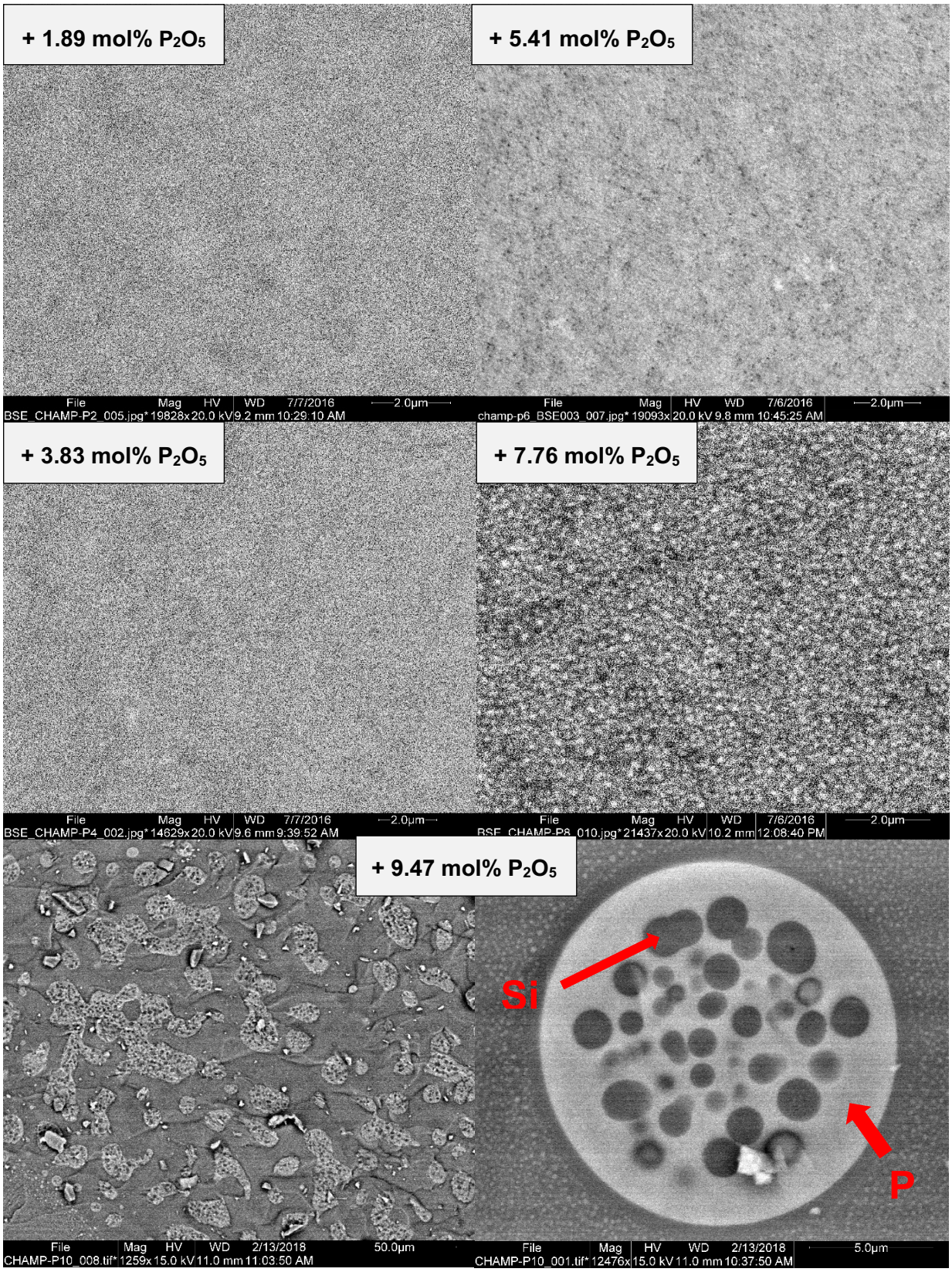

***Fig. 40**: Backscattered electron micrographs of Champagne melt with different P_2O_5 concentrations. With increasing P_2O_5 concentration the melt unmixed into two separate melts which are apparent as light-grey spheres in a continuous dark-grey matrix.*

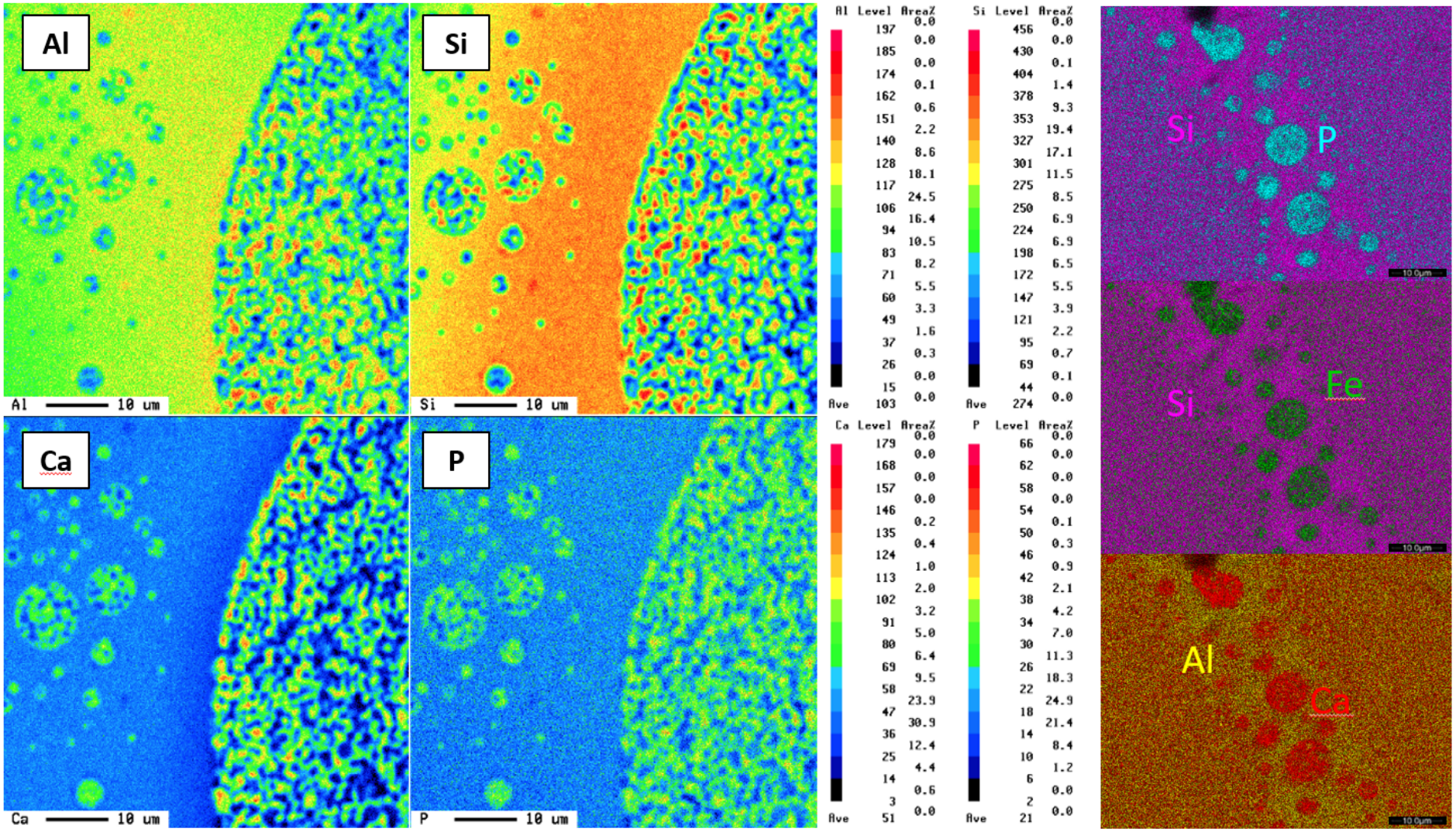

***Fig. 41**: EMPA (left) and EDX mappings (right) of CHAMP-P10 melt containing 9.47 mol% P_2O_5. Mappings show the enrichment of Si, Al, Ca, Fe and P in the separate melt phases.*

4.5 Discussion

4.5.1 Structural Changes due to the Addition of P_2O_5

The addition of P_2O_5 to the melt increases the Fe^{2+}/Fe_{tot} ratio. This effect is stronger at higher temperatures. In melts under oxidizing conditions the ferric iron is known to be partly occupying tetrahedral positions. Toplis et al. (1994) mentioned that the addition of P_2O_5 to the melt destabilizes the tetrahedrally coordinated iron and thus, results in a reduction of ferric to ferrous iron combined with the release of formally charge balancing metal cations which then act as network modifiers. This structural change would result in a depolymerisation of the melt structure.

However, the addition of P_2O_5 to the melt increases viscosity up to a maximum around 5.41 mol% P_2O_5. Further addition of P_2O_5 to the melt results in a decrease of viscosity (Fig. 42). For better comparison of CHAMP series with other P_2O_5-bearing melts $\Delta\log_{10}\eta$ was calculated. It is the change in viscosity with respect to the P_2O_5-free melts calculated from Arrhenian fits for the temperature at which the viscosity of the P_2O_5-free melt equals 10^{12} Pa s for each melt composition. For all peralkaline melts the viscosity increases with increasing P_2O_5 concentration up to a maximum viscosity and then decreases with further addition of P_2O_5. The maximum for CHAMP series appears at the highest P_2O_5 concentration (~6.2 mol%) in comparison to the other peralkaline compositions. The increase in viscosity before the maximum is stronger than for the simple Na_2O-Al_2O_3-SiO_2 (NAS19) and CaO-Al_2O_3-SiO_2 (CAS19) melts, but lower than for combined Na_2O-CaO-Al_2O_3-SiO_2 melts. The decrease in viscosity after the maximum follows a similar slope as the decrease in viscosity for peraluminous (NCAS10) melts (see Chapter 3). Similar trends for peralkaline and peraluminous P_2O_5-bearing Na_2O-Al_2O_3-SiO_2 glasses have been described by Toplis and Dingwell (1996b) who investigated the effect of P_2O_5 on the viscosity of Na_2O-Al_2O_3-SiO_2 melts with differing SiO_2 content. This behaviour implies a polymerisation of the melt with the addition of P_2O_5, followed by a depolymerisation after the viscosity maximum is reached.

Heat capacity data showed the same results. However, while the maximum viscosity was measured between 5.41 mol% and 7.76 mol% of P_2O_5, the highest T_g temperature was measured for the melt containing 7.76 mol% P_2O_5. The reason why there is a difference remains unclear, but it is possible that CHAMP-P6 shows another peak at higher temperatures since the heat capacity increases slightly at the end of the measurement. C_p^{conf} and S^{conf} were calculated only for samples containing up to 5.41 mol% P_2O_5 since for higher P_2O_5 concentrations there are two separate melt phases and the calculation of S^{conf} would be assuming a single melt. Unfortunately, CHAMP, CHAMP-P2 and CHAMP-P4

crystallized during heat capacity measurements which was evident from a prominent exothermal peak appearing at the glass transition range during the first measurement. However, the crystal amount is < 1 Vol% and therefore does not change the original melt composition significantly.

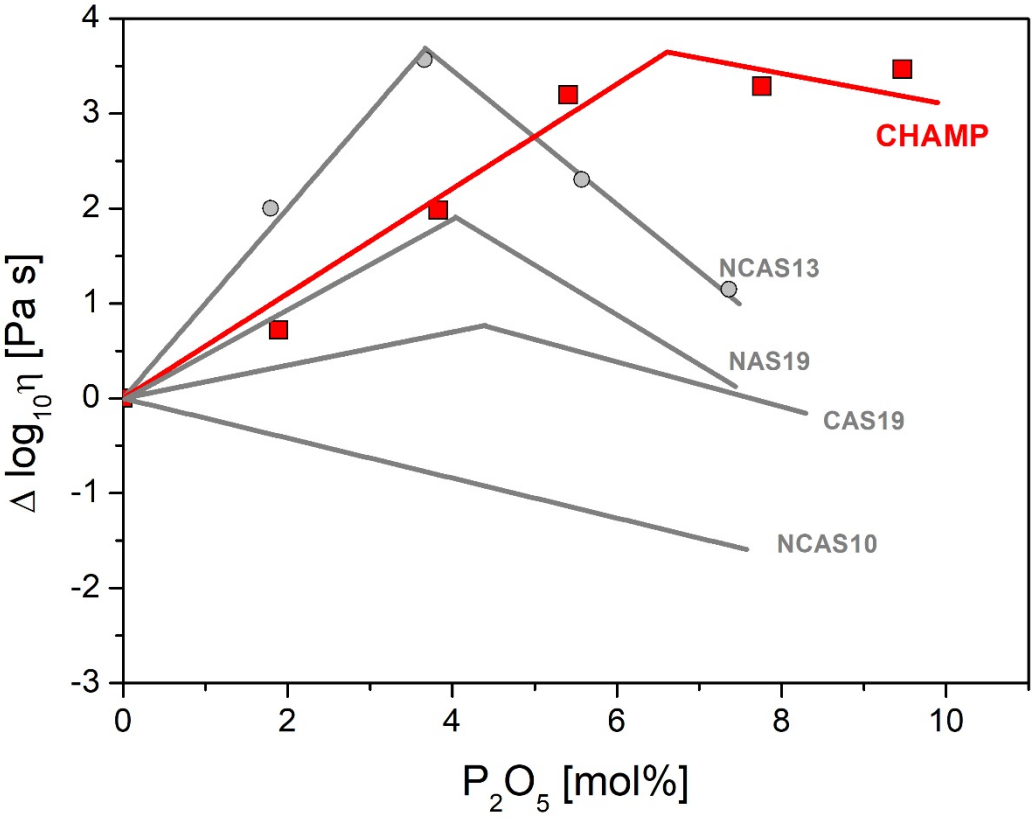

***Fig. 42**: Comparison of change in viscosities with increasing P_2O_5 concentration for Champagne melt with simple aluminosilicate melts from Chapter 3.*

Mysen (1992), Toplis et al. (1994b) as well as many other authors proposed that P_2O_5 enters the melt structure as PO_4^{3-} species. This is confirmed in this study by the appearance of the PO_4^{3-} band around 950 cm^{-1} in the measured Raman spectra of the melts. The high frequency peak consists of several overlapping peaks of Si-O stretching vibrations, which are mainly silicon Q^1-species at 900 cm^{-1}, Q^2 at ~970 cm^{-1} and Q^3 at ~ 1090-1100 cm^{-1} (Mysen et al. 1982; Mysen 1992; Gan and Hess 1992a). Fe^{3+}-O stretching vibrations are found near 920 cm^{-1} and 1000 cm^{-1} (Mysen 1992).

In the low frequency range Q^4 species is found around 500 cm^{-1} (Mysen 1998a) together with various overlapping bending and stretching vibrations which are related to the more polymerised structural units such as e.g. different Si-O-Si bending modes at ~600 cm^{-1} (Mysen 1998b) and oxygen rocking motions at approximately 480 – 540 cm^{-1} (Mysen 1992). The slight shoulder around 1100 cm^{-1} which appears in the spectra of the melts with high

P_2O_5 contents results from stretching vibrations of structural units similar to $AlPO_4$ structural units in berlinite (Mysen 1998a; Gan and Hess 1992a).

4.5.2 Incorporation Mechanism of Phosphorus

Peralkaline melts consist of irregular chains of SiO_4 tetrahedra which are connected via bridging oxygens (Stebbins 2016). Al^{3+} also prefers tetrahedral coordination which results in a negative charge of the AlO_4^- tetrahedra. This resulting negative charge is charge balanced by metal cations (e.g. Mysen and Toplis 2007; Stebbins 2016). In peralkaline melts there are more alkali and alkaline earth elements present in the melt than needed for the charge balancing of the AlO_4^- tetrahedra. These excess metal cations act as network modifiers. They bond to oxygens of SiO_4 and AlO_4^-, which results in a depolymerisation of the melt structure and thus decrease the NBO/T ratio (Mysen et al. 1981b; Toplis et al. 1997a; Shelby 2005; Stebbins 2016).

PO_4^{3-} bonds to the excess metal cations in network modifying positions, resulting in the freeing of oxygens which are then able to bond to other SiO_4 and AlO_4^- tetrahedra and thus decrease the NBO/T of the melt which result in an increase of viscosity (Toplis and Dingwell 1996a).

$$2\ \text{Si-O-M} + \text{P-O-P} \Leftrightarrow \text{Si-O-Si} + 2\ \text{P-O-M}$$

This process continues up to the point, where all excess alkalis and alkaline earth elements are bonded to PO_4^{3+} and the melt reaches the highest polymerisation and maximum viscosity (Toplis and Dingwell 1996a). The viscosity maximum for this particular melt composition was calculated to be reached at 6.2 mol% of P_2O_5. Further addition of P_2O_5 to the melt results in a change in incorporation mechanism for PO_4^{3-}. When no excess alkalis and alkaline earth elements are present in the melt, PO_4^{3-} bonds to Al^{3+} from AlO_4 tetrahedra which results in the formation of a species similar to $AlPO_4$ and the freeing of alkalis and alkaline earth elements which were in former charge balancing roles (Mysen et al. 1981a ; Toplis and Dingwell 1996a; Mysen 1996).Those elements act as network modifiers and decrease melt polymerisation and thus results in the observed decreasing viscosity. Another probable mechanism is the bonding to pyrophosphate P_2O_7 (e.g. Mysen 1996; Toplis and Dingwell 1996a).

CHAMP-series follows the same trend as the peralkaline melts of CAS19, NCAS13 and NAS19 previously described in this work as well as peralkaline Na_2O-Al_2O_3-SiO_2-P_2O_5 melts described in the study of Toplis and Dingwell (1996a). It is a typical and expected viscosity trend for phosphorus-bearing peralkaline aluminosilicate melts.

PO_4^{3-} has been found to destabilize tetrahedrally coordinated ferric iron, resulting in a reduction of ferric to ferrous iron (Mysen 1992; Borisov et al. 2013b). At the same time, PO_4^{3-} bonds to excess network modifying cations and thus results in the formation of more Si-O-Si bonds, which has a polymerizing effect on the melt structure. The resulting effect on viscosity relies on both reactions, depending on which is the dominant one. In this study the formation of more polymerising Si-O-Si bonds outweighs the depolymerizing effect of the Fe^{3+} to Fe^{2+} reduction.

4.5.3 Effect of P_2O_5 on Unmixing and Implications for Natural Systems

Kushiro (1975), Ryerson and Hess (1980), Toplis et al. (1994a) as well as many other authors have mentioned that the addition of phosphorus to the melt results in the removal of metal cations in network modifying position to form PO_4^{3-} tetrahedra that reside outside the melt network. This study shows that at P_2O_5 concentrations > 5 mol% the melt separates into two different melt phases, which can be detected with electron microscopy. Furthermore, unmixed melts show two different glass transition temperatures in one heat capacity curve.

Phosphorus enhances immiscibility as the spheres grow in size with increasing P_2O_5 concentration at the same melting temperature and time. Measurements and mappings of spheres and matrix composition for sample CHAMP-P10 have shown, that the original homogeneous melt separates into a silica- and aluminum-rich melt a highly calcium-, iron- and phosphorus-rich melt. Furthermore, there is evidence that divalent metal cations also prefer the Ca-Fe-P-rich melt. Therefore, we suggest that the ferrous iron preferably enters the Ca-Fe-P-rich melt while the ferric iron probably remains within the Si-Al-rich matrix melt in a tetrahedral coordination state.

These results prove the previous implications that PO_4^{3-} resides outside the silicate network, seemingly preferring to form a second melt phase. While unmixing was not observed for samples CHAMP-P2 and CHAMP-P4, we suggest that these melts are also unmixed due to the fact that PO_4^{3-} tetrahedra together with divalent metal cations favour the separation into a second melt phase, but because of the lower P_2O_5 concentration unmixing cannot be observed with the used methods. It is also a matter of debate when unmixing actually occurs and can be measured. The measurements show that unmixing is observed when the size of the unmixed phases reaches at least nm range, but further experiments are needed in order to answer this particular question.

Understanding the affinity of melts to separate is essential in order to gain better comprehension of magmatic processes. Melt separation is likely to affect crystallization

processes due to the changing melt composition. For instance, the addition of fluorine and/or water to an unmixed melt results in the immediate crystallization of apatite from the Ca-Fe-P-rich melt (see Chapter 5). For Champagne rocks Usui et al. (2008) proposed that the high P_2O_5 concentrations result from incorporation of merrillite crystals from host rocks by explosive eruption or impact. This study, however, presents another possible explanation for the formation of P_2O_5-rich Champagne rocks, which is the direct crystallization from an unmixed phosphorus-rich magma.

In fact, the crystallization of large apatite crystals or crystal layers from unmixed melts is currently a matter of discussion. Liquid immiscibility in natural samples was first recognized experimentally in lunar rocks (Roedder and Weiblen 1971b; Charlier et al. 2013). Recently, experimental studies have demonstrated the affinity of phosphorus-rich ferrobasalts and basalts along the tholeiitic line of descent to unmix (Charlier et al. 2011; Charlier and Grove 2012; Charlier 2015). There is also evidence in form of melt inclusions in apatite crystals for a separated Si-rich and Fe-P-(Ca)-rich host melt of the Bushveld intrusion (Fischer et al. 2016). In addition, Hou et al. (2018) present experimental data on a development of liquid immiscibility in intermediate magmas, responsible for the formation of iron oxide-apatite ore deposits. Liquid immiscibility as a process for crystallization of cumulate rocks has also been reported for Skaergaard intrusion (Jakobsen et al. 2005, 2011; Holness et al. 2011) as well as Sept Iles layerd intrusion (Charlier and Grove 2012).

All of the previous experiments on basalts or rocks similar to basalts were conducted at temperatures of ore formation for layered intrusions between ~940°C - ~1100°C and contain crystals. Champagne was synthesized at higher temperatures to gain a crystal-free melt in order to focus solely on the effect on melt structure. Unfortunately, the melts are not completely free of crystals, but since their amount is < 1 Vol% they do not change the original melt compositions significantly. Despite their crystal size being too small for analysis they show dendritic growth and cannot be confused with unmixed melt phases. Nevertheless, the results are the same as reported in previous studies on liquid immiscibility, implying that mainly phosphorus but also calcium and iron play an important role in the development of liquid immiscibility.

4.5.4 Comparison with Models

The viscosities of CHAMP series have been modelled after Giordano et al. (2008a) and the results are shown in Fig. 43. For all samples the model overestimates the viscosity data. The P_2O_5-free sample is closest to the 1:1 regression line. With higher P_2O_5 concentrations the deviation of the model with respect to the measured values becomes higher. One explanation is that the model does not include phosphorus in its calculation and is therefore

not applicable for this particular melt composition. However, it is observed that seemingly not only the concentration of P_2O_5 effects the viscosity but also the incorporation mechanism. It can be observed that with the addition of P_2O_5 to CHAMP melt the deviation between the modelled and measured viscosities increases while melt viscosity also increases. When the maximum viscosity is reached and the incorporation mechanism of P_2O_5 in the melt changes, the deviation between modelled and measured viscosities remains constant. Liquid immiscibility of the melts which was observed for the samples with high P_2O_5 concentrations also causes deviation from the modelled values.

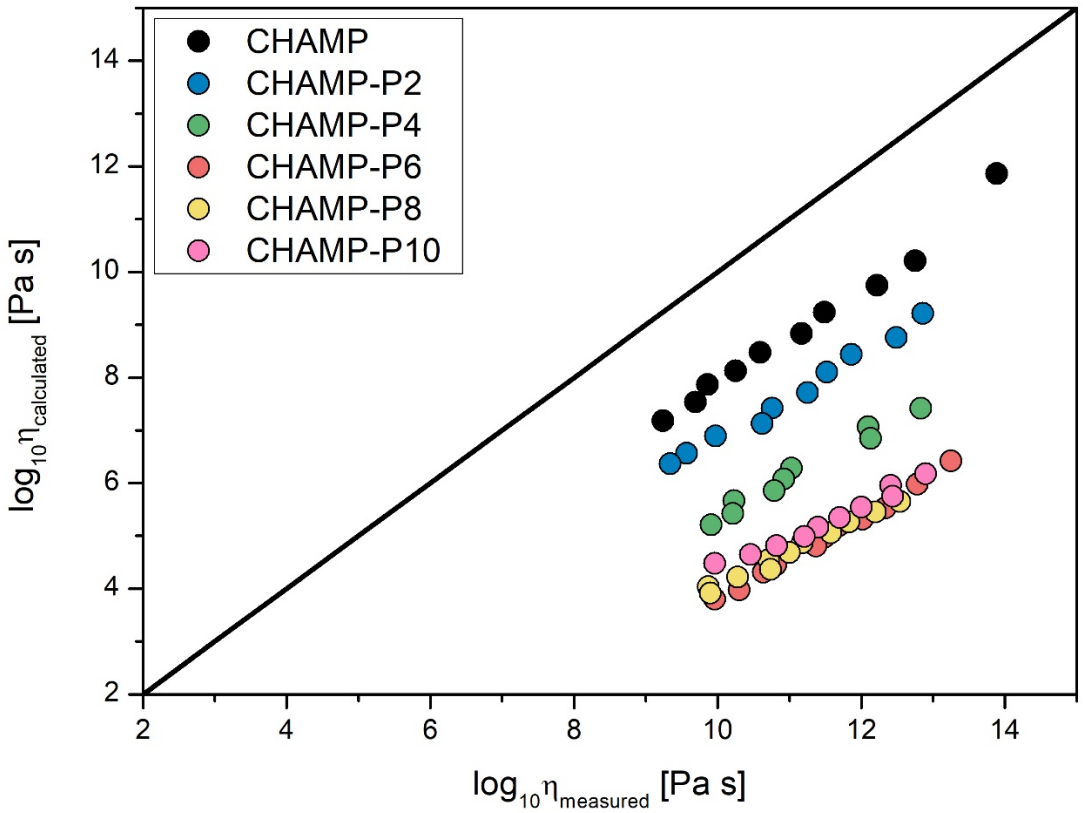

***Fig. 43**: A comparison of measured and modelled viscosities for Champagne melts. Viscosities were calculated using the model after Giordano et al. (2008a).*

Additionally, C_{pg} and C_{pl} values have been modelled after Richet (1987) (model for C_{pg}) as well as after Richet (1985b) and Stebbins et al. (1984) (models for C_{pl}) and the results are illustrated in Fig. 44. All models underestimate the calculated values by approximately 10 J g^{-1} K^{-1}. This is expected for the modelled C_{pl} values, since they do not include P in their calculation and viscosity results and heat capacity data of this study as well as previous studies (e.g. Toplis and Dingwell 1996b) have shown the strong polymerizing effect of P_2O_5 on the structure of peralkaline melts. The best fit is given for C_{pl} values calculated after Stebbins et al. (1984). Unmixing of the melts results in two different glass transition peaks which also cannot be modelled.

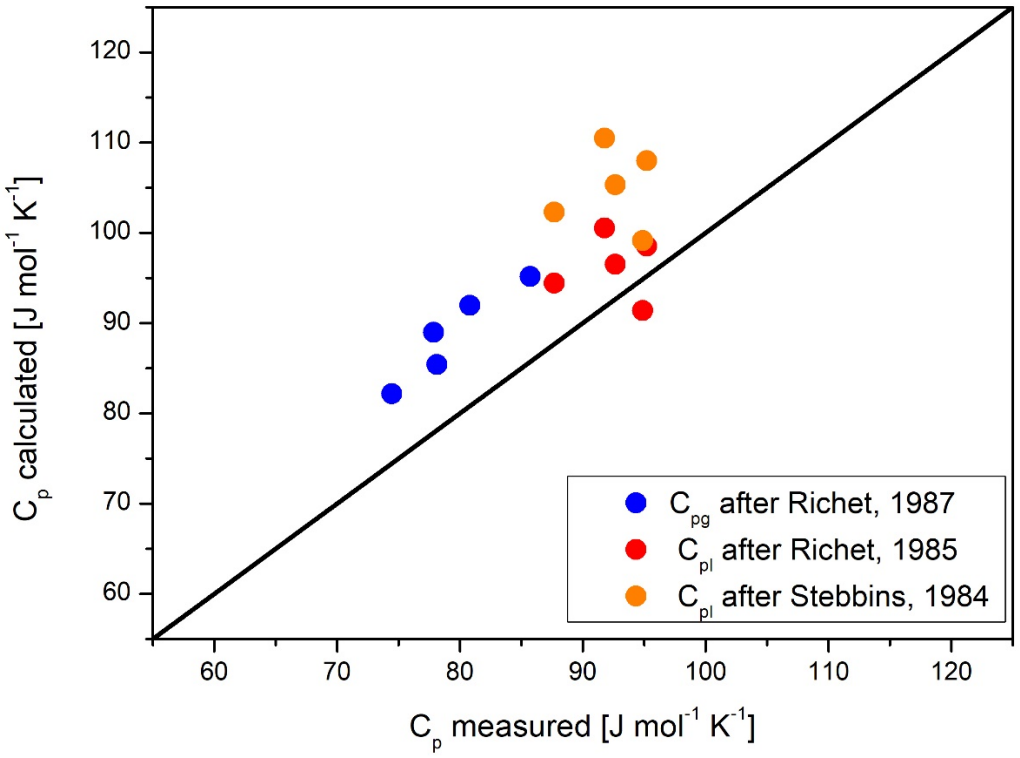

***Fig. 44**: A comparison of measured and modelled heat capacities for glass (C_{pg}) and liquid (C_{pl}) using the model of Richet (1987) for C_{pg} and Stebbins et al. (1984) and Richet and Bottinga (1985) for C_{pl}.*

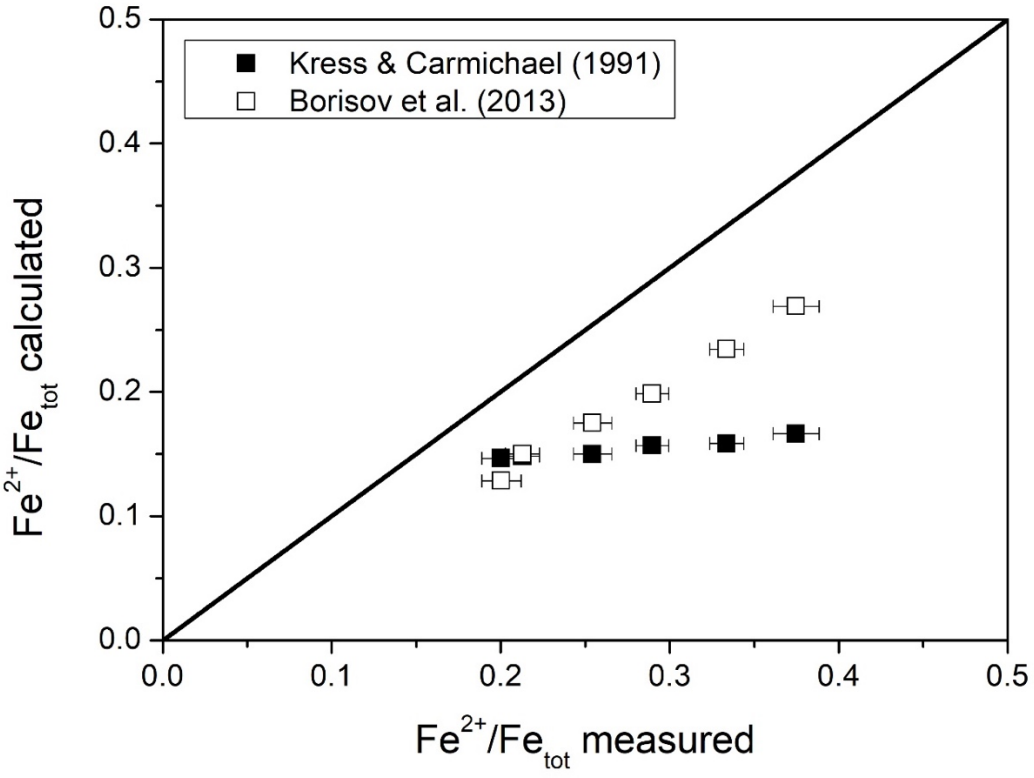

***Fig. 45**: A comparison of measured and modelled Fe_{2+}/Fe^{tot} ratios. Ratios were calculated using the models of Kress and Carmichael (1991) and Borisov et al. (2013).*

The Fe^{2+}/Fe_{tot} ratios measured with the wet chemistry method were compared to the models after Borisov et al. (2013) and Kress and Carmichael (1991) and the results are given in Fig. 45. The model after Kress and Carmichael (1991) does not predict a significant increase of Fe^{2+}/Fe_{tot} ratios with increasing P_2O_5 concentration. The calculated Fe^{2+}/Fe_{tot} ratios from Borisov et al. (2013) show a similar increasing trend as the measured Fe^{2+}/Fe_{tot}. However, the calculated values are considerably lower than the measured values which is probably caused by the fact that Borisov et al. (2013) take only the effect of SiO_2, TiO_2 and P_2O_5 into account.

4.6 Conclusions

The addition of P_2O_5 to the melt structure results in an increasing Fe^{2+}/Fe_{tot} ratio, and is consistent with the results of previous studies (Borisov et al. 2013). Increasing the amount of network-modifying iron should also result in a depolymerisation of the melt structure, but despite this fact, viscosity measurements as well as Raman-spectra imply that there is as stronger polymerisation of the melt structure. This contradiction can be explained by heat capacity data as well as the backscattered electron micrographs. For the melt compositions containing more than 5 mol% of P_2O_5 there is a second and in case of sample CHAMP-P8 even a third glass transition peak present, indicating the existence of separated melts. The melt separation is also visible in backscattered electron micrographs, where the unmixed phases appear as small light and dark spheres with diameters ranging from ~100 nm (CHAMP-P6) up to 300 µm (CHAMP-P10). The melts unmix into a Si-Al-rich (matrix) and into a Fe-Ca-P-rich melt (spheres). Albeit unmixing was not observed for lower P_2O_5 concentration than 5.41 mol%, we suggest that these melts are also unmixed, but the size of the unmixed phases is too small for detection with the used analytical techniques in this study.

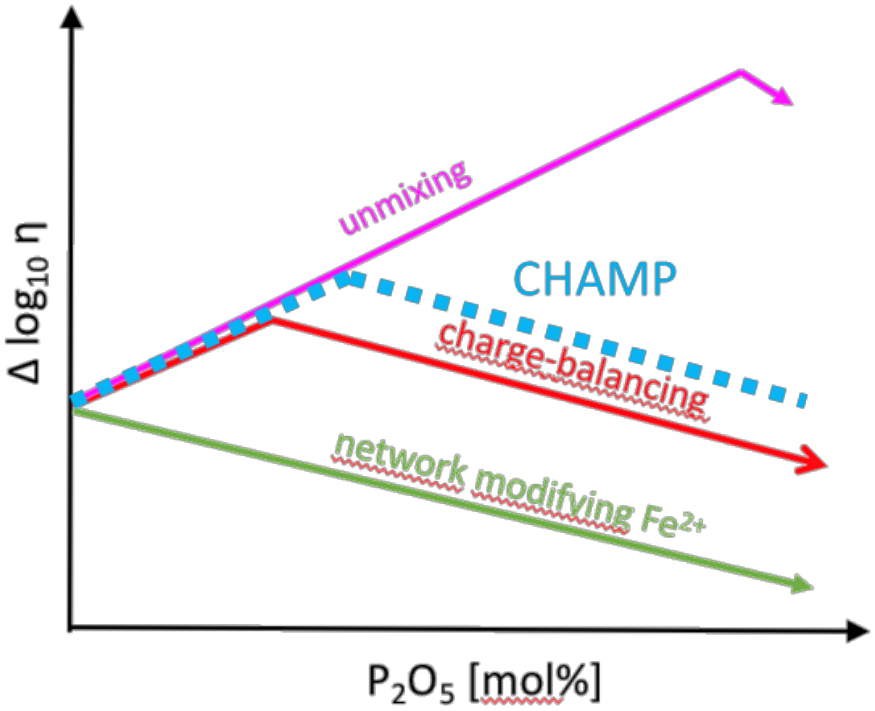

***Fig. 46**: Overview over the main mechanisms affecting the viscosity of Champage melt.*

This study shows that P_2O_5 triggers unmixing events in basaltic melts. At high P_2O_5 concentrations (> 5 mol%) unmixing is observed and with increasing P_2O_5 content of the melt the spheres of the second melt phase grow in size up to µm range. The Ca-Fe-P-rich melt composition has a lower glass transition temperature than the Si-Al-rich melt. Due to the separation of the low viscosity Ca-Fe-P melt, the SiO_2 concentration in the matrix melt increases with respect to the same melt composition without unmixing. This process is likely to continue until the low viscosity Ca-Fe-P rich melt composition dominates.

The viscosity of Champagne is affected by three different competing mechanisms at the same time which are summarized in Fig. 46. The three processes caused by the presence of P_2O_5 in the melt are the reduction of ferric to ferrous iron, the charge balancing effect of PO_4^{3-} units on excess metal cations and the unmixing of the melt. However, the charge balancing role of PO_4^{3-} has the largest impact on viscosity.

This study demonstrates the complex behaviour of P_2O_5 incorporation in the melts structure and its importance for better understanding of magmatic and especially ore-forming processes.

5 The combined effect of P_2O_5, B_2O_3, F^- and H_2O on structure and rheology of silicate melts

5.1 Abstract

In order to investigate the combined effect of P_2O_5, B_2O_3, F^- and H_2O on the unmixing of melts, unmixed as well as homogeneous P_2O_5-bearing melts were selected from chapter 3 and 4 of this study. The melts were doped with up to 8 mol% B_2O_3, 6 mol% F^- and 6 mol% H_2O. The water-free melts were synthesized in a 1 atm furnace at ~1573 – 1873 K in air whereby the synthesis of the H_2O-bearing melts was performed in an Internally Heated Pressure Vessel (IHPV) at 1533 K and 2 kbar. Apatite was found to crystallize in all water-bearing samples as well as fluorine-bearing melts of P_2O_5-bearing Champagne composition. The melts were analysed with respect to their rheology and structure. The viscosity of the melts was determined in the range $10^{8.5}$ to $10^{13.5}$ Pa s by micropenetration viscometry. The heat capacity of the melts was measured by Differential Scanning Calorimetry (DSC). The structure of the melts was investigated using Raman spectroscopy as well as Scanning Electron Microscopy (SEM). The addition of B_2O_3 as well as F^- results in a decrease of viscosity and thus a depolymerisation of the melts. No unmixing was observed for F^--bearing melts. The effect of B_2O_3 on unmixing of P_2O_5-bearing melts is controversial. Whereas the addition of low B_2O_3 concentrations to NCAS13-P8 melt results in a homogenisation of the previously unmixed melt, higher concentrations of B_2O_3 result in a renewed phase separation. The addition of low B_2O_3 concentrations to CHAMP-P8 melt, however, result in an enhancement of unmixing. At higher B_2O_3 concentrations this melt composition begins to slowly homogenise, as observed from heat capacity data as well as BSE images. While this process is not completely understood, it is apparent that the homogenisation of the P_2O_5- and B_2O_3-bearing melts is linked to the presence of BPO_4 structural units. Furthermore, we suggest that in the crystallized melts apatite crystallized from the P_2O_5-rich phase of a two-liquid melt rather than from a homogeneous melt.

5.2 Introduction

Previous studies of the effect of P_2O_5 on melt structure have shown that P_2O_5 can act as a network former as well as a network modifier, depending on the peralkalinity of the melts. P_2O_5 enters the melt structure in form of terahedrally coordinated PO_4^{3-} and also pyrophosphate P_2O_7. In peralkaline melts, PO_4^{3-} bonds to cations in network modifying positions, resulting in the formation of metal-phosphate complexes, resulting in an increase in bridging oxygen bonds in the aluminosilicate melt network (Mysen et al. 1981a; Gan and Hess 1992b; Toplis et al. 1994c; Toplis and Dingwell 1996a; Mysen 1996). Gan and Hess (1992b) argued that these complexes reside outside the silicate melt network. However, there is no evidence for this hypothesis in present studies.

Gan and Hess (1992b), Mysen (1998b,1996) as well as Toplis and Dingwell (1996a) have shown, that in peraluminous melts PO_4^{3-} acts as a network modifier by bonding from Al^{3+} from tetrahedral positions and forming structural units similar to $AlPO_4$ in berlinite. This leads to the freeing of former charge balancing cations which decrease the number of bridging oxygen bonds in the silicate melt network.

B_2O_3 can act as a network former as well as a modifier depending on the structure. BO_3 triangles act as network modifier by decreasing the NBO/T ratio of the melt. In the presence of network modifying cations part of BO_3 triangles will be transformed into network forming BO_4^- tetrahedra (Konijnendijk 1975; Manara et al. 2009; Koroleva et al. 2011).

The viscosity decreasing effect of F^- and H_2O has been reported by several authors (Bartels et al. 2011; Robert et al. 2013; Baasner et al. 2013b). The water content in natural melts can contain up to 6 wt%, as observed for Island Arc basalts (Wanless et al. 2011).

5.3 Starting Material

The aim of this study was to investigate the effect of combined P_2O_5 and B_2O_3 as well as H_2O and F^- on the unmixing of melts. Therefore, the peralkaline NCAS13-P2 and NCAS13-P8 as well as the peraluminous NCAS10-P6 melt compositions were chosen for the investigation of the combined effect of P_2O_5 and B_2O_3. Glasses were synthesized by mixing oxide compounds. The synthesis of those samples is described in chapter 2. 4 and 8 mol% of B_2O_3 were added to the P_2O_5-bearing melts in form of H_3BO_3. After homogenisation, the glasses were melted at least two times for 1 – 5 h at 1773 K to 1873 K in a 1 atm furnace and quenched in water.

In order to investigate the effect of F^- and H_2O on unmixing, melts of the peralkaline compositions NCAS13-P6, NCAS13-P8B4 and CHAMP-P8 were chosen. The synthesis of those melts is described in chapter 2, 3 and 4. Afterwards, 3 mol% and 6 mol% F^- and H_2O were added to the melts. F^- was added in form of NH_4F.In order to compensate for the F loss during melting twice of the desired amount of F was weighted into the samples. The flouring-bearing melts were synthesized in a 1 atm furnace at temperatures between 1573 K and 1873 K for a duration of 30 min – 3 h for at least 3 times and afterwards quenched in water.

Water was added in form of liquid H_2O to the F^--bearing melts and the synthesis was performed in an Internally Heated Pressure Vessel (IHPV). Samples were weighted into AuPd capsules and closed by welding. IHPV experiments were performed at 1533 K and 2 kbar pressure for a duration of 24 h. Samples were quenched by using a rapid quench device. The exact description of sample preparation as well as IHPV experiments is described in Chapter 2.

All H_2O- and F^-- bearing samples as well as the only F^--bearing CHAMP-P8 melt crystallized during experiments. Therefore, it was not possible to measure the viscosity and heat capacity of these samples. For this reason, no further experiments were performed on these samples. The other samples were checked with an optical microscope and are free of crystals.

The exact compositions of the glasses were measured with a JEOL JXA 8900RL electron microprobe with a beam diameter of 30 µm and an accelerating voltage of 15 kV and are shown in Table 21 and Table 22. The microprobe was calibrated by using Wollastonite (Si), Anorthite (Ca, Al), Albite (Na), Hematite (Fe), Olivine (Mg), Apatite (P), Danburite (B) and Topas (F) standards.

Samples containing B_2O_3 were measured with a beam diameter of 30 µm and an accelerating voltage of 10 kV. Boron is very difficult to measure with an electron microprobe and it has to be noted that while measuring B_2O_3 all samples contained a small amount of B_2O_3 (<0.4 wt%), even the B_2O_3-free samples. Therefore, it has to be noted that the measured B_2O_3 concentrations are slightly higher than the actual concentrations in the glasses, but since the error is more or less constant it does not change the observed trends in this study.

***Table 21**: Melt compositions in wt% measured by Electron Micropobe Analysis*

Sample	SiO_2	2σ	Al_2O_3	2σ	Na_2O	2σ	CaO	2σ	MgO	2σ	FeO	2σ	P_2O_5	2σ	B_2O_3	2σ	F	2σ	total
NCAS13-P2B4	56.50	0.07	19.62	0.04	10.46	0.04	5.69	0.04	-	-	-	-	3.81	0.03	3.62	0.06	-	-	99.70
NCAS13-P2B8	55.80	0.12	19.28	0.07	9.34	0.06	5.39	0.06	-	-	-	-	3.39	0.04	5.60	0.11	-	-	98.79
NCAS13-P6F3	54.41	0.15	19.71	0.09	9.69	0.08	5.11	0.07	-	-	-	-	10.96	0.15	-	-	0.82	0.15	100.70
NCAS13-P6F6	53.65	0.15	19.49	0.09	9.58	0.08	5.13	0.07	-	-	-	-	10.75	0.14	-	-	1.80	0.14	100.39
NCAS13-P8B4	53.54	0.15	18.50	0.08	8.33	0.07	4.75	0.07	-	-	-	-	12.09	0.09	2.53	0.11	-	-	99.75
NCAS13-P8B4F3	51.41	0.14	18.42	0.08	7.98	0.07	5.15	0.07	-	-	-	-	13.20	0.16	3.12	0.08	0.61	0.16	99.89
NCAS13-P8B4F6	51.60	0.14	18.54	0.09	8.30	0.07	4.93	0.07	-	-	-	-	13.22	0.16	2.81	0.09	1.08	0.16	101.09
NCAS13-P8B8	50.10	0.14	17.45	0.08	7.88	0.07	4.89	0.07	-	-	-	-	12.81	0.09	5.64	0.14	-	-	98.77
NCAS10-P6B4	50.45	0.15	23.54	0.09	7.25	0.07	3.79	0.06	-	-	-	-	10.60	0.09	3.40	0.12	-	-	99.03
NCAS10-P6B8	48.63	0.07	22.68	0.05	7.10	0.03	3.59	0.03	-	-	-	-	10.17	0.04	6.30	0.07	-	-	98.47
CHAMP-P8B4	35.56	0.12	11.46	0.07	4.53	0.06	12.56	0.11	2.47	0.03	11.46	0.12	15.11	0.17	3.71	0.07	-	-	96.86
CHAMP-P8B8	33.72	0.12	12.07	0.07	4.38	0.06	12.06	0.10	2.39	0.03	10.92	0.12	14.39	0.16	7.18	0.07	-	-	97.12

Results are mean values of 10 single point measurements

***Table 22**: Melt compositions in mol% as measured by Electron Microprobe*

Sample	SiO_2	2σ	Al_2O_3	2σ	Na_2O	2σ	CaO	2σ	MgO	2σ	FeO	2σ	P_2O_5	2σ	B_2O_3	2σ	F	2σ	γ	NBO/T	g.atom
NCAS13-P2B4	63.46	0.39	12.99	0.06	11.39	0.06	6.85	0.13	-	-	-	-	1.81	0.04	3.51	0.29	-	-	0.58	0.00	3.33
NCAS13-P2B8	63.23	0.57	12.87	0.07	10.26	0.06	6.54	0.20	-	-	-	-	1.62	0.06	5.47	0.29	-	-	0.57	-0.02	3.37
NCAS13-P6F3	61.75	0.50	13.18	0.13	10.66	0.10	6.22	0.12	-	-	-	-	5.27	0.08	-	-	2.93	0.71	0.56	-0.19	3.35
NCAS13-P6F6	59.50	0.62	12.74	0.10	10.30	0.19	6.09	0.17	-	-	-	-	5.05	0.10	-	-	6.32	0.71	0.56	-0.11	3.27
NCAS13-P8B4	63.05	0.40	12.84	0.05	9.51	0.10	5.99	0.17	-	-	-	-	6.03	0.15	2.58	0.12	-	-	0.55	-0.31	3.49
NCAS13-P8B4F3	59.97	0.19	12.66	0.06	9.02	0.08	6.43	0.06	-	-	-	-	6.51	0.12	3.14	0.12	2.26	0.20	0.55	-0.28	3.47
NCAS13-P8B4F6	59.11	0.48	12.52	0.12	9.22	0.16	6.05	0.09	-	-	-	-	6.41	0.10	2.78	0.22	3.92	0.59	0.55	-0.25	3.42
NCAS13-P8B8	59.96	0.64	12.31	0.06	9.15	0.12	6.27	0.24	-	-	-	-	6.49	0.15	5.82	0.23	-	-	0.56	-0.34	3.56
NCAS10-P6B4	60.91	0.10	16.75	0.07	8.49	0.05	4.90	0.05	-	-	-	-	5.42	0.06	3.54	0.07	-	-	0.44	-0.35	3.57
NCAS10-P6B8	58.96	0.14	16.21	0.03	8.35	0.09	4.67	0.03	-	-	-	-	5.22	0.05	6.60	0.10	-	-	0.45	-0.33	3.62
CHAMP-P8B4	42.44	0.21	8.97	0.07	5.24	0.06	16.07	0.13	4.39	0.04	11.44	0.10	7.63	0.07	3.82	0.11	-	-	0.81	0.11	3.24
CHAMP-P8B8	40.63	0.18	8.57	0.06	5.12	0.06	15.57	0.13	4.30	0.07	11.01	0.10	7.34	0.08	7.47	0.10	-	-	0.81	0.11	3.31

γ = (Na_2O + CaO) / (Na_2O + CaO + Al_2O_3) from mole fractions (e.g. Toplis et al. 1997a; Webb et al. 2007; Baasner et al. 2013b)

NBO/T: non-bridging oxygens per tetrahedral unit as an indicator for the degree of melt polymerization

g.atoms: number of atoms in one mole of melt (Sehlke and Whittington 2016)

5.4 Results

5.4.1 The Combined Effect of P_2O_5 and B_2O_3 on Viscosity

The results of the micropenetration measurements of the P_2O_5-, B_2O_3- and F^--bearing melts are summarized in Table 23. The data was fitted using an Arrhenian equation (*Eq. X*) of the type:

$$\log\eta = \log A + \frac{10000\ B}{T}$$

Where A and B represent fit parameters, which are listed in Table 24.

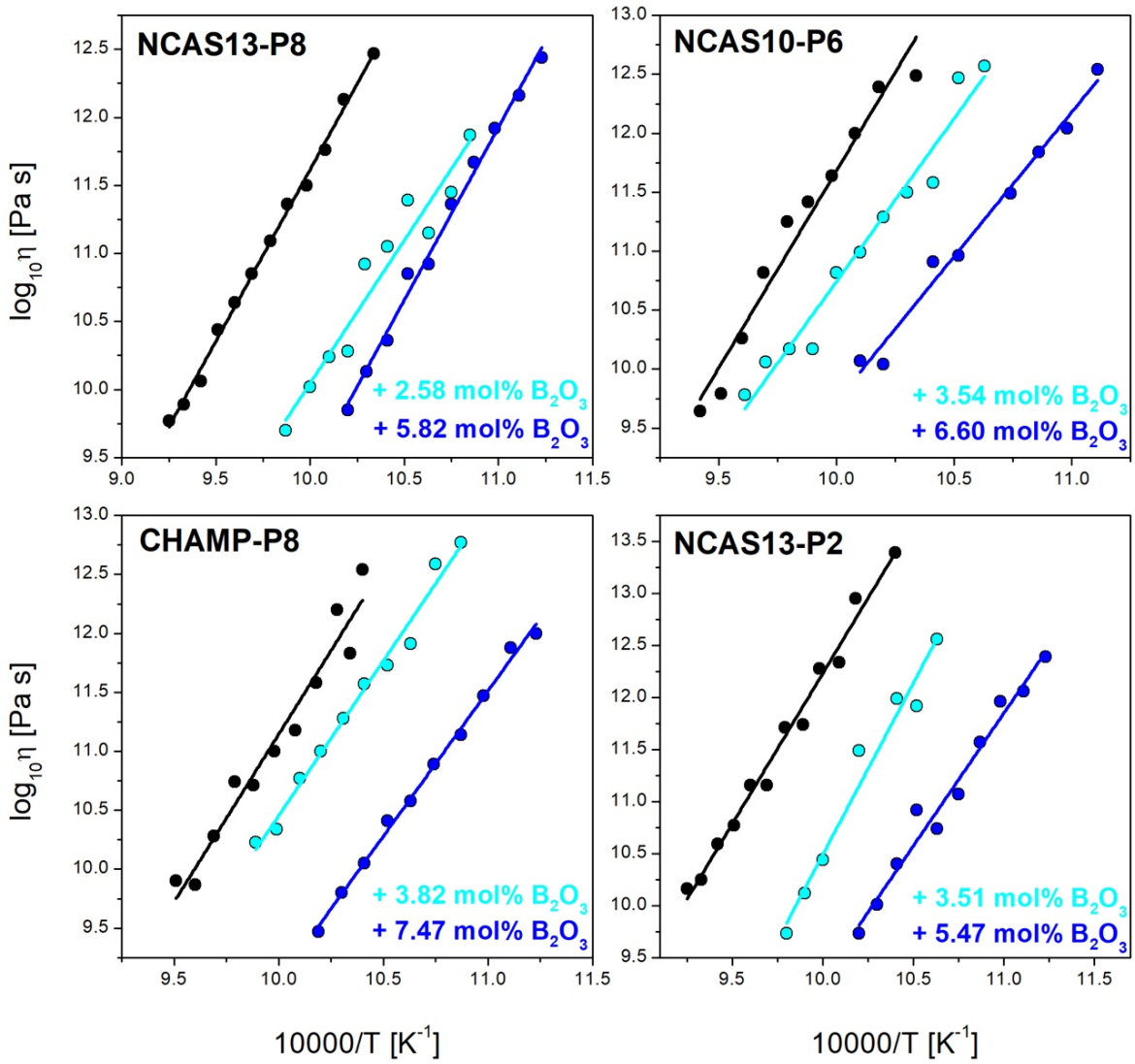

***Fig. 47**: Viscosities of P_2O_5- and B_2O_3-bearing melts. Samples NCAS13-P2, NCAS13-P8 and CHAMP-P8 are of peralkaline and NCAS10-P6 is of peraluminous melt composition. The NCAS13-P8 as well as CHAMP-P8 melt without B_2O_3 are unmixed.*

***Table 23**: Viscosities of P_2O_5-, B_2O_3- and F^--bearing melts measured by micropenetration technique*

NCAS13-P2B4		NCAS13-P2B8		NCAS13-P8B4		NCAS13-P8B8	
T [K]	$\log_{10}\eta$ [Pa s]	T [K]	$\log_{10}\eta$ [Pa s]	T [K]	$\log_{10}\eta$ [Pa s]	T [K]	$\log_{10}\eta$ [Pa s]
940.4	12.56	890.3	12.39	921.3	11.87	890.4	12.44
950.4	11.92	900.3	12.06	930.4	11.45	900.3	12.16
960.4	11.99	910.4	11.96	940.4	11.15	910.4	11.92
980.5	11.49	920.3	11.57	950.4	11.39	920.4	11.67
1000.4	10.44	930.4	11.07	960.4	11.05	930.4	11.36
1010.4	10.12	940.4	10.74	971.6	10.92	940.4	10.92
1020.4	9.73	950.6	10.92	980.6	10.28	950.4	10.85
		960.4	10.40	990.4	10.24	960.4	10.36
		970.5	10.01	1000.5	10.02	970.8	10.13
		980.6	9.73	1012.7	9.70	980.4	9.85

NCAS10-P6B4		NCAS10-P6B8		CHAMP-P8B4		CHAMP-P8B8	
T [K]	$\log_{10}\eta$ [Pa s]	T [K]	$\log_{10}\eta$ [Pa s]	T [K]	$\log_{10}\eta$ [Pa s]	T [K]	$\log_{10}\eta$ [Pa s]
940.5	12.57	900.4	12.54	920.4	12.77	890.6	12.00
950.4	12.47	910.4	12.04	930.4	12.59	900.4	11.88
960.4	11.58	920.6	11.84	940.4	11.91	910.4	11.47
970.4	11.50	930.9	11.49	950.4	11.73	920.4	11.14
980.4	11.29	950.4	10.96	960.6	11.57	930.8	10.89
990.4	10.99	960.4	10.91	970.4	11.28	940.4	10.58
1000.4	10.82	980.6	10.04	980.6	11.00	950.4	10.41
1010.5	10.17	990.4	10.07	990.5	10.77	960.4	10.05
1020.5	10.17			1000.6	10.34	970.5	9.80
1030.6	10.06			1010.6	10.23	981.1	9.47
1040.5	9.78						

NCAS13-P8B4F3		NCAS13-P8B4F6		NCAS13-P6F3		NCAS13-P6F6	
T [K]	$\log_{10}\eta$ [Pa s]	T [K]	$\log_{10}\eta$ [Pa s]	T [K]	$\log_{10}\eta$ [Pa s]	T [K]	$\log_{10}\eta$ [Pa s]
860.3	12.24	820.3	12.48	940.4	11.03	860.3	11.60
890.4	11.50	840.4	11.52	950.4	11.02	880.3	10.89
900.3	10.79	850.4	11.05	960.5	10.78	890.4	10.60
910.4	10.62	870.4	10.92	970.4	10.56	900.4	10.57
920.5	10.32	880.4	10.26	980.5	10.25	910.6	10.35
930.5	10.13	890.3	10.27	990.5	10.10	920.4	10.07
940.6	10.16	910.5	9.77	1000.5	9.92	930.6	9.86
950.6	9.81			1010.7	9.66	950.4	9.47
				1020.8	9.50		
				1030.6	9.21		

The results for the P_2O_5- and B_2O_3-bearing peralkaline NCAS13-P2, NCAS13-P8 and CHAMP-P8 as well as peraluminous NCAS10-P6 melt are illustrated in Fig. 47. For all melt compositions it is observed, that viscosity decreases with addition of B_2O_5 to a P_2O_5-bearing melt. In case of NCAS13-P2 and NCAS10-P6 melts, viscosity decreases steadily by approximately 3.2 log units with the addition of up to 5.47 mol% B_2O_5 for NCAS13-P2 and by approximately 2.2 log units with an addition of up to 6.60 mol% B_2O_5 in NCAS10-P6 melt.

The previously unmixed NCAS13-P8 and CHAMP-P8 melts, however, show a different and controversial decrease in viscosity. In case of NCAS18-P8 melt, viscosity decreases strongly by ~2.5 log units at the beginning with addition of 2.58 mol% B_2O_3. Further addition of up to 5.82 mol% P_2O_5 decreases viscosity less strongly by ~0.7 log units.

The opposite is observed for CHAMP-P8 melt. The addition of low concentrations of 3.82 mol% B_2O_3 causes a decrease of viscosity by approximately 0.7 log units whereas further addition of up to 7.47 mol% B_2O_3 to the melt decreases viscosity more strongly by ~1.5 log units.

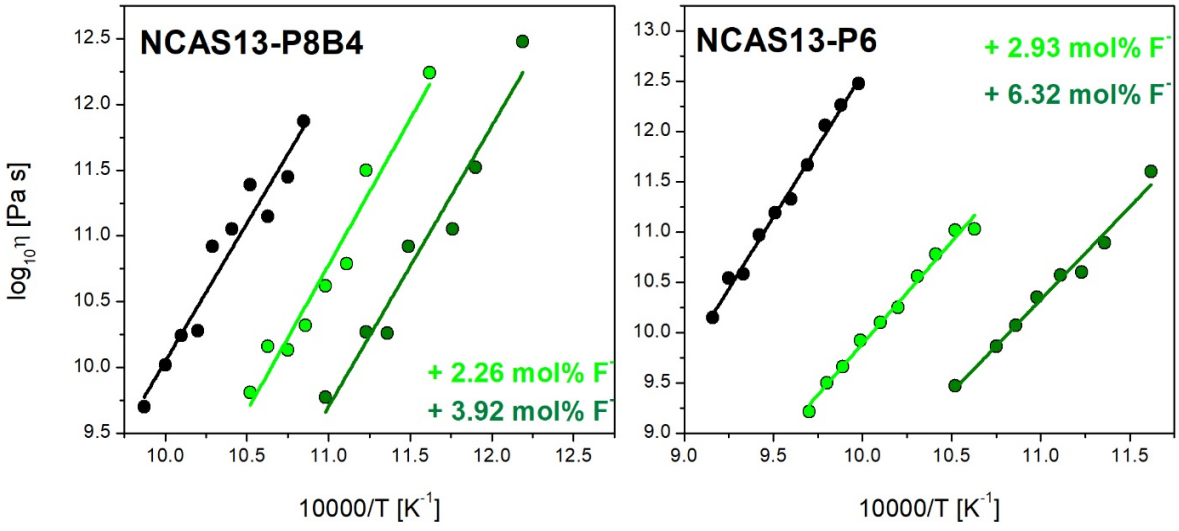

***Fig. 48**: Viscosities of fluorine-bearing melts measured by micropenetration technique.*

The viscosities of the fluorine-bearing samples NCAS13-P8B4 and NCAS13-P6 are illustrated in Fig. 48. In both melts the addition of F^- to the melt results in a strong decrease of viscosity. In the P_2O_5 and B_2O_3-bearing melt viscosity decreases by approximately 2.3 log units up to a F^- concentration of 3.92 mol%.

The addition of F^- to the only P_2O_5-bearing NCAS13-P6 melt results in a much stronger decrease of viscosity. In the melt, increasing the F^- concentration up to 6.32 mol% leads to a decrease of viscosity by approximately 3.9 log units.

***Table 24**: Arrhenian fit parameters for viscosities of P_2O_5-, B_2O_3- and F^--bearing melts*

Sample	A	Δ A	B	Δ B	E	T_g^{12}	Δ T_g^{12}	m
	$\log_{10}$ Pa s	$\log_{10}$ Pa s	$\log_{10}$ Pa s 10^4 K	$\log_{10}$ Pa s 10^4 K	kJ mol^{-1}	K	K	
NCAS13-P2B4	-22.47	2.80	3.30	0.27	631.11	956.2	1.2	34.5
NCAS13-P2B8	-16.18	1.55	2.55	0.14	487.95	904.2	0.9	28.2
NCAS13-P6F3	-10.41	0.76	2.03	0.08	388.68	905.8	0.6	22.4
NCAS13-P6F6	-9.96	1.14	1.84	0.10	353.17	839.8	0.9	22.0
NCAS13-P8B4	-10.97	1.96	2.10	0.19	402.36	914.9	1.4	23.0
NCAS13-P8B4F3	-13.65	2.13	2.22	0.19	425.23	865.8	1.4	25.6
NCAS13-P8B4F6	-13.78	2.45	2.13	0.21	408.80	828.1	1.7	25.8
NCAS13-P8B8	-16.02	0.82	2.54	0.08	486.44	906.8	0.5	28.0
NCAS10-P6B4	-16.93	1.77	2.77	0.17	529.79	956.5	0.9	28.9
NCAS10-P6B8	-14.77	1.37	2.45	0.13	469.07	915.2	0.8	26.8
CHAMP-P8B4	-15.80	1.14	2.63	0.11	502.66	944.4	0.6	27.8
CHAMP-P8B8	-15.59	0.60	2.46	0.06	471.77	893.0	0.4	27.6

E: activation energy for viscous flow

T_g^{12}: temperature at which the viscosity of the melt equals 10^{12} Pa s

m: fragility of the melt

5.4.2 Heat Capacity

Differential Scanning Calorimetry was applied on the samples to obtain heat capacity data. Fig. 49 illustrates the heat capacity curves for all four P_2O_5- and B_2O_3-bearing melts. All melts show a shift of the glass transition peak T_g to lower temperatures with the addition of B_2O_3, indicating a depolymerisation of the melts. This observation is consistent with viscosity data. The B_2O_3-free NCAS13-P8 and CHAMP-P8 melts are unmixed (see Chapter 3 and 4).

In case of NCAS13-P2 melt the T_g peak shifts from 1055 K to 962 K with the addition of up to 5.47 mol% B_2O_3. In NCAS13-P8 melt, the T_g peak shift from ~1050 K to 966 K with the increasing B_2O_3 concentration of 5.82 mol%. Furthermore, a strong decrease in C_{pg} is observed for this melt containing B_2O_3. Sample NCAS10-P6 exhibits a shift of the glass transition peak from ~1100 K to ~ 980 K at a B_2O_3 concentration of 6.60 mol%.

The B_2O_3-free CHAMP-P8 melt exhibits three glass transition peaks at ~800 K, 1087 K and 1201 K, indicating the presence of separated melts. Increasing the B_2O_3 concentration up to 3.82 mol% results in a shift of the two glass transition peaks at higher temperatures to ~900 K and 1150 K. In addition, the T_g peak at 1150 K is more pronounced. Further addition

of B_2O_3 to the melts results in the disappearance of two T_g peaks and a shift to lower temperatures to ~941 K.

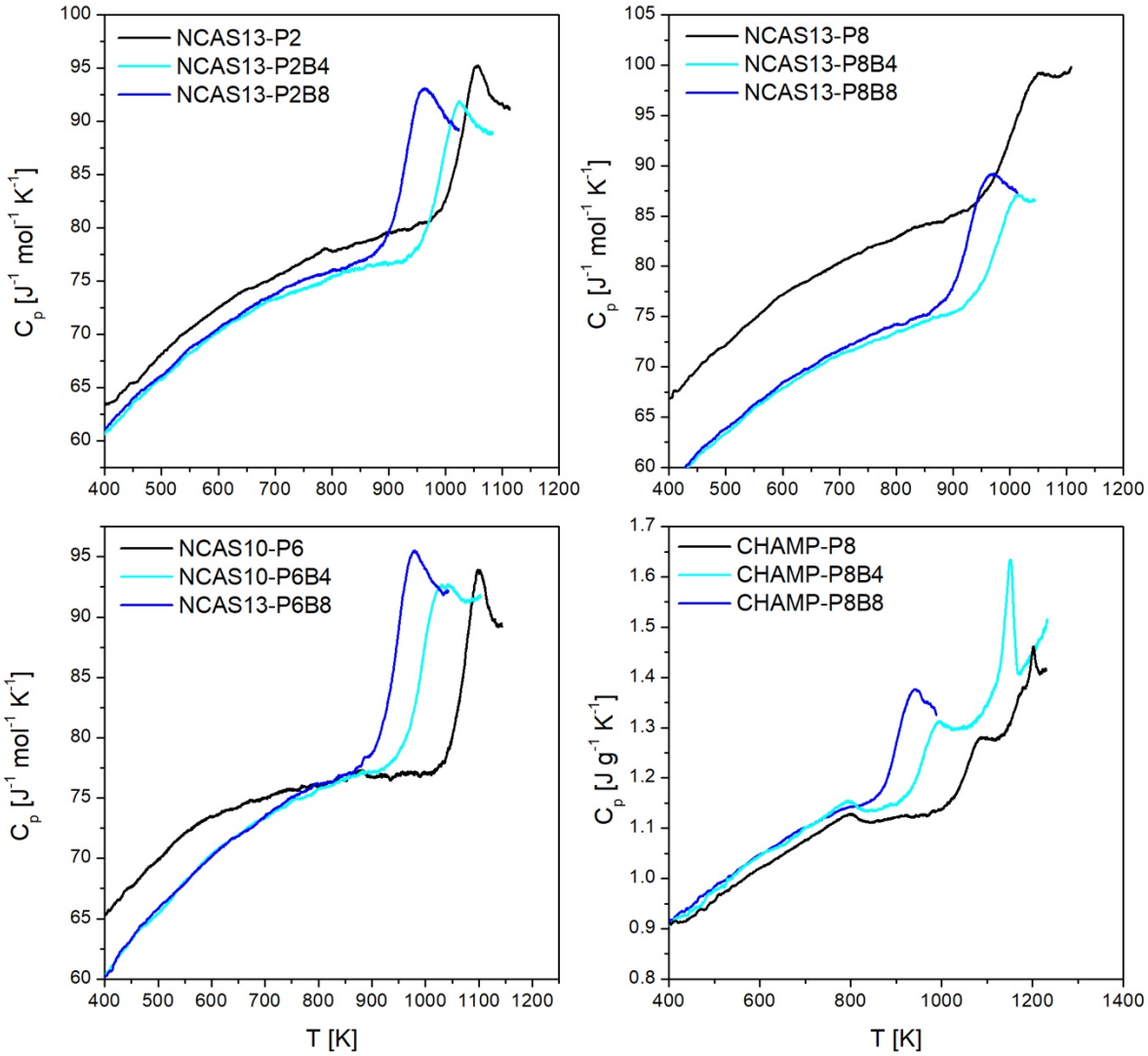

***Fig. 49**: Heat capacity of P_2O_5- and B_2O_3-bearing melts*

The heat capacity curves of the fluorine-bearing NCAS13-P8B4 and NCAS13-P6 melts are shown in Fig. 50. Both F-free melts were previously identified to be unmixed. The addition of F^- to these two melts results in a shift of the T_g-peak to lower temperatures. This observation is in agreement with results obtained from viscosity measurements.

The addition of 2.26 mol% F^- to NCAS13-P8B4 melt results in a slight shift of the T_g peak from ~1020 K to ~1015 K and a slight broadening of the T_g peak. Further increase of F^- concentration in the melt up to 3.92 mol% leads to a stronger shift to 975 K and a strong broadening of the T_g peak.

The F^--free NCAS13-P6 melt exhibits two T_g peaks at ~810 K and ~1093 K. With addition of F^- to the melt, the second T_g peak at 810 K disappears. Furthermore, a shift of the T_g

peak from 1093 K to ~962 K up to a F^- concentration of 6.32 mol% is observed as well as a broadening of the T_g peak at F^- concentrations up to 2.93 mol%. Further increase of F^- in the melt to 6.32 mol% results in a narrowing of the T_g peak.

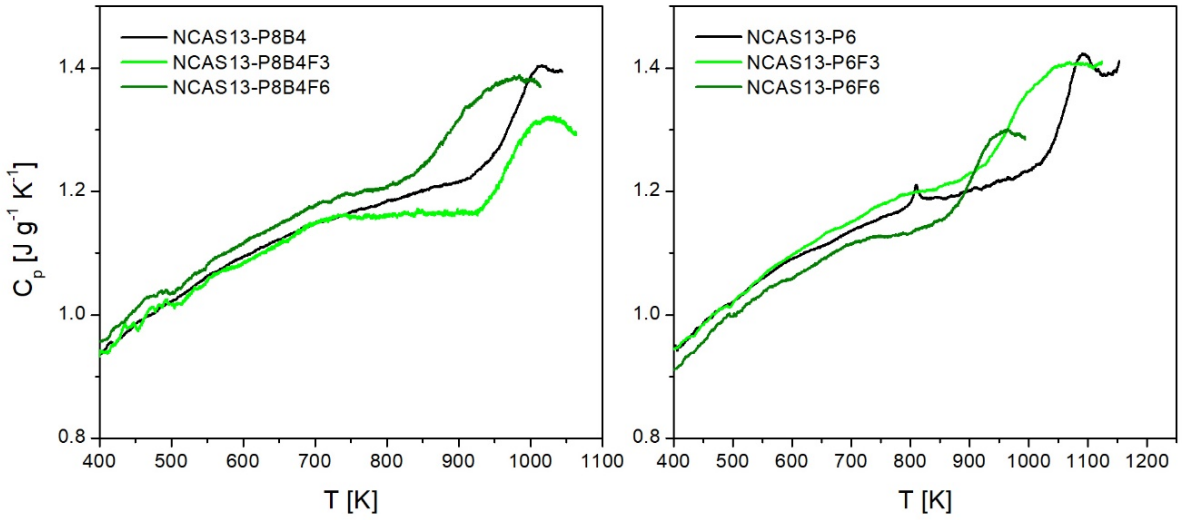

***Fig. 50**: Heat Capacity of fluorine-bearing melts.*

The heat capacity curves were used to calculate the heat capacities of the glass and liquid (C_{pg} and C_{pl}), the configurational heat capacity C_p^{conf}, the fictive temperature T_f', the activation energy B_e as well as the configurational entropy S_{conf} of the melts.

C_{pg} and C_{pl} are calculated directly from heat capacity measurements by use of the Maier-Kelley equation (Maier and Kelley 1932) of the type:

$$C_{pg} = a + bT + CT^{-2} \qquad (Eq.\ IV)$$

The parameters of the Maier-Kelley fit are summarized in Table 24. The configurational heat capacity is calculated from the difference between the heat capacity of the liquid (C_{pl}) and the heat capacity of the glass (C_{pg}) as follows:

$$C_p^{conf} = C_{pl} - C_{pg} \qquad (Eq.\ XII)$$

The fictive temperature T_f' was calculated using the method described by Moynihan et al. (1976). S_{conf}, B_e and C_p^{conf} are calculated from the heat capacity curves as well as viscosity data by applying the Adam-Gibbs theory of viscosity (Adam and Gibbs 1965; Webb 2008) using the following equation:

$$log_{10}\eta(T) = A_e + \frac{B_e}{\ln 10 * [S_{conf}(T_g) + \int_{T_g}^{T} \frac{C_p^{conf}}{T} dT] * T} \qquad (Eq.\ XI)$$

Where A_e and B_e are constants, T is the temperature in K, η the viscosity and C_p^{conf} the configurational heat capacity. The calculated C_{pg}, C_{pl}, C_p^{conf}, B_e and S_{conf} and T_f' are given in Table 26. For CHAMP-P8 melts the terms were only calculated for sample CHAMP-P8B8. Due to the presence of three T_g peaks in CHAMP-P8 and CHAMP-P8B4 melt, it is not possible to calculate C_{pg}, C_{pl}, C_p^{conf}, T_f', B_e and S_{conf}.

***Table 25**: Maier-Kelley fit parameters for P_2O_5-, B_2O_3 and F^--bearing melts*

	a	Δ a	b	Δ b	c	Δ c
sample	J g^{-1} K^{-1}	J g^{-1} K^{-1}	10^{-4} J g^{-1} K^{-2}	10^{-4} J g^{-1} K^{-2}	10^{4} J g^{-1} K	10^{4} J g^{-1} K
NCAS13-P2B4	1.08	0.00	1.73	0.02	-3.47	0.02
NCAS13-P2B8	1.02	0.00	2.47	0.02	-2.95	0.02
NCAS13-P6F3	0.97	0.00	3.31	0.02	-2.62	0.02
NCAS13-P6F6	1.04	0.00	1.89	0.03	-3.30	0.03
NCAS13-P8B4	1.02	0.00	2.62	0.00	-3.20	0.01
NCAS13-P8B4F3	1.22	0.00	0.18	0.04	-5.02	0.04
NCAS13-P8B4F6	0.96	0.00	3.70	0.04	-2.31	0.03
NCAS13-P8B8	1.00	0.00	3.06	0.00	-2.97	0.02
NCAS10-P6B4	1.07	0.00	2.02	0.02	-3.53	0.02
NCAS10-P6B8	0.98	0.00	3.02	0.02	-2.75	0.02
CHAMP-P8B8	0.86	0.00	3.85	0.02	1.68	0.02

***Table 26**: Parameters of Adam-Gibbs equation together with T_f' of P_2O_5-, B_2O_3- and F^--bearing melts*

	A_e	B_e	Δ B_e	S_{conf}	Δ S_{conf}	C_{pg}	C_{pl}	C_p^{conf}	Δ C_p^{conf}	T_f'
sample		kJ mol^{-1}	kJ mol^{-1}	J mol^{-1} K^{-1}	J mol^{-1} K^{-1}	J mol^{-1} K^{-1}	J mol^{-1} K^{-1}	J mol^{-1} K^{-1}	J mol^{-1} K^{-1}	K
NCAS13-P2B4	-4.55	310.33	53.03	8.53	1.50	79.59	89.30	9.71	1.20	978.7
NCAS13-P2B8	-4.55	383.36	52.67	11.13	1.57	80.54	88.99	8.44	1.20	901.2
NCAS13-P6F3	-4.55	526.08	74.45	15.22	2.24	89.92	96.10	6.18	1.32	1000.4
NCAS13-P6F6	-4.55	576.55	117.82	17.99	3.79	79.55	86.24	6.69	1.17	905.2
NCAS13-P8B4	-4.55	381.26	84.35	17.80	5.71	78.77	86.22	7.44	1.17	970.7
NCAS13-P8B4F3	-4.55	381.26	84.35	11.55	2.64	83.75	90.79	7.04	1.24	954.2
NCAS13-P8B4F6	-4.55	284.17	70.91	9.00	2.31	91.42	97.04	5.63	1.33	604.7
NCAS13-P8B8	-4.55	284.17	70.91	10.84	0.90	79.13	87.16	8.04	1.18	914.4
NCAS10-P6B4	-4.55	457.79	62.37	12.56	1.76	80.82	91.09	10.26	1.22	982.7
NCAS10-P6B8	-4.55	543.89	73.70	15.60	2.16	81.72	92.01	10.29	1.23	922.7
CHAMP-P8B8	-4.55	407.51	24.20	9.00	2.31	84.34	93.32	8.99	1.26	890.9

Error of the fictive Temperature T_f' is 3 K

Error of C_{pg} and C_{pl} is < 1%

Fig. 51 illustrates the configurational heat capacity of the melts containing P_2O_5 and B_2O_3 as a function of B_2O_3 concentration. C_p^{conf} is defined as the required energy to move the structure from the glassy to the liquid state.

The peraluminous NCAS10-P6 melts exhibit the highest configurational heat capacities whereas the lowest heat capacities are observed for peralkaline NCAS13-P8 melts. No significant changes in C_p^{conf} are observed with increasing B_2O_3 concentration within the error bars.

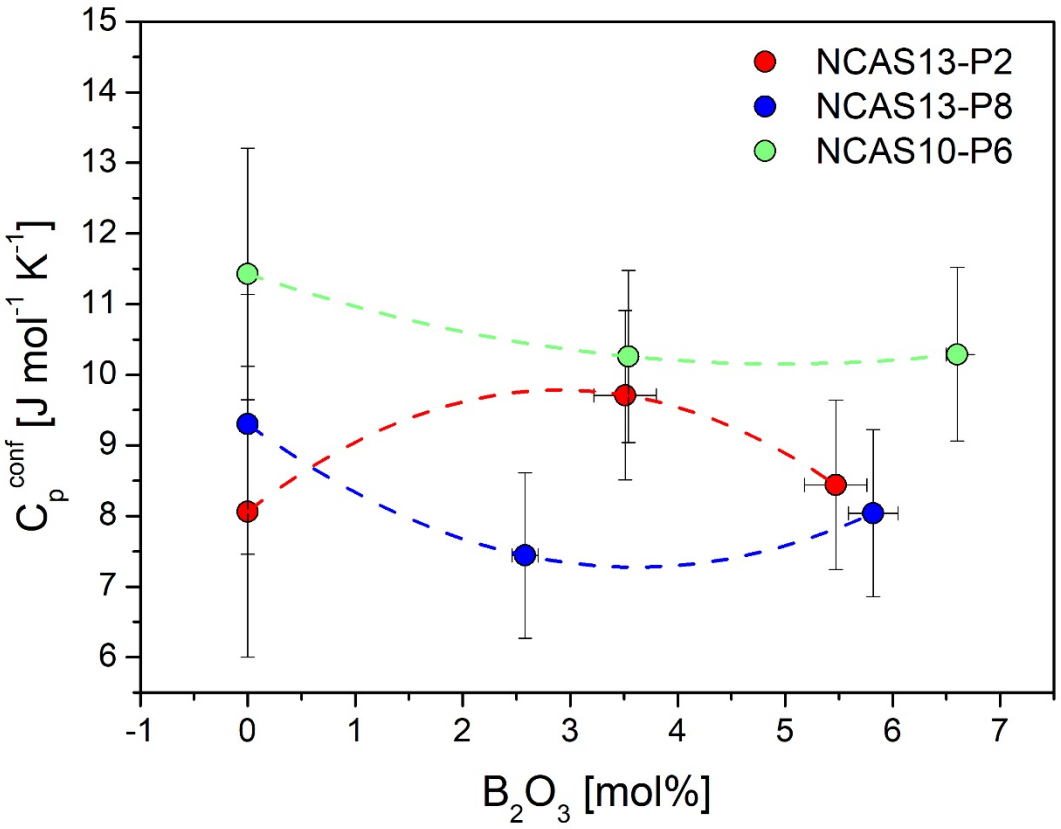

***Fig. 51**: C_p^{conf} as a function of B_2O_3 concentration for P_2O_5- and B_2O_3-bearing melts.*

The fictive temperature T_f' as a function of B_2O_3 concentration is demosntrated in Fig. 52. In all melts T_f' decreases with increasing B_2O_3 concentration. The highest T_f' are observed in the peraluminous NCAS10-P6 melt, whereas the the peralkaline NCAS13-P8 melt exhibits the lowest T_f' values. For the melts containing high P_2O_5 concentrations such as the peralkaline NCAS13-P8 and peraluminous NCAS10-P6 T_f' decreases almost linearily. In case of sample NCAS10-P6 T_f' decreases from 1054 K to 923 K with the addition of up to 6.6 mol% B_2O_3 and in case of NCAS13-P8 melt from 1000 K to 914 K up to a B_2O_3 concentration of 5.82 mol%. In NCAS13-P2 melt T_f' decreases more strongly from 1008 K to 901 K with the addition of up to 5.47 mol% B_2O_3.

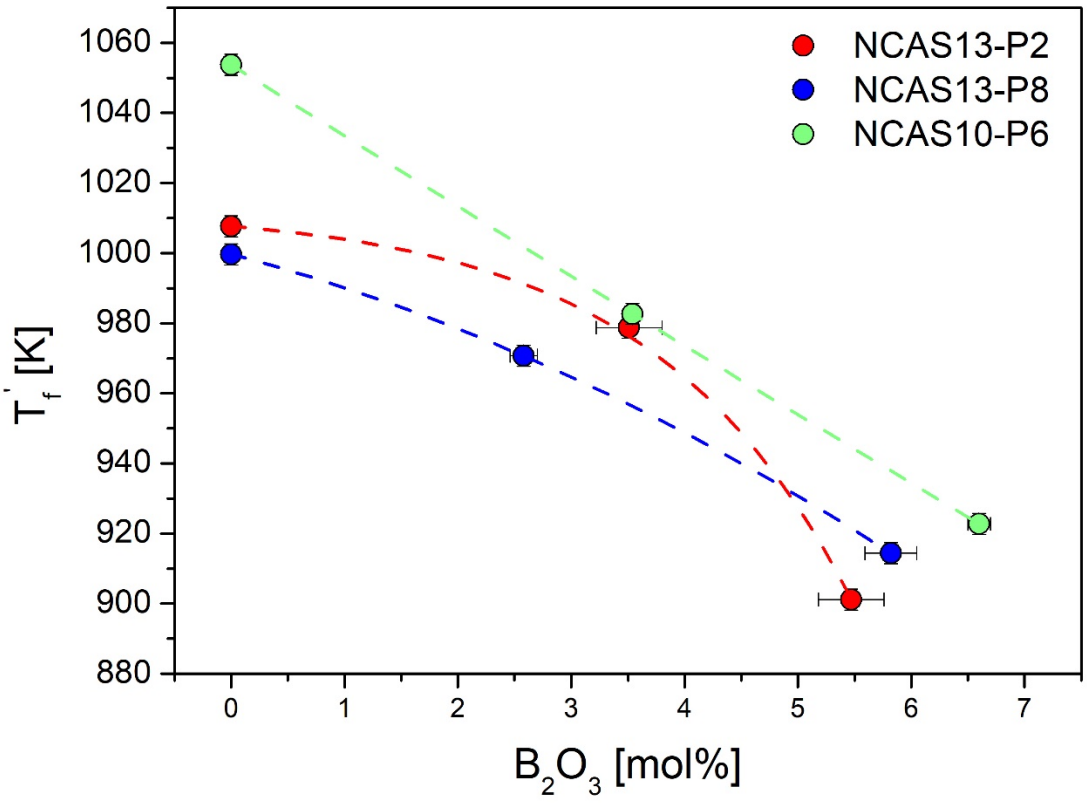

***Fig. 52**: Fictive temperatures T_f' of melts containing both P_2O_5 and B_2O_3.*

The configurational entropy S_{conf} is a measure for the degree of disorder in the melt and is illustrated in Fig. 53 for melts containing both P_2O_5 and B_2O_3. NCAS13-P8 melts exhibits the highest S_{conf}. The lowest S_{conf} are observed in NNCAS13-P2 melt. In both peralkaline melts S_{conf} decreases with increasing B_2O_3 concentration in the melt. In NCAS13-P8 melt S_{conf} decreases from 15,88 J mol^{-1} K^{-1} to 10,84 J mol^{-1} K^{-1}.

In case of NCAS13-P2 melt S_{conf} decreases from 10.66 J mol^{-1} K^{-1} to 8.53 J mol^{-1} K^{-1} with the addition of 3.51 mol% B_2O_3 and increases at higher B_2O_3 concentration to 11.13 J mol^{-1} K^{-1} with the addition of 5.47 mol% B_2O_3. In case of the peraluminous NCAS10-P6 melt an almost linear increase in S_{conf} is observed from 9.77 J mol^{-1} K^{-1} to 15.6 J mol^{-1} K^{-1}.

The B_e term of the melts is shown in Fig. 54 as a function of B_2O_3 concentration in the melt. The highest B_e in the B_2O_3-free melts are observed in the peralkaline NCAS13-P8 melt, the lowest B_e are found in the peralkaline NCAS13-P2 melt. At B_2O_3 concentrations > 3 mol% the highest B_e are found in the peraluminous NCAS10-P6 melt. In this melt, B_e increases with increasing B_2O_3 concentration from to 389.93 kJ mol^{-1} to 543.89 kJ mol^{-1} almost linearily.

In the peralkaline melts, B_e decreases with increasing B_2O_3 concentration. The decrease in B_e is stronger in the NCAS13-P8 melt containing higher P_2O_3 concentrations, where B_e decreases from 596.14 kJ mol^{-1} to 284.17 kJ mol^{-1}. In case of NCAS13-P2 melt, B_e decreases from 408.69 kJ mol^{-1} to 310.33 kJ mol^{-1} up to a B_2O_3 concentration of ~3.51 mol% and increases slightly at higher B_2O_3 concentrations to 383.36 kJ mol^{-1}.

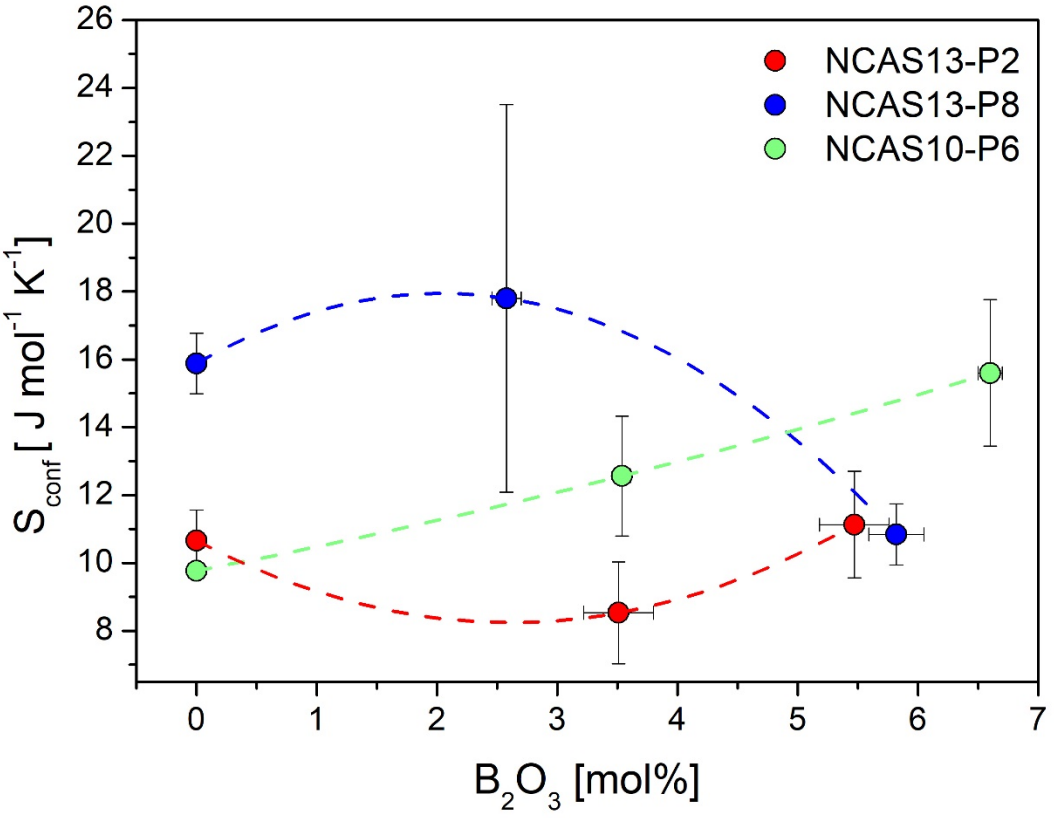

***Fig. 53**: S_{conf} as a function of B_2O_3 concentration of melts containing P_2O_5 as well as B_2O_3.*

The B_e/S_{conf} of the P_2O_5 and B_2O_3-bearing melts is illustrated in Fig. 55 for the peralkaline NCAS13-P2 and NCAS13-P8 as well as the peraluminous NCAS10-P6 melt. B_e/S_{conf} decreases almost linearily in case of sample NCAS13-P2 and NCAS10. The strongest decrease is observed in the peralkaline NCAS13-P8 melt. B_e/S_{conf} decreases up to a B_2O_3 concentration of approximately 2.6 mol% B_2O_3 and increases with further increasing B_2O_3 concentration.

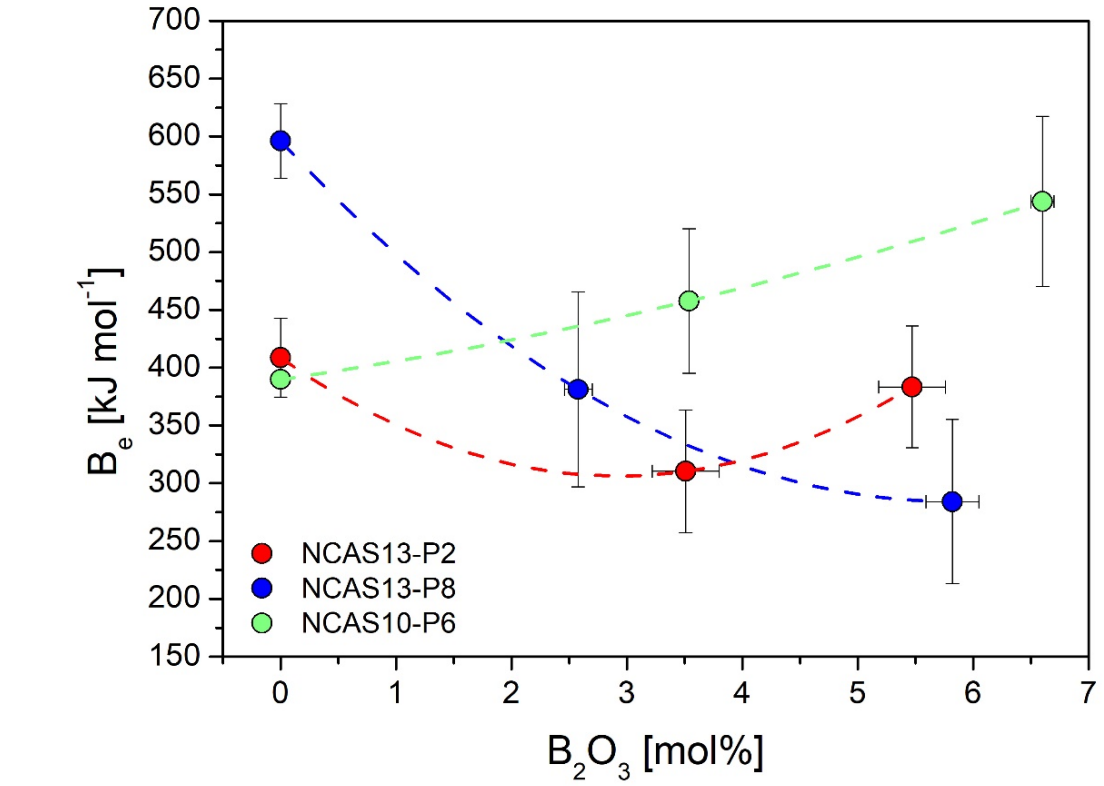

***Fig. 54**: B_e as a function of B_2O_3 concentration for B_2O_3- and P_2O_5-bearing melts.*

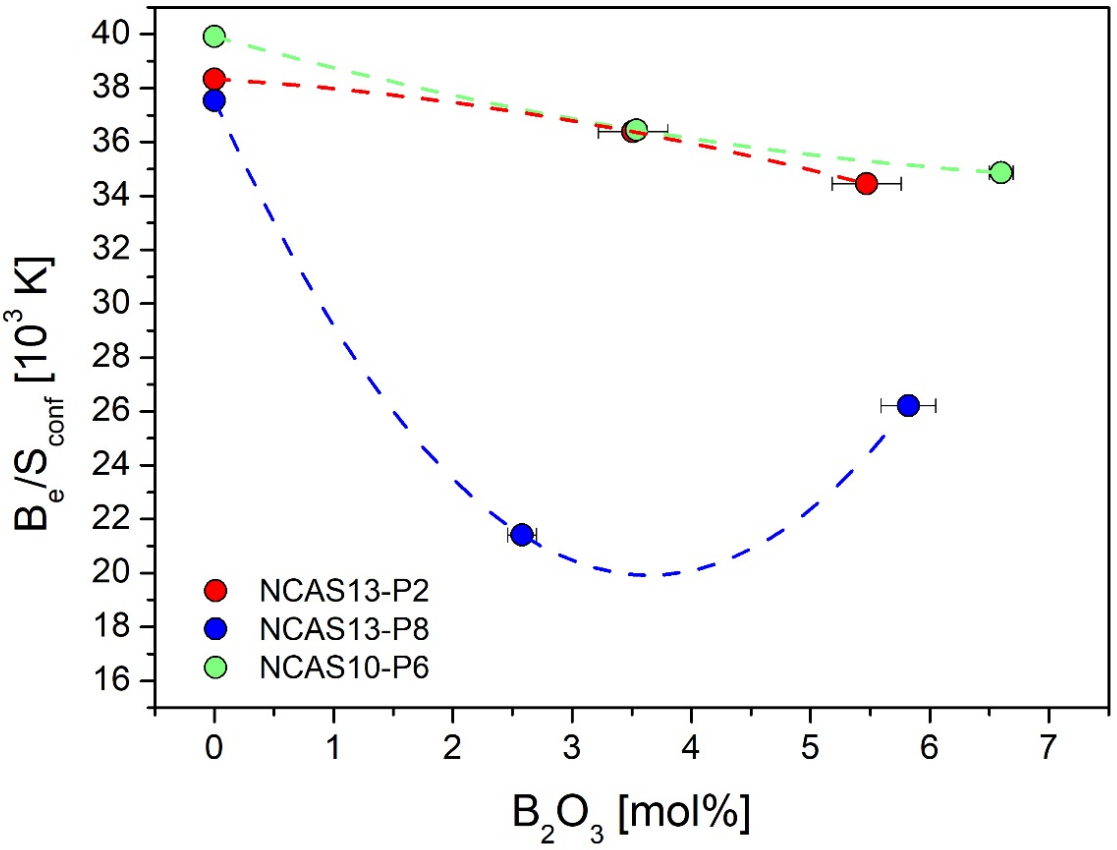

***Fig. 55**: B_e/S_{conf} as a function of B_2O_3 concentration of melts containing both B_2O_3 and P_2O_5.*

B_e as a function of S_{conf} of the P_2O_5- and B_2O_3-bearing peralkaline NCAS13-P2 and NCAS13-P8 as well as peraluminous NCAS10-P6 melt is illsutrated in Fig. 56. A linear trend between B_e and S_{conf} is observed for all melts, which is expected since B_e and S_{conf} are highly correlated parameters in the Adam-Gibbs-Equation. The melt of NCA13-P8 which exhibits much higher S_{conf} of approximately 18 J mol^{-1} K^{-1} exhibits a high error and therefore still fits the oberved linear trend.

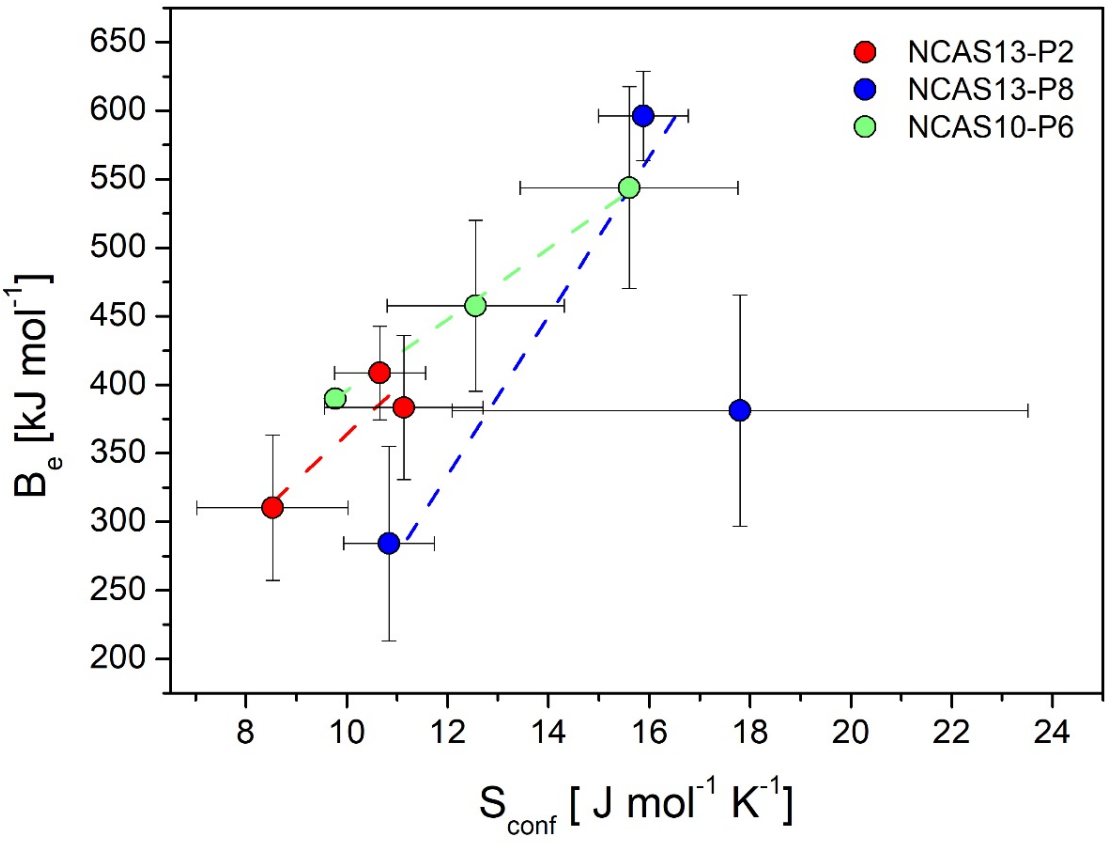

***Fig. 56**: B_e as a function of S_{conf} for melts containing P_2O_5 as well as B_2O_3.*

The configurational heat capcities of the flourine-bearing melts as a function of fluorine content are illustrated in Fig. 57 for the previously unmixed NCAS13-P6 as well as NCAS13-P8B4 melt. NCAS13-P6 melt exhibits higher C_p^{conf} than the NCAS13-P8B4 melt. No significant change in C_p^{conf} is apparent with the addition of fluorine to both melts within the error range, though a decrease in C_p^{conf} with increasing F^- content is expected.

Fig. 58 illustrates the fictive temperatures T_f' of the melts as a fuction of fluorine concentration. The NCAS13-P6 melt exhibits the highest fictive temperatures. Similar to what was observed in viscosity data, T_f' decreases in both melts with increasing fluorine concentration in the melt.

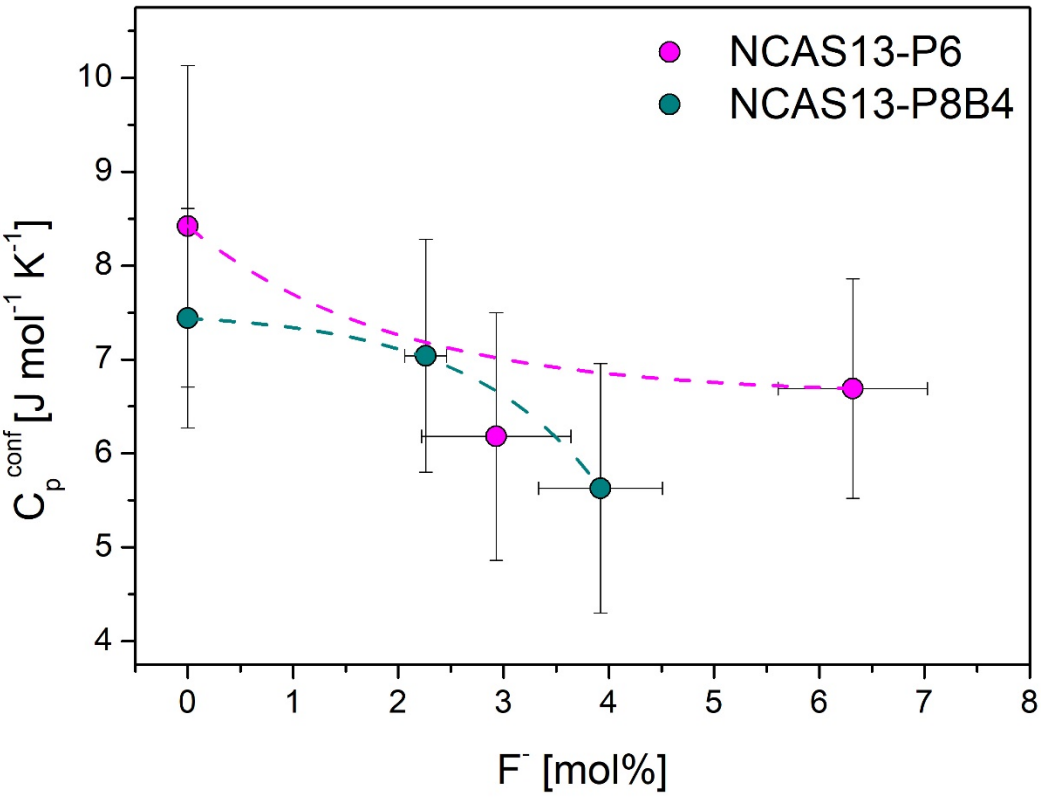

***Fig. 57**: Configurational heat capacity C_p^{conf} as a function of fluorine content in the melt.*

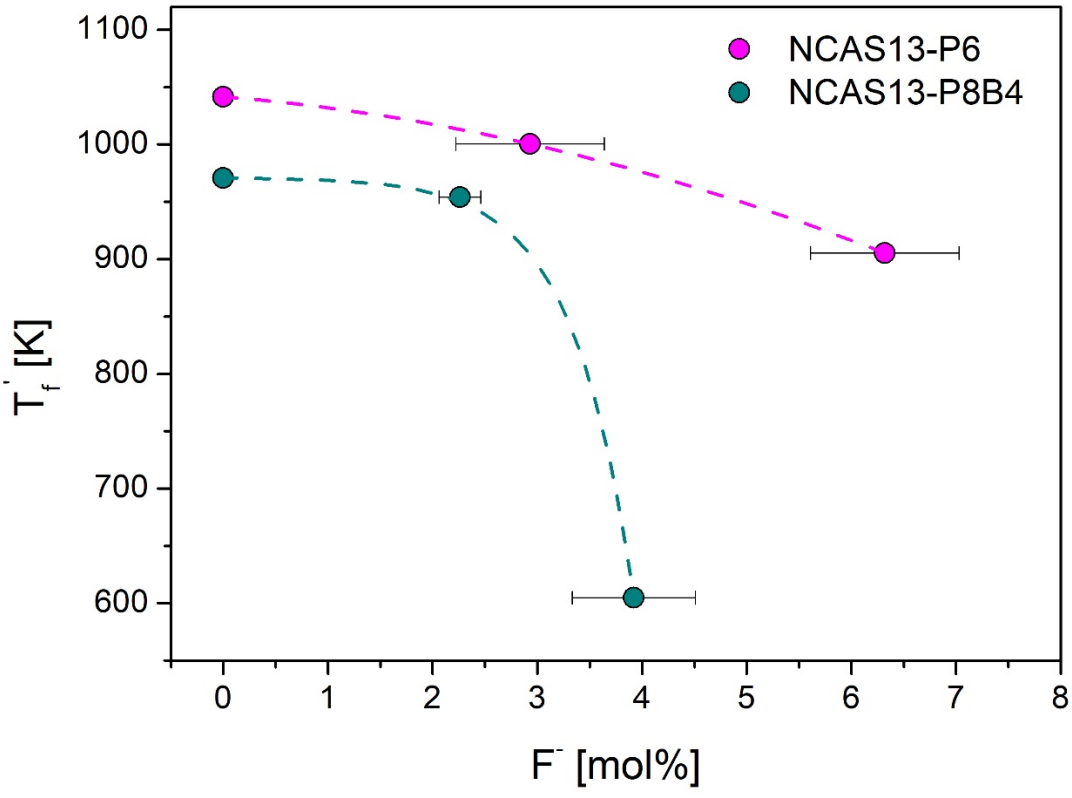

***Fig. 58**: Fictive temperature T_f' as a function of fluorine content in the melt.*

In the only P_2O_5-bearing NCAS13-P6 melt T_f' decreases almost linearily from to 1042 K to 905 K with increasing F^-- concentration in the melt.

In case of the P_2O_5- and B_2O_3-bearing NCAS13-P8B4 melt T_f' decreases only slightly from 971 K to 954 K with the addition of 2.26 mol% F^- and then decreases strongly from 954 K to 605 K with the adition of up to 3.92 mol% F^-.

The configurational entropies S_{conf} as a function of fluorine content of the NCAS13-P6 and NCAS13-P8B4 melts are shown in Fig. 59. With increasing fluorine concentration in the melt an increase in S_{conf} is observed for the only P_2O_5-bearing NCAS13-P6 melt from 1167 J mol^{-1} K^{-1} to17.99 J mol^{-1} K^{-1}. In case of the P_2O_5- and B_2O_3-bearing NCAS13-P8B4 melt a decrease of S_{conf} from 17.80 J mol^{-1} K^{-1} to 9.00 J mol^{-1} K^{-1} is observed with increasing fluorine concentration in the melt.

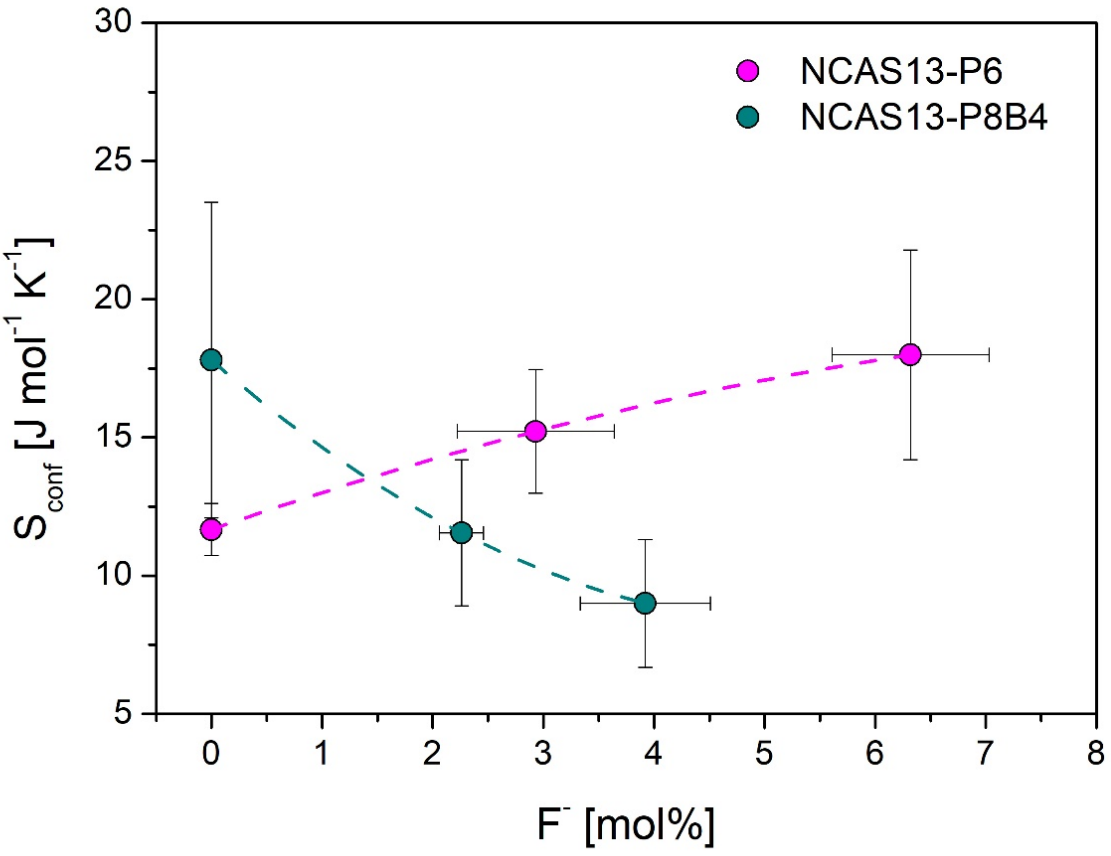

***Fig. 59**: Configurational entropy S_{conf} as a function of fluorine concentration.*

The B_e term as a function of fluorine concentration is illustrated in Fig. 60 for the NCAS13-P6 and NCAS13-P8B4 melt. NCAS13-P6 melt exhibits the higher B_e values. No significant changes in B_e are observed for both melts within the error range.

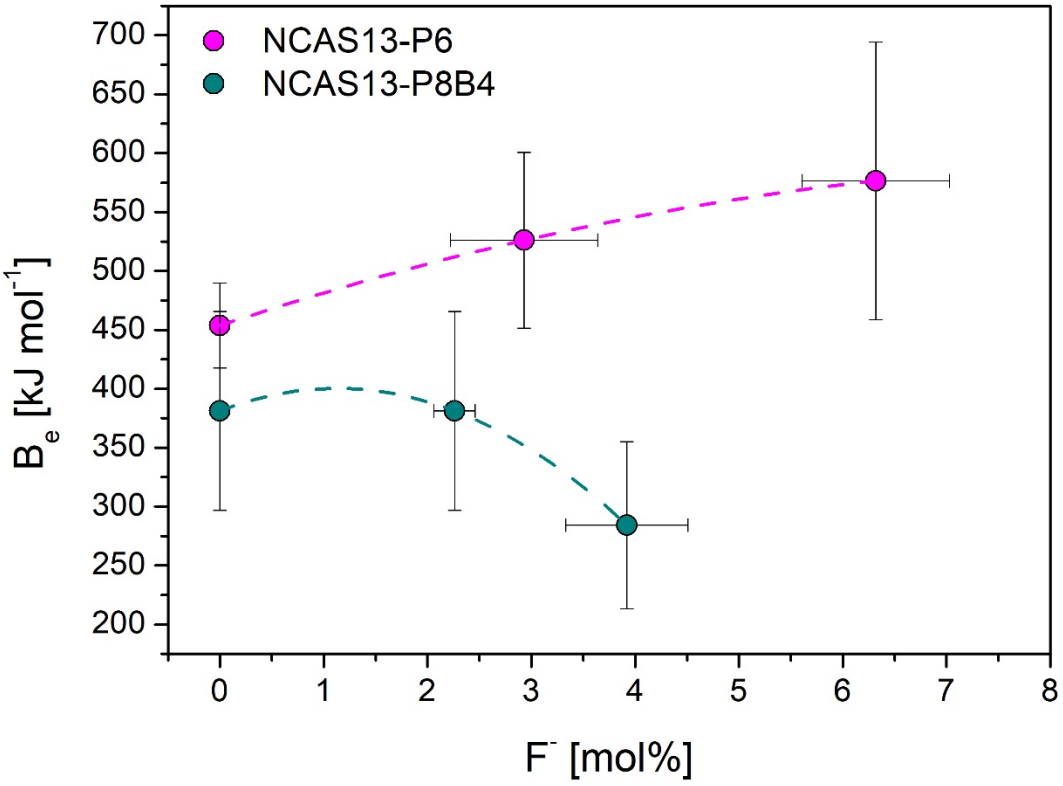

***Fig. 60**: Activation energy for viscous flow (B_e) as a function of fluorine content.*

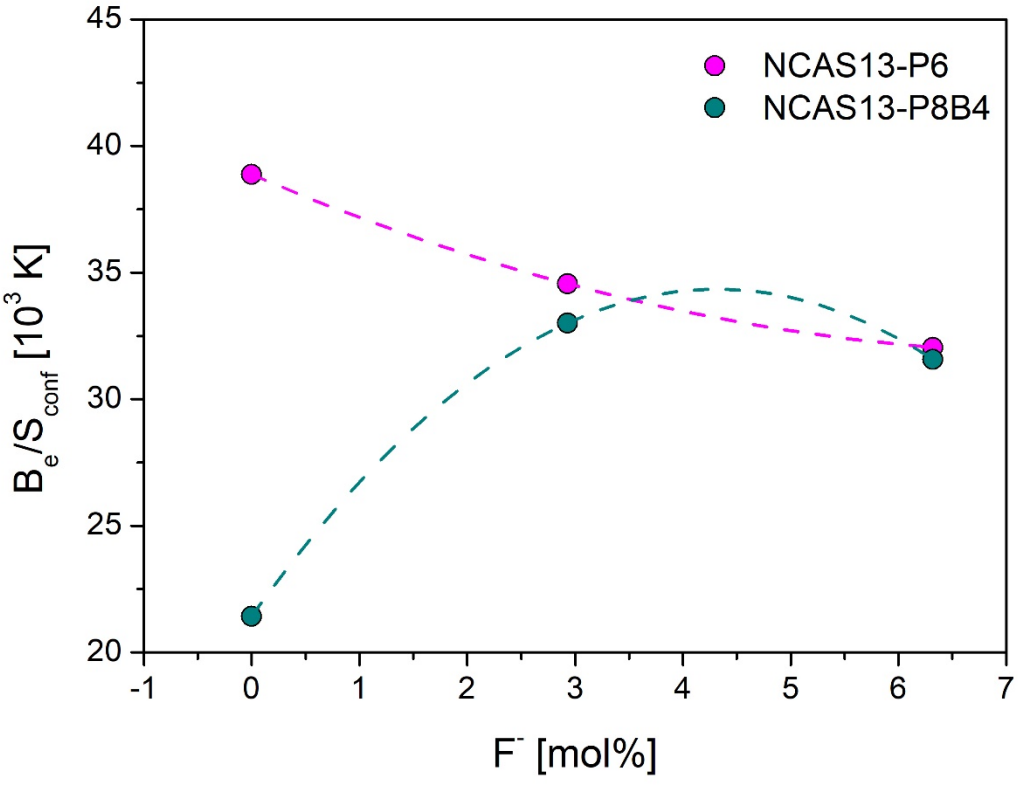

***Fig. 61**: B_e/S_{conf} as a function of fluorine concentration.*

The B_e/S_{conf} term for both melts is illustrated in Fig. 61 as a function of fluorine content. B_e/S_{conf} decreases with increasing fluorine content in the melt for NCAS13-P6 melt. In case of NCAS13-P8B4 melt B_e/S_{conf} increases with increasing fluorine concentration.

B_e as a function of S_{conf} for both fluorine-bearing melts is given in Fig. 62. The samples show a linear trend for both melts, which is expected since B_e and S_{conf} are strongly correlated parameters in the Adam-Gibbs equation.

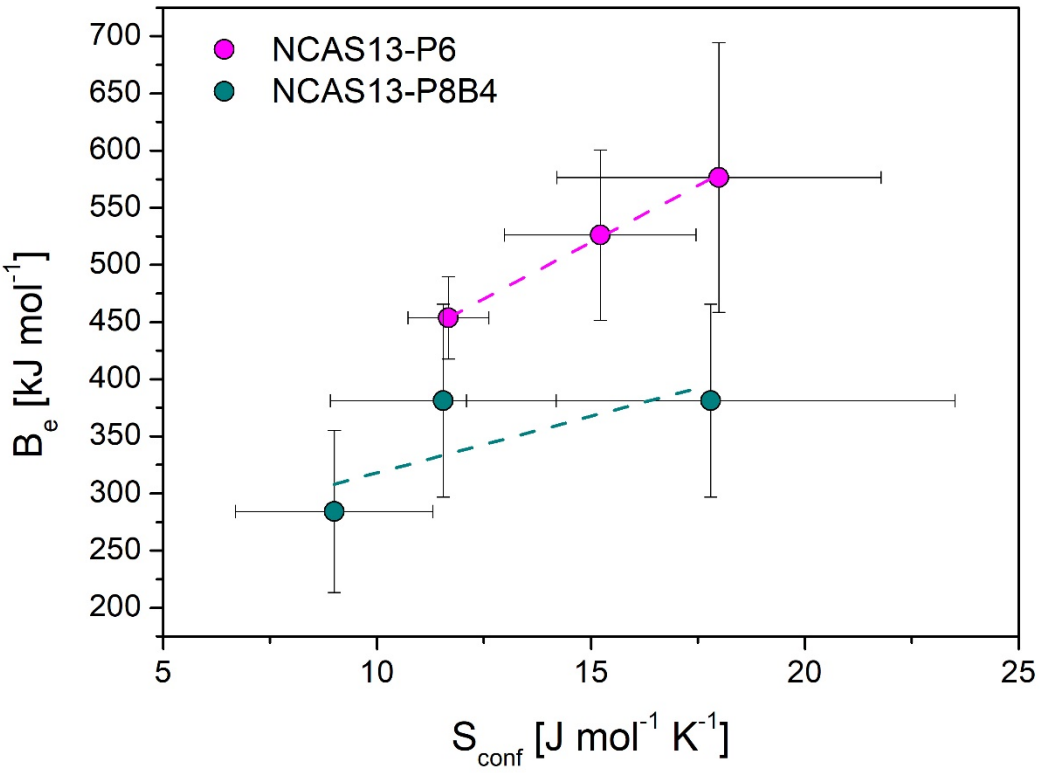

***Fig. 62**: Be as a function of S_{conf} for fluorine-bearing melts.*

5.4.3 Raman Spectroscopy

The baseline-corrected spectra of the P_2O_5- and B_2O_3-bearing peralkaline NCAS13-P2, NCAS13-P8, CHAMP-P8 and peraluminous NCAS10-P6 melt are presented in Fig. 63. For better comparison the spectra were normalized to the intensity of the peak around 490 cm^{-1} for each melt composition. In all melts vibrations are observed mainly in two vibrational regions, that being the low frequency region around 500 cm^{-1} and the high frequency region around 1000 cm^{-1}.

The only P_2O_5-bearing NCAS13-P2 melt shows a vibrational band around 490 cm^{-1} accompanied by a shoulder at ~580 cm^{-1}. The peak in the high frequency region appears at ~1055 cm^{-1}. At ~965 cm^{-1} another peak of high intensity emerges from the peak at 1055 cm^{-1}. The addition of 3.51 mol% B_2O_3 to the melt does not result in significant changes

in the low frequency region. Only a decrease in intensity of the shoulder at approximately 580 cm^{-1}. Further increasing B_2O_3 concentration does not cause any changes in the low frequency region. In the high frequency region, an asymmetric broadening of the peak to higher wavenumbers is observed. Furthermore, the high intensity peak at ~965 cm^{-1} disappears and is replaced by a shoulder at ~995 cm^{-1}. At further increasing B_2O_3 concentrations up to 5.60 mol% a slight decrease in intensity of the high frequency peak with respect to the low frequency peak is observed.

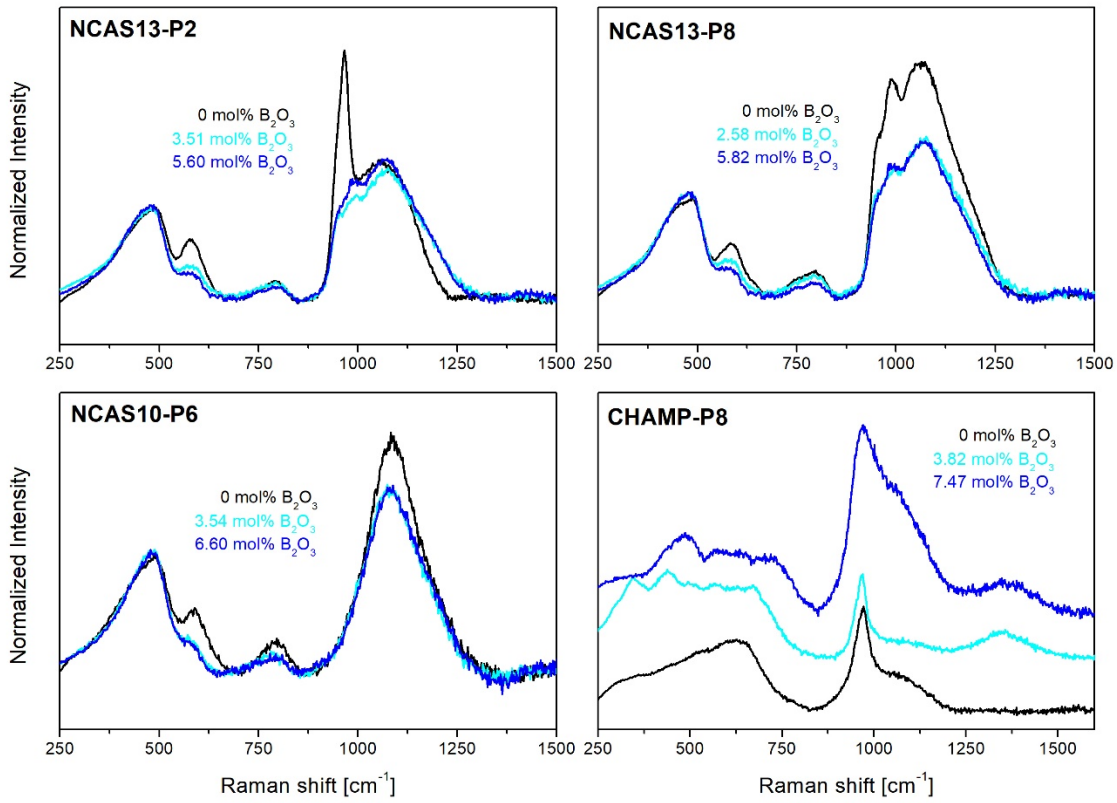

***Fig. 63**: Long- and baseline-corrected Raman spectra of P_2O_5- and B_2O_3-bearing melts. Spectra were normalized to 550 cm^{-1} peak.*

The B_2O_3-free NCAS13-P8 melt also exhibits a peak in the low frequency region at ~490 cm^{-1} with a shoulder at ~580 cm^{-1} as well as a peak in the high frequency region at ~1060 cm^{-1} with a shoulder at 985 cm^{-1}. The addition of 2.58 mol% B_2O_3 results in a decrease in intensity of the shoulder at 580 cm^{-1} as well as a decrease of the high frequency band with respect to the low frequency band. Further increase of B_2O_3 concentration does not cause any changes in the high frequency region. Solely a slight decrease of the intensity of the peak at 580 cm^{-1} can be observed.

The B_2O_3-free CHAMP-P8 melt exhibits a broad and asymmetric peak in the low frequency region at 630 cm^{-1} and a peak in the high frequency region at ~1030 cm^{-1}. A huge peak of high intensity emerges from the 1035 cm^{-1} peak at 965 cm^{-1}. The addition of 3.82 mol%

B_2O_3 to the melt results in an increase of the intensity of the low frequency peak relatively to the high frequency peak at 1035 cm^{-1}. Additionally, a new peak appears at ~1350 cm^{-1}. With further increasing B_2O_3 concentration up to 7.47 mol% B_2O_3, the intensity of the high frequency band increases with respect to the low frequency band. Furthermore, the intensity of the strong peak at 965 cm^{-1} decreases compared to the 1035 cm^{-1} peak.

The Raman spectra of the peraluminous B_2O_3-free NCAS10-P6 melt shows two prominent peaks, one in the low frequency region at ~490 cm^{-1} with a shoulder at ~585 cm^{-1} and a high frequency peak at ~1090 cm^{-1}. With the addition of 3.54 mol% B_2O_3 the intensity of the peak at 1090 cm^{-1} as well as 585 cm^{-1} decreases with respect to the 490 cm^{-1} peak. Further increase of B_2O_3 concentration to 6.60 mol% does not cause any changes in the Raman spectra of the melt.

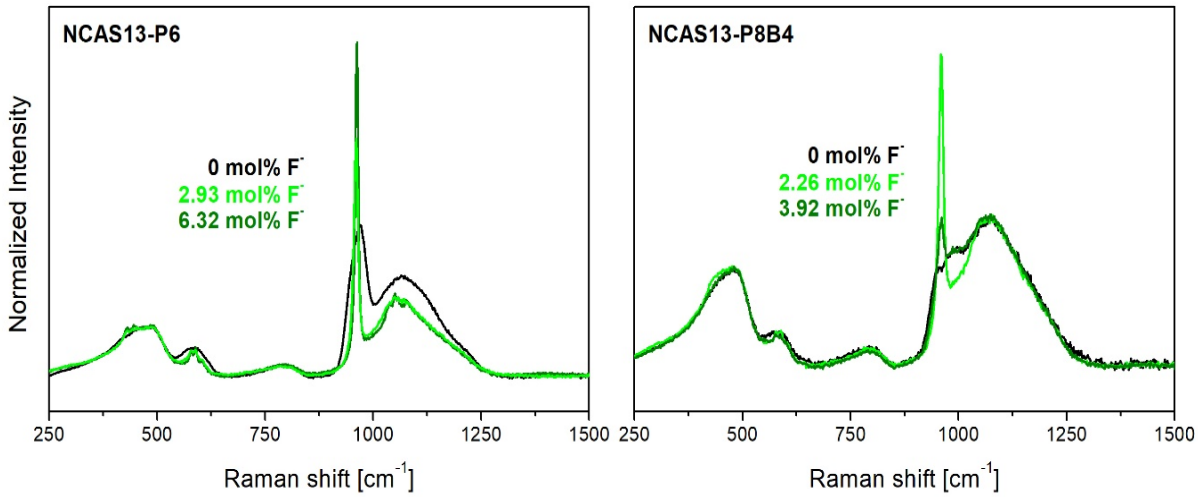

***Fig. 64**: Long- and baseline-corrected Raman spectra of fluorine-bearing melts. Spectra were normalized to 550 cm^{-1} peak.*

The Raman spectra of the fluorine-bearing NCAS13-P6 and NCAS13-P8B4 melt are illustrated in Fig. 64. The NCAS13-P6 melt exhibits two main vibrational bands, one in the low frequency region at ~470 cm^{-1} with a prominent shoulder at ~585 cm^{-1} and one in the high frequency region at ~1070 cm^{-1}. Furthermore, a sharp peak at ~965 cm^{-1} emerges from the high frequency peak. The addition of fluorine to the melt does not result in any significant changes in the low frequency region. In the high frequency region, the addition of 2.93 mol% F^- leads to a decrease in intensity of the 1070 cm^{-1} band with respect to the low frequency band. Moreover, a sharpening and further increase of intensity of the 965 cm^{-1} band is observed in comparison to the 1070 cm^{-1}. Further addition of up to 6.32 mol% fluorine to the melt solely results in a further increase of intensity of the 955 cm^{-1} band.

The fluorine-free NCAS13-P8B4 melt, shows a vibrational band at ~480 cm^{-1} accompanied by a shoulder at approximately 585 cm^{-1} in the low frequency range and band at ~1070 cm^{-1}, accompanied by a shoulder at ~985 cm^{-1}. The only changes caused by the addition of fluorine to the melt occur in the 940 cm^{-1} – 990 cm^{-1} region. The addition of 2.26 mol% F^- to the melt results in the disappearance of the shoulder at 990 cm^{-1}.

This shoulder is replaced by the appearance of a sharp peak of high intensity, which emerges from the 1070 cm^{-1} peak at ~960 cm^{-1}. Increasing the concentration of fluorine up to 3.92 mol% results in a decrease of intensity of the 960 cm^{-1} band.

5.4.4 SEM

The backscattered electron images of the P_2O_5 and B_2O_3-bearing samples are shown in Fig. 65. The addition of B_2O_5 to the low P_2O_5-bearing NCAS13-P2 melt does not results in any obvious changes of the structure. The addition of 2.58 mol% B_2O_3 to the previously unmixed melt results in a mixing of the melt. There is no evidence for unmixed spheres as observed in the B_2O_3-free NCAS13-P8 melt. With increasing B_2O_3 concentration up to 5.82 mol%, small spheres of a light-grey colour and an average diameter of approximately 50 nm begin to form. The addition of 3.82 mol% B_2O_3 to the CHAMP-P8 melt results in a slight growth of the light-grey coloured spheres from an average 300 nm diameter up to 500 nm, indicating an ongoing melt separation. With further addition of up to 7.47 mol% B_2O_3 in the melt, the spheres slightly shrink in size to an average diameter of 100-300 nm.

The backscattered images of the fluorine- and water-bearing samples are shown in Fig. 68 for the melts containing 3 mol% water. All samples crystalized during the IHPV experiments. The crystals were measured with EDX and found to be of apatite composition. The apatite crystals are idiomorphic and surrounded by a Si- and Al-rich glass matrix. In case of CHAMP-P8 melt, crystals show a hexagonal shape, whereas crystals in NCAS13-P6 and NCAS13-P8B4 melts developed a long, prismatic shape.

The structure of the melts containing 6 mol% of water is shown in Fig. 69. As observed for the 3 mol% water-bearing samples, apatite crystallized in all melts. In case of CHAMP-P8F3 melt (Fig. 66) crystals are xenomorphic and the average crystal size is only ~1µm compared to the other melts. The apatite crystals in NCAS13-P6F3, NCAS13-P8B4F3 as well as NCAS13-P8B4F6 melt developed a long, prismatic shape whereas the apatite crystals in CHAMP-P8F6 and NCAS13-P6F6 melt exhibit a hexagonal shape. Both, the prismatic as well as the hexagonal apatite crystals are idiomorphic.

The addition of fluorine to CHAMP-P8 melt results in crystallisation of apatite, which is shown in EMPA mappings in Fig. 66 for CHAMP-P8F3 and Fig. 67 for CHAMP-P8F6 melt.

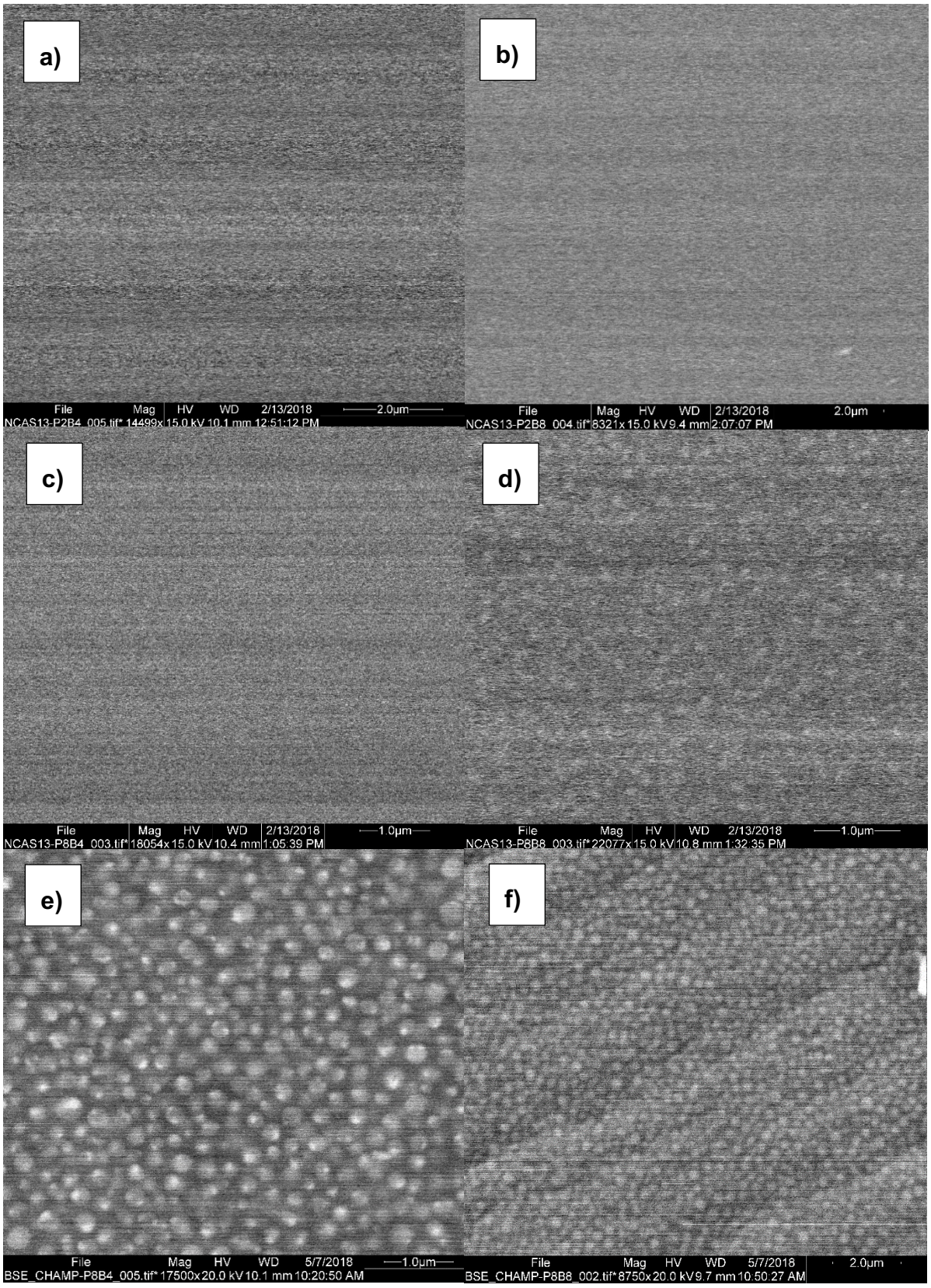

***Fig. 65**: BSE images of P_2O_5- and B_2O_3-bearing melts for a) NCAS13-P2B4, b) NCAS13-P2B8, c) NCAS13-P8B4, d) NCAS13-P8B8, e) CHAMP-P8B4, f) CHAMP-P8B8.*

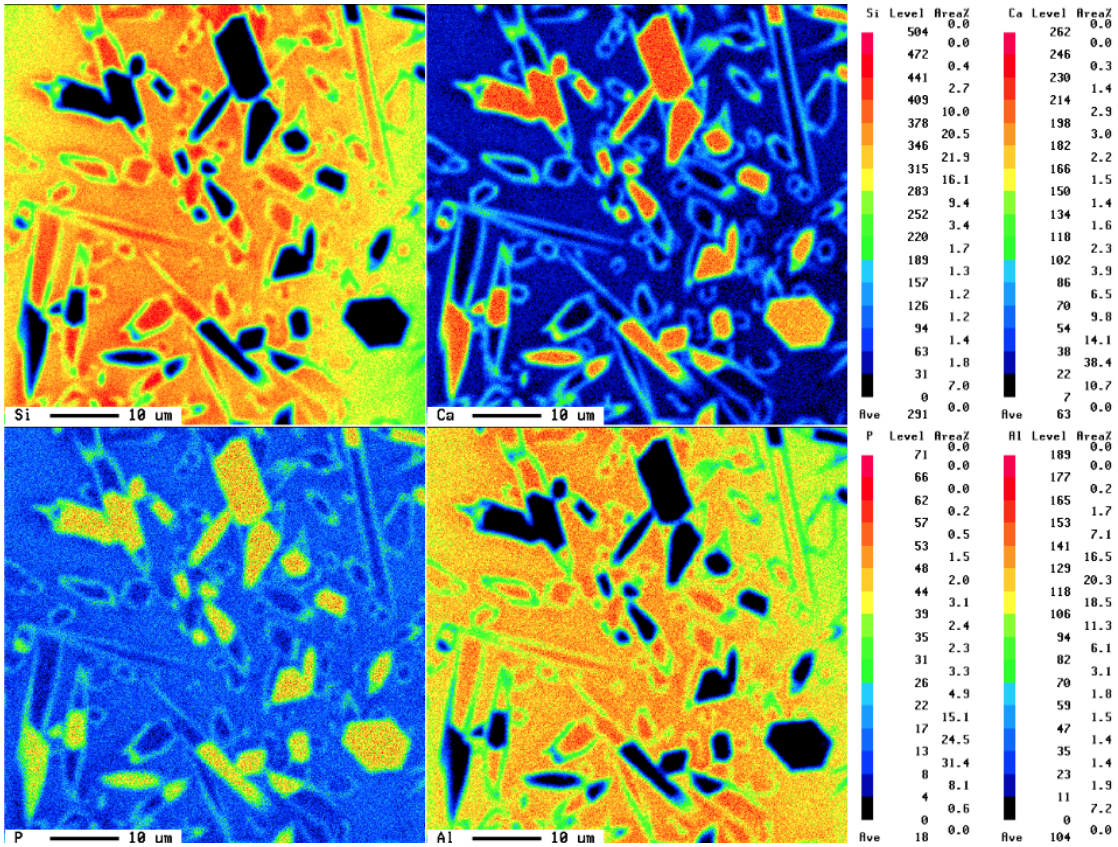

***Fig. 66**: Mappings obtained with EMPA for CHAMP-P8F3 showing apatite crystals in as Si- and Al-rich glass matrix.*

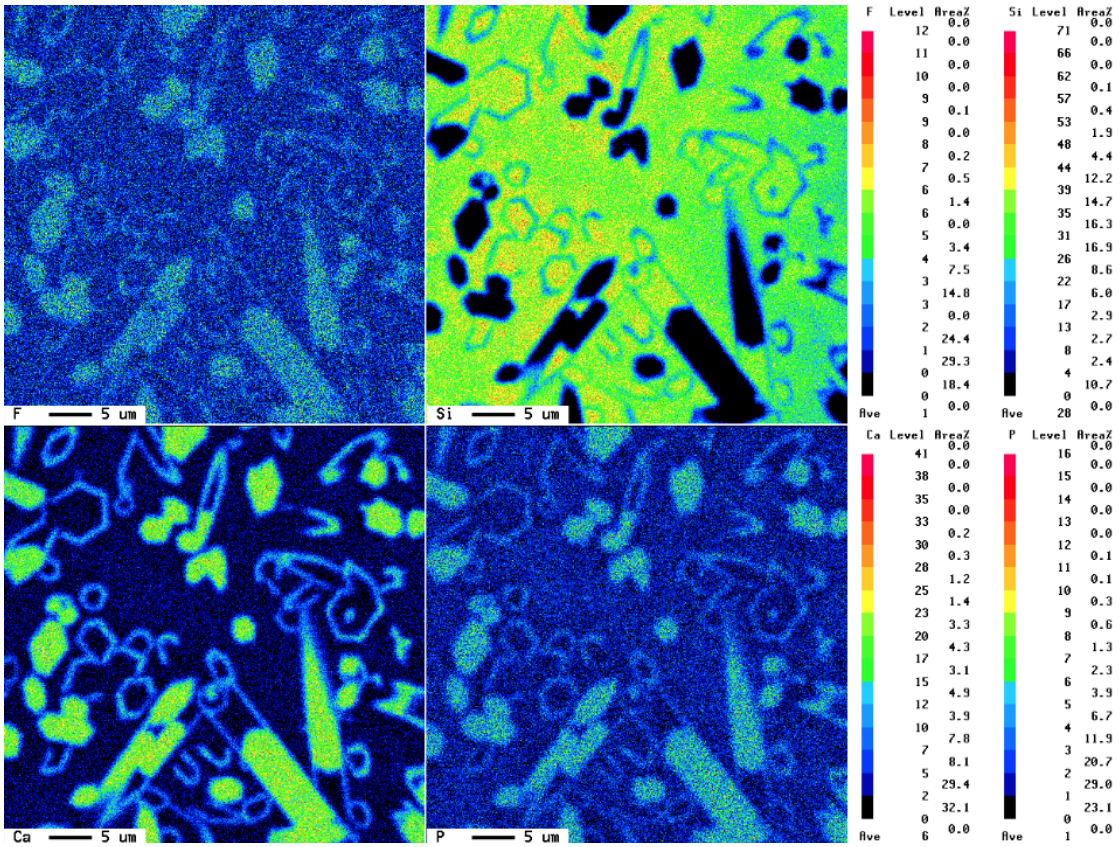

***Fig. 67**: Mappings obtained with EMPA for CHAMP-P8F6 showing apatite crystals in as Si- and Al-rich glass matrix.*

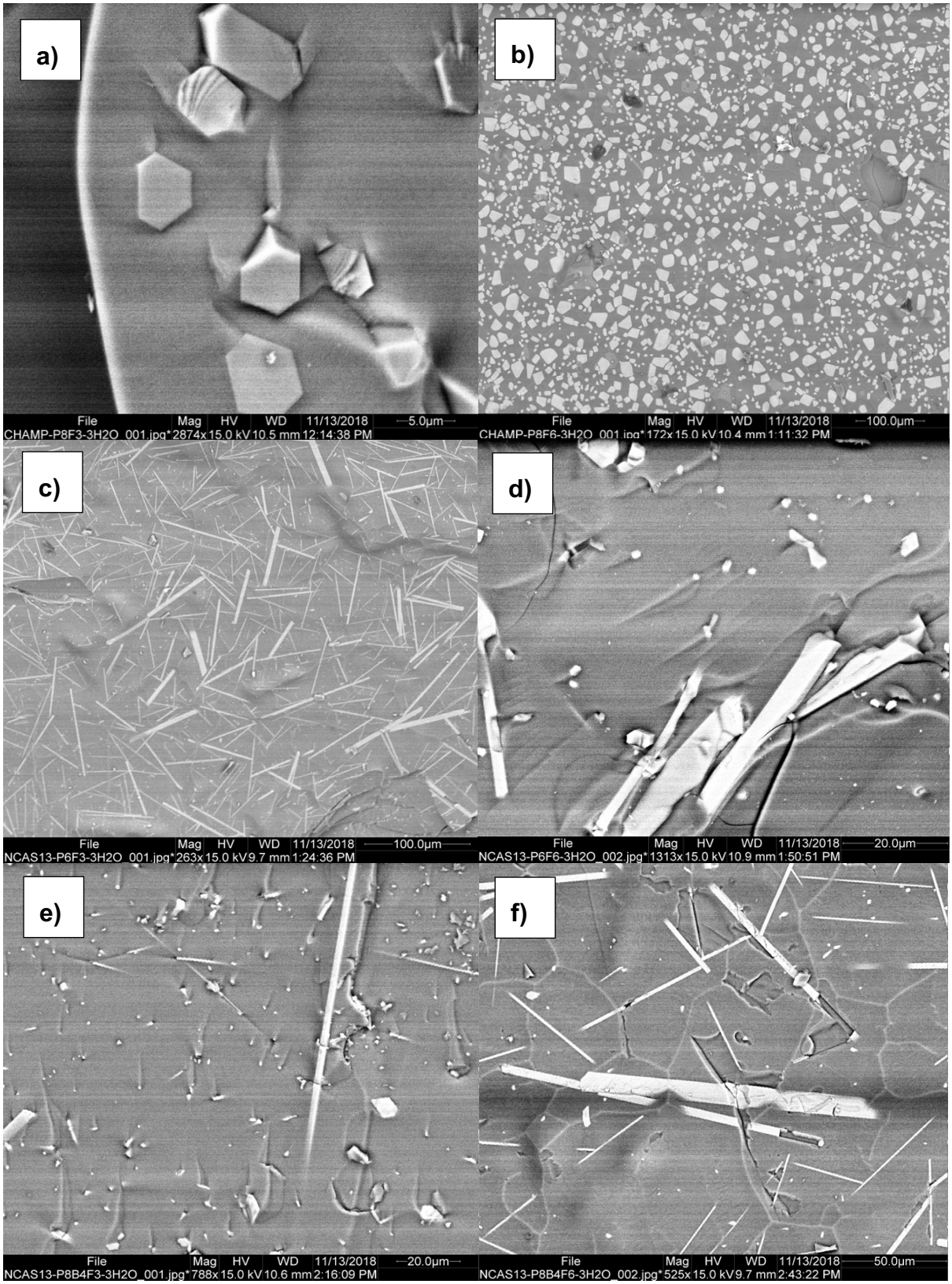

***Fig. 68**: BSE images of samples synthesized in IHPV containing 3 mol% H_2O for a) CHAMP-P8F3-3H2O, b) CHAMP-P8F6-3H2O, c) NCAS13-P6F3-3H2O, d) NCAS13-P6F6-3H2O, e) NCAS13-P8B4F3-3H2O and f) NCAS13-P8B4F6-3H2O. BSE images show apatite crystals in a Si- and Al-rich matrix.*

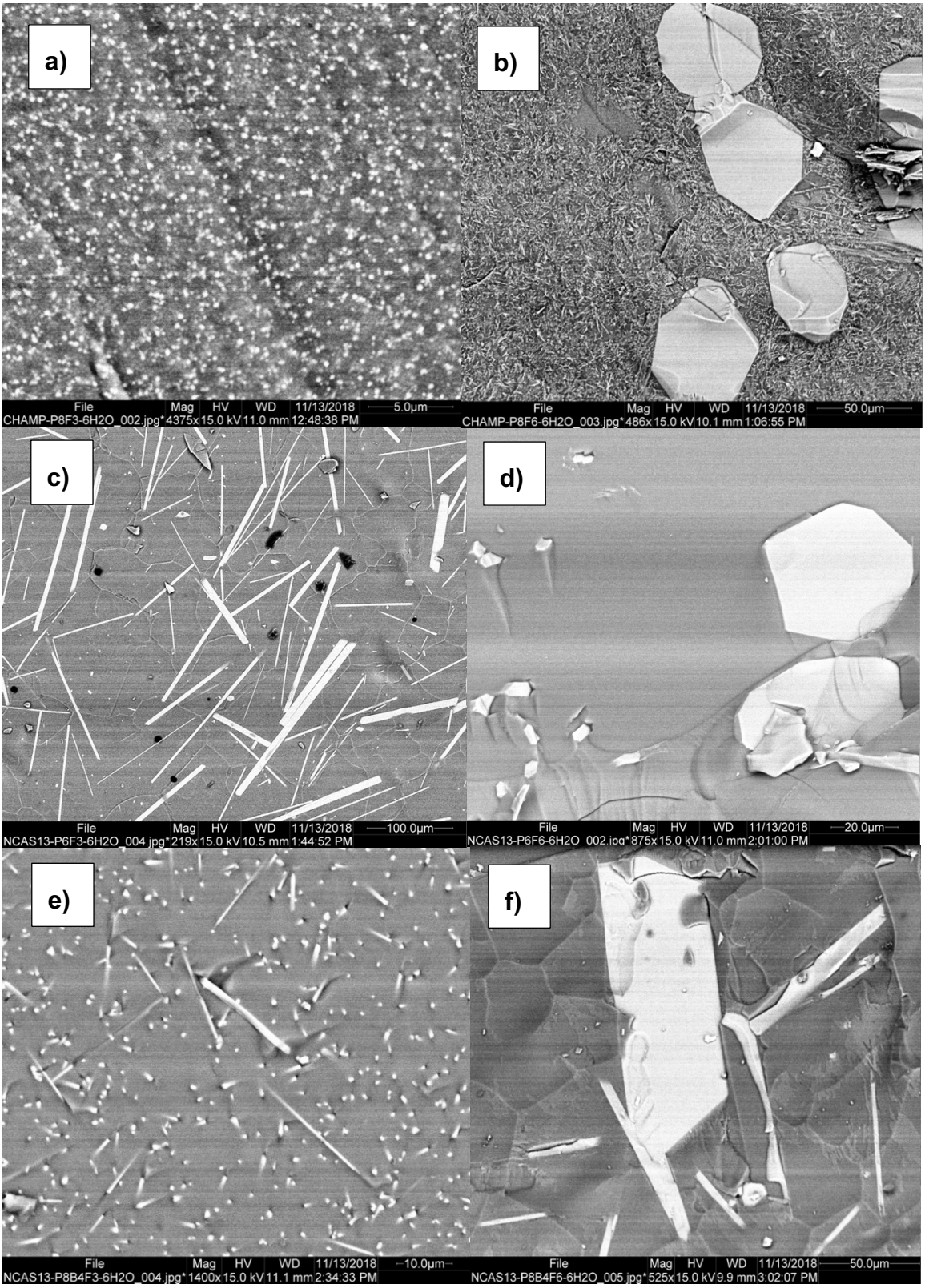

***Fig. 69**: BSE images of samples synthesized in IHPV containing 6 mol% H_2O for a) CHAMP-P8F3-6H2O, b) CHAMP-P8F6-6H2O, c) NCAS13-P6F3-6H2O, d) NCAS13-P6F6-6H2O, e) NCAS13-P8B4F3-6H2O and f) NCAS13-P8B4F6-6H2O. BSE images show apatite crystals in a Si- and Al-rich matrix.*

5.5 Discussion

5.5.1 The Combined Effect of P_2O_5, B_2O_3 and F^- on the Structure of Melts

The structure of silicate melts consists of several structural units of the aluminosilicate network which can be described by vibrational Raman bands. The melts exhibit a broad band in the low frequency area (300-600 cm^{-1}) as well as in the high frequency area (800-1300 cm^{-1}). The low frequency peak consist of various bending and stretching vibrations of the more polymerised structural units of the melt such as vibrations of silicon Q^4 species at ~500 cm^{-1}, Si-O-Si bending modes at 600 cm^{-1} Si-O^0 rocking motions at ~450 cm^{-1} and other delocalized vibrations of the polymerised aluminosilicate network (McMillan et al. 1982; Gan and Hess 1992b; McMillan et al. 1992; Mysen 1998b). The high frequency peak consists of several overlapping peaks of Si-O stretching vibrations, which are mainly silicon Q^1-species at 900 cm^{-1}, Q^2 at ~970 cm^{-1} and Q^3 at ~1090 - 1100 cm^{-1} (Mysen 1992; Gan and Hess 1992a).

Many authors suggested that P_2O_5 enters the melt network as PO_4^{3-} species (Gan and Hess 1992b; Mysen 1992, 1998b). This is confirmed in this study by the appearance of the PO_4^{3-} band around 950 cm^{-1} – 980 cm^{-1}, which is visible in form of a sharp peak in the spectra of peralkaline B_2O_3-free NCAS13-P2 and CHAMP-P8 melt and as a small shoulder for B_2O_3-free NCAS13-P8 melt. In peraluminous melts Gan and Hess (1992a) and Mysen (1998a) have shown that PO_4^{3-} bonds to tetrahedrally coordinated Al^{3+} from the aluminosilicate network, resulting in vibrations of structural units similar to $AlPO_4$ in berlinite which is found at ~1200 cm^{-1}.

The structure of borosilicate melts is well investigated due to their technical importance. In previous studies of boron in silicate melts it was found that B_2O_3 enters the melt network as BO_3 or BO_4^- (e.g. Konijnendijk 1975; Lenoir et al. 2008; Cochain et al. 2013). The vibrations of BO_3 rings are found at 610 cm^{-1} – 670 cm^{-1} and at ~1400 cm^{-1} for BO_3 with one NBO. Vibrations of the BO_4^- groups are found at ~770 cm^{-1} – 800 cm^{-1}. Furthermore, B_2O_3 may link to form chain-type metaborate units $(BO_2)^{1-}$ which show vibrations at ~660 cm^{-1} (Meera and Ramakrishna 1993; Bykov et al. 2011; Koroleva et al. 2011; Cochain et al. 2013). However, there is no evidence in the Raman spectra of the investigated melts in this study for the presence of these metaborate chains. The vibrational bands of BO_3 triangles and BO_4^- tetrahedra are overlapping with other vibrational bands from the aluminosilicate network.

The decrease of the high frequency band due to the addition of B_2O_3 to a P_2O_5-bearing melt, indicates a decreasing amount of Q^2 and Q^3 species and thus a depolymerisation of the

melt. Furthermore, B_2O_3 links to PO_4^{3-}, resulting in the formation of BPO_4 units which exhibit a vibrational band at ~1116 cm^{-1} (Money and Hariharan 2008). This is consistent with results from this study, where a decrease in intensity for the PO_4^{3-} band at ~950 cm^{-1} is observed together with a broadening of the high frequency band in NCAS13-P2 and CHAMP-P8 melt. It is suggested that this broadening occurs doe to the presence of BPO_4 units. The highest increase of intensity of the BPO_4 band is observed for CHAMP-P8 melt containing 7.47 mol% B_2O_3. No broadening of the high frequency peak is observed in NCAS13-P8 and NCAS10-P6 melt due to the overlap with silicon Q^2 bands.

The addition of fluorine to the melt is accompanied by the sharpening and increasing intensity of the band at ~950 cm^{-1}. This results are consistent with data from Mysen and Virgo (1985b) who describe a Si-F stretch band in fluorinated silicate complexes at approximately 935 cm^{-1}, which lies in the same region as that of PO_4^{3-} structural units. In aluminosilicate melts, F^- bonds additionally to Al, resulting in the formation of Al-F bonds (Mysen and Virgo 1985a). The study of Zeng and Stebbins (2000) demonstrates that F^- prefers the bonding to Al over Si. Therefore, it is suggested that the increasing peak intensity at ~930 - 950 cm^{-1} in our melts results from the formation of Al-F as well as some Si-F bonds.

5.5.2 The Combined Effect of P_2O_5 and B_2O_3 on the Viscosity of Melts

For better comparison of the effect on viscosity, T_g^{12} as a function of B_2O_3 concentration was plotted for the P_2O_5- and B_2O_3-bearing peralkaline (NCAS13-P2, NCAS13-P8, CHAMP-P8) and peraluminous (NCAS10-P6) melts and is illustrated in Fig. 70. Tg^{12} is the temperature at which the viscosity of the melts equals 10^{12} Pa s.

For all melts it is observed that the addition of B_2O_3 to a P_2O_5-bearing melt results in a decrease of T_g^{12} for all melt compositions. The strongest changes are observed for the CHAMP-P8 melt composition, whereas the lowest changes in T_g^{12} are observed for NCAS13-P8 melt. In case of the NCAS13-P8 melt, it is observed that the decrease in T_g^{12} is stronger at low B_2O_3 concentrations. Further increasing B_2O_3 concentration in the melt decreases T_g^{12} only slightly. In case of NCAS13-P2 melt, the decrease in T_g^{12} is stronger at higher B_2O_3 concentration. The same was observed in the heat capacity data (see Fig. 49 and Table 24).

In order to understand the mechanism behind the viscosity decrease it is essential to understand the incorporation mechanism of P_2O_5 and B_2O_3 into the melt. P_2O_5 is known to act as a network modifier as well as a network former. P_2O_5 acts as a network former by entering the melt structure as tetrahedrally coordinated PO_4^{3-} and removing cations in

network modifying positions and thus increasing the NBO/T of the. In peraluminous melts P_2O_5 act as a network modifier by removing Al^{3+} from tetrahedral positions to form structural units similar to $AlPO_4$ and thus decreasing the NBO/T ratio of the melt (Ryerson and Hess 1980; Mysen 1992, 1996; Toplis and Dingwell 1996a; Mysen 1998a). The detailed mechanism of P_2O_5 incorporation in the melt is described in chapter 3 and chapter 4.

B_2O_3 can enter the melt also as a network former as tetrahedrally coordinated BO_4^- or as a network modifier in form of BO_3 triangles. BO_3 triangles are converted to BO_4^- tetrahedra in the presence of excess metal cations which are in network modifying positions (Konijnendijk 1975; Meera and Ramakrishna 1993; Manara et al. 2009; Koroleva et al. 2011; Cochain et al. 2013; Möncke et al. 2015). The detailed incorporation mechanism of B_2O_3 into the melt is described in chapter 3.

The B_2O_3-free NCAS13-P8 as well as CHAMP-P8 melts were found to be unmixed. In case of those unmixed melts a stronger decrease in T_g^{12} is observed at low B_2O_3 concentrations, whereas the other melts show a more or less steady decrease in T_g^{12}, indicating that the viscosity decreasing effect of B_2O_3 on a P_2O_5-bearing melt is stronger in unmixed melts.

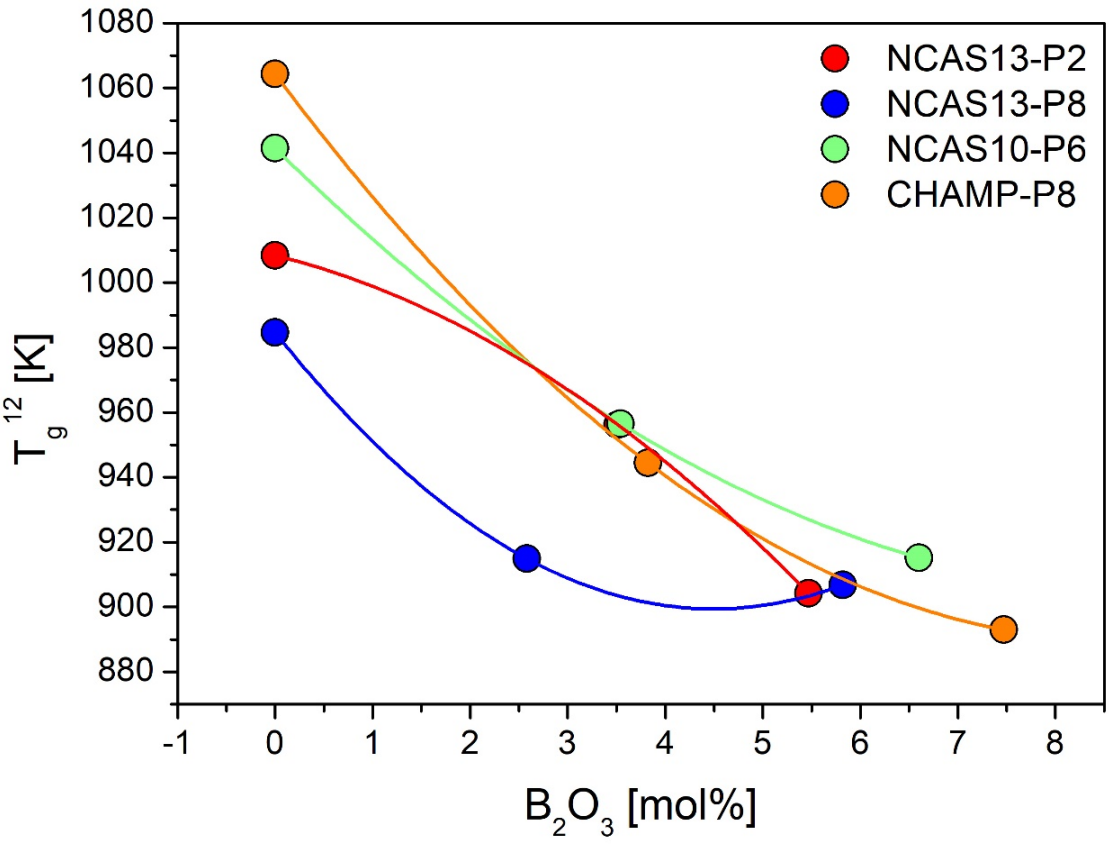

***Fig. 70**: T_g^{12} as a function of B_2O_3 for melts containing P_2O_5 as well as B_2O_3.*

NCAS10-P6, NCAS13-P8 and also CHAMP-P8 are of peraluminous melt composition. The NCAS13-P8 and CHAMP-P8 melts, which were of previously peralkaline composition are considered as peraluminous melts for the description of the incorporation mechanism of B_2O_3 since at these high P_2O_5 concentrations all excess metal cations are used by PO_4^{3-} tetrahedra and form a separate melt phase. Hence, there are no cations in network modifying position to be used by B_2O_3 and B_2O_3 enters the melt as network modifying BO_3 triangles, resulting in the observed depolymerisation of the melt. The same mechanism takes place in the peraluminous NCAS10-P6 melt.

In the peralkaline NCAS13-P2 melt there are still metal cations in network modifying positions present in the melt. Therefore, a small part of the BO_3 triangles is converted to BO_4^- tetrahedra and acts as a network former. At the same time, the remaining BO_3 triangles act as network modifiers. As observed from the decrease in viscosity with the addition of B_2O_3 to the melt, the depolymerising effect of B_2O_3 is stronger than the polymerising effect of BO_4^-. At higher B_2O_3 concentrations there are no more cations in network modifying positions left, leaving only the depolymerising effect of BO_3 triangles resulting in the observed stronger decrease of T_g^{12}.

5.5.3 Effect of Fluorine on Viscosity

T_g^{12} as a function of fluorine content of the previously unmixed NCAS13-P8B4 and NCAS13-P6 melts are illustrated in Fig. 71 together with fluorine-bearing peralkaline NACS and peraluminous ANCS melt from Baasner et al. (2013a).

For both melts T_g^{12} decreases with increasing F^- concentration in the melt. In case of the phosphorus- and boron-bearing NCAS13-P8B4 melt, T_g^{12} decreases almost linearly whereas in the only P_2O_5-bearing melt the stronger decrease in T_g^{12} is observed at lower F^- concentrations. The observed decreasing trends for the fluorine-bearing melts are in good agreement with data from Baasner et al. (2013a), who also observed a decrease in T_g^{12} for the peraluminous ANCS and peralkaline NACS melt with increasing F^- concentration.

From nuclear magnetic resonance studies (NMR) it was observed that in peraluminous melts F^- favors Al-F as well as some minor Si-F environments, resulting in the breaking of formally bridging Si-O-(Si,Al) bonds (Kohn et al. 1991; Zeng and Stebbins 2000; Baasner et al. 2013a, 2013b; Baasner et al. 2014). Hence, the polymerisation of the melt decreases, which leads to the observed decrease in T_g^{12}. In peralkaline melts, F^- also bonds to Na and Ca, resulting in the formation of Na-F and Ca-F sites, whereby F^- favours Ca-F over Na-F bonds (Zeng and Stebbins 2000; Baasner et al. 2013a).

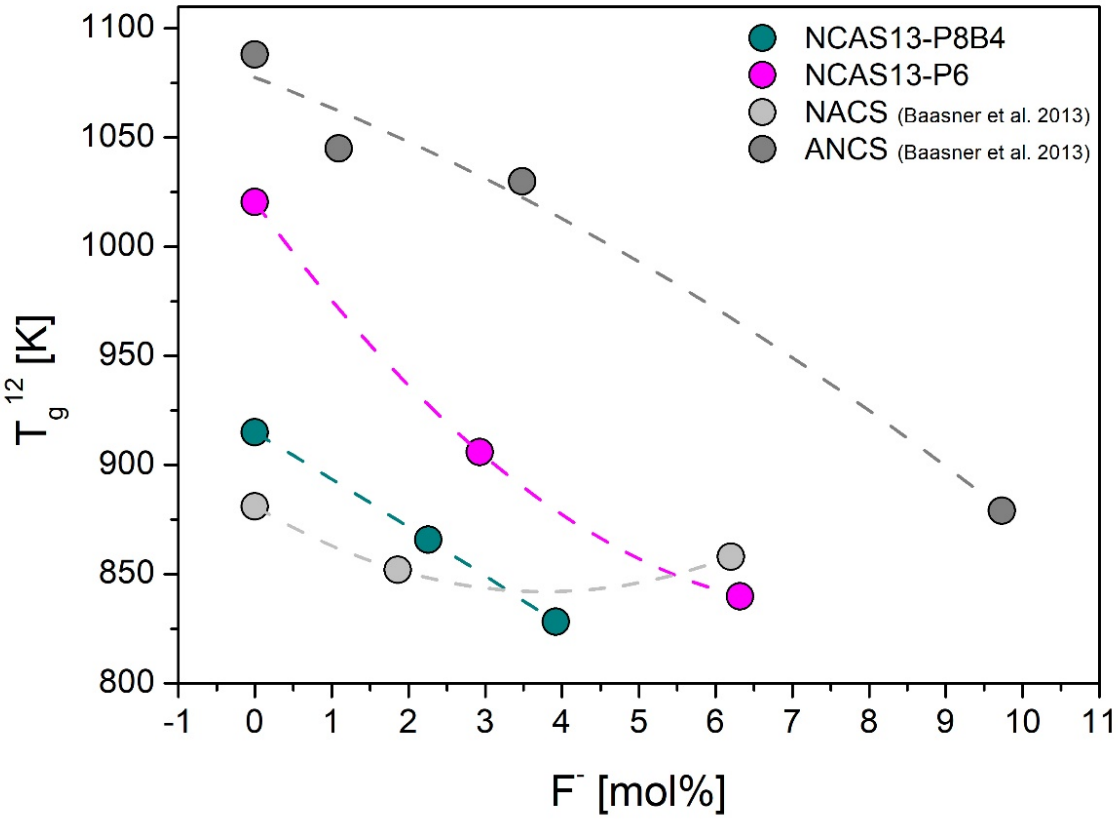

***Fig. 71**: T_g^{12} as a function of fluorine concentration for NCAS13-P8B4 and NCAS13-P6 melt together with aluminosilicate melts of Baasner et al. (2013a).*

The addition of fluorine to the previously peralkaline and unmixed melts in this study results in a mixing of the Si-Al- and Ca-P-rich melt as observed from heat capacity spectra. Based on the known facts of fluorine incorporation from previous studies we suggest that F^- results in the formation of depolymerising Al-F and Si-F as well as some Ca-F and Na-F sites.

5.5.4 The Combined Effect of P_2O_5, B_2O_3, F^- and H_2O on Unmixing and Implications for Natural Systems

The single effect of P_2O_5 and B_2O_3 on unmixing was studied in chapter 3 and 4. In this study the focus lies on the combined effect of P_2O_5, B_2O_3 and also F^- and H_2O on unmixing. For this purpose, B_2O_3 was added to the previously unmixed NCAS13-P8 melt as well as to two other melts. One of those two melts is NCAS13-P2, where unmixing was not detected but is expected and the other melt the peraluminous NCAS10-P6 melt, where no unmixing is present. Fluorine and water were added to the unmixed NCAS13-P6 and CHAMP-P8 melt as well as to the unmixed NCAS13-P8B4 melt.

From heat capacity measurements it is observed that the addition of B_2O_3 as well as F^- to a previously unmixed P_2O_5-bearing melt results in a mixing of the separated melts as evident by the disappearance of the second glass transition peak. It needs to be pointed out that

NCAS13-P8B4 never showed a second glass transition peak, even though unmixing was clearly observed in BSE images. One exception is posed by sample CHAMP-P8, where the disappearance of the second and third T_g peak occurs for the melt containing 7.47 mol% B_2O_3. The addition of only 3.82 mol% B_2O_3, however results in an increase in intensity of the T_g peak at the highest temperature, indicating an enhanced unmixing caused by the addition of B_2O_3 to the melt.

***Table 27**: Overview over the melt kinetics resulting from the combination of oxides as observed in this study*

	P_2O_5	**B_2O_3**	**F^-**	**H_2O**
P_2O_5	peralkaline melts containing Ca (and Fe): unmixing peraluminous melts: no unmixing	unmixing or mixing	homogeneous melt or crystallisation	crystallisation
B_2O_3	unmixing or mixing	no unmixing	-	crystallisation
F^-	homogeneous melt or crystallisation	-	mixing or crystallisation	crystallisation
H_2O	crystallisation	crystallisation	crystallisation	crystallisation

From backscattered electron images of these melts, it was observed that in case of NCAS13-P8 melt the addition of B_2O_3 to the melt does in fact results in a mixing of the formally separated melt phases at low B_2O_3 concentrations, as evident from the absence of separated melt spheres (Fig 65c). At higher B_2O_3 concentrations, however, the melt begins to unmix again. This is observed in the reappearance of light-grey spheres of a diameter of ~100 nm (Fig. 65d). The opposite is observed for CHAMP-P8 melt. Low B_2O_3 concentrations enhance the unmixing of the melt, where the spheres grow in size to an average diameter of 500-600 nm (Fig. 65e) compared to ~300 nm in the B_2O_3-free melt (see chapter 3). Higher B_2O_3 concentrations result in a shrinkage of the separated melt spheres back to approximately 300 nm (Fig. 65f). No structural changes are observed in NCAS13-P2 melt.

As observed from Raman spectra of the B_2O_3-bearing NCAS13-P2 and CHAMP-P8 melt, a vibrational band at ~1116 cm^{-1} caused by the presence of BPO_4 units appears (Money and Hariharan 2008). Since the presence of BPO_4 units correlates with mixing of previously unmixed melts, we suggest that B_2O_3 bonds to PO_4 units from the second melt phase and, somehow, bonds to the silicate melt network.

In case of CHAMP-P8 melt, at low B_2O_3 concentrations B_2O_3 is expected to bond to the aluminosilicate network, since no vibrational band was observed at 1116 cm^{-1} indicating the presence of BPO_4 units. At higher B_2O_3 concentrations, however, B_2O_3 prefers the BPO_4 bonding. The exact opposite occurs in NCAS13-P8 melt, where low B_2O_3 concentrations result in a mixing of the previously unmixed melt spheres, but the increasing B_2O_3 concentration in the melt results in a new unmixing of the melts. How exactly this process occurs and what triggers it is not clear at the moment and further investigations are needed to answer this particular question. From chapter 4 it was observed that the melts separate into a Si-Al- and a Ca-P-rich melt. It is also not clear in which melt phase B_2O_3 is enriched, since the spheres are too small for analysis with the used methods and boron is generally difficult to measure.

The addition of fluorine to CHAMP-P8 melt melts results in the crystallisation of apatite (see Fig. 66 and 67). The addition of F^- to NCAS13-P8B4 melt did not result in an unmixing of the melt. From heat capacity data it is observed that the addition of F^- to the previously unmixed NCAS13-P6 melt results in a mixing of the previously separated Si-Al- and Ca-P-rich melt. From Raman spectra as well as Literature data it is suggested that F^- bonds to Al as well as Si from the aluminosilicate network (Baasner et al. 2013a, 2013b). Baasner et al. (2014) showed that in peralkaline melts F^- prefers the bonding to Ca and Na.

However, there are no studies on the effect of F^- on unmixed melts. The Si-Al-rich melt is of peraluminous composition due to the fact that all cations from formally network modifying positions are enriched in the Ca-P-rich melt. Therefore, we suggest that both mechanism occur, resulting in the formation of Al-F, Si-F as well as (Ca,Na)-F bonds. How this observation results in a mixing of those melts cannot be answered at this point and is a matter for future studies.

Another important fact is that unmixing is dependent on time and temperature (Wheaton and Clare 2007). The fact that in case of CHAMP-P8 melt the addition of fluorine results in crystallisation of apatite leaves the possibility that the melts may unmix upon cooling. If this is the case, F^- would become enriched in the Ca-P-rich melt, based on the fact that F^- prefers Ca-F bonds over Si-F and Al-F bonds. The addition of F^- would then result in direct crystallisation of apatite from the phosphorus-rich melt. The direct crystallisation of apatite crystals from an unmixed Ca-Fe-P-rich melt is currently a matter of discussion for the formation of layered intrusions (e.g. Fischer et al. 2016; Hou et al. 2018) and is discussed in detail in chapter 4.

The addition of water also results in the crystallisation of apatite in all H_2O-bearing melts. In order to better investigate the effect of water on unmixing higher temperatures in the IHPV are needed to acquire a crystal-free melt.

Understanding the affinity of a melt to unmixing is essential in order to understand natural magmatic processes. Due to the changing melt composition during phase separation, unmixing is likely to affect crystallisation. The importance of unmixing is already described in the formation of layered intrusions (e.g. Jakobsen et al. 2005, 2011; Charlier et al. 2011; Fischer et al. 2016; Hou et al. 2018) . However, the effect of B_2O_3, F^- and H_2O needs further investigations and will be significant in pegmatitic melts, which are naturally enriched in B_2O_3 and F^- (e.g. London 2008, 2009).

5.5.5 Comparison with Models

A comparison of the modelled and measured heat capacities of the glasses (C_{pg}) and liquids (C_{pl}) is shown in Fig. 72 for all P_2O_5-, B_2O_3- as well as F^--bearing melts. The heat capacities of the glass are calculated after Richet (1987). C_{pl} was calculated after the model of Richet and Bottinga (1985) as well as Stebbins et al. (1984).

Generally, a significant deviation from the model is observed for all P_2O_5-, B_2O_3- and also F^--bearing melts, which is expected since none of those oxides is included in the calculation. Merely P_2O_5 could be included into the calculation of C_{pg} by using the molar heat capacities for P_2O_5 glasses from Robie et al. (1978a), which probably explains the stronger deviation from the model observed for the C_{pl} values.

The calculated C_{pl} after Stebbins et al. (1984) are closer to the measured values than the values calculated after Richet and Bottinga (1985). The model for C_{pl} after Stebbins works surprisingly well for the NCAS13-P2 melt containing B_2O_3. Generally, it is observed that the models underestimate the C_{pl} values. C_{pg} is underestimated for the NCAS13-P2 and CHAMP-P8 melt containing B_2O_3 as well as the fluorine-bearing melts and overestimated for the NCAS13-P8 and NCAS10-P6 melts containing B_2O_3.

This study as well as previous studies (e.g. Mysen et al. 1981a; Mysen and Virgo 1985a; Dingwell et al. 1992; Meera and Ramakrishna 1993; Toplis et al. 1994c; Toplis and Dingwell 1996a; Mysen 1998a; Zeng and Stebbins 2000; Manara et al. 2009; Baasner et al. 2013a, 2013b;) demonstrate the strong effect of P_2O_5, B_2O_3 and F^- on the structure of melts. It is expected that these significant structural changes affect the models. Therefore, we suggest that the effect of those oxides should be included in the development of future models.

The viscosities of the P_2O_5-, B_2O_3 as well as F^--bearing melts were calculated by using the model after Giordano et al. (2008b) and are illustrated in Fig. 73. For the P_2O_5 and B_2O_3-bearing melts, the starting B_2O_3-free composition of the melts is underestimated by the model. This is expected since P_2O_5 is not included in the calculation and all of those melts

contain P_2O_5. In chapter 3 of this study we have shown that P_2O_5 increases the viscosity of peralkaline melts up to a maximum viscosity after which viscosity decreases with further increasing P_2O_5 concentration and that P_2O_5 decreases the viscosity of peraluminous melts.

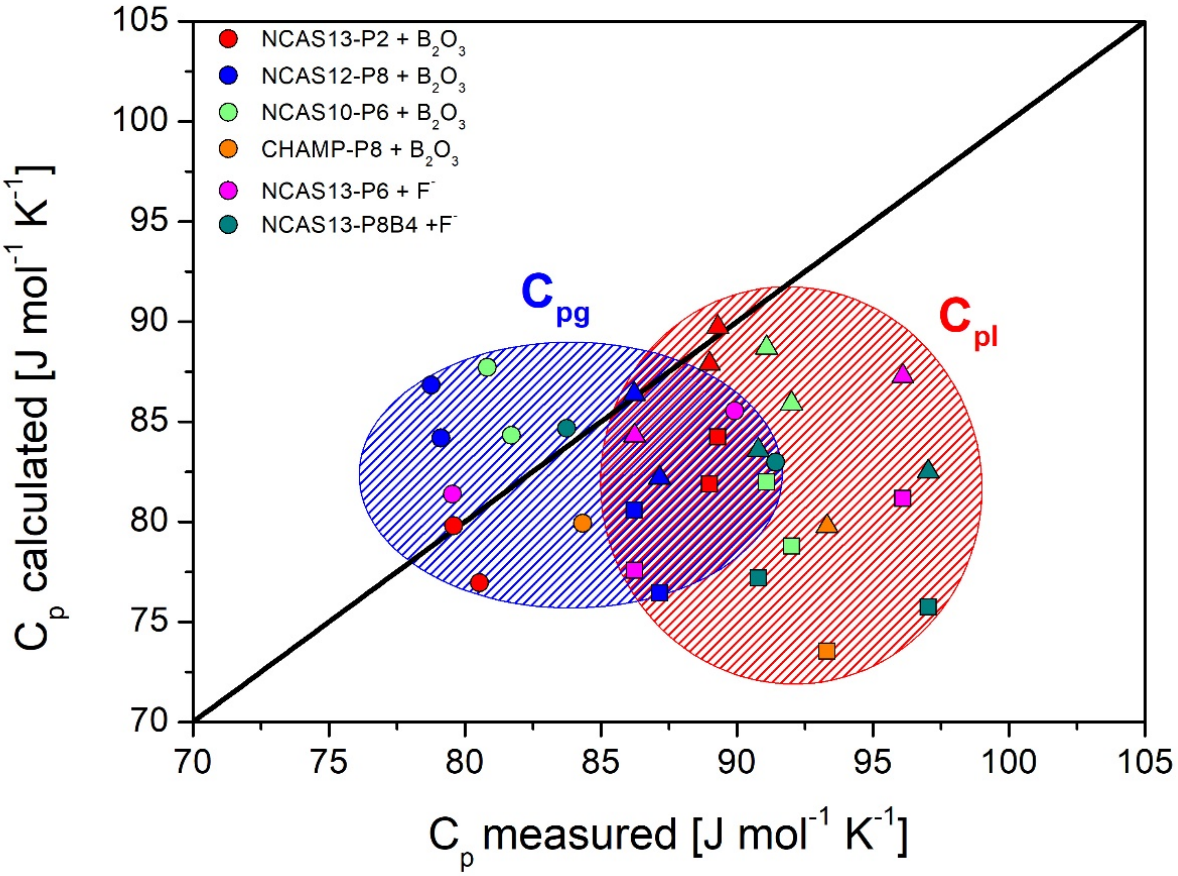

***Fig. 72**: C_{pg} calculated after Richet (1987) and C_{pl} calculated after Richet and Bottinga (1985) and Stebbins et al. (1984) for P_2O_5-,B_2O_3- and F^--bearing melts compared to measured values. Squares represent C_{pl} modelled after Richet and Bottinga (1985) and triangles represent C_{pl} modelled after Stebbins et al. (1984). Circles dedescribe C_{pg} values. Blue area represents C_{pg} values whereas red area represents C_{pl} values.*

B_2O_3 is also not included in the viscosity calculations after Giordano et al. (2008b). However, the calculated viscosities of B_2O_3-bearing NCAS13-P8 and NCAS10-P6 are almost in good agreement with the measured values. For the CHAMP-P8 as well as NCAS13-P2 melt compositions the calculated values get closer to the measured viscosities with increasing B_2O_3 concentration.

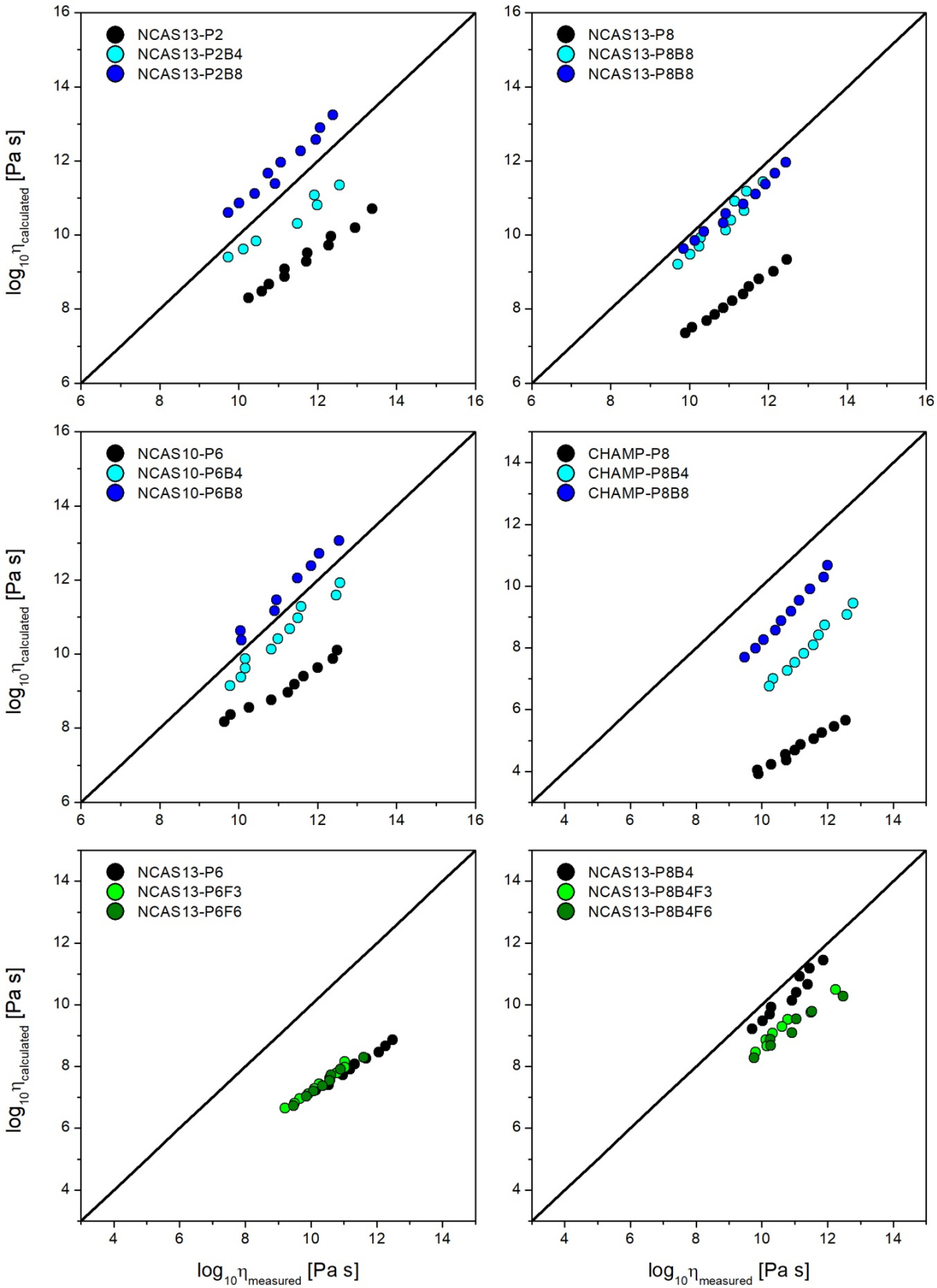

***Fig. 73**: Viscosities of P_2O_5, B_2O_3- and F^--bearing peralkaline NCAS13 and peraluminous NCAS10 melt calculated after Giordano et al. (2008b).*

This effect is caused solely by that fact that B_2O_3 decreases the viscosity of the melts as shown in chapter 2. Since the measured viscosities of the P_2O_5-bearing melts are higher than the calculated values, the decrease in viscosity caused by the incorporation of B_2O_3 results to a shift up to the point where the viscosity increasing effect of P_2O_5 is reversed by the viscosity decreasing effect of B_2O_3, resulting in a seemingly accuracy of the model.

For the fluorine bearing samples no significant changes with the addition of fluorine are observed, which is also expected since the model after Giordano et al. (2008b) includes fluorine in the calculation of viscosity. The model underestimates the viscosities of the NCAS13-P6 melts since P_2O_5 increases melt viscosity, which is not considered by the model. The model fits the measured viscosities for fluorine-bearing NCAS13-P8B4 melt quite well merely because the viscosity increasing effect of P_2O_5 is reversed by the viscosity decreasing effect of B_2O_3.

This study demonstrates the strong effect of P_2O_5 and B_2O_3 on melt viscosity. These may play an important role in the formation of pegmatites, where high P_2O_5 and B_2O_3 concentrations in the melt are found. Therefore, these oxides should be included in future viscosity models.

5.6 Conclusions

In this study we have investigated the combined effects of P_2O_5, B_2O_3, F^- and H_2O on the unmixing of aluminosilicate melts. In chapter 3 and 4 we have shown that P_2O_5 has the strongest effect on unmixing, as the addition of P_2O_5 to peralkaline melts results in the phase separation into a Si-Al- as well as a Ca-(Fe)-P-rich melt.

The incorporation of B_2O_3 into previously unmixed melts shows controversial results. While the addition of B_2O_3 to NCAS13-P8 melt results in a mixing of the separate melts at low B_2O_3 concentrations, the addition of a similar B_2O_3 concentration to CHAMP-P8 melt results in an enhancement of the observed unmixing. At higher B_2O_3 concentrations NCAS13-P8 begins to unmix again, while higher B_2O_3 concentrations in CHAMP-P8 melt result in the beginning of a mixing of the Si-Al rich- and Ca-Fe-P-rich melt.

It is not clear how this process works in detail. However, from Raman spectra it was observed that the mixing of formally separated melts is linked to the appearance of BPO_4 structural units. The addition of B_2O_3 to the peraluminous NCAS10-P6 melt does not result in an unmixing. Furthermore, the addition B_2O_3 to NCAS13-P2 melt which is expected to exhibit small-scale melt separation even though it could not be detected with the used methods also shows no unmixing. It is observed that linking BPO_4 units are present in these melts.

The addition of fluorine to the melts results in crystallisation of apatite in CHAMP-P8 melt and in the formation of Al-F together with some Si-F bonds in NCAS13-P6 and NCAS13-P8B4 melt. Due to previously published data where it is described that in peralkaline melts F^- favors Ca-F bonds over Al-F and Si-F bonds (Baasner et al. 2014) as well as the fact that the fluorine-free CHAMP-P8 melt consists of a Si-Al- and Ca-Fe-P rich melt, we suggest that in unmixed melts fluorine will be enriched in the Ca-rich melt and in the presence of phosphorus will result in the crystallisation of apatite. Since crystallisation is dependent on the temperature, we suggest that decreasing the melting temperature of fluorine-bearing NCAS13-P8B4 as well as NCAS13-P6 melts will lead to an unmixing followed by crystallisation of apatite.

The addition of water to the P_2O_5- and F^--bearing samples also results in crystallisation of apatite. In this case we also suggest that at a certain temperature range the melts will unmix before the crystallisation of apatite takes place. The role of water could not be investigated in this study due to the mentioned crystallisation effects. However, there is a strong possibility that water will also become enriched in the Ca-P-rich melt since apatite is the hydrous mineral. In order to perform more detailed investigation on the effect of water on unmixing further IHPV experiments at higher temperatures are needed.

The results from this study are of importance for the understanding of complex magmatic processes where unmixing is known to be the driving mechanism for crystallisation as is the case with layered intrusion (e.g. Jakobsen et al. 2005; Fischer et al. 2016; Hou et al. 2018). Furthermore, the combined effect of P_2O_5, B_2O_3, F^- and H_2O may be of interest in the petrogenesis of pegmatites, which are known to exhibit naturally high concentrations of those elements (e.g. Thomas and Webster 2000; London 2008, 2009;).

6 The Influence of Tempering on Unmixing of Melts

6.1 Abstract

In this study we investigate the effect of tempering on unmixing of peralkaline, P_2O_5-bearing melts from the CaO-Al_2O_3-SiO_2 system as described in Chapter 3 of this study. Tempering experiments were conducted in a 1 atm furnace at 1273 – 1373 K for a duration of 2 – 8 h. After tempering experiment the colour of all P_2O_5-bearing melts changed from previously clear to a white colour and a characteristic light scattering between orange and blue. The melts were characterised with respect to their viscosity, heat capacity and structure. The viscosity of the melts was determined in the range $10^{8.5}$ to $10^{13.5}$ Pa s with the micropenetration viscometry technique. The heat capacities of the samples were measured with Differential Scanning Calorimetry (DSC). The structure of the melts was analysed by Scanning Electron Microscopy (SEM). A change in viscosity is observed for CAS19-P8 melt as the unmixing progresses. The original, homogeneous melt shows an intermediate viscosity. After short heat treatments but before unmixing can be determined with the used methods, the viscosity of the melt increases. With the appearance of phase separation the viscosity of the melt decreases and is lower than the viscosity of the homogeneous melt. Tempering at 1273 – 1323 K results in an enhancement of unmixing but also in crystallisation. Unmixing is observed by the splitting of the T_g peak to lower and higher temperatures as well as BSE images. Longer duration times result in crystal growth. Tempering at 1373 K results in crystal-free and unmixed melts for CAS19-P6 and -P8 melt, whereby unmixing is observed with SEM rather than DSC. Due to the change in colour and characteristic light scattering we suggest the melts with lower P_2O_5 concentration are also unmixed, but the size of the separated phases is too small for analysis with the used methods. This study demonstrates the effect of tempering on unmixing of P_2O_5-bearing melts, whereby the melts presumably separate into a Si-Al- and a Ca-P-rich melt.

6.2 Introduction

The motivation for tempering experiments in this study originates from observations during viscosity measurements of the peralkaline, calcium-bearing sample CAS19-P8 containing 8 mol% P_2O_5. Viscosity experiments resemble tempering experiments in the way that the sample is heated and held at a desired temperature for a specific amount of time. Previous studies of Wheaton and Clare (2007) have demonstrated the influence of tempering on the growth of unmixed melt spheres.

After viscosity measurements above 1110 K the formerly crystal-clear glass sample showed a blueish-hue and strong changes in viscosity, indicating structural changes in the glass that occurred with temperature and time.

Therefore, we chose the P_2O_5-bearig samples from this melt composition for additional experiments. Experiments were performed at different temperatures as well as different tempering durations. Samples were afterwards analysed by using micropenetration viscometry, Differential Scanning Calorimetry (DSC) as well as Scanning Electron Microscopy (SEM).

6.3 Starting Material

First experiments were performed on solely the peculiar sample CAS19-P8 for different duration times as well as at varying temperatures. Afterwards, tempering experiments were extended to all other P_2O_5-bearing melts from CAS19 series. The phosphorus-bearing samples CAS19-P2, -P4, -P6 and –P8 were tempered in a 1 atm furnace at 1373 K for a duration of 2 h in a $Pt^{95}Au^5$ crucible. Tempering experiments on sample CAS19-P8 were also performed at 1323 K for 2 h as well as 1273 K for 2, 5 and 8 h. In addition, sample CAS19-P8 was re-melted and cooled slowly by 10 K min-1 to 1373 K before quenching.

***Table 28**: Composition of CAS19 glass series chosen for tempering experiments measured by EMPA.*

oxide	CAS19	2σ	CAS19-P2	2σ	CAS19-P4	2σ	CAS19-P6	2σ	CAS19-P8	2σ
					composition in wt%					
SiO_2	60.26	0.17	57.57	0.16	54.91	0.16	52.40	0.16	51.01	0.15
Al_2O_3	21.02	0.10	19.69	0.09	18.77	0.09	17.81	0.09	17.37	0.09
CaO	17.17	0.10	16.64	0.10	15.87	0.10	15.13	0.10	14.40	0.10
P_2O_5	-	-	3.82	0.09	7.36	0.12	10.79	0.14	15.74	0.17
total	**98.45**		**97.73**		**96.91**		**96.13**		**98.52**	
					composition in mol%					
SiO_2	66.18	0.19	64.96	0.10	63.78	0.11	62.62	0.15	61.21	0.21
Al_2O_3	13.61	0.09	13.10	0.04	12.85	0.06	12.54	0.08	12.28	0.08
CaO	20.21	0.13	20.12	0.10	19.75	0.13	19.38	0.10	18.51	0.14
P_2O_5	-	-	1.83	0.04	3.62	0.03	5.46	0.05	8.00	0.12
γ	0.60		0.61		0.61		0.61		0.60	
NBO/T	0.14		0.15		0.15		0.16		0.15	
g.atom	3.07		3.13		3.20		3.28		3.38	

Results are mean values of 10 single point measurements

All samples showed a change in colour after the tempering experiments. The glasses that have been previously colourless turned white. The white glasses are shimmering in a slightly blueish hue and shine orange through transmitted light.

The compositions of the quenched samples were measured with a JEOL JXA 8900RL electron microprobe and are given in Table 28. The composition was measured with a 15 kV and 15 nA electron beam which was defocused by 30µm.

6.4 Results

6.4.1 Effect of Tempering on Viscosity

Since strong and visible changes in viscosity occurred in sample CAS19-P8 during the measurements, further investigations were performed on this sample composition. Fig. 74 summarizes the viscosity data of the quenched melt, the melt after previous viscosity measurements and the same melt which was slowly cooled.

Viscosity data was fitted using an Arrhenian equation of the type:

$$\log\eta = \log A + \frac{10000\ B}{T} \qquad \text{(Eq. X)}$$

Where *A* and *B* are fit parameters and *T* represents the temperature in K. The viscosity data is summarised in Table 29. Parameters of the Arrhenian fit are presented in Table 30 together with the activation energy for viscous flow E, the calculated T_g[12] and fragility m of the melts.

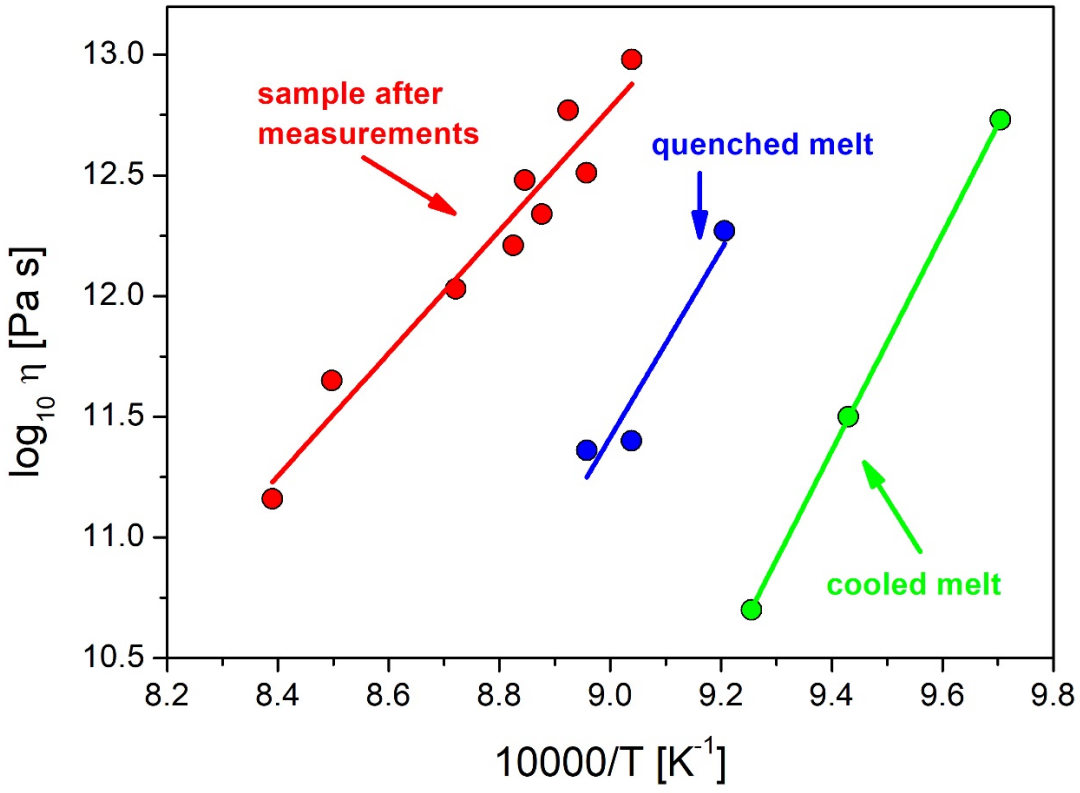

***Fig. 74**: Viscosities of CAS19-P8 melt after quenching (blue), slow cooling to 1273 K (green) and after heat treatment due to previous viscosity measurements (red).*

After previous viscosity measurements the viscosity of the sample increases by ~1.3 log units in comparison to the quenched melt. The viscosity of the slowly cooled sample, however, decreases with respect to the quenched melt by approximately 1.5 log units.

The fragility of the melts was calculated from viscosity data using following term (e.g. Toplis et al. 1997b; Webb et al. 2007) :

$$m = \left.\frac{\partial(log_{10}\eta)}{\partial(T_g/T)}\right|_{T_g} = \frac{B}{T_g^{12}} \qquad \text{(Eq. XV)}$$

The lowest fragility of the melts is observed for the sample after previous viscosity measurements whereas the cooled melt shows the highest fragility.

***Table 29**: Viscosities of CAS19-P8 melt after different heat treatments measured by micropenetration technique*

quenched		measured sample		cooled	
T [K]	**$log_{10}\eta$ [Pa s]**	**T [K]**	**$log_{10}\eta$ [Pa s]**	**T [K]**	**$log_{10}\eta$ [Pa s]**
1106.4	11.40	1106.4	12.98	1030.4	12.73
1116.4	11.36	1116.4	12.51	1060.5	11.50
1086.2	12.27	1120.6	12.77	1080.5	10.70
		1126.5	12.34		
		1130.5	12.48		
		1133.5	12.21		
		1146.6	12.03		
		1176.8	11.65		
		1191.9	11.16		

***Table 30**: Arrhenian fit parameters for viscosities of CAS19-P8 melt after different heat treatments*

Sample	A	ΔA	B	ΔB	E	T_g^{12}	$\Delta T_g 12$	m
	log_{10} Pa s	log_{10} Pa s	log_{10} Pa s 10^4 K	log_{10} Pa s 10^4 K	kJ mol^{-1}	K	K	
quenched	-23.57	10.30	3.89	1.14	744.32	1092.8	3.8	36
measured	-10.10	2.03	2.54	0.23	486.87	1150.3	1.1	22
cooled	-31.02	0.25	4.51	0.03	863.36	1048.0	0.1	43

E: activation energy for viscous flow

T_g^{12}: Temperature at which the viscosity of the melt equals 10^{12} Pa s

m: fragility of the melt

6.4.2 Effect of Tempering on Heat Capacity Curves

The effect of time during tempering at 1273 K on sample CAS19-P8 containing 8 mol% P_2O_5 is illustrated in Fig. 75. The melt was tempered for a duration of 2 h, 5 h and 8 h. After 2 h no changes are observed in the heat capacity curves. The heat capacity curve of the tempered sample for 2 h is exactly the same as for quenched and also for the slowly cooled sample, showing a glass transition peak at ~ 1095 K. Therefore, only one curve is shown in Fig. 75.

Interesting changes in the heat capacity curves occur after 5 h and 8 h. For these two samples a split in the original glass transition peak is observed to higher and also lower temperatures. Instead of the previously present T_g peak at 1095 K, two T_g peaks are present in both, the melt tempered for 5 h as well as 8 h, at ~1157 K and ~777 K. The presence of two T_g peaks indicates the existence of two separate melts.

The glass transition peaks are more pronounced after a duration of 8 h. It can be also observed that C_{pg} and C_{pl} are lower after a tempering time of 8 h. Since the melts contain more than one glass transition peak, it is not possible to calculate C_{pg}, C_{pl}, T_f', S_{conf} and B_e.

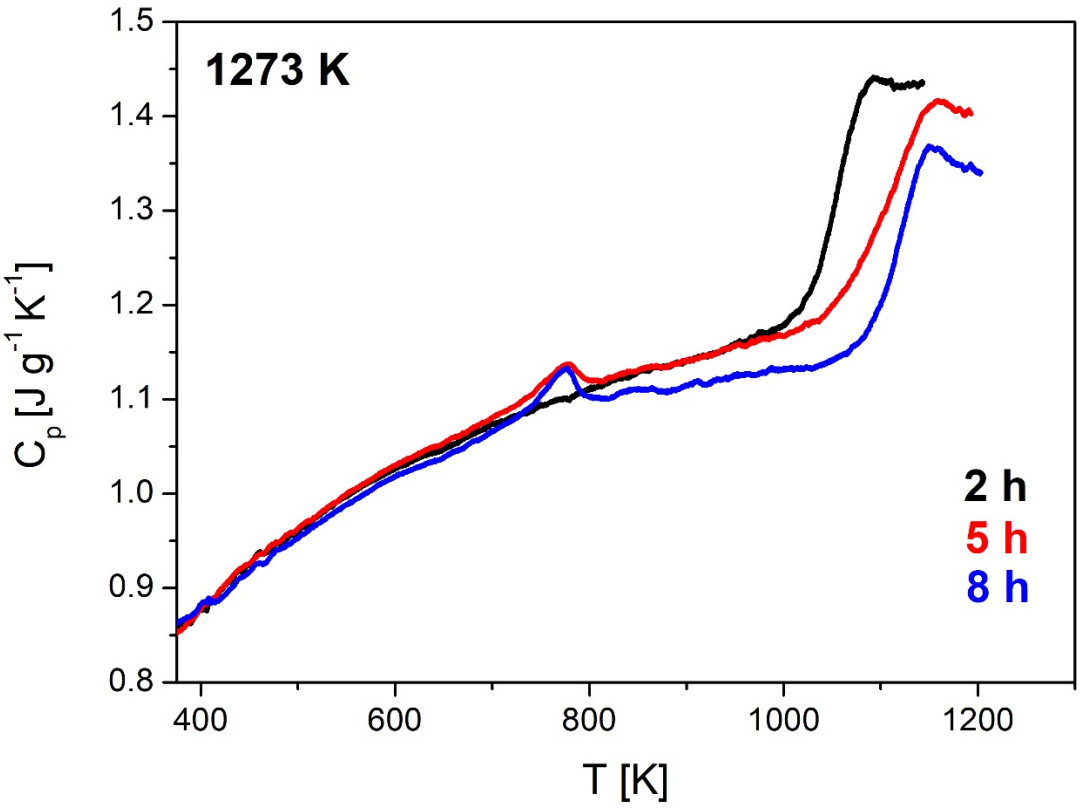

***Fig. 75**: Heat capacities of sample CAS19-P8 tempered at 1273 K for a duration of 2 h, 5 h and 8 h.*

The heat capacity curves for sample CAS19-P8 tempered for a duration of 2 h at three different temperatures are illustrated in Fig. 76. The T_g peak of sample CAS19-P8 tempered at 1273 K lies at ~1095 K, which is the exact same position as in the quenched and also slowly cooled sample. No changes are observed after tempering for 2 h at 1273 K.

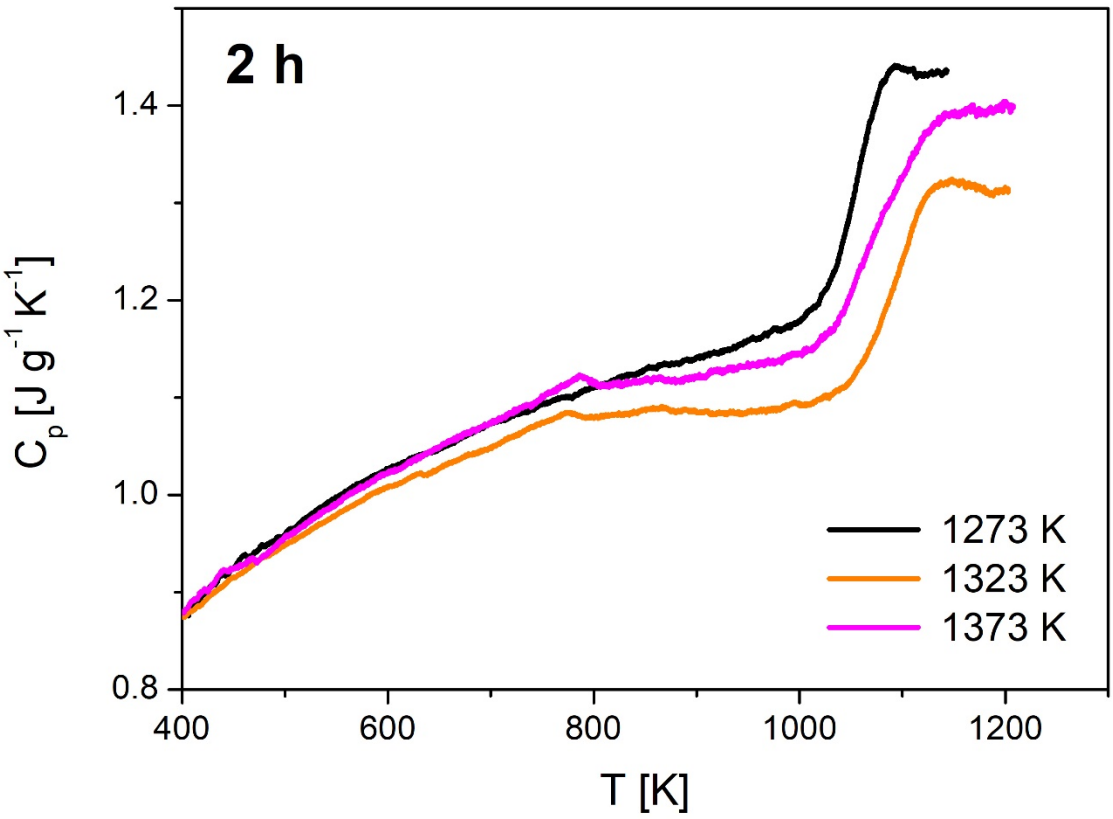

***Fig. 76**: Heat capacities of sample CAS19-P8 tempered for 2h at 1273 K, 1323 K and 1373 K.*

After tempering at 1323 K as well as 1373 K the original T_g peak at approximately 1095 K splits into two glass transition peaks. One is found and lower temperatures at ~780 K and the other peak at higher temperatures at ~1150 K for both melts. The presence of two glass transition peaks indicates the presence of two separate melts. It is observed that C_{pg} and C_{pl} are lower for the melt tempered at the highest temperature of 1373 K.

Due to the existence of more than one glass transition peak it is not possible to calculate C_{pg}, C_{pl}, T_f', S_{conf} and B_e.

The heat capacity curves for all P_2O_5-bearing melts from CAS19 series after tempering at 1373 K for a duration of 2 h is illustrated in Fig. 77. For all melts containing up to 5.46 mol% P_2O_5 no changes occur in the heat capacity curves in comparison to the quenched melts.

Sample CAS19-P8 is the only melt showing changes in heat capacity curves after tempering. This sample contains two glass transition peaks at ~780 K and ~1150 K,

whereas the quenched sample exhibits only one glass transition peak at ~1095 K (see Fig. 77).

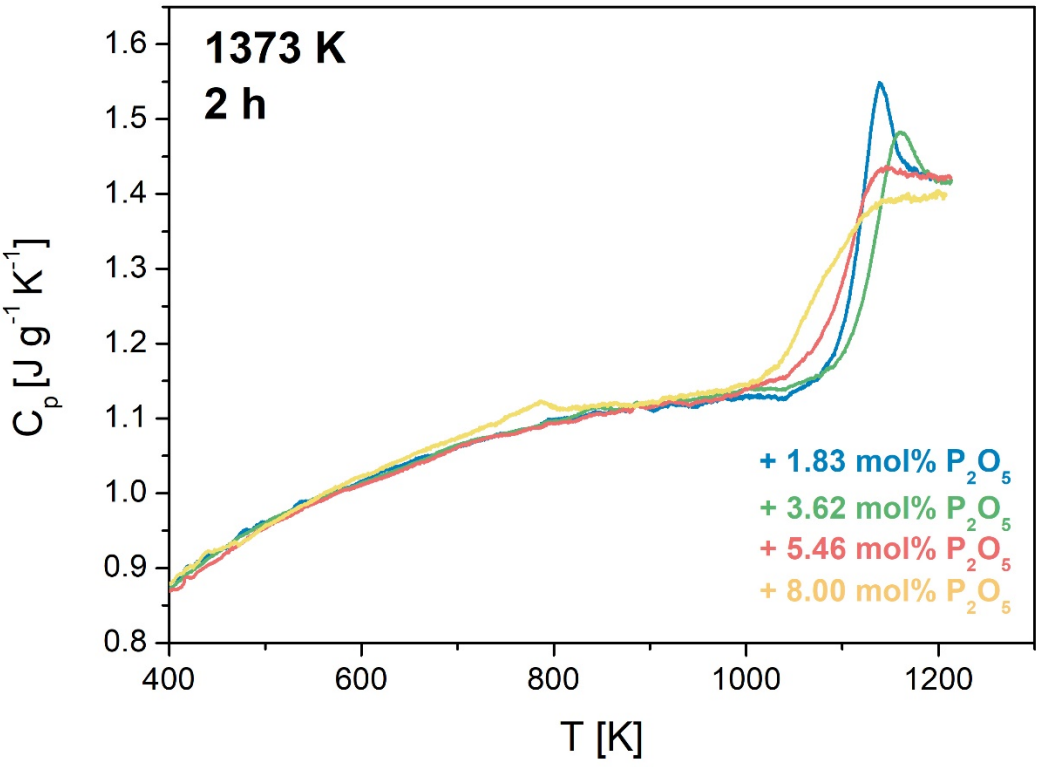

***Fig. 77**: Heat capacities of all P_2O_5-bearing melts of CAS19 series tempered for 2 h at 1373 K.*

6.4.3 Effect of Tempering on Structure

In order to visualize the structural and chemical changes occurring in the samples as a result of tempering, backscattered electron micrographs of the samples were collected. Fig. 78 shows the BSE images of the quenched CAS19-P8 melt containing 8 mol% P_2O_5 (a) as well as CAS19-P8 melt after slowly cooling the melt to 1273 K before quenching (b). The piece of sample CAS19-P8 which was previously used for viscosity measurements was also analysed with SEM, but since no structural changes are visible this sample is not shown. Its structure resembles the structure of the quenched melt shown in Fig. 78a.

The first changes in melt structure are visible in the slowly cooled sample (Fig. 78b). Upon cooling the melt structure rearranged itself, separating into small spheres in the 50 – 200 nm range of light-grey and dark-grey colours.

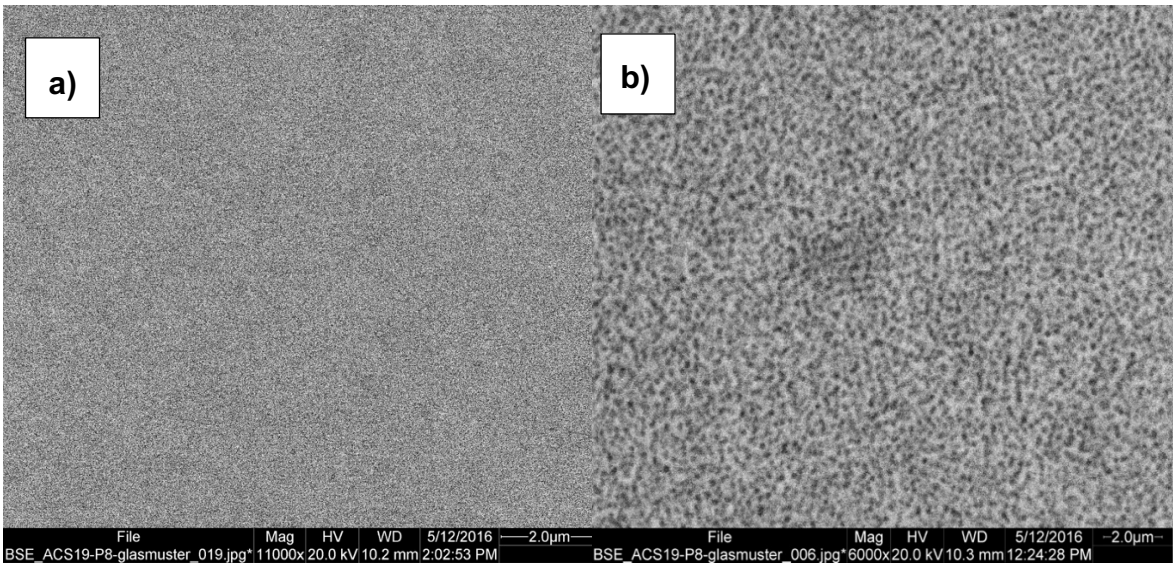

***Fig. 78**: BSE images CAS19-P8 melt for a) the quenched melt and b) the slowly to 1273 K cooled melt. The structure of the sample from previous viscosity measurements resembles the homogeneous structure of the quenched melt (a).*

The backscattered electron micrographs for sample CAS19-P8 tempered at 1273 K for a duration of 2 h, 5 h and 8 h are presented in Fig. 79. Fig. 79a shows the structure of the sample tempered for 2 h. During tempering at this temperature, small dendritic crystals (2 – 3 µm) begin to grow, which is visible in form of white specks and elongated white lines. These crystals are embedded in a glass matrix which shows unmixing similar to that observed in the slowly cooled sample. The separated melt spheres are of light-grey and dark-grey colours and in 10 – 200 nm range (Fig. 79b).

With longer tempering time, the small dendritic crystals begin to grow, forming rosettes of 10 – 20 µm size, as observed for CAS19-melt tempered for 5 h (Fig. 79c,d). Furthermore, small white accumulations of approximately 500 nm are found within the dark grey glass matrix.

After increasing the tempering time to 8 hours the progress of crystal growth is observed (Fig. 79 e,f). The rosettes grow in size up to 20 – 40 µm and develop and internal structure. The matrix consists of small dendritic crystals as well as small crystal accumulations in 500 nm – 5 µm range, which are embedded in a glass matrix.

The backscattered electron micrographs of sample CAS19-P8 tempered for 2 hours at 1323 K as well as 1373 K are shown in Fig. 80. In comparison to the sample tempered at 1273 K (Fig. 79a) the increase of temperature by 50 K (Fig. 80a) results in a decrease of crystal amount in the melt.

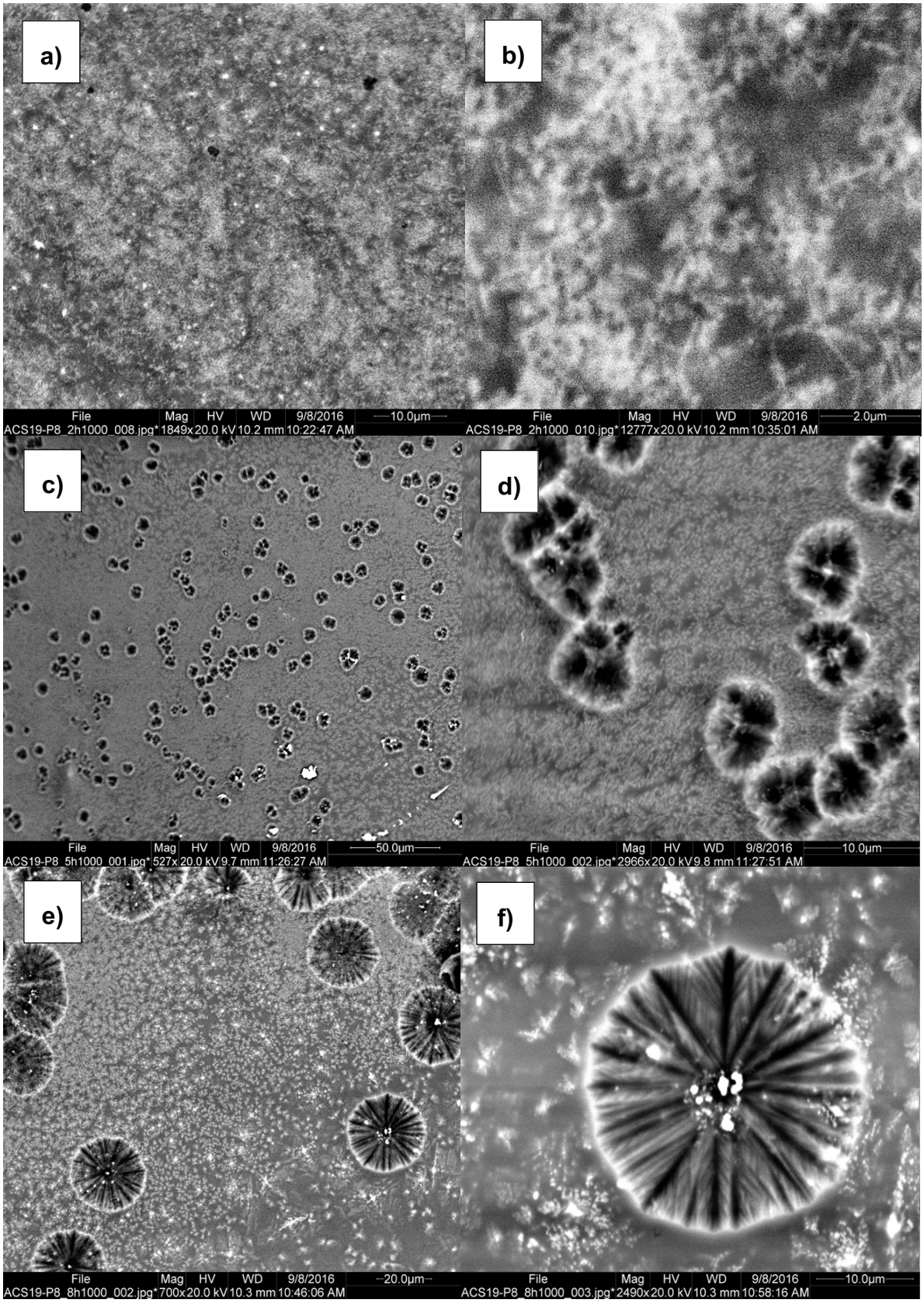

***Fig. 79**: BSE images of CAS19-P8 melt after tempering experiments at 1273 K for a+b) 2 h, c+d) 5 h and e+f) 8 h.*

The effect of further increase of temperature by 50 K up to 1373 K is shown in Fig. 80b. It is observed that after tempering at this temperature, no crystals are found compared to tempering experiments at 1273 K and 1323 K. The structure of the melt consists of light-grey and dark-grey spheres, indicating the presence of two separate melts.

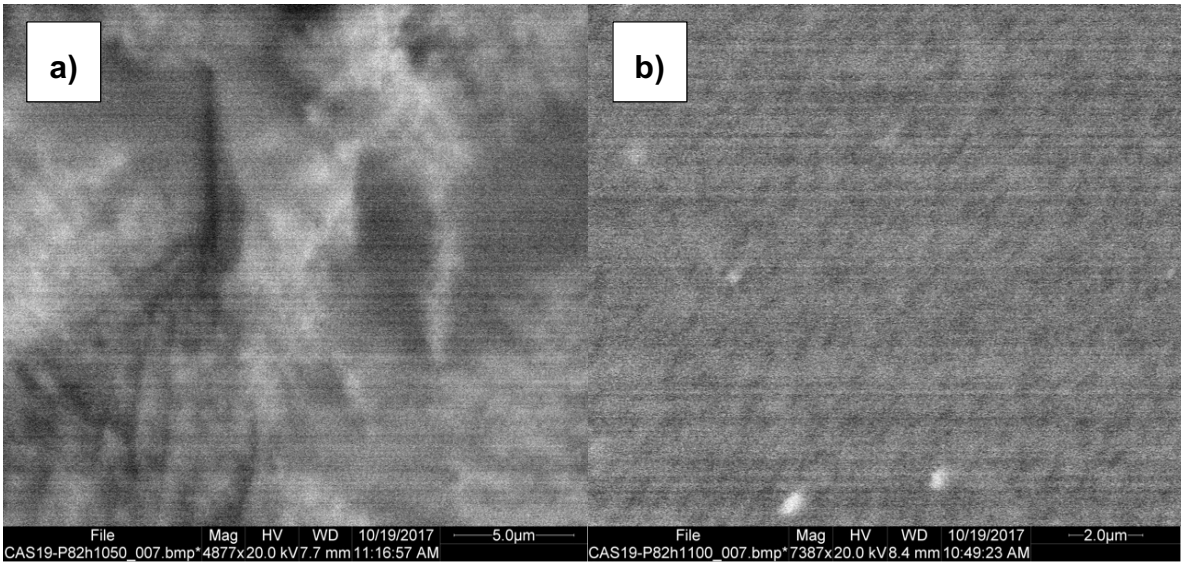

***Fig. 80**: BSE images of sample CAS19-P8 tempered for 2 h at a) 1323 K and b) 1373 K.*

The BSE images of other P_2O_5-bearing melts from CAS19 series are shown in Fig. 81 for a) CAS19-P2 and b) CAS19-P6 melt. No changes in structure are observed for the CAS19-P2 as well as CAS19-P4 melt. The structure of CAS19-P4 resembles the structure of CAS19-P2 and therefore is not shown here. In CAS19-P6, however, small white spheres of approximately 50 nm diameter appear in the glass matrix.

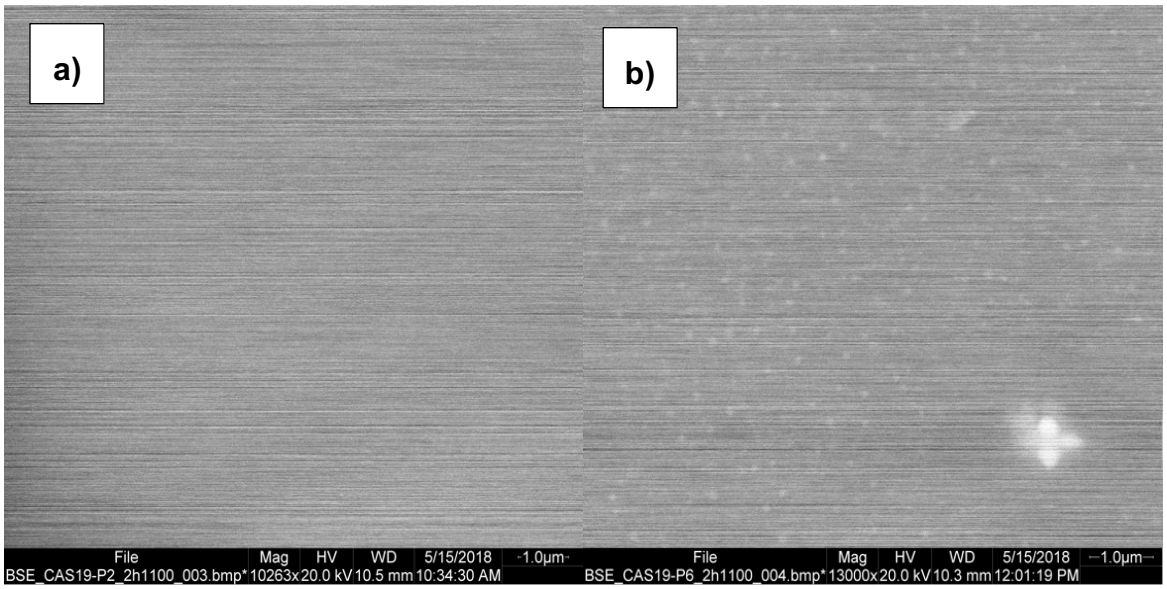

***Fig. 81**: BSE images of P_2O_5-bearing melts from CAS19 series tempered at 1373 K for a duration of 2 h for a) CAS19-2 and b) CAS19-P6 melt. The structure of CAS19-P4 melt resembles the homogeneous structure of CAS19-P2 melt.*

6.5 Discussion

6.5.1 Effect of Tempering on Unmixing and Crystallisation

Results have shown that sample CAS19-P8 has a strong affinity to unmix. Unmixing is a temperature- and time-dependant process (e.g. Wys 1960; Shelby 2005; Wheaton and Clare 2007; Hodroj et al. 2013). Wheaton and Clare (2007) have demonstrated, that separated melt phases are able to grow with time.

In this study, unmixing was observed between 1273 K and 1373 K. In the 1273 K to 1323 K field, the miscibility gap of this melt composition overlaps with the crystallisation field, resulting in a phase separation of the melt but also the beginning of crystallisation (Fig. 79). Despite the results of Wheaton and Clare (2007), no growth of the separated melts spheres was observed with time for this particular melt composition, but it is possible that it will occur at higher temperatures and with longer tempering time.

With longer tempering duration, the effect on the crystallisation was observed to be stronger than the effect on unmixing. Even though heat capacity spectra clearly showed two separated melt phases (Fig. 75), it could not be observed in backscattered electron images. Somewhere between 1323 K and 1373 K the stability field of crystallisation ends, leaving an unmixed, crystal-free melt at this temperature (Fig. 80b).

Tempering on other P_2O_5-bearing melts from CAS19-series results in unmixing solely for the CAS19-P6 melt. No evidence for unmixing was found for CAS19-P2 and CAS19-P4 melt with the used methods. However, it has to be pointed out that for all unmixed melts from P_2O_5-bearing CAS19 series, the colour of the samples changed from crystal clear to white. Thinner pieces of those melts show a blueish hue and the samples turn orange when observed with transmitted light, indicating a light scattering caused by the small unmixed melt spheres present in the melt.

This observation is important, since no unmixing was observed for the tempered sample CAS19-P2 and CAS19-P4. However, even though unmixing could not be detected with electron microscopy or heat capacity measurements, the samples still show this characteristic change in colour as well as light scattering after tempering, indicating a phase separation of the melts.

Therefore, we suggest that these melts are also unmixed. Experiments in this study have shown that unmixing was detected when the size of the separated melt spheres reaches at least nm range. The results from tempering experiments, however, show that these structural changes can be observed with the simple eye in formally colourless melts in form

of a characteristic light scattering, even if the methods fail to detect the separated phases due to the size.

Understanding the affinity of melts to unmix is important for geological as well as technical processes. Phase separation is very likely to affect crystallization due to the changing melt composition. Furthermore, unmixing was observed to change physical properties of the melts such as e.g. viscosity and heat capacity. The effect of phase separation on viscosity is of high importance, since viscosity is the parameter which describes the flow mechanism of the melts (e.g. Webb 1997; Webb and Dingwell 1995).

6.5.2 Effect of Unmixing on Viscosity

In this study it was observed that the viscosity of the sample changes during the development of liquid immiscibility. The intermediate viscosity was observed in the quenched melt. Viscosity measurements can be viewed as short tempering experiments since the samples are heated to a certain temperature and held at this temperature for a specific amount of time.

The previously measured sample showed a strong increase in viscosity compared to the quenched melt. From previous studies (e.g. Mysen et al. 1981a; Mysen 1992, 1996; Toplis and Dingwell 1996a; Mysen 1998a) as well as chapter 3 and 4 from this study it is known, that P_2O_5 enters the melt as tetrahedrally coordinated PO_4^{3-}. In peralkaline melts, where metal cations are present in network modifying positions, PO_4^{3-} bonds to those cations in network modifying positions, resulting in the formation of metal phosphate structural units and thus more bridging oxygen bonds. This stronger polymerisation of the melt results in higher viscosities.

The slowly cooled sample had more time to develop liquid immiscibility, which is also visible in BSE images of the samples. The two separate melt phases should have different viscosities. The viscosity of the Ca-P-rich and Si-poor melt is expected to be lower than the viscosity of the Si-Al-rich melt. Since unmixing occurs in nm scale and the spheres used for micropenetration viscometry have an average diameter of 2000 µm we always measure the average viscosity resulting from both melt phases which is even lower than the viscosity of the quenched melt.

It is not clear why and how the viscosity is increased during the beginning of unmixing and decreased when unmixing occurred.

However, this observation implies that before the melt separates into two or more different melt phases, the structural units of the second melt phase are at first incorporated into the Si-Al melt network, resulting in its polymerisation. This structure probably exhibits a high enthalpy, which can be lowered by the separation into two liquids.

6.6 Conclusions

In this study we have shown that tempering has an effect on phase separation of the P_2O_5-bearing peralkaline CAS19 melt. Depending on the temperature, increasing tempering duration time resulted in either crystal growth (at T = 1273 K) or the formation of detectable phase separation (at T ≥ 1323 K).

The stability fields of unmixing and crystal growth are overlapping in the peralkaline system of the highly P_2O_5-bearing CAS19-P8 melt (8 mol%) as observed from tempering experiments at 1323 K, where both, unmixing as well as crystallisation were observed. In the other P_2O_5-bearing samples of CAS19 series, unmixing after tempering was observed solely for sample CAS19-P6 containing 5.46 mol% P_2O_5. No unmixing was detected for the samples with lower P_2O_5 concentrations.

One characteristic of unmixed melts which were previously colourless has been found to be the change in colour to a milky white as well as a characteristic light scattering of the unmixed samples. We suggest that even though unmixing was not detected with the used methods for the melts with lower P_2O_5 concentration, that these samples are also unmixed due to the change in colour. The phase separation in these samples is simply too small for detection with the used methods. It has to be tested in future whether this small-scale unmixing can be resolved with TEM.

An increase in viscosity before phase separation indicates the formation of more polymerised structural units of the melts before separation into a Si-Al- and a Ca-P-rich melt takes place. How exactly this process works is unclear and a matter of debate for future studies.

The decrease in viscosity of the cooled melt is a result of unmixing, whereby the melt separates into a Si-Al-rich and an Ca-P-rich melt. The viscosity of the Si-Al-rich melt is expected to be higher than the viscosity of the homogeneous melt whereas the viscosity of the Ca-P-rich melt is lower than the viscosity of the formerly homogeneous melt. The measured viscosity of the unmixed melt is the resulting viscosity of both melts.

7 Final Conclusions

We have studied the sole effect of P_2O_5 and B_2O_3 as well as the combined effect of P_2O_5, B_2O_3, F^- and H_2O on rheology, structure and unmixing of aluminosilicate melts. Therefore, we have chosen six melts of the peralkaline and peraluminous Na_2O-Al_2O_3-SiO_2, CaO-Al_2O_3-SiO_2 and Na_2O-CaO-Al_2O_3-SiO_2 system as well as Champagne melt found on Gusev Crater on Mars. Champagne resembles a melt of basaltic composition and yields naturally high P_2O_5 concentrations of up to 10 wt% (Usui et al. 2008).

The results of our study agree with previous studies which suggest that in peralkaline melts the addition of P_2O_5 results in an increase in viscosity and thus polymerisation of the melt up to a viscosity maximum due to PO_4^{3-} taking out network modifying cations to form phosphate complexes (e.g. Mysen 1998a; Toplis and Dingwell 1996a). The viscosity maximum occurs at the P_2O_5 concentration at which all network modifying cations are charge balanced by PO_4^{3-} units (Toplis and Dingwell 1996a). The suggestion of e. g. Mysen et al. (1981a), Ryerson and Hess (1980), Gan and Hess (1992b), Toplis and Dingwell (1996a) and Mysen (1998b) that in peraluminous melts PO_4^{3-} bonds to Al^{3+} from tetrahedral positions resulting in the formation of units similar to $AlPO_4$ as observed in Raman spectra of berlinite and thus a depolymerisation and decrease of viscosity by freeing former charge-balancing cations which now act as network modifiers could be also confirmed with our data.

Furthermore, we found proof for the suggestion of Gan and Hess (1992b) who argued that the cation phosphates reside outside the aluminosilicate melt structure. In our samples, unmixing was observed for peralkaline Ca- as well as Ca- and Na- bearing melts in form of melt droplets of approximately 300-500 nm diameter, whereby unmixing is more pronounced in melts containing both Na and Ca. The best unmixing was observed for P_2O_5-bearing Champagne melt, whereby the size of the separated melt spheres reaches from 500 nm up to 100 µm size. Measurements of this melt composition showed, that the melt indeed separates into a Si-Al and a Ca-(Fe)-P-rich melt. In addition, there is evidence that divalent cations preferably become enriched in in the Ca-(Fe)-P-rich melt.

No unmixing is observed in peraluminous P_2O_5-bearing melts. However, the biggest unmixed melt spheres are visible after the viscosity maximum where no network modifying cations are left and PO_4 forms $AlPO_4$ structural units as observed in peraluminous melts. Therefore, we conclude that while $AlPO_4$ units do not form a separate melt phase, they preferably become enriched in a P-rich melt rather than in a Si-Al-rich melt and enhance previous unmixing, as is the case in P_2O_5-bearing peralkaline melts.

B_2O_3 is known to enter the melt as either network modifying BO_3 triangles or as network forming BO_4^- tetrahedra, whereby BO_3 triangles are converted to BO_4^- tetrahedra in the presence of network modifying cations (e.g. Konijnendijk 1975; Meera and Ramakrishna 1993; Lenoir et al. 2008; Manara et al. 2009). Despite this fact, the addition of B_2O_3 to peralkaline as well as peraluminous melts of our study results only in a decrease in viscosity and thus depolymerisation of the melt. However, in peralkaline melts a stronger decrease in viscosity is observed approximately at the B_2O_3 concentration where all network modifying cations would be charge balanced by BO_4^- tetrahedra. Thus, we come to the conclusion that in peralkaline melts the addition of low B_2O_3 concentrations up to approximately 6 mol% results in two competing mechanisms.

Firstly, BO_3 triangles are converted into BO_4^- tetrahedra which act as network former an increase the polymerisation. Second, at the same time BO_3 triangles act as network modifier and decrease the polymerisation of the melt. We suggest that the network modifying role of BO_3 tetrahedra shows a stronger effect on melt structure than the network forming role of BO_4^-, resulting in the observed decrease in viscosity. When no network modifying cations are left only the network modifying BO_3 triangles remain and the viscosity decreases more strongly. No unmixing of only B_2O_3-bearing melts was observed in this study with our melt compositions and at the used synthesis temperatures.

The combined effect of P_2O_5, B_2O_3, F^- and H_2O is very complex. In all melts, a decrease of viscosity as a result of melt depolymerisation is observed. In all water- and fluorine-bearing melts apatite crystallised during the synthesis in an IHPV at the used temperature and pressure. The addition of B_2O_3 to a previously unmixed melt can result in a mixing of both melts as well as an enhancement in unmixing. With increasing B_2O_3 concentration this effect is reversed. While this mechanism is not completely understood, it is observed that the mixing of the Si-Al- and Ca-(Fe)-P-rich melt is linked to the presence of BPO_4 structural units, which are absent in unmixed melts.

The addition of fluorine to the only P_2O_5- as well as P_2O_5- and B_2O_3-bearing melts results in a viscosity decrease and thus depolymerisation of the melt. No unmixing is observed in these samples at our synthesis conditions. From previous literature it is known that in peraluminous melts fluorine results in the formation of Al-F and Si-F bonds (e.g. Mysen and Virgo 1985a; Mysen and Virgo 1985b; Zeng and Stebbins 2000; Baasner et al. 2013a, 2013b; Baasner et al. 2014). In peralkaline melts, additionally Ca-F and Na-F bonds are formed, whereby F^- favours the bonding to Ca (Baasner et al. 2014). Therefore, we conclude that while no unmixing was observed under the used synthesis conditions, upon cooling the melt will most probably reach an immiscibility field where the melt separates into a Si-Al- and a Ca-P- rich melt. F^- will than become enriched in the Ca-P-rich melt and result in the

direct crystallisation of apatite from this melt. Presumably, the same may happen with water in the melt structure. However, more experiments at different temperatures are needed in order to proof this hypothesis.

Similar to what was observed by Wheaton and Clare (2007), the peralkaline CAS19 melt shows unmixing upon tempering. Furthermore, tempering of Fe-free colourless melts results in a change in colour to white with a characteristic light scattering, caused by tiny unmixed melt spheres of 300 nm size or lower. This scattering of light resembles Rayleigh scattering, which is known from processes in the atmosphere (McCartney 1976). This scattering is also observed in tempered samples with low P_2O_5 concentrations, where no unmixing could be detected with the used methods. We suggest that these melts are also unmixed due to the characteristic change in colour and light scattering. The size of the separated melt spheres is probably too small for detection with SEM and DSC.

The changes in viscosity of the melts with increasing P_2O_5, B_2O_3 and F^- concentration can be explained by the different incorporation mechanism. Unmixing does not significantly affect melt viscosity in this study. Mostly, the separated melt spheres are much smaller than the used spheres for the measurements of viscosity. Therefore, the resulting viscosity of both melts is measured. The effect of unmixing on the viscosity of melts becomes more important if the size of melt spheres increases. Furthermore, the development of veins which are enriched with one melt composition will also affect viscosity more strongly.

The results of our study demonstrate the complex incorporation behaviour of mainly P_2O_5 but also B_2O_3 and F^- on melt structure and unmixing. We found that mainly P_2O_5 but also CaO and FeO show a strong effect on unmixing of melts. Understanding the affinity of a melt to unmix is essential in order to gain better understanding of magmatic processes. Unmixing is likely to affect crystallisation due to the changing melt composition. It is also of importance in better understanding of the formation of large layered intrusions such as e.g. the Bushveld complex, where previous studies have introduced unmixing as the main mechanism for crystallisation of large apatite layers (e.g. Jakobsen et al. 2005; Fischer et al. 2016; Hou et al. 2018). Furthermore, it may play an important role in the petrogenesis of pegmatitic melts, which exhibit naturally high P_2O_5, B_2O_5 and F^- concentrations.

8 Outlook

This study investigates mainly the effect of P_2O_5 on unmixing of melts, but also the effect of B_2O_3, F^- and H_2O is taken into account. The results of this study have brought new insight into the unmixing process in melts, but also lead to new questions.

Tempering experiments on other melt compositions would give more insight into phase separation and the affinity of elements to cause unmixing. In this study tempering experiments were conducted solely on samples, where structural changes due to a heat treatment were apparent. From our results, there is no unmixing in peraluminous P_2O_5-bearing melts as well as in only Na-bearing peralkaline P_2O_5-bearing melts. Also, no unmixing is observed for only B_2O_3-bearing melts. Tempering experiments on these melts can further prove this observation or give new insight into the complex behaviour of phase separation of those elements.

The structural bonds resulting from incorporation of P_2O_5, B_2O_3 and F^- into the melt are based on the Raman spectra obtained in this study as well as results from previous studies. However, there are no studies which directly investigate the structural bonding or the change in those due to unmixing. An NMR study on unmixed melts can bring new findings in this matter. The combined effect of P_2O_5 and B_2O_3 on unmixing and the formation of BPO_4 groups in homogeneous melts as well as their absence in unmixed melts is thereby of particular interest.

Furthermore, this study describes limitations of the used models for calculation of viscosity, C_{pg} and C_{pl}. The results have shown that P_2O_5 as well as B_2O_3 and F^- but also the peralkalinity of the melt have a strong effect on melt viscosity as well as the liquid and glassy heat capacities. These observations should be considered in the development of future models.

9 References

Adam, Gerold; Gibbs, Julian H. (1965): On the Temperature Dependence of Cooperative Relaxation Properties in Glass-Forming Liquids. In *The Journal of Chemical Physics* 43 (1), pp. 139–146. DOI: 10.1063/1.1696442.

Ahmed, I.; Lewis, M.; Olsen, I.; Knowles, J. C. (2004): Phosphate glasses for tissue engineering: Part 1. Processing and characterisation of a ternary-based P2O5–CaO–Na2O glass system. In *Biomaterials* 25 (3), pp. 491–499. DOI: 10.1016/S0142-9612(03)00546-5.

Arvidson, R. E.; Squyres, S. W.; Anderson, R. C.; Bell, J. F.; Blaney, D.; Brückner, J. et al. (2006): Overview of the Spirit Mars Exploration Rover Mission to Gusev Crater. Landing site to Backstay Rock in the Columbia Hills. In *J. Geophys. Res.* 111 (E2), pp. 1–22. DOI: 10.1029/2005JE002499.

Baasner, A.; Schmidt, B. C.; Dupree, R.; Webb, S. L. (2014): Fluorine speciation as a function of composition in peralkaline and peraluminous Na2O–CaO–Al2O3–SiO2 glasses: A multinuclear NMR study. In *Geochimica et Cosmochimica Acta* 132, pp. 151–169. DOI: 10.1016/j.gca.2014.01.041.

Baasner, A.; Schmidt, B. C.; Webb, S. L. (2013a): Compositional dependence of the rheology of halogen (F, Cl) bearing aluminosilicate melts. In *Chemical Geology* 346, pp. 172–183. DOI: 10.1016/j.chemgeo.2012.09.020.

Baasner, A.; Schmidt, B. C.; Webb, S. L. (2013b): The effect of chlorine, fluorine and water on the viscosity of aluminosilicate melts. In *Chemical Geology* 357, pp. 134–149. DOI: 10.1016/j.chemgeo.2013.08.020.

Bartels, Alexander; Vetere, Francesco; Holtz, Francois; Behrens, Harald; Linnen, Robert L. (2011): Viscosity of flux-rich pegmatitic melts. In *Contrib Mineral Petrol* 162 (1), pp. 51–60. DOI: 10.1007/s00410-010-0582-3.

Borisov, Alexander; Behrens, Harald; Holtz, Francois (2013a): The effect of titanium and phosphorus on ferric/ferrous ratio in silicate melts. An experimental study. In *Contrib Mineral Petrol* 166 (6), pp. 1577–1591. DOI: 10.1007/s00410-013-0943-9.

Borisov, Alexander; Behrens, Harald; Holtz, Francois (2013b): The effect of titanium and phosphorus on ferric/ferrous ratio in silicate melts: an experimental study. In *Contrib Mineral Petrol* 166 (6), pp. 1577–1591. DOI: 10.1007/s00410-013-0943-9.

Bykov, V. N.; Ivanova, T. N.; Koroleva, O. N. (2011): Raman spectroscopy of borosilicate and germanate-silicate glasses and melts. In *Russ. Metall.* 2011 (8), pp. 719–722. DOI: 10.1134/S0036029511080040.

Cassidy, W. A.; Segnit, E. R. (1955): Liquid Immiscibility in a Silicate Melt. In *Nature* 4476, p. 305.

Charlier, B.; Namur, O.; Toplis, M. J.; Schiano, P.; Cluzel, N.; Higgins, M. D.; Auwera, J. V. (2011): Large-scale silicate liquid immiscibility during differentiation of tholeiitic basalt to granite and the origin of the Daly gap. In *Geology* 39 (10), pp. 907–910. DOI: 10.1130/G32091.1.

Charlier, Bernard (2015): Stable and metastable silicate liquid immiscibility in ferrobasalts. In *American Mineralogist* 100 (11-12), pp. 2367–2368. DOI: 10.2138/am-2015-5448.

Charlier, Bernard; Grove, Timothy L. (2012): Experiments on liquid immiscibility along tholeiitic liquid lines of descent. In *Contrib Mineral Petrol* 164 (1), pp. 27–44. DOI: 10.1007/s00410-012-0723-y.

Charlier, Bernard; Namur, Olivier; Grove, Timothy L. (2013): Compositional and kinetic controls on liquid immiscibility in ferrobasalt–rhyolite volcanic and plutonic series. In *Geochimica et Cosmochimica Acta* 113, pp. 79–93. DOI: 10.1016/j.gca.2013.03.017.

Cochain, B.; Neuville, D. R.; Ligny, D. de; Malki, M.; Testemale, D.; Pinet, O.; Richet, P. (2013): Dynamics of iron-bearing borosilicate melts: Effects of melt structure and composition on viscosity, electrical conductivity and kinetics of redox reactions. In *Journal of Non-Crystalline Solids* 373-374, pp. 18–27. DOI: 10.1016/j.jnoncrysol.2013.04.006.

De Wys. E. C. (1960): A possible explanation of immiscibility in silicate melts. In *Mineralogical Magazine* 32, pp. 471–479.

Di Muro, Andrea; Métrich, Nicole; Mercier, Maxime; Giordano, Daniele; Massare, Dominique; Montagnac, Gilles (2009): Micro-Raman determination of iron redox state in dry natural glasses: Application to peralkaline rhyolites and basalts. In *Chemical Geology* 259 (1-2), pp. 78–88. DOI: 10.1016/j.chemgeo.2008.08.013.

Dingwell, D. B.; Knoche, R.; Webb, S. L.; Pichavant, M. (1992): The effect of B2O3 on the viscosity of haplogranitic liquids. In *American Mineralogist* 77, pp. 457–461.

Dixon, S.; Rutherford, M. J. (1979): PLAGIOGRANITES AS LATE-STAGE IMMISCIBLE LIQUIDS IN OPHIOLITE AND MID-OCEAN RIDGE SUITES AN EXPERIMENTAL STUDY. In *Earth and Planetary Science Letters* 45, pp. 45–60.

Fischer, Lennart A.; Wang, Meng; Charlier, Bernard; Namur, Olivier; Roberts, R. James; Veksler, Ilya V. et al. (2016): Immiscible iron- and silica-rich liquids in the Upper Zone of the Bushveld Complex. In *Earth and Planetary Science Letters* 443, pp. 108–117. DOI: 10.1016/j.epsl.2016.03.016.

Gan, Hao; Hess, Paul C. (1992a): Phosphate speciation in potassium aluminosilicate glasses. In *American Mineralogist* (77), pp. 495–506.

Gan, Hao; Hess, Paul C. (1992b): Phosphate speciation in potassium aluminosilicate glasses. In *American Mineralogist* 77, pp. 495–506.

Gellert, R.; Rieder, R.; Brückner, J.; Clark, B. C.; Dreibus, G.; Klingelhöfer, G. et al. (2006): Alpha Particle X-Ray Spectrometer (APXS). Results from Gusev crater and calibration report. In *J. Geophys. Res.* 111 (E2), pp. n/a-n/a. DOI: 10.1029/2005JE002555.

Giordano, Daniele; Russell, James K.; Dingwell, Donald B. (2008a): Viscosity of magmatic liquids. A model. In *Earth and Planetary Science Letters* 271 (1-4), pp. 123–134. DOI: 10.1016/j.epsl.2008.03.038.

Giordano, Daniele; Russell, James K.; Dingwell, Donald B. (2008b): Viscosity of magmatic liquids: A model. In *Earth and Planetary Science Letters* 271 (1-4), pp. 123–134. DOI: 10.1016/j.epsl.2008.03.038.

Gwinn, Rosa; Hess, Paul C. (1993): The role of phosphorus in rhyolitic liquids as determined from the homogeneous iron redox equilibrium. In *Contr. Mineral. and Petrol.* 113 (3), pp. 424–435. DOI: 10.1007/BF00286932.

Ha, Ming-Tai; Garofalini, Stephen H. (2017): Local structure of network modifier to network former ions in soda-lime alumino-borosilicate glasses. In *J Am Ceram Soc.* 100 (2), pp. 563–573. DOI: 10.1111/jace.14565.

Haller, W.; Blackburn, D. H.; Wagstaff, F. E.; Charles, R. J. (1970): Metastable Immiscibility Surface in the System Na2O-B2O3-SiO2 53, pp. 34–39.

Hill, Robert G.; Brauer, Delia S. (2011): Predicting the bioactivity of glasses using the network connectivity or split network models. In *Journal of Non-Crystalline Solids* 357 (24), pp. 3884–3887. DOI: 10.1016/j.jnoncrysol.2011.07.025.

Hodroj, Abbas; Simon, Patrick; Florian, Pierre; Chopinet, Marie-Hélène; Vaills, Yann; Mauro, J. (2013): Phase Separation and Spatial Morphology in Sodium Silicate Glasses by AFM, Light Scattering and NMR. In *J. Am. Ceram. Soc.* 96 (8), pp. 2454–2460. DOI: 10.1111/jace.12459.

Holness, M. B.; Stripp, G.; Humphreys, M. C. S.; Veksler, I. V.; Nielsen, T. F. D.; Tegner, Christian (2011): Silicate Liquid Immiscibility within the Crystal Mush: Late-stage Magmatic Microstructures in the Skaergaard Intrusion, East Greenland. In *Journal of Petrology* 52 (1), pp. 175–222. DOI: 10.1093/petrology/egq077.

Hou, Tong; Charlier, Bernard; Holtz, François; Veksler, Ilya; Zhang, Zhaochong; Thomas, Rainer; Namur, Olivier (2018): Immiscible hydrous Fe-Ca-P melt and the origin of iron oxide-

apatite ore deposits. In *Nature communications* 9 (1), p. 1415. DOI: 10.1038/s41467-018-03761-4.

Jakobsen, J. K.; Veksler, I. V.; Tegner, C.; Brooks, C. K. (2005): Immiscible iron- and silica-rich melts in basalt petrogenesis documented in the Skaergaard intrusion. In *Geol* 33 (11), p. 885. DOI: 10.1130/G21724.1.

Jakobsen, J. K.; Veksler, I. V.; Tegner, C.; Brooks, C. K. (2011): Crystallization of the Skaergaard Intrusion from an Emulsion of Immiscible Iron- and Silica-rich Liquids: Evidence from Melt Inclusions in Plagioclase. In *Journal of Petrology* 52 (2), pp. 345–373. DOI: 10.1093/petrology/egq083.

Kathryn Lynn Goetschius: The effect of composition on the viscosity, crystallization and dissolution of simple borate glasses and compositional design of borate based bioactive glasses.

Kohn, S. C.; Dupree, R.; Mortuza, M. G.; Henderson, C.M.B. (1991): NMR evidence for five- and six-coordinated aluminum fluoride complexes in F-bearing aluminosilicate glasses. In *American Mineralogist* 76, pp. 309–312.

Konijnendijk, W. WillemL (1975): The structure of borosilicate glasses. With assistance of J. M. Stevels, G. C.A. Schuit.

Koroleva, O. N.; Shabunina, L. A.; Bykov, V. N. (2011): Structure of borosilicate glass according to raman spectroscopy data. In *Glass Ceram* 67 (11-12), pp. 340–342. DOI: 10.1007/s10717-011-9293-0.

Kress, Victor C.; Carmichael, Ian S. E. (1991): The compressibility of silicate liquids containing Fe2O3 and the effect of composition, temperature, oxygen fugacity and pressure on their redox states. In *Contr. Mineral. and Petrol.* 108 (1-2), pp. 82–92. DOI: 10.1007/BF00307328.

Kushiro, I. (1975): On the nature of silicate melt and its significance in magma genesis: Regularities in the shift of the liquidus boundaries involving olivine, pyroxene and silica minerals. In *American Journal of Science* 275, pp. 411–431.

Lenoir, M.; Grandjean, A.; Linard, Y.; Cochain, B.; Neuville, D. R. (2008): The influence of Si,B substitution and of the nature of network-modifying cations on the properties and structure of borosilicate glasses and melts. In *Chemical Geology* 256 (3-4), pp. 316–325. DOI: 10.1016/j.chemgeo.2008.07.002.

Lester, G. W.; Clark, A. H.; Kyser, T. K.; Naslund, H. R. (2013): Experiments on liquid immiscibility in silicate melts with H2O, P, S, F and Cl. Implications for natural magmas. In *Contrib Mineral Petrol* 166 (1), pp. 329–349. DOI: 10.1007/s00410-013-0878-1.

London, D. (2008): Pegmatites. Special Publication 10: Mineralogical Association of Canada.

London, D. (2009): THE ORIGIN OF PRIMARY TEXTURES IN GRANITIC PEGMATITES. In *The Canadian Mineralogist* 47 (4), pp. 697–724. DOI: 10.3749/canmin.47.4.697.

London, David (1987): Internal differentiation of rare-element pegmatites: Effects of boron, phosphorus, and fluorine. In *Geochimica et Cosmochimica Acta* 51 (3), pp. 403–420. DOI: 10.1016/0016-7037(87)90058-5.

Long, D. A. (1977): The Raman effect. A unified treatment of the theory of Raman scattering by molecules. Chichester, New York: Wiley.

Maier, Chas. G.; Kelley, K. K. (1932): AN EQUATION FOR THE REPRESENTATION OF HIGH-TEMPERATURE HEAT CONTENT DATA 1. In *J. Am. Chem. Soc.* 54 (8), pp. 3243–3246. DOI: 10.1021/ja01347a029.

Manara, D.; Grandjean, A.; Neuville, D. R. (2009): Structure of borosilicate glasses and melts: A revision of the Yun, Bray and Dell model. In *Journal of Non-Crystalline Solids* 355 (50-51), pp. 2528–2531. DOI: 10.1016/j.jnoncrysol.2009.08.033.

McCartney, J. (1976): Optics of the Atmosphere - Scattering by Molecules and Particles. New York: Wiley (Wiley Series in Pure and Applied Optics).

McMillan, Paul; Piriou, Bernard; Navrotsky, Alexandra (1982): A Raman spectroscopic study of glasses along the joins silica-calcium aluminate, silica-sodium aluminate, and silica-potassium aluminate. In *Geochimica et Cosmochimica Acta* 46 (11), pp. 2021–2037. DOI: 10.1016/0016-7037(82)90182-X.

McMillan, Paul F.; Wolf, George H.; Poe, Brent T. (1992): Vibrational spectroscopy of silicate liquids and glasses. In *Chemical Geology* 96 (3-4), pp. 351–366. DOI: 10.1016/0009-2541(92)90064-C.

McSween, H. Y.; Ruff, S. W.; Morris, R. V.; Gellert, R.; Klingelhöfer, G.; Christensen, P. R. et al. (2008): Mineralogy of volcanic rocks in Gusev Crater, Mars. Reconciling Mössbauer, Alpha Particle X-Ray Spectrometer, and Miniature Thermal Emission Spectrometer spectra. In *J. Geophys. Res.* 113 (E6). DOI: 10.1029/2007JE002970.

McSween, H. Y.; Wyatt, M. B.; Gellert, R.; Bell, J. F.; Morris, R. V.; Herkenhoff, K. E. et al. (2006): Characterization and petrologic interpretation of olivine-rich basalts at Gusev Crater, Mars. In *J. Geophys. Res.* 111 (E2). DOI: 10.1029/2005JE002477.

Meera, B. N.; Ramakrishna, J. (1993): Raman spectral studies of borate glasses. In *Journal of Non-Crystalline Solids* 159 (1-2), pp. 1–21. DOI: 10.1016/0022-3093(93)91277-A.

Möncke, Doris; Tricot, Gregory; Winterstein-Beckmann, Anja; Wondraczek, Lothar; Kamitsos, Efstratios I. (2015): On the connectivity of borate tetrahedra in borate and borosilicate glasses. In *Phys. Chem. Glasses: Eur. J. Glass Sci. Technol. B* 56 (5), pp. 203–211. DOI: 10.13036/1753-3562.56.5.203.

Money, Benson K.; Hariharan, K. (2008): Glass formation and electrical conductivity studies of melt quenched and mechanically milled 50Li2O:(50−x) P2O5:xB2O3. In *Solid State Ionics* 179 (27-32), pp. 1273–1277. DOI: 10.1016/j.ssi.2007.12.068.

Moynihan, Cornelius T.; Easteal, Allen J.; Debolt, Mary Ann de; Tucker, Joseph; seph Tucker (1976): Dependence of the Fictive Temperature of Glass on Cooling Rate. In *J. Am. Ceram. Soc.* 59, pp. 12–16.

Mysen, B. O. (1998a): Phosphorus solubility mechanisms in haplogranitic aluminosilicate glass and melt: effect of temperature and aluminum content. In *Contr. Mineral. and Petrol.* 133, pp. 38–50.

Mysen, B. O.; Finger, L. W.; Virgo, D.; Seifert, F. A. (1982): Curve fitting of Raman spectra of silicate glasses. In *American Mineralogist* 67, pp. 686–695.

Mysen, B. O.; Ryerson, F. J.; Virgo, D. (1981a): The structural role of phosphorus in silicate melts. In *American Mineralogist* (66), pp. 106–117.

Mysen, B. O.; Toplis, M. J. (2007): Structural behavior of Al3+ in peralkaline, metaluminous, and peraluminous silicate melts and glasses at ambient pressure. In *American Mineralogist* 92 (5-6), pp. 933–946. DOI: 10.2138/am.2007.2334.

Mysen, B. O.; Virgo, D.; Kushiro, I. (1981b): The structural role of aluminum in silicate melts a raman spectroscopic study at 1 atm. In *American Mineralogist* 66, pp. 678–701.

Mysen, Bjorn O. (1992): Iron and phosphorus in calcium silicate quenched melts. In *Chemical Geology* 98 (3-4), pp. 175–202. DOI: 10.1016/0009-2541(92)90184-7.

Mysen, Bjorn O. (1996): Phosphorus speciation changes across the glass transition in highly polymerized alkali silicate glasses and melts. In *American Mineralogist* 81, pp. 1531–1534.

Mysen, Bjorn O. (1998b): Phosphorus solubility mechanisms in haplogranitic aluminosilicate glass and melt: effect of temperature and aluminum content. In *Contrib Mineral Petrol* 133 (1-2), pp. 38–50. DOI: 10.1007/s004100050435.

Mysen, Bjorn O.; Virgo, David (1985a): Structure and properties of fluorine-bearing aluminosilicate melts: the system Na2O-Al2O3-SiO2-F at 1 atm. In *Contrib Mineral Petrol* 91, pp. 205–220.

Mysen, Bjrn O.; Virgo, David (1985b): Interaction between fluorine and silica in quenched melts on the joins SiO2-AlF3 and SiO2-NaF determined by raman spectroscopy. In *Phys Chem Minerals* 12 (2), pp. 77–85. DOI: 10.1007/BF01046830.

Pocklington, H. C. (1940): Rough measurement of high viscosities. In *Math. Proc. Camb. Phil. Soc.* 36 (04), p. 507. DOI: 10.1017/S0305004100017564.

Richet, P. (1985a): Heat capacity of aluminum-free liquid silicates. In *Geochimica et Cosmochimica Acta* 49, pp. 471–486.

Richet, P. (1985b): Heat capacity of aluminum-free liquid silicates. In *Geochimica et Cosmochimica Acta* 49, pp. 471–486.

Richet, Pascal (1987): Heat capacity of silicate glasses. In *Chemical Geology* 62 (1-2), pp. 111–124. DOI: 10.1016/0009-2541(87)90062-3.

Richet, Pascal; Bottinga, Yan (1985): Heat capacity of aluminum-free liquid silicates. In *Geochimica et Cosmochimica Acta* 49 (2), pp. 471–486. DOI: 10.1016/0016-7037(85)90039-0.

Richet, Pascal; Robie, Richard A.; Hemingway, Bruce S. (1986): Low-temperature heat capacity of diopside glass (CaMgSi2O6). A calorimetric test of the configurational-entropy theory applied to the viscosity of liquid silicates. In *Geochimica et Cosmochimica Acta* 50, pp. 1521–1533.

Robert, Geneviève; Whittington, Alan G.; Stechern, André; Behrens, Harald (2013): The effect of water on the viscosity of a synthetic calc-alkaline basaltic andesite. In *Chemical Geology* 346, pp. 135–148. DOI: 10.1016/j.chemgeo.2012.10.004.

Robie, R. A.; Hemingway, B. S.; Fisher, J. R. (1978a): Thermodynamic Properties of Minerals and Related Substances at 298.15 K and 1 Bar (10^5 Pascals) Pressure and at Higher Temperatures. Washington: U.S. Geological Survey Bulletin (1452).

Robie, R. A.; Hemingway, B. S.; Wilson, W. H. (1978b): Low-temperature heat capacities and entropies of feldspar glasses and of anorthite. In *American Mineralogist* 63, pp. 109–123.

Roedder, Edwin; Weiblen, Paul W. (1971a): Petrology of silicate melt inclusions, Apollo 11 and Apollo 12 and terrestrial equivalents. In *Proceedings of the Lunar Science Conference* 2, pp. 507–528.

Roedder, Edwin; Weiblen, Paul W. (1971b): Petrology of silicate melt inclusions, Apollo 11 and Apollo 12 and terrestrial equivalents. In *Proceedings of the Lunar Science Conference* 2, pp. 507–528.

Ruff, S. W.; Christensen, P. R.; Blaney, D. L.; Farrand, W. H.; Johnson, J. R.; Michalski, J. R. et al. (2006): The rocks of Gusev Crater as viewed by the Mini-TES instrument. In *J. Geophys. Res.* 111 (E12). DOI: 10.1029/2006JE002747.

Ryerson, F. J.; Hess, P. C. (1978): IMPLICATIONS OF LIQUID-LIQUID DISTRIBUTION COEFFICIENTS TO MINERAL-LIQUID PARTITIONING. In *Geochimica et Cosmochimica Acta* 42, pp. 921–932.

Ryerson, F. J.; Hess, P. C. (1980): The role of P2O5 in silicate melts. In *Geochimica et Cosmochimica Acta* 44, pp. 611–624.

Schuessler, J. A.; Botcharnikov, R. E.; Behrens, H.; Misiti, V.; Freda, C. (2008): Amorphous Materials: Properties, structure, and Durability: Oxidation state of iron in hydrous phono-tephritic melts. In *American Mineralogist* 93 (10), pp. 1493–1504. DOI: 10.2138/am.2008.2795.

Sehlke, Alexander; Whittington, Alan G. (2016): The viscosity of planetary tholeiitic melts. A configurational entropy model. In *Geochimica et Cosmochimica Acta* 191, pp. 277–299. DOI: 10.1016/j.gca.2016.07.027.

Shelby, James E. (2005): Introduction to Glass Science and Technology. Cambridge, UK: The Royal Society of Chemistry.

Squyres, Steven W.; Arvidson, Raymond E.; Blaney, Diana L.; Clark, Benton C.; Crumpler, Larry; Farrand, William H. et al. (2006): Rocks of the Columbia Hills. In *J. Geophys. Res.* 111 (E2). DOI: 10.1029/2005JE002562.

Stebbins, J. F.; Carmichael, I. S. E.; Moret, L. K. (1984): Heat capacities and entropies of silicate liquids and glasses. In *Contr. Mineral. and Petrol.* 86 (2), pp. 131–148. DOI: 10.1007/BF00381840.

Stebbins, Jonathan F. (2016): Glass structure, melt structure, and dynamics: Some concepts for petrology. In *American Mineralogist* 101 (4), pp. 753–768. DOI: 10.2138/am-2016-5386.

Thomas, R.; Webster, J. D. (2000): Strong tin enrichment in a pegmatite-forming melt. In *Mineralium Deposita* 35 (6), pp. 570–582. DOI: 10.1007/s001260050262.

Thompson, A. B.; Aerts, M.; Hack, A. C. (2007): Liquid Immiscibility in Silicate Melts and Related Systems. In *Reviews in Mineralogy and Geochemistry* 65 (1), pp. 99–127. DOI: 10.2138/rmg.2007.65.4.

Tomozawa, Minoru; Sridharan, Srinivasan; Takamori, Takeshi (1992): Origin of Viscosity Increase of Phase-Separated Borosilicate Glasses. In *J American Ceramic Society* 75 (11), pp. 3103–3110. DOI: 10.1111/j.1151-2916.1992.tb04394.x.

Toplis, M. J.; Dingwell, D. B. (1996a): The variable influence of P2O5 on the viscosity of melts of differing alkali/aluminium ratio: Implications for the structural role of phosphorus in silicate melts. In *Geochimica et Cosmochimica Acta* 60 (21), pp. 4107–4121. DOI: 10.1016/S0016-7037(96)00225-6.

Toplis, M. J.; Dingwell, D. B. (1996b): The variable influence of P2O5 on the viscosity of melts of differing alkali/aluminiumratio: Implications for the structural role of phosphorus in silicate melts. In *Geochimica et Cosmochimica Acta* (60), pp. 4107–4121.

Toplis, M. J.; Dingwell, D. B.; Libourel, G. (1994a): The effect of phosphorus on the iron redox ratio, viscosity, and density of an evolved ferro-basalt. In *Contr. Mineral. and Petrol.* 117 (3), pp. 293–304. DOI: 10.1007/BF00310870.

Toplis, M. J.; Dingwell, D. B.; Tomasso, L. (1997a): Peraluminous viscosity maxima in Na2O-Al2O3-SiO2 liquids. The role of triclusters in tectosilicate melts. In *Geochimica et Cosmochimica Acta* 61, pp. 2605–2612.

Toplis, M.J; Reynard, B. (2000): Temperature and time-dependent changes of structure in phosphorus containing aluminosilicate liquids and glasses: in situ Raman spectroscopy at high temperature. In *Journal of Non-Crystalline Solids* 263-264, pp. 123–131. DOI: 10.1016/S0022-3093(99)00628-6.

Toplis, Michael J.; Dingwell, Donald B.; Hess, Kai-Uwe; Lenci, Tommaso (1997b): Viscosity, fragility, and configurational entropy of melts along the join SiO 2 -NaAlSiO 4. In *American Mineralogist* 82 (9-10), pp. 979–990. DOI: 10.2138/am-1997-9-1014.

Toplis, Michael J.; Libourel, Guy; Carroll, Michael R. (1994b): The role of phosphorus in crystallisation processes of basalt: An experimental study. In *Geochimica et Cosmochimica Acta* (Vol. 58), pp. 797–810.

Toplis, Michael J.; Libourel, Guy; Carroll, Michael R. (1994c): The role of Phosphorus in crystallisation processes of basalt: An experimental study. In *Geochimica et Cosmochimica Acta* (58), pp. 797–810.

Toplis, Michael J.; Schaller, Torsten (1998): A 31P MAS NMR study of glasses in the system xNa2O-(1-x)Al2O3-2SiO2-yP2O5. In *Journal of Non-Crystalline Solids* 224, pp. 57–68.

Usui, Tomohiro; McSween, Harry Y.; Clark, Benton C. (2008): Petrogenesis of high-phosphorous Wishstone Class rocks in Gusev Crater, Mars. In *J. Geophys. Res.* 113 (E12). DOI: 10.1029/2008JE003225.

Wanless, V. D.; Perfit, M. R.; Ridley, W. I.; Wallace, P. J.; Grimes, C. B.; Klein, E. M. (2011): Volatile abundances and oxygen isotopes in basaltic to dacitic lavas on mid-ocean ridges:

The role of assimilation at spreading centers. In *Chemical Geology* 287 (1-2), pp. 54–65. DOI: 10.1016/j.chemgeo.2011.05.017.

Webb, Sharon L. (1997): Lecture Notes in Earth Sciences. Silicate Melts. Berlin-Heidelberg: Springer.

Webb, Sharon L. (2008): Configurational heat capacity of Na 2 O–CaO–Al 2 O 3 –SiO 2 melts. In *Chemical Geology* 256 (3-4), pp. 92–101. DOI: 10.1016/j.chemgeo.2008.04.003.

Webb, Sharon L.; Banaszak, Magdalena; Köhler, Ursula; Rausch, Svenja; Raschke, Gerrit (2007): The viscosity of Na_2O-CaO-Al_2O_3-SiO_2 melts. In *Eur.J.Mineral.* 19 (5), pp. 681–692. DOI: 10.1127/0935-1221/2007/0019-1765.

Webb, Sharon L.; Dingwell, Donald B. (1995): Viscoelasticity. In *Reviews in Mineralogy* 32, pp. 95–119.

Wheaton, Bryan R.; Clare, Alexis G. (2007): Evaluation of phase separation in glasses with the use of atomic force microscopy. In *Journal of Non-Crystalline Solids* 353 (52-54), pp. 4767–4778. DOI: 10.1016/j.jnoncrysol.2007.06.073.

Wilson, A. D. (1960): The Micro-determination of Ferrous Iron is Silicate Minerals by a Volumetric and Colorimetric Method. In *Analyst* 85, pp. 823–827.

Wu, Jingshi; Stebbins, Jonathan F. (2009): Effects of cation field strength on the structure of aluminoborosilicate glasses: High-resolution 11B, 27Al and 23Na MAS NMR. In *Journal of Non-Crystalline Solids* 355 (9), pp. 556–562. DOI: 10.1016/j.jnoncrysol.2009.01.025.

Wys, E. Christiaan de (1960): A possible explanation of immiscibility in silicate melts. In *Mineral. mag. j. Mineral. Soc.* 32 (249), pp. 471–479. DOI: 10.1180/minmag.1960.032.249.06.

Zeng, Qiang; Stebbins, Jonathan F. (2000): Fluoride sites in aluminosilicate glasses: High-resolution 19F NMR results. In *American Mineralogist* 85, pp. 863–867.